Geogrid Reinforced Aggregate Base Stiffness for Mechanistic Pavement Design

John Siekmeier, Principal Investigator
Minnesota Department of Transportation

July 2016

To request this document in an alternative format call 651-366-4718 or 1-800-657-3774 (Greater Minnesota) or email your request to ADArequest.dot@state.mn.us. Please request at least one week in advance.

Technical Report Documentation Page

1. Report No. MN/RC 2016-24	2.	3. Recipients Accession No.	
4. Title and Subtitle Geogrid Reinforced Aggregate Base Stiffness for Mechanistic Pavement Design		5. Report Date July 2016	
		6.	
7. Author(s) John Siekmeier, Joseph Casanova		8. Performing Organization Report No.	
9. Performing Organization Name and Address Minnesota Department of Transportation Office of Materials and Road Research 1400 Gervais Avenue, MS 645 Maplewood, MN, 55109		10. Project/Task/Work Unit No.	
		11. Contract (C) or Grant (G) No. (c) LAB4006	
12. Sponsoring Organization Name and Address Minnesota Department of Transportation Research Services & Library 395 John Ireland Boulevard, MS 330 St. Paul, Minnesota 55155-1899		13. Type of Report and Period Covered Final Report	
		14. Sponsoring Agency Code	
15. Supplementary Notes http://www.lrrb.org/pdf/201624.pdf			

16. Abstract (Limit: 250 words)

The pavement design package created by Itasca extends the capabilities of PFC3D to support triaxial testing of a synthetic unsaturated aggregate base containing geogrid. The geogrid provides lateral restraint to the aggregate base as a result of interlocking and friction between the geogrid and the aggregate particles. The macroscopic system properties are affected by the microstructural system properties. Therefore, the modeled system was used to study and quantify the effect of microstructural properties on the macroscopic properties, which include the stress-strain curves produced during triaxial tests at different confinements. The microstructural properties of the aggregate base include: particle size, particle type (density, Young's modulus, and Poisson's ratio of each particle; and friction between particles), aggregate base moisture content (suction and gap), and initial aggregate base porosity. The microstructural properties of the geogrid include: geometry (aperture and rib dimensions), Young's modulus, bond stiffness, and grid-grain interface behavior. The pavement design package provides a mechanistically defensible model for aggregate-geogrid interaction, which was used to improve pavement design by estimating geogrid gain factors for typical geogrid-reinforced aggregate roadways. It is anticipated that a simplified geogrid gain factor adjustment will be trialed during pavement design for projects where geogrid is being considered. As expected, this study concludes that geogrid provides benefit and that this benefit varies during the year. Therefore, it is recommended that the seasonal effects be included during implementation. This would allow the fatigue and rutting to be more accurately estimated over the expected pavement design life.

17. Document Analysis/Descriptors geogrids, mechanistic design, performance measurement, aggregates		18. Availability Statement No restrictions. Document available from: National Technical Information Services, Alexandria, Virginia 22312	
19. Security Class (this report) Unclassified	20. Security Class (this page) Unclassified	21. No. of Pages 206	22. Price

Geogrid Reinforced Aggregate Base Stiffness for Mechanistic Pavement Design

Final Report

Prepared by:
John Siekmeier
Joseph Casanova
Minnesota Department of Transportation

July 2016

ACKNOWLEDGMENTS

Table of Contents

LIST OF FIGURES

LIST OF TABLES

EXECUTIVE SUMMARY

In Minnesota geogrid has traditionally been used to provide a more stable construction platform by improving the strength of the pavement foundation when weak soils are present (Clyne 2011). A more recent geogrid application has been to provide additional stiffness to the aggregate base layer, which can then more effectively protect the underlying soil layers from traffic loads. Geogrid reinforcement is known to help increase aggregate compaction during construction, and it is also expected to improve both the short-term and long-term performance of roadways (Skallman 2010). However greater justification of this expectation was desired, and therefore the investigation described in this report was undertaken in two phases to better understand and quantify the structural benefit of geogrid on the performance of asphalt surfaced roadways. Phase one of the investigation combined the analyses completed by Braun Intertec (Oman 2013) with analyses using the mechanistic-empirical pavement design program, MnPAVE (Tanquist 2012). During spring 2013, Braun Intertec conducted falling weight deflectometer (FWD) tests on two trunk highways in the Bemidji District to compare roadways with geosynthetics to roadways without geosynthetics. It was concluded that the geogrid generally reduces pavement deflection, but it was not possible to accurately quantify the structural benefit due to variability of the recycled aggregate base produced by full depth reclamation (FDR) and the variability of the in-situ soil layers (Casanova and Siekmeier 2013). Therefore, phase two of this investigation began in 2014 when Itasca Consulting Group was contracted by MnDOT to enhance its distinct element software Particle Flow Code 3D (PFC3D). PFC3D was then used to estimate the increased stiffness of geogrid-reinforced aggregate base for use in MnPAVE. The conclusions contained in this report are based on field and laboratory testing combined with numerical analyses performed using both PFC3D and MnPAVE.

The pavement design package created by Itasca extends the capabilities of PFC3D to support triaxial testing of a synthetic unsaturated aggregate base containing geogrid. The geogrid provides lateral restraint to the aggregate base as a result of interlocking and friction between the geogrid and the aggregate particles. The macroscopic system properties are affected by the microstructural system properties. Therefore, the modeled system was used to study and quantify the effect of microstructural properties on the macroscopic properties, which include the stress-strain curves produced during triaxial tests at different confinements. The microstructural properties of the aggregate base include: particle size, particle type (density, Young's modulus, and Poisson's ratio of each particle; and friction between particles), aggregate base moisture content (suction and gap), and initial aggregate base porosity. The microstructural properties of the geogrid include: geometry (aperture and rib dimensions), Young's modulus, bond stiffness, and grid-grain interface behavior. The pavement design package provides a mechanistically defensible model for aggregate-geogrid interaction, which was used to improve pavement design by estimating geogrid gain factors for typical geogrid-reinforced aggregate roadways. It is anticipated that a simplified geogrid gain factor adjustment will be trialed during pavement design for projects where geogrid is being considered. As expected, this study concludes that geogrid provides benefit and that this benefit varies during the year. Therefore, it is recommended that the seasonal effects be included during implementation. This would allow the fatigue and rutting to be more accurately estimated over the expected pavement design life.

CHAPTER 1: INTRODUCTION

In Minnesota geogrid has traditionally been used to provide a more stable construction platform by improving the strength of the pavement foundation when weak soils are present (Clyne 2011). A more recent geogrid application has been to provide additional stiffness to the aggregate base layer, which can then more effectively protect the underlying soil layers from traffic loads. Geogrid reinforcement is known to help increase aggregate compaction during construction and it is also expected to improve both the short-term and long-term performance of roadways (Skallman 2010). However greater justification of this expectation was desired and therefore the investigation described in this report was undertaken in two phases to better understand and quantify the structural benefit of geogrid on the performance of asphalt surfaced roadways. Phase one of the investigation combined the analyses completed by Braun Intertec (Oman 2013) with analyses using the mechanistic-empirical pavement design program, MnPAVE (Tanquist 2012). During the spring of 2013 Braun Intertec conducted falling weight deflectometer (FWD) tests on two trunk highways in the Bemidji District to compare roadways with geosynthetics to roadways without geosynthetics. It was concluded that the geogrid generally reduces pavement deflection, but it was not possible to accurately quantify the structural benefit due to variability of the recycled aggregate base produced by full depth reclamation (FDR) and the variability of the in situ soil layers (Casanova and Siekmeier 2013). Therefore phase two of this investigation began in 2014 when Itasca Consulting Group was contracted by MnDOT to enhance its distinct element software Particle Flow Code 3D (PFC3D). PFC3D was then used to estimate the increased stiffness of geogrid-reinforced aggregate base for use in MnPAVE. The conclusions contained in this report are based on field and laboratory testing combined with numerical analyses performed using both PFC3D and MnPAVE.

1.1 Geosynthetics

The two main types of geosynthetics used in roadways are geotextiles and geogrids. This report is focused on geogrids and therefore the benefits of geotextiles will not be discussed. The structural benefits of geogrid have been described as: lateral restraint, modified failure surface, and tensioned membrane (Erickson and Drescher 2001). Lateral restraint occurs when the properly placed geogrid constrains the unbound material (Figure 1.1). Modified failure surface occurs when the geogrid reinforces a potential failure surface and increases the bearing capacity. Tensioned membrane occurs when deflection is resisted by the tensile stiffness of the geogrid acting similar to a trampoline. Geogrid is a petroleum product typically made of polypropylene or polyethylene that is punched and stretched, or woven, to create a planar structure. Geogrid can be further split into three broad categories: uniaxial, biaxial, and triaxial. Uniaxial geogrid provides tensile stiffness and strength mainly in one planar direction. Biaxial geogrid, which is the type of geogrid investigated in this report, provides tensile stiffness and strength both longitudinally and laterally. And triaxial geogrid provides tensile stiffness and strength more uniformly in the plane of the geogrid.
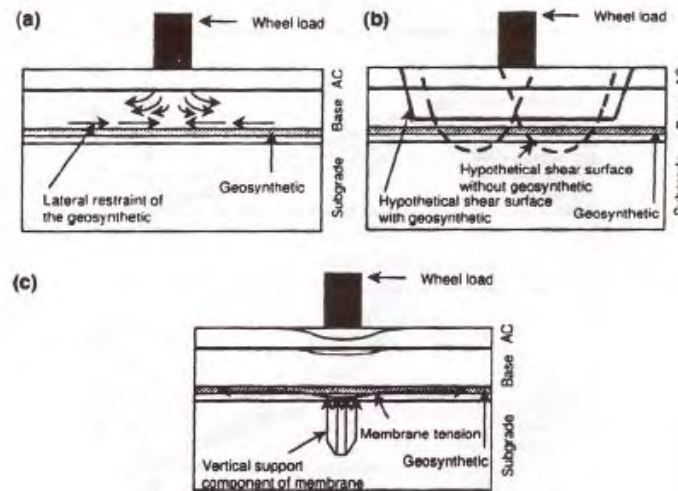
Figure 1.1. Geosynthetic reinforcement functions (a) Lateral restraint, (b) Modified failure surface, and (c) Tensioned membrane (Perkins and Ismeik, 1997)

1.2 Falling Weight Deflectometer

The falling weight deflectometer (FWD) is a trailer-mounted pavement testing device designed to simulate the deflection of pavements due to truck loads. A large mass is dropped and the deflection basin measured using sensors at the pavement surface. FWDs are particularly useful for estimating the in situ layer moduli of asphalt, aggregate base, granular subbase, and engineered soil using backcalculation (Schmalzer 2006). The FWD includes a load cell, which measures the force delivered to the road surface, and several geophones, which measure velocities that are used to calculate deflections. The FWD also measures air temperature and pavement surface temperature.

Braun Intertec was contracted by MnDOT to perform FWD testing on geosynthetic reinforced test sections in District 2 during the spring of 2013 just after the thaw was complete. Braun Intertec concluded that properly placed geogrid can reduce pavement deflection, however this benefit had contingencies as noted in the report. Braun Intertec also recommended further analyses be done using more advanced modeling such as layered elastic methods and distinct element methods (Oman 2013).

Using the information delivered by Braun Intertec, two of the District 2 test sections were investigated in more detail using the layered elastic analyses. One test section included biaxial geogrid and the second test section was very similar in structure and materials, but did not include geogrid. As a result of that comparison it was confirmed that geogrid provides benefit, but the relative amount of benefit was uncertain due to soil variability under the roadway. Therefore phase two of the research presented in this report was undertaken. For more information about phase one, please refer to reports included as Appendix A and Appendix B.

1.3 Mechanistic-Empirical Pavement Design

MnPAVE (Tanquist 2012) is MnDOT's mechanical empirical flexible pavement design method that consists of three general inputs: climate, traffic, and structure; and three design levels: basic, intermediate, and advanced. MnPAVE has been adopted as MnDOT's pavement design method because unlike other methods MnPAVE can better optimize materials (Skok et. al 2003). The effect of traffic on the pavement structure is simulated in MnPAVE using layered elastic analysis (LEA) (Tanquist 2002). MnPAVE uses the WESLEA software routine to perform the LEA calculations (Van Cauwelaert 1989). MnPAVE assumes that the pavement layers are isotropic in all directions and infinite in the horizontal direction. The fifth layer is also assumed to be infinite in the vertical direction. MnPAVE inputs include layer thickness, modulus, Poisson's ratio, and an index indicating the degree of slip between layers. MnPAVE assumes zero slip between interfaces. The estimated pavement life is calculated using a damage factor based on Miner's hypothesis. MnPAVE's climate inputs include five seasons (fall, winter, early spring, late spring, and summer) based on FWD measured material properties. Spring is split into two seasons because of important differences in behavior between the aggregate base and subgrade soil during the spring thaw. Seasonal temperatures are determined using local weather data at specific locations. When using the advanced structure tab, the moduli of the asphalt, aggregate base, granular subbase, and engineered soil can be entered directly.

1.4 Evaluation of Layer Moduli

ELMOD (Dynatest 2012) was used to estimate the layer moduli of the TH 72 test sections in order to better understand the variation in moduli along the roadway. ELMOD uses layer thickness and measured surface deflections to estimate layer moduli. The program is based on the Odemark-Boussinesq method and iterates until convergence using goodness of fit criteria. The ELMOD results were used as MnPAVE inputs to provide better estimates of the layer moduli at each FWD testing location along TH 72.

1.5 Pavement Condition Assessment

Pavement condition data are collected annually using MnDOT's digital inspection vehicle (DIV). This vehicle contains lasers and cameras that collect various data of the roadway and the adjacent area. The lasers gather information on the rutting and roughness of the roadway. And the cameras gather information such as pavement distress, which includes cracking and patching. This information is then used to calculate three indices. One index is the ride quality index (RQI), which is based on the roughness of the road and ranges from 0 to 5. The second index is the surface rating (SR), which is based on the pavement distress and is on a scale of 0 to 4. And the third index is the pavement quality index (PQI), which is a combination of the first two indices (MnDOT 2011). After reviewing the pavement condition data, it was determined that maintenance activities had occurred on the roadway, but it was not possible to determine geogrid benefit from the pavement condition data.

1.6 Numerical Modeling

The distinct element method (DEM) (Cundall and Strack 1979) is a type of numerical modeling that computes the motion of individual particles and the forces between particles by

applying Newton's laws of motion to the particles (Hart and Cundall 1992). This is different than the finite element method (FEM), which is intended for modeling continuum problems where simulating the interaction of distinct particles is not desired. DEM was used for this project because it is important to better understand and quantify the interaction of the aggregate particles with the geogrid.

Itasca Consulting Group (Itasca) was contracted by MnDOT to develop a PFC3D numerical model capable of simulating compression testing of an aggregate base material containing geogrid. The model boundary conditions were determined using the FWD measurements and MnPAVE analyses described above. Modeling capabilities were delivered in three phases. The first phase included aggregate base material development and the ability to simulate compression tests. The second phase added moisture to the simulated aggregate base by implementing research funded by MnDOT that had been completed by the University of Minnesota (Tan, Hill, and Khazanovich 2014). The third phase added geogrid to the simulated aggregate base by implementing research funded by Tensar International Corporation that had been completed by Itasca in Germany. During phase three, Itasca completed development of the PFC3D pavement design package that supports creation and compression testing of a synthetic material containing geogrid. The synthetic material is embodied in a PFC3D DEM model that simulates the movement and interaction of hundreds or thousands of particles. The particles may be spherical grains or arbitrarily-shaped clumps of grains that move independently, both translating and rotating. Each particle interacts with adjacent particles at their contacts. Contact mechanics are controlled by particle interaction laws and the internal forces and moments are updated using a time evolution method, which dynamically solves Newton's laws of motion (Potyondy 2015).

CHAPTER 2: LITERATURE SUMMARY

The following publications were reviewed and are briefly described below.

2.1 Jas, Stahl, Konietzky, Kamp, and Oliver (2015) "Discrete Element Modeling of a Trafficked Sub-Base Stabalized with Biaxial and Multi-Axial Geogrids to Compare Stabilization Mechanisms."

The authors describe the simulation of geogrid-stabilized subbase over weak soil under traffic loads. To model the soil in PFC3D it was necessary to look into the effect of fines, angularity, and the distribution of particle shapes and compare the model to laboratory tests. To reduce computational time, the clay particles in the simulation were much bigger than actual, but these differences were accounted for through calibration of the model to lab tests. The geogrid was modeled by creating a geogrid composed of overlapping spherical particles of varying size and using parallel bond logic to simulate the physical behavior of the geogrid. The wheel load simulation was conducted using a square testing box created with geometry of 40 x 40 x 12 centimeters. The top of the box was subdivided into nine different walls, which were used to distribute contact forces. The layers within the box were divided such that there was a four centimeter thick soft clay layer at the bottom of the box with an eight centimeter thick base layer with the geogrid between the layers. Once the particles had been numerically generated, wheel load tests were applied by rolling a wheel along the length of the box back and forth at a rate of 0.5 meters per second for a total of ten repetitions. From this testing four important conclusions were found. First, the geogrids were not only under tension, but were also under compression in some areas. Second, due to the very low forces and strains, the tensile strength of the geogrid was not very relevant during subbase stabilization applications. Third, the loads were relatively small and therefore smaller volumes of particles relatively close to the geogrid were constrained by the geogrid. Fourth, hexagonal multi-axial geogrids transfer forces in a near circular shape and confine the granular particles due to a tension-ring effect. This study showed that PFC3D can be used to simulate the interactions between particles and geogrids during the loading of granular subbase.

2.2 Stahl, Konietzky, Kamp, and Jas (2013) "Discrete Element Simulation of Geogrid-Stabilized Soil."

The authors describe the use of PFC3D to model a geogrid pullout test. The soil was modeled using clumps of particles of varying grain size, shape, strength, and contact friction. The majority of the article described modeling the geogrid, which including flexible ribs and relatively stiff joints. The final contact simulations included simple junctions, which connected half ribs to one another. A pullout test was simulated in PFC3D and it was found that the model accurately simulated a laboratory pullout test for a given grain size distribution, relative density, normal stress, geogrid stiffness, and installation technique. It was concluded that the stresses and strains measured in the model result from confinement of the particles by the geogrid.

2.3 Tutumluer, Qian, Hashash, Ghaboussi, and Davis, (2013) "Discrete Element Modelling of Ballasted Track Deformation Behavior."

An image-based DEM simulation platform developed at the University of Illinois at Urbana-Champaign (UIUC) was used to simulate the behavior of railroad ballast using polyhedron shaped discrete elements. This was done to establish a quantitative performance simulation tool. The DEM model was used to predict ballast settlement trends of four test sections created in 2010 at the TTC FAST test track. For this project, the image-aided DEM software developed by UIUC was used to create rigid three dimensional polyhedrons. The University of Illinois Aggregate Image Analyzer (UIAIA) quantified the morphological indices (flat and elongated ratio, angularity index, and the surface texture index) to generate a 3D model of the aggregate in the DEM simulation. Using different ballast types, the compaction level and density of the field ballast were compared. Using a simple box placed within the grade during construction, a general idea of the compaction, porosity, and density could be measured. When the initial porosity and density were similar, the settlement predictions by the model compared well with the field measured settlements. Some discrepancies were caused by fracture of the ballast and aggregate porosity, however the final DEM simulation was found to provide reasonable results.

2.4 Qian, Mishra, Tutumluer, and Kwon (2013) "Comparative Evaluation of Different Aperture Geogrids for Ballast Reinforcement through Triaxial Testing and Discrete Element Modeling."

The authors describe research focused on the permanent deformation of geogrid reinforced railroad ballast. Tests were conducted both in the lab and simulated using PFC. Laboratory tests were completed using a custom made triaxial cell large enough to hold railroad ballast. The lab results were then compared to the simulations to determine biaxial and triaxial geogrid influence on deflection. The simulation built on previous work done by the University of Illinois using the University of Illinois Aggregate Image Analyzer (UIAIA), which takes into account the grain size distribution, aggregate shape properties, flat and elongated ratio, angularity index, and the surface texture index. Laboratory tests included 10,000 repetitions and found that the triaxial geogrid had the smallest deformation, followed by the biaxial geogrid, and finally by no geogrid. Simulations included only 1000 repetitions due to time constraints. It was found that the deformations measured in the lab and the simulation did not match, but that the qualitative ranking did. The authors concluded that the simulation worked well, but that further research was needed to refine the UIAIA.

2.5 Potyondy (2012) "The Bonded Particle Model as a Tool for Rock Mechanics Research and Application: Current Trends and Future Directions."

The author gives an overview of the Bonded Particle Model (BPM) and the current advances and uses for the BPM. The first section discusses the different microstructural physics of intact rocks and how the BPM simulates this through brittle failure. This is then compared to the linear elastic fracture mechanics and through this comparison it is shown that the BPM interaction accurately depicts the microcrack growth and interaction. This is done at the centimeter scale and the intact rock is simulated as spheres cemented together.

The first example models anisotropic material and the effects of swell and contraction due to saturation. This model includes bedding planes and fractures both within and across these bedding planes, internal mechanical suction arising from capillary pressure, and the creep-like behavior from sustained stress. An ideal simulation would incorporate all of these mechanisms; however, the BPM only provides the first two mechanisms. Even with only incorporating the first two, the model provides an accurate representation of the effects of saturation on the material. This simulation effectively incorporates interfaces softer than layers and interfaces weaker than layers, along with an accurate representation of the strength between the grain-grain contacts.

The next example is the uniaxial tensile strength of a typical rock. A limitation for the BPM is that, if the direct tensile strength matches the unconfined-compressive strength, then the direct tensile strength will be too large. To handle this limitation, the BPM uses the difference between fully bonded and fully unbonded with a frictional state resisting relative rotation. When this is incorporated, the model matches the physical situation well, but the Poisson's ratio is underestimated and the volumetric-strain reversal does not occur before peak load. Despite these limitations the BPM does an effective job describing particle motion.

The last example applied the PFC2D model inside a larger FLAC model to simulate the fracturing around an advancing stope in quartzite. This coupled model allows the BPM to simulate boundary-value problems. The FLAC model uses a strain-hardening/softening material model that effectively models the behavior of the quartzite and the PFC2D model uses a parallel-bonded material. The combined model was compared to previous physical tests and calibrated to behave similarly. To measure the effectiveness of the model, it was compared to actual stope fracture. The PFC2D model allowed a greater amount of detail than the FLAC model and can allow for a better understanding of what may occur in the rock.

In conclusion, the examples clearly demonstrated the potential of the BPM, though it does have limitations as stated in each example. It is anticipated that increasing computing power will allow more complex systems to be solved. The potential of the BPM is vast and while only three examples were discussed, the flexibility of the BPM means that there are many situations to which the BPM could be applied.

2.6 Xiao, Tutumluer, and Siekmeier (2011) "Mechanistic-Empirical Evaluation of Aggregate Base and Granular Subbase Quality Affecting Flexible Pavement Performance in Minnesota."

This report describes the effect of aggregate quality on pavement performance using the mechanistic-empirical pavement program MnPAVE for two different climatic regions in Minnesota. Aggregate inputs for resilient modulus and peak deviator stress at failure encompassed many different quality ranges within Minnesota. In addition to MnPAVE, the finite element method GT-PAVE was used to estimate the fatigue and rutting life expectancies. From these analyses, several important observations were found. First, the use of local marginal material on roads with traffic less than 1.5 million ESALS can be cost effective. Second, for more than 1.5 million ESALS, the need for higher quality in the base and subgrade becomes more important. Third, a bridging effect was found when a high quality stiff subbase was placed over lower quality subgrade. It was concluded that marginal quality locally available materials

should be considered and it was recommended that the research findings be validated using field performance data.

2.7 Lemos (2011) "Recent Developments and Future Trends in Distinct Element Methods UDEC, 3DEC and PFC Codes."

The author provides an explanation of the several codes (UDEC, 3DEC and PFC) associated with the distinct element method (DEM). DEM applies to the wide class of numerical methods that simulate the physical behavior of a system of particles, grains, or blocks. DEM has been used to better understand the micro-mechanics of many types of granular materials. DEM has also been applied to concrete dam foundation analyses to better understand the forces acting on the dam structure as well as the interface between the dam foundation and the underlying geomaterials. DEM has great potential and encouraging advances in computational power continue to allow DEM to solve more elaborate and complex models.

2.8 Stahl and Konietzky (2010) "Discrete Element Simulation of Ballast and Gravel under Special Consideration of Grain Shape, Grain Size, and Relative Density."

The authors describe the creation of a particle based numerical simulation of ballast and granular material. It is shown that only three inputs are needed; friction coefficient, shear stiffness, and normal stiffness to reproduce the behavior of the dry aggregate. The paper discusses grain shape along with an in-depth look at several laboratory test methods compared to the simulation. Clumps were used in the simulation to best reproduce the results found in the laboratory. These clumps were created using computerized particle analysis along with caliper measurements. The measured values were necessary to best represent the aggregates three dimensionally in the model. Once the calibration of the clumps had been completed, some basic tests were simulated and compared to laboratory results. These simulated tests included oedometer, triaxial, and multi-stage shear tests. It was found that the model sufficiently and accurately simulated these tests.

2.9 Garcia-Rojo, McNamara, and Herrmann (2008) "Influence of Contact Modeling on the Macroscopic Plastic Response of Granular Soils under Cyclic Loading."

The objective was to determine the influence of the contact model on the macroscopic elasto-plastic response during a stress-controlled cyclic loading test. Two contact models, molecular dynamics (MD) and contact dynamics (CD), were compared using a two dimensional biaxial test. During MD modeling, the forces were calculated using the overlap between the particles known as Hertz-Mindlin contact modeling. During CD modeling, no overlap is considered between particles. The CD and MD models were compared and it was found that the results were strongly affected by the type of contact model selected.

2.10 Konietzky, Kwon, and Tutumluer (2008) "Aggregate Base Residual Stresses Affecting Geogrid Reinforced Flexible Pavement Response."

The authors present an analytical study on the effects of unbound aggregate residual stresses on the resilient response behavior of geogrid reinforced flexible pavements. Stresses were computed using both a finite element model (FEM) and distinct element model (DEM) and

those stresses were compared to the stresses measured in laboratory tests. The FEM approach considered the nonlinear, stress-dependent pavement foundation as well as the isotropic and anisotropic behavior of the base and subbase. An axisymmetric FEM mesh for the mechanistic model was used and the geosynthetic was placed at the bottom one third of the aggregate base. The unbound aggregate base was modeled using the Uzan model, which considers both the confining stress and the deviator stress. The geosynthetic was modeled as a three-node axisymmetric membrane element that provided resistance to tension, but no resistance to bending. The interface between the soil and the geosynthetic was modeled as a six-node interface element. It was found that varying the geogrid modulus had quite small effects on model behavior. This may have been due to factors that were not fully taken into account in the FEM. To better understand the effects of confinement and aggregate-geogrid interlock, a DEM was applied using the 3D particle flow code (PFC3D). The development of the PFC3D model occurred in three stages; numerical set-up and calibration of the geogrid, calibration and set-up of the aggregate material, and simulation of the interaction between geogrid and aggregate. It was determined that compaction caused the stiffness of the aggregate material near the geogrid to increase due to locked in residual stresses. The DEM model increased understanding of how geogrid stiffens the surrounding material by helping to increase the interlock and confinement of the aggregate.

2.11 McDowell, Harireche, Konietzky, Brown, and Tho (2006) "Discrete Element Modeling of Geogrid Reinforced Aggregates."

The authors investigated the behavior of a geogrid reinforced aggregate using discrete element modeling to simulate laboratory pull-out tests. The first part of the paper focused on the role of the particle shape and therefore the simulations compared spheres to clumps. It was found that particle shape and friction resulted in different stresses and strains and therefore it was recommended that particle shape be included. The simulations included several types of clumps, which compared to the results found in the lab for a single-rib pull out test. The ballast in the model was created using clumps, which had shape, porosity, and friction similar to those measured in the laboratory. The main conclusions from these simulations were that the geogrid aperture size is important for aggregate interlock and that this interlock provides benefit in a limited zone of influence near the geogrid.

2.12 McDowell (2006) "The Importance of Modelling Ballast Particle Shape in the Discrete Element Method."

This paper describes the modeling of ballast particles using clumps, which are overlapping spheres used to create more complex shapes. A procedure is described that controls sphericity, angularity, and surface texture of the clump. Cyclic loading was applied to the simulated ballast sleeper box to compare different types of clumps. It was found that the simple procedure described was effective at representing the important characteristics of the ballast. Also, the effects of the clumps during loading and unloading resembled more realistically the behavior of the ballast compared to uniform spheres.

9

2.13 Zeghal (2005) "Discrete-Element Method Investigation of the Resilient Behavior of Granular Materials."

This paper describes a preliminary investigation into the resilient behavior of granular material using a 2D discrete element method (DEM). A total of sixteen simulations were conducted using different confining and deviator stress levels. It was found that increasing the confining pressure resulted in higher resilient moduli and that this affect was more pronounced at lower deviator stresses. In addition, it was found that the deviator stress plays a significant role at low confining pressure.

2.14 Konietky, teKamp, Groeger and Jenner (2004) "Use of DEM to Model the Interlocking Effect of Geogrids Under Static and Cyclic Loading."

The authors investigate the interlocking effect geogrid has when properly placed. To accomplish this task, the authors used discrete element modeling, which allowed a detailed view into the effect of interlocking particles. Two models were investigated, one model was a pull-out test and the second was a model for cyclic loading. Before the two models could be used the geogrid matrix had to be calibrated. To calibrate the system three different tests were performed: a single rib test, a single junction test, and an in-plane rotation. Using these tests and adjusting the variables it was found that a better match could be achieved by further adjustment of micro-properties. The numerical pull-out tests used a box 70 cm in height and 18 cm by 18 cm. This box was then filled with a typical grain size distribution and the geogrid was placed within the apparatus. From this setup three different load situations were considered: gravitational load, 13.2 kPa vertical load plus gravitational load, and 35.4 kPa vertical load plus gravitational load. The results showed a complex mixture of tensile, compressive, shear and bending forces within the geogrid. These simulations demonstrated increased contact forces and provided a clear indication of the interlocking effect. It was also noted that this effect is restricted to small heights around 20 cm. The cyclic loading setup was similar to the single load pull-out tests. The results of the cyclic loading further confirmed the findings in the single load pull-out test and the geogrid has an effective area of about 20 cm. This report enhanced understanding of geogrid and how interlocking results in unbound aggregate stabilization.

2.15 Hart and Cundall (1992) "Microcomputer Programs for Explicit Numerical Analysis in Geotechnical Engineering."

Authors discuss microcomputer programs Fast Lagrangian Analysis of Continua (FLAC), Universal Distinct Element Code (UDEC), and 3-Dimensional Distinct Element Code (3DEC). An explicit numerical analysis uses an explicit timestep to solve the algebraic equations and allows for the modeling of nonlinear, large strain, and physical instability problems very well. The main issue with an explicit numerical analysis is the timestep, which needs to be made small enough so that the equations of motion remain valid. The central concept of the explicit numerical analysis is that the calculations "wave speed" is always ahead of the physical wave speed. This comes with the disadvantage that the timestep will often be very small, which will then result in very many steps, and therefore require a great amount of computer time.

FLAC is a continuum model that uses an explicit (Langrangian) finite difference code that is good at modeling large displacements. FLAC models are composed of finite difference

meshes built from quadrilateral elements, which are further subdivided into two constant strain triangular elements. Triangles are used to prevent hourglass deformations. FLAC is able to achieve steady state conditions with relatively modest computational effort and is generally numerically stable. UDEC and 3DEC models are built from an assemblage of discrete blocks and are ideal for simulating the behavior of a jointed rock mass.

2.16 Ng and Dobry (1992) "Numerical Simulations of Monotonic and Cyclic Loading of Granular Soil."

This paper describes the use of DEM simulations to investigate the effect of particle rotation and the angle of intergranular friction, as well as monotonic drained loading with constant mean stress and cyclic constant volume loading. To complete this task, the authors used three simulated granular specimens assigned the same properties of quartz. The simulations included: drained monotonic compression test, drained monotonic shear test, and constant volume cyclic shear test. Results from the monotonic loading into the effect of particle rotation, strain failure, and intergranular friction found that inhibiting particle rotation created higher shear strength, greater stiffness, and stronger dilation compared to allowing rotation. The compression test for the three samples had similar small strain failures, due to particle shape and grain size uniformity as opposed to rotation or lack of dimension. Lastly, larger microscopic friction angle was found that increasing the friction increased shear strength, modulus, and greater dilation. Cyclic loading simulation particle rotation was explored and it was found that when rotation was prohibited, the secant modulus is greatly increased. However, when considering the damping ratio, there was only a small increase and this was an indication that the damping is mostly associated with particle sliding and rearrangement. These simulations made clear the validity of the granular material models. The issues included excessive rotations seen in the simulation and the failure at lower shear strains. This was mostly attributed to the round particle shape, small number of grain sizes, and gradation. It was also noted that a linear force dependent sliding contact law was a reasonable approximation for rounded granular soil and reproduced laboratory results well.

CHAPTER 3: FALLING WEIGHT DEFLECTOMETER MEASUREMENTS

Falling weight deflectometer (FWD) testing and analyses were performed by Braun Intertec under contract with MnDOT (Oman 2013). The testing occurred on trunk highways TH11 and TH72 in Lake of the Woods, Koochiching, and Beltrami Counties during the spring of 2013 and was completed within the first week following complete thaw. MnDOT helped identify eighteen different pavement sections of varying length and year of construction. MnDOT also provided information about the layer thicknesses, geosynthetics used, and traffic data. Appendix B contains the complete report by Braun Intertec.

3.1 Conclusion

Braun Intertec concluded that properly placed geogrid provided a structural benefit, however this benefit was contingent upon the caveats noted in their report and noted briefly here. Braun Intertec found that geogrid provided an increase in the granular equivalence (GE) of several inches in some situations (Table 3.1). GE is a factor that provides a means of comparing the structural performance of materials in the road structure. In Minnesota, the GE is related to the structural performance of MnDOT Class 5 aggregate base. For example, a GE of 1 inch is expected to be structurally equivalent to 1 inch of MnDOT Class 5 aggregate base. It must be noted that the Braun report contains several caveats. The first was that soil data was not available to quantify the soil variability at each FWD test location and therefore subgrade soil support was assumed to be equal. Second, pavement layer thickness was estimated using the plan thickness not as-built thickness. Third, the relatively short test sections meant that it was difficult to quantify variations. These caveats created significant difficulty interpreting the results and therefore MnDOT needed additional information before geogrid benefit could be quantified.

3.2 Recommendation

Braun Intertec recommended that MnDOT consider additional evaluation so that Technical Memorandum 10-SA-03 "Geogrids (multiaxial) General Specification, Granular Equivalent and Design Guidelines" could be utilized beyond State Aid routes for use on all trunk highways. Braun Intertec also recommended that further analyses be done using more advanced modeling such as layered elastic methods and discrete element methods. It was noted that an FWD load of 9,000 pounds may not be large enough to fully mobilize the geogrid. If additional FWD testing were to be done, it was suggested that a 15,000 pound load be used to better mobilize the geogrid.

Table 3.1 Braun Intertec Results

Test Section	Pavement Section	Ave R-value	StdDev of Ave Eff R-value	Ave Eff GE (in)	StdDev of Ave Eff GE (in)
Q	4.5" Bit, 9" Reclaim, Grid @ 6"	34.0	3.3	36.9	0.9
R	4.5" Bit, 9" Reclaim	46.9	8.8	31.6	2.0
G	6" Bit, 6" CL 5 base, 8" SGB, Grid @14"	39.6	2.7	40.2	1.0
I	6" Bit, 6" CL 5, 8" Geocell w/ SGB below base	39.2	4.0	37.9	1.1
F	5" Bit, 10" Reclaim, Grid @ 6"	50.3	3.9	29.7	1.3
K	5" Bit, 10" Reclaim, Grid @ 8"	31.4	3.9	31.0	1.1
G	6" Bit, 6" CL 5 base, 8" SGB, Grid @14"	39.6	2.7	40.2	1.0
H	6" Bit, 6" CL 5 base, 8" SGB, fabric @14"	34.7	3.5	40.2	1.0
H	6" Bit, 6" CL 5 base, 8" SGB, fabric @14"	34.7	3.5	40.2	1.0
I	6" Bit, 6" CL 5, 8" Geocell w/ SGB below base	39.2	4.0	37.9	1.1
H	6" Bit, 6" CL 5 base, 8" SGB, fabric @14"	34.7	3.5	40.2	1.0
J	6" Bit, 18" CL 5, fabric under base	35.4	4.5	37.5	1.5
C	6" Bit, 12" Reclaim, Grid @ 6"	29.0	5.5	34.4	1.1
D	7" Bit, 12" Reclaim, Grid @ 6"	19.0	1.1	39.6	1.2
L	5" Bit, 10" Reclaim, Grid @ 8" (4" stab, 6" non-stab)	36.2	2.9	38.6	0.7
N	4" Bit, 10" Reclaim, Grid @ 8" (4" stab, 6" non-stab)	26.1	3.3	36.5	1.0
K	5" Bit, 10" Reclaim, Grid @ 8"	31.4	3.9	31.0	1.1
M	4" Bit, 10" Reclaim, Grid @ 8"	26.5	3.4	34.8	1.1
A	6" Bit, 12" Reclaim, Grid @ 6"	30.7	2.8	34.3	0.8
C	6" Bit, 12" Reclaim, Grid @ 6"	29.0	5.5	34.4	1.1
K	5" Bit, 10" Reclaim, Grid @ 8"	31.4	3.9	31.0	1.1
L	5" Bit, 10" Reclaim, Grid @ 8" (4" stab, 6" non-stab)	36.2	2.9	38.6	0.7
M	4" Bit, 10" Reclaim, Grid @ 8"	26.5	3.4	34.8	1.1
N	4" Bit, 10" Reclaim, Grid @ 8" (4" stab, 6" non-stab)	26.1	3.3	36.5	1.0

CHAPTER 4: MNPAVE FALLING WEIGHT DEFLECTOMETER SIMULATIONS

4.1 Discussion

MnPAVE's FWD simulator was used to compare sections "Q" and "R" (Table 4.1) described in the Braun report. The comparison utilized information collected by Braun as well as soils logs and construction plans from District 2 to better understand the roadway structure. ELMOD was used to calculate layer moduli at the FWD testing locations for a five layer pavement structure consisting of the asphalt pavement, FDR base, engineered soil, undisturbed soil, and a saturated soil layer. These five layers were discussed with District 2 personnel and an analysis matrix created (Table 4.2). A range of values from the ELMOD backcalculation were used as MnPAVE input values and simulated FWD deflection basins plotted along with the FWD measurements. Only the morning test drops from 9 kips (40 kN) were used for each test section to reduce temperature and load variability. Measurements from one hundred and twenty FWD test locations were split into subsections and compared.

Table 4.1 Construction Information on Test Sections Q and R

Test Section	Constructed	Project Number	Asphalt	Base	Geosynthetic
Q	2005	SP 0413-30	4.5"	9" FDR	Geogrid @ 6" in FDR
R					none

Table 4.2 MnPAVE Input Matrix

Material	Modulus (MPa)	Number of Values
Asphalt	3200	1
FDR base	400, 800, 1200	3
Engineered Soil	30, 60, 90	3
Undisturbed Soil	50% of Engineered Soil	1
Saturated Soil	5000	1
Total:		**9**
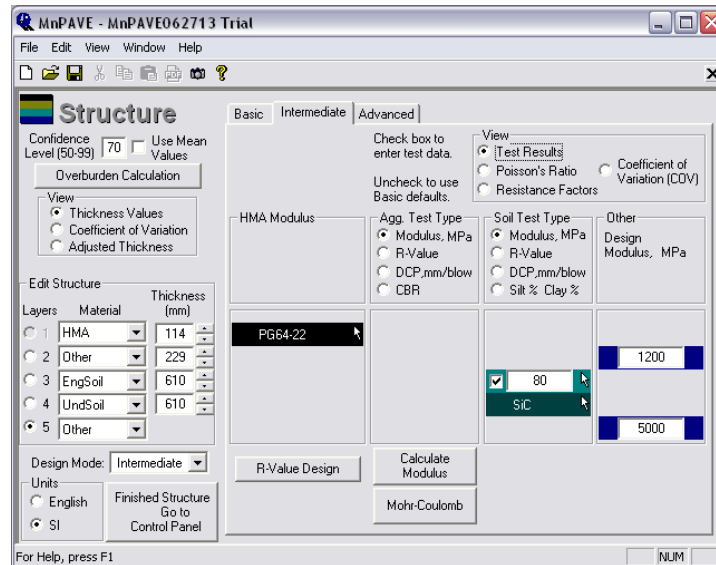
Figure 4.1 MnPAVE Sample of Roadway Structure for Analysis Matrix

4.2 Conclusions

Test sections Q6 and Q3, which include geogrid, were compared to section R4, no geogrid, and demonstrate that geogrid reduced deflection. However when test section Q4 was compared to R2 the results were inconclusive meaning that there may be a benefit due to the geogrid, but further measurements and analyses were needed. This was likely due to the spatial variability of the soils and FDR, as well as temperature effects on the asphalt and FDR base material, which contained asphalt (Edil, Tinjum, and Benson 2012).

The ELMOD backcalculation and MnPAVE FWD simulation determined that the stiffness of the asphalt and FDR were higher than anticipated, which made it difficult to measure the relative benefit of geogrid. Varying the soil and FDR moduli within the range found in ELMOD helps to explain the large deflection variation measured in test sections Q6, Q3, and R4. This difference can be noted in Figure 4.2 and 4.3. Figure 4.2 shows small difference found from the FWD testing of sections Q4, Q6, R4, and R2. This is contrasted in Figure 4.3, which shows simulated FWD deflections for decreasing soil stiffness. These two figures illustrate the effect of variable soil and FDR moduli and how that variability creates uncertainty about the relative benefit of the geogrid. Therefore it was not possible to determine the structural benefit of the geogrid from the FWD measurements alone because of the soil and FDR variability.
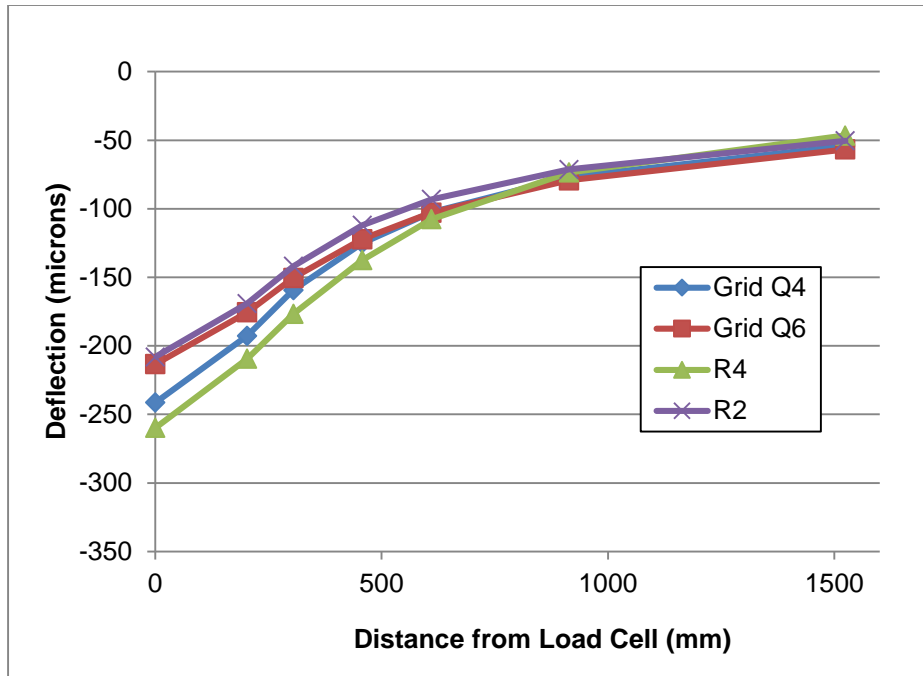
Figure 4.2 Measured FWD deflections sections Q, with grid, and R, without grid
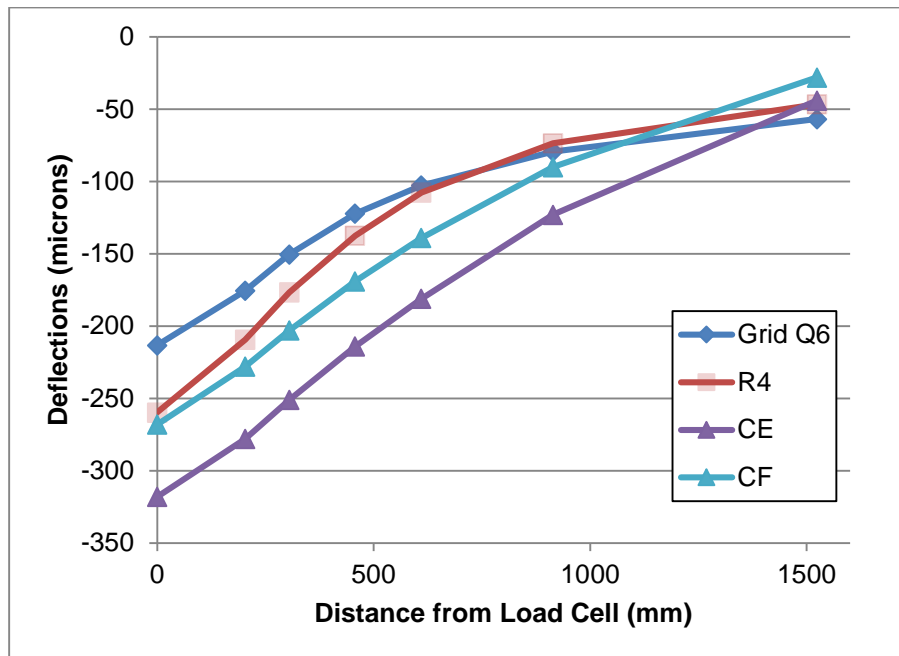
Figure 4.3 MnPAVE FWD Simulations variable soil (CD, CE, CF) and FWD measurements grid section Q6 and no grid section R4

CHAPTER 5: EFFECT OF GEOGRID ON PAVEMENT DESIGN LIFE

MnPAVE was used to estimate fatigue and rutting damage, and also to calculate the stress and deflection boundary conditions on the aggregate base layer, which were needed for the DEM numerical modeling described in Chapter 6.

5.1 MnPAVE Setup

ELMOD backcalculation was applied to the FWD deflection measurements to develop the input parameters for the MnPAVE analyses (Table 5.1).

Table 5.1 MnPAVE Input Parameters

	Thickness		Moduli	
	mm	**in**	**MPa**	**ksi**
Asphalt	102, 152	4, 6	2500	363
Aggregate	203, 254, 305	8, 10, 12	40, 60, 80, 120, 160	5.8, 8.7, 11.6, 17.4, 23.2
Engineered Soil	203, 610, 914	8, 24, 36	20, 30, 40	2.9, 4.4, 5.8
Undisturbed Soil	N/A	N/A	25% of Engineered Soil	

The inputs were varied to simulate different road structures during late spring season under loading similar to the FWD testing. Late spring criteria were used because it was during this period that the roadway foundation was at its weakest due to near saturation of the soil and base layers. For climate input (Figure 5.1), the air temperature was set to 12° C taken from the average air temperature value for late spring thaw during the 2013 FWD testing. It should be noted that MnPAVE used a single late spring season air temperature value during all the simulations meaning that no other seasonal affects were considered when calculating fatigue and rutting damage as well as boundary conditions. The temperature has important effects on the stiffness of the asphalt surface, reclaimed aggregate base, and the geogrid.
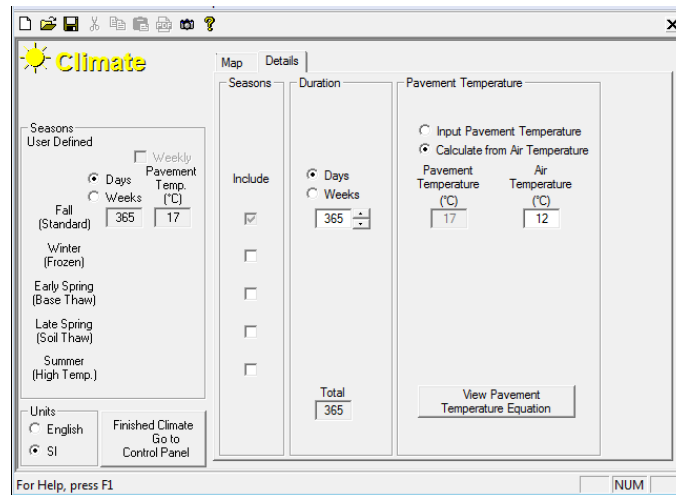
Figure 5.1 MnPAVE Climate Input Values

The structure advanced settings tab (Figure 5.2) was used to input the layer moduli and thicknesses for the road structure as noted in Table 5.1. 600,000 single axle repetitions were

simulated at a value of 44 kN to normalize the fatigue and rutting damage factors into a convenient range of values (Figure 5.3). Once the climate, traffic, and structure tab are filled out the output tab can be used to calculate the damage and transfer functions, which are calculated by using the equations shown in Figure 5.4

Figure 5.2 Structural Input Values

Figure 5.3 Traffic Input Values

Figure 5.4 Damage Transfer Functions

The range of thicknesses and moduli were selected to calculate high, moderate, and low values of the fatigue damage, rutting damage, vertical stress, and vertical deflection. The critical locations where the vertical stress and deflection were collected are the top, middle, and bottom of the aggregate base as well as a fourth measurement at the bottom of the engineered soil (Figure 5.5).

Figure 5.5 Vertical Stress Output

5.2 Results

The MnPAVE analyses demonstrate the relationship between the aggregate layer modulus and pavement fatigue damage and rutting damage. The improvement of the aggregate base due to the geogrid is expressed as a gain factor with the aggregate base resilient moduli

19

normalized to 40 MPa. Figure 5.6 shows the effect of a low soil modulus (20 MPa) on aggregate base damage factors for varying base thickness (8 and 12 inches). It can be seen that increasing the base thickness reduces the damage, but only slightly changes the shape of the curve. It can also be seen that increasing the base thickness is more relevant to rutting damage for the 8 and 12 inch aggregate base thickness than to fatigue damage for these pavement structures. Figure 5.7 and Figure 5.9 compare the increase in aggregate layer thickness and increasing the engineered soil thickness with a strong engineered soil base (40MPa). Comparing these two scenarios it can be seen that increasing aggregate thickness has a greater effect than increasing the engineered soil thickness. Figure 5.10 shows the dramatic effect that adding two inches of asphalt can have on both fatigue and rutting damage.

5.3 Conclusions

The fatigue and rutting damage can be used to quantify the effects of aggregate base stiffness and thickness. MnPAVE also quantifies the effects of the engineered soil stiffness and its thickness. An important conclusion from these analyses is that it is more effective to increase in the stiffness of the overlying materials when the soils are weak. Therefore geogrid reinforced aggregate base is likely to provide the most effective benefit when the pavement foundation materials are weak.
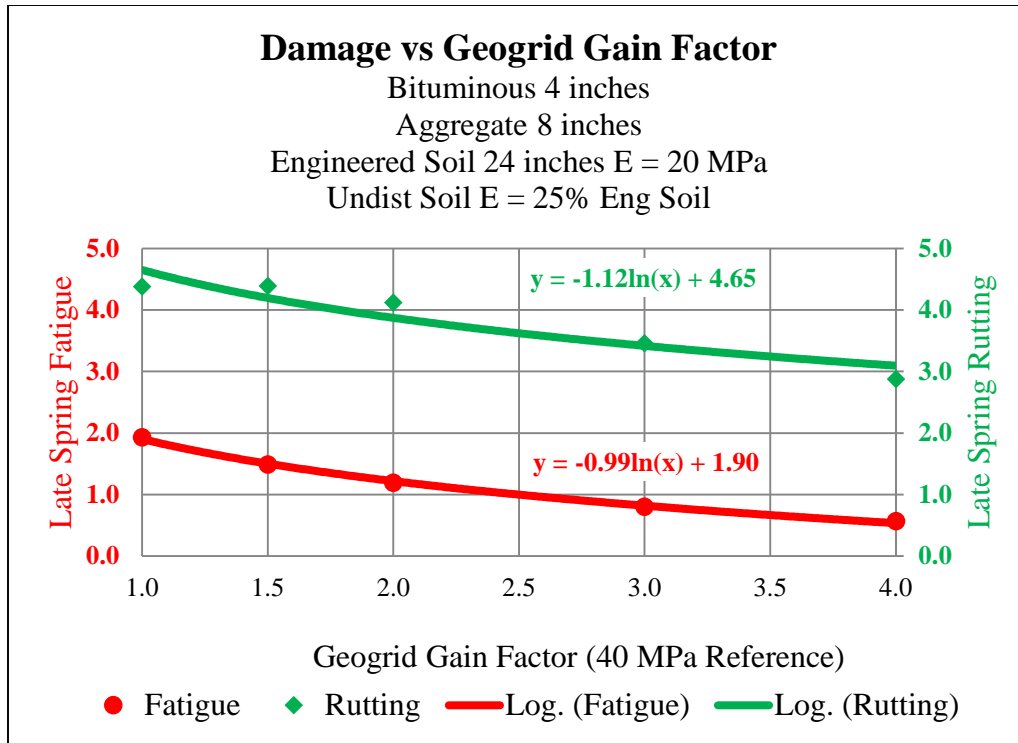
(a)
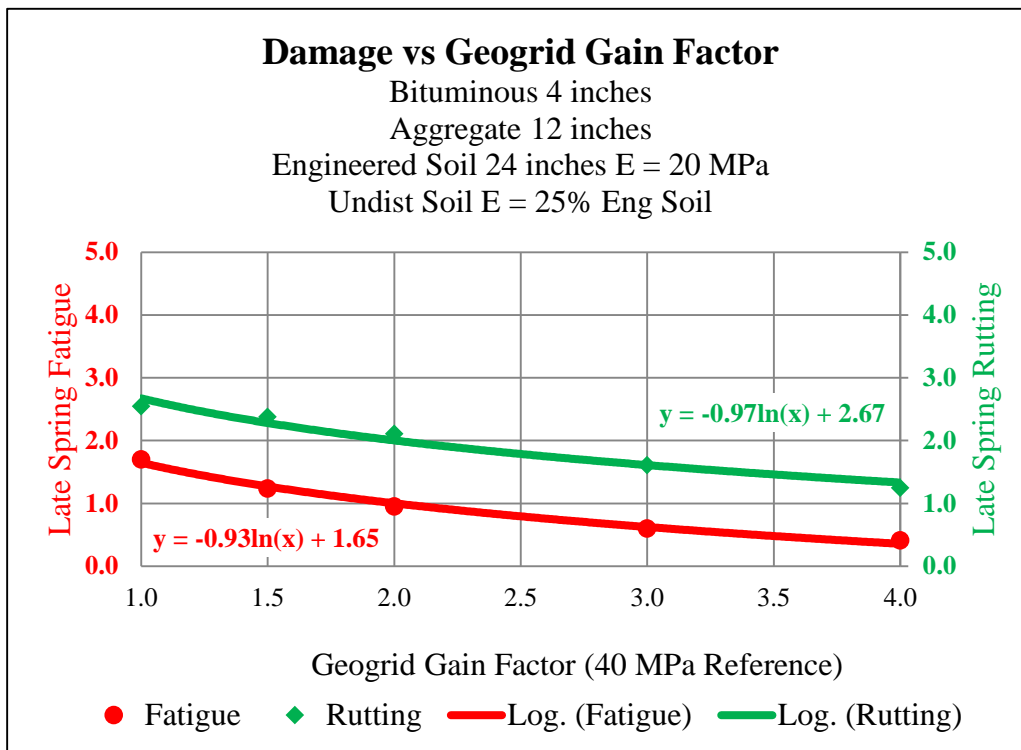
(b)

Figure 5.6 Fatigue and Rutting Damage with 20 MPa Subgrade Modulus and Varying Base Thickness

21
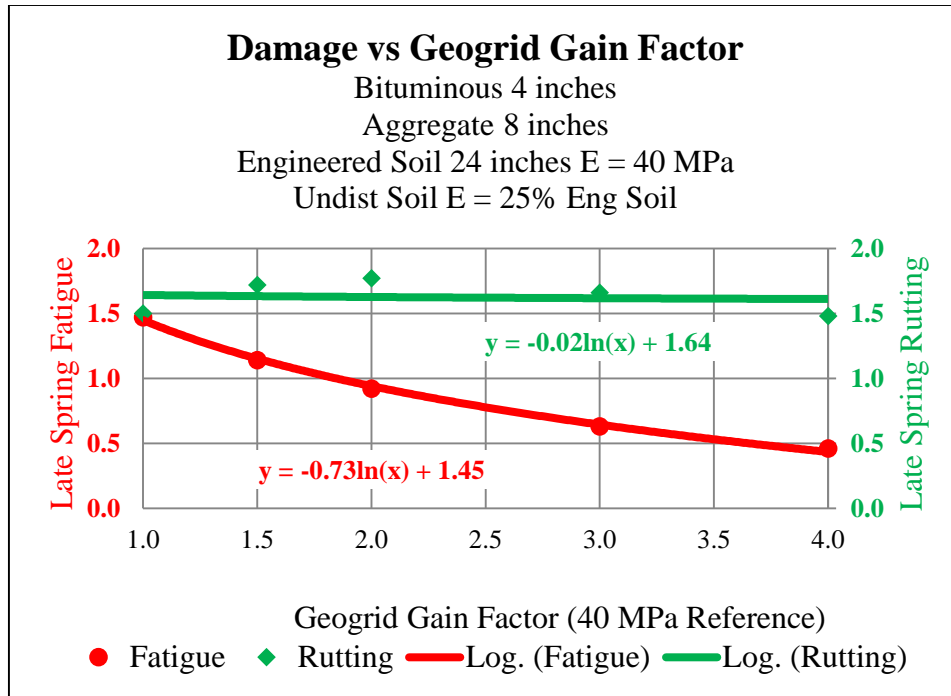
(a)
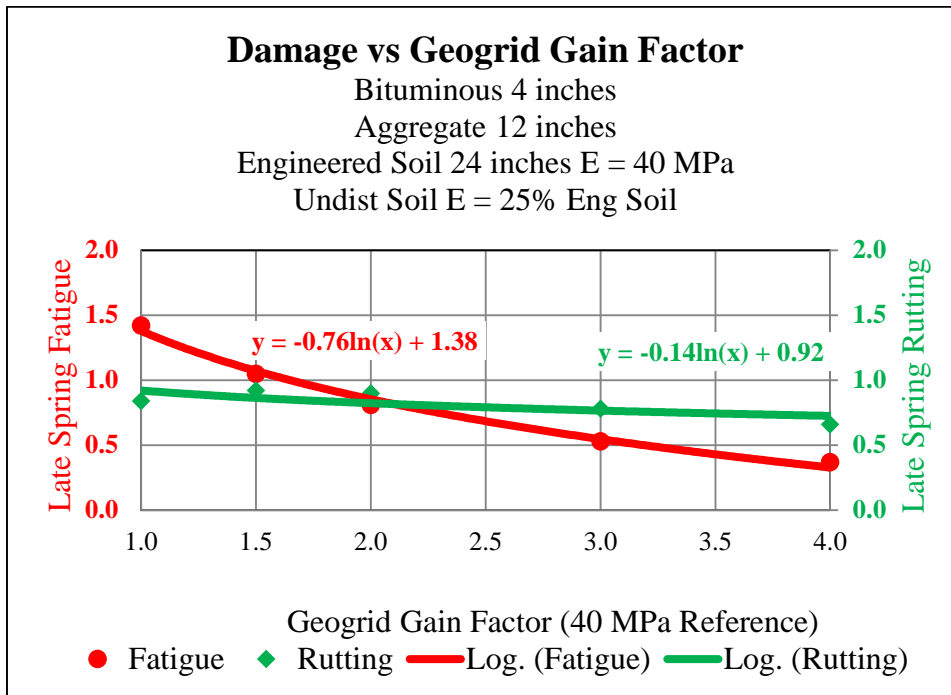
(b)

Figure 5.7 Fatigue and Rutting Damage with 40 MPa Subgrade Modulus and Varying Base Thickness
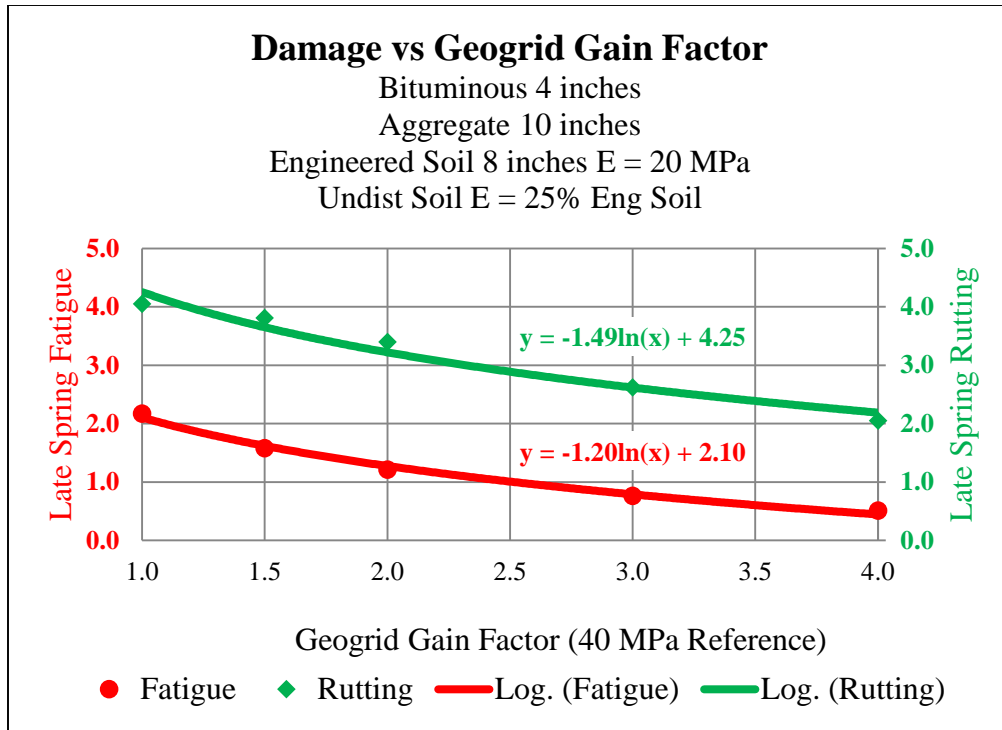
(a)
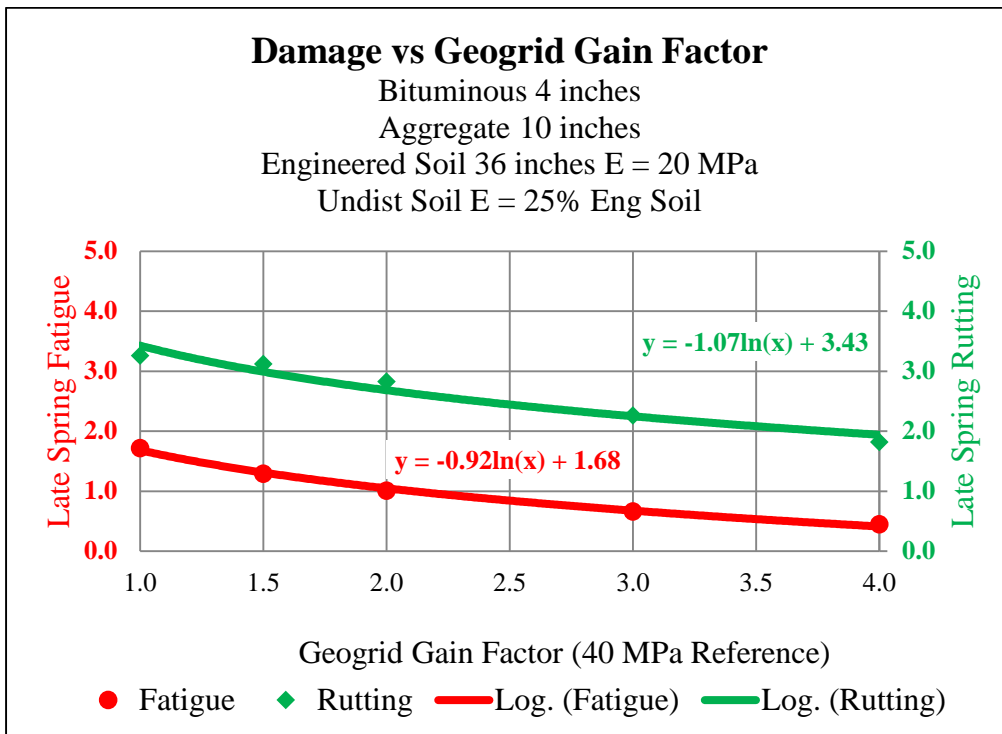
(b)

Figure 5.8 Fatigue and Rutting Damage with 20 MPa Subgrade Modulus and Varying Engineered Soil Thickness
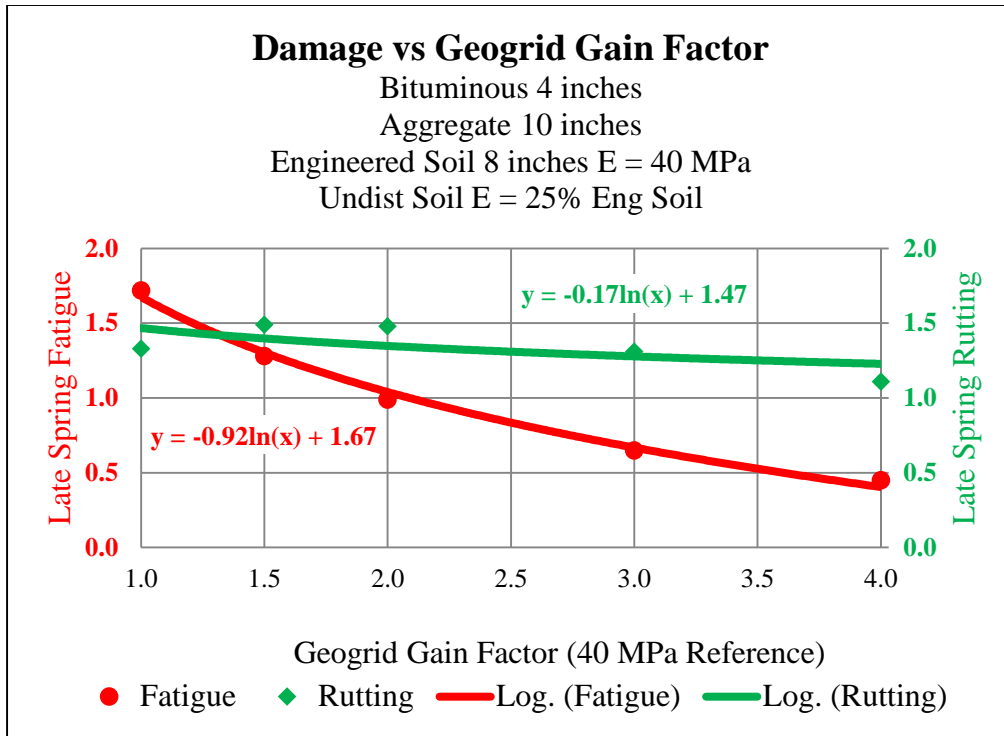
(a)
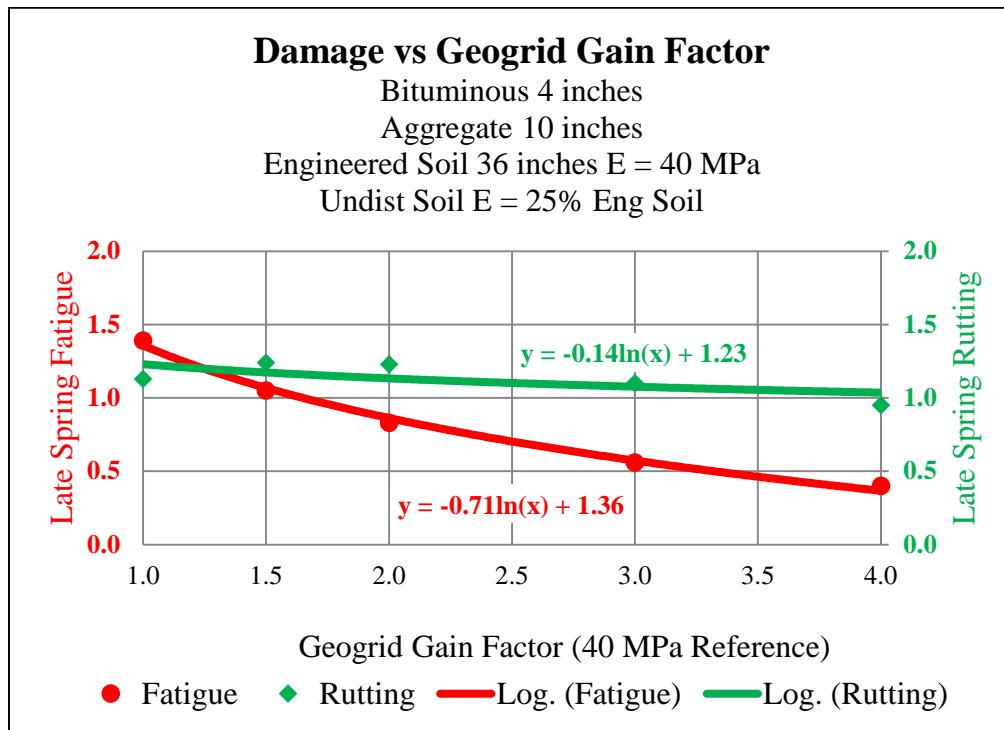
(b)

Figure 5.9 Fatigue and Rutting Damage with 40 MPa Subgrade Modulus and Varying Engineered Soil Thickness
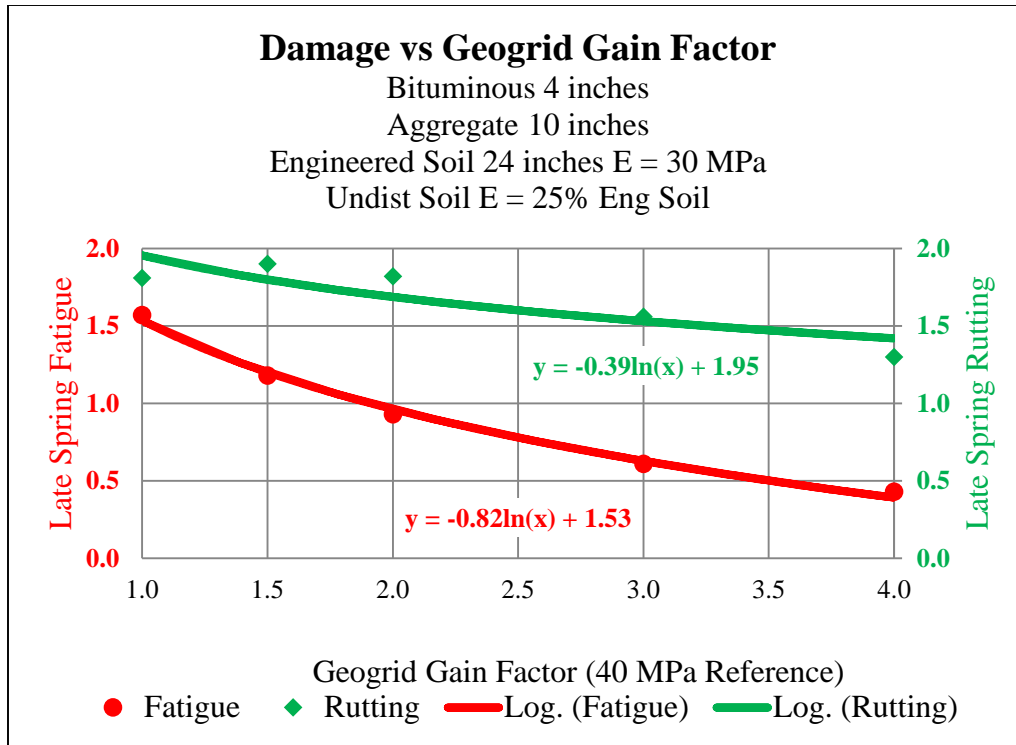
(a)
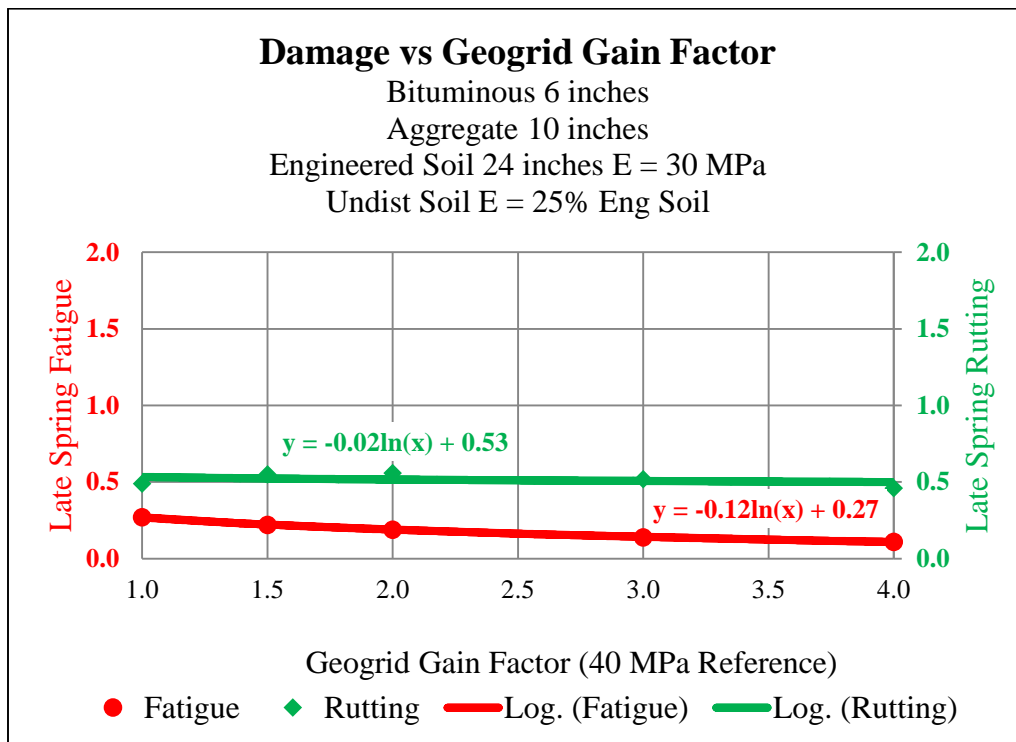
(b)

Figure 5.10 Fatigue and Rutting Damage with Varying Asphalt Thickness

CHAPTER 6: DISTINCT ELEMENT MODELING

Particle Flow Code 3D (PFC3D) (Itasca, 2015) is numerical modeling software based on the distinct element method (DEM) (Cundall and Strack, 1975). The numerical model is composed of distinct particles, which are modelled as rigid bodies, with forces acting at the contacts. This means that all deformation occurs at the contacts between the particles. PFC3D provides a general purpose, DEM modeling framework that includes a computational engine and a graphical user interface. The PFC3D model can simulate the movement and interaction of thousands of finite-sized particles with model size primarily limited only by computer processor speed and memory. Each particle has a defined size with finite mass and a well-defined surface. These particles are rigid bodies that move independently of one another and can translate, rotate, and interact with other particles at their contacts. Contact mechanics is embodied in particle-interaction laws that update the forces and moments. The time evolution of the modeled system is computed via the DEM, which provides an explicit dynamic solution to Newton's laws of motion. In summary, the PFC3D model simulates a granular material consisting of an assembly of rigid particles that interact at contacts (Potyondy 2015c).

Geogrid was included in the synthetic material described above and the modeling performed in three stages. Stage one used simple linear particle contacts that did not include moisture. Stage two applied the hill particle contact model, which includes moisture. And stage three included geogrid interaction with the hill particles. PFC3D tracks particles and contacts and creates new contacts as the gap closes between particles. PFC3D performs an iterative process that refreshes existing contacts, detects new contacts, and applies selected contact models (Figure 6.1).
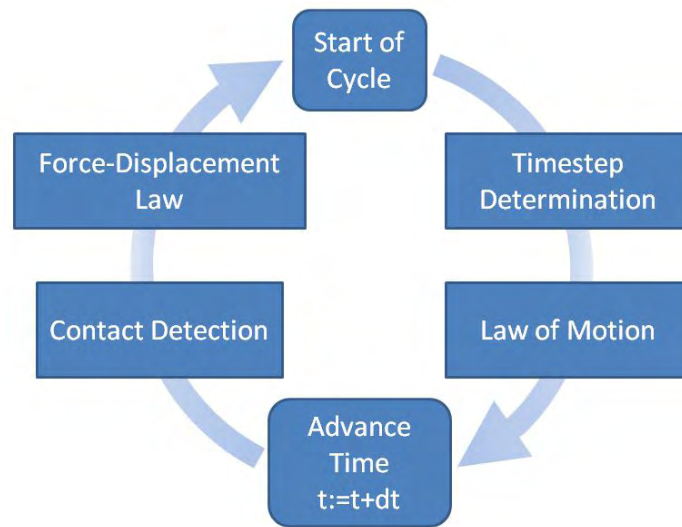
Figure 6.1 PFC3D Model Formulation

Once a contact has been established, a contact plane is defined and force-displacement laws are applied to both particles. For linear contact models a linear spring and dashpot

component act in parallel. The hill model adds an additional criterion for moisture (Figure 6.2).
The material genesis procedure produces a homogenous, isotropic, and well-connected grain
assembly within a material vessel, which can be a cylindrical or polyaxial cell.
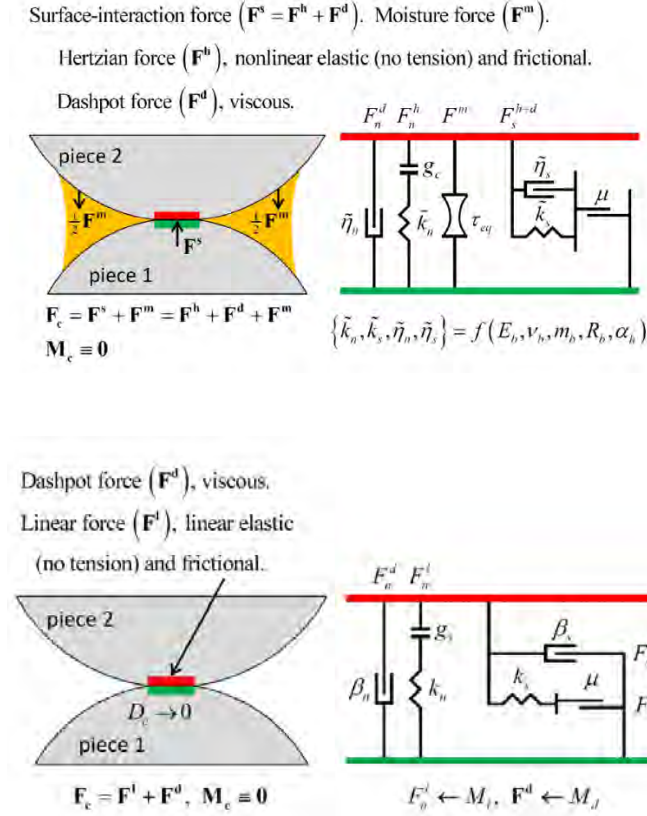
Figure 6.2 Behavior and Components of the
"Hill" and Linear Model

6.1 Stage One

During stage one, the modulus of the numerical model was calculated from
measurements at the model boundaries for various combinations of particle friction, particle
diameter, and confining pressure. Figure 6.3 shows an example of the PFC environment during
material genesis and triaxial test simulation. The cylindrical vessel in the simulation can be
given the same dimensions as the laboratory triaxial test specimen. Other cylindrical or
polyaxial vessels can be easily defined by the user.
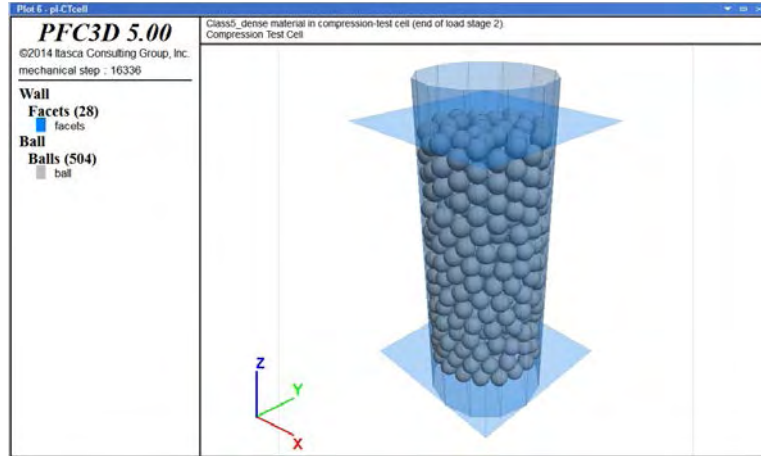
Figure 6.3 Screenshot of PFC Environment

These initial triaxial simulations were done using a cylindrical vessel 600 mm tall with a 300 mm diameter. Uniform spheres 40 mm diameter were used and only one cycle of load/unload was completed. During each simulation the confining pressure was 1 MPa and the total axial strain was 1%.

$$M_r = \frac{1.33 \times 10^6}{(10 - 2.3) \times 10^{-3}} \cong 173 \text{MPa}$$

$$M_r = \frac{0.94 \times 10^6}{(10 - 3.6) \times 10^{-3}} \cong 147 \text{MPa}$$
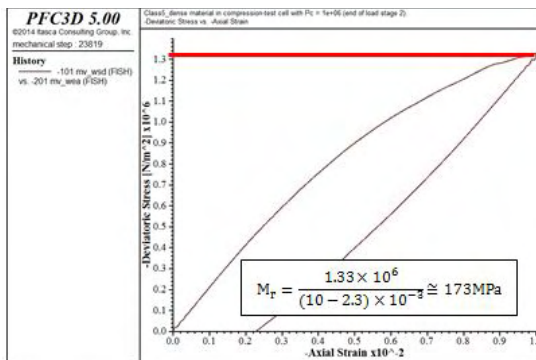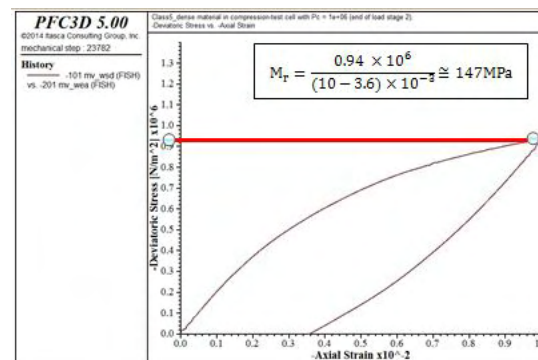
a) Friction Coefficient of 0.6   b) Friction Coefficient of 0.3
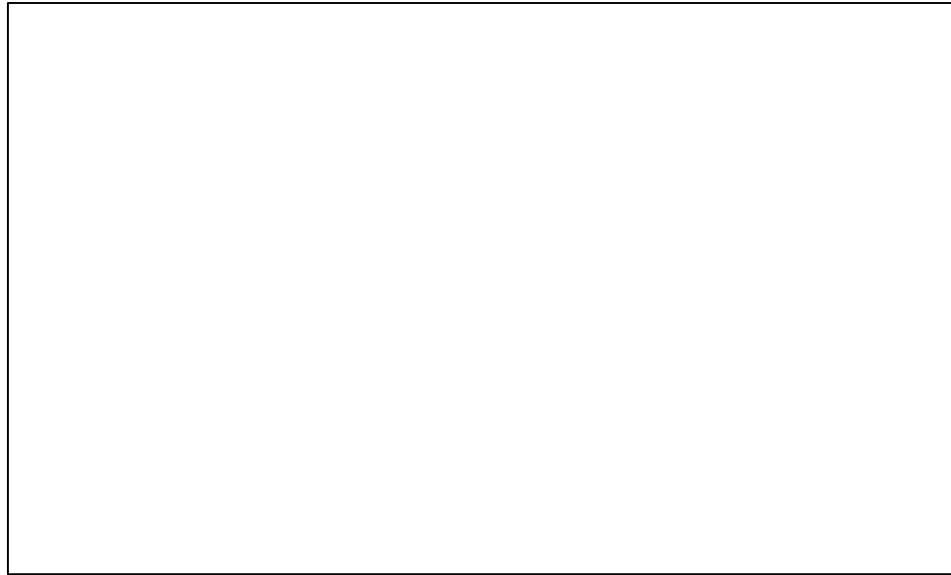
c) Modulus at Various Friction Coefficients

Figure 6.4 Effect of the Particle Contact Friction on Modulus

Figure 6.4 shows that increasing the friction between particles from 0.3 to 0.6 increases in the modulus. Figure 6.5 shows the effect on the modulus of changing the confining pressure and the total axial strain using the data points in Table 6.1. When the total axial strain at peak deviator stress was decreased, the modulus increased. Also when the confining pressure was increased, the resilient modulus increased. This behavior is consistent with what is observed during laboratory triaxial tests.

The resilient modulus is dependent on the confining stress and deviator stress (Table 6.2). These test sequence guidelines are found in "Laboratory Determination of Resilient Modulus for Flexible Pavement Design" (NCHRP 1-28A 2003). Nine points were selected to approximate the general modulus function (Table 6.3).

Table 6.1 Resilient Modulus (MPa) at Various Strains and Confining Pressures

	Confining Pressure (kPa)				
Strain (%)	**20.7**	**41.4**	**69.0**	**103.5**	**138.0**
1.0	8.3	26.6	26.1	40.0	40.8
0.5	20.0	29.3	35.0	59.5	85.7
0.1	58.8	96.0	110.3	141.1	162.0

Table 6.2 Test Sequence for Base/Subbase Materials

Procedure Ia (Base/Subbase Materials)									
Sequence	Confining Pressure		Contact Stress		Cyclic Stress		Maximum Stress		Nrep
	kPa	psi	kPa	psi	kPa	psi	kPa	psi	
0	103.5	15.0	20.7	3.0	207.0	30.0	227.7	33.0	1000
1	20.7	3.0	4.1	0.6	10.4	1.5	14.5	2.1	100
2	41.4	6.0	8.3	1.2	20.7	3.0	29.0	4.2	100
3	69.0	10.0	13.8	2.0	34.5	5.0	48.3	7.0	100
4	103.5	15.0	20.7	3.0	51.8	7.5	72.5	10.5	100
5	138.0	20.0	27.6	4.0	69.0	10.0	96.6	14.0	100
6	20.7	3.0	4.1	0.6	20.7	3.0	24.8	3.6	100
7	41.4	6.0	8.3	1.2	41.4	6.0	49.7	7.2	100
8	69.0	10.0	13.8	2.0	69.0	10.0	82.8	12.0	100
9	103.5	15.0	20.7	3.0	103.5	15.0	124.2	18.0	100
10	138.0	20.0	27.6	4.0	138.0	20.0	165.6	24.0	100
11	20.7	3.0	4.1	0.6	41.4	6.0	45.5	6.6	100
12	41.4	6.0	8.3	1.2	82.8	12.0	91.1	13.2	100
13	69.0	10.0	13.8	2.0	138.0	20.0	151.8	22.0	100
14	103.5	15.0	20.7	3.0	207.0	30.0	227.7	33.0	100
15	138.0	20.0	27.6	4.0	276.0	40.0	303.6	44.0	100
16	20.7	3.0	4.1	0.6	62.1	9.0	66.2	9.6	100
17	41.4	6.0	8.3	1.2	124.2	18.0	132.5	19.2	100
18	69.0	10.0	13.8	2.0	207.0	30.0	220.8	32.0	100
19	103.5	15.0	20.7	3.0	310.5	45.0	331.2	48.0	100
20	138.0	20.0	27.6	4.0	414.0	60.0	441.6	64.0	100
21	20.7	3.0	4.1	0.6	103.5	15.0	107.6	15.6	100
22	41.4	6.0	8.3	1.2	207.0	30.0	215.3	31.2	100
23	69.0	10.0	13.8	2.0	345.0	50.0	358.8	52.0	100
24	103.5	15.0	20.7	3.0	517.5	75.0	538.2	78.0	100
25	138.0	20.0	27.6	4.0	690.0	100.0	717.6	104.0	100
26	20.7	3.0	4.1	0.6	144.9	21.0	149.0	21.6	100
27	41.4	6.0	8.3	1.2	289.8	42.0	298.1	43.2	100
28	69.0	10.0	13.8	2.0	483.0	70.0	496.8	72.0	100
29	103.5	15.0	20.7	3.0	724.5	105.0	745.2	108.0	100
30	138.0	20.0	27.6	4.0	966.0	140.0	993.6	144.0	100

Table 6.3 Subset of Aggregate Base Stresses

Sequence	Confining Pressure (kPa)	Maximum Stress (kPa)
1	21	15
3	69	48
5	138	97
11	21	46
12	69	152
15	138	304
26	21	149
28	69	497
30	138	994

a) 20.7 kPa Confining Pressure 1% Strain

b) 138 kPa Confining Pressure 0.1% Strain
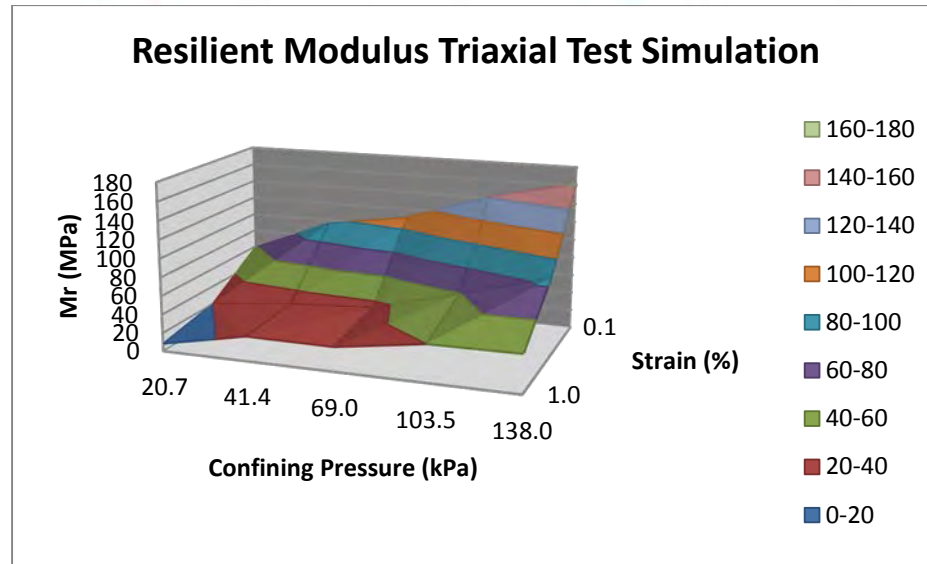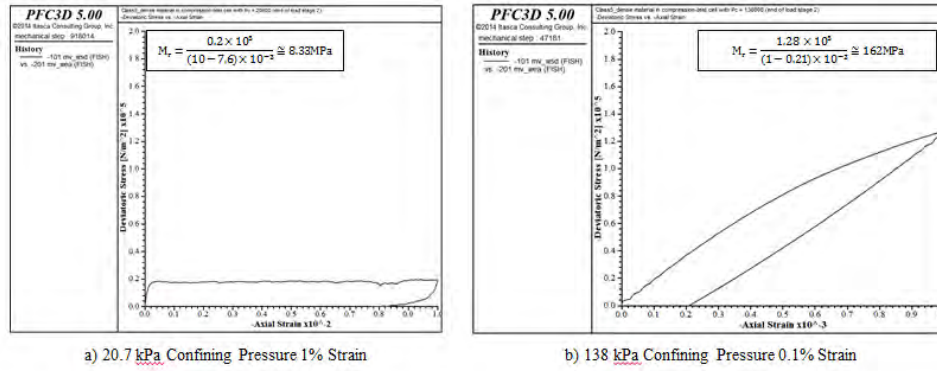
c) Resilient Modulus Simulations at Various Strains and Confining Pressures

Figure 6.5 Triaxial Tests Results at Various Strains and Confining Pressures

6.2 Stage Two

The hill contact model was provided in the material modeling support package for PFC3D. A hill material is defined as a granular assembly in which the hill contact model exists at all grain-grain contacts allowing this material to behave similar to an unsaturated granular material. Unsaturated behavior during simulated triaxial testing was studied using the hill model parameters to represent a typical aggregate base layer (Table 6.4) (Potyondy, 2016b).

Table 6.4 Hill Model Parameters

Name	Symbol	Range
Friction Coefficient	μ	$[0.0,\infty)$
Suction Coefficient	τ_{eq}	$[0.0,\infty)$
Damping Constant	α	$[0.0,1.0]$
Young's Modulus	E_b	$[0.0,\infty)$
Poison's Ratio	ν_b	$(-1.0,0.5]$

31

6.3 Stage Three

During stage three, the PFC3D environment was enhanced to include geogrid during the simulation and the geogrid was placed at mid-depth within the base. Based on MnDOT district construction and performance experience, it is expected that geogrid increases the aggregate base layer modulus, which is an important property that influences the performance of the asphalt surface. Therefore it is expected that more financially effective pavement structures will be constructed in Minnesota by quantifying the benefit of geogrid when it is included in the aggregate base layer. In order to determine geogrid benefit, geogrid reinforced and non-reinforced roadway sections in northern Minnesota were simulated during stage three.

6.3.1 Background

The research described in phase three is part of a larger research initiative by MnDOT to better understand and quantify the structural benefit of including geogrid in the aggregate base layer of asphalt surfaced roadways. The initial phase of the investigation combined the analyses completed by Braun Intertec (Oman 2013) with analyses using the mechanistic-empirical flexible pavement design program MnPAVE (Casanova and Siekmeier 2013, Tanquist 2012, Tanquist et al 2002). Quantifying the structural benefit of geogrid was further advanced when Itasca Consulting Group was contracted by MnDOT to develop a PFC3D numerical model capable of simulating the creation and triaxial testing of an unsaturated aggregate base material containing geogrid (Potyondy et al 2016, Potyondy 2015, 2015a, 2015b). Moisture was added to the synthetic material by implementing research funded by MnDOT and the Local Road Research Board that had been completed by the University of Minnesota (Gupta et al 2007, 2005, Tan at al 2014, Yonannes et al 2009). Finally geogrid was added to the synthetic material by implementing research funded by Tensar International that had been completed by Itasca Consultants GmbH (Jas et al 2015). During stage three, Itasca completed development of the pavement design package that supports creation and triaxial testing of the synthetic system consisting of unsaturated granular material containing geogrid.

6.3.2 Summary of Falling Weight Deflectometer Field Measurements

Braun Intertec performed FWD testing in order to compare geogrids on two trunk highways, TH 11 and TH 72 in Lake of the Woods, Koochiching, and Beltrami Counties (Oman 2013). The objective was to measure pavement structure benefits resulting from the use of biaxial geogrid placed in the base layer. FWD measurements were compared for two test sections on TH 72, one with geogrid in the base layer and one without. The FWD testing occurred May 7 and 8, 2013, following complete thaw with the expectation that the pavement foundation would be at its weakest during this period and therefore the geogrid benefit would be more easily measured. Based on the deflection measurements it was concluded that the geogrid did provide benefit, but that it was not possible using these measurements alone to accurately estimate the structural benefit (Casanova and Siekmeier 2013).

6.3.3 Simulation of Falling Weight Deflectometer

MnPAVE's FWD simulator was used to calculate deflection basins and compare test sections Q and R to better understand the roadway structure described in Table 6.5. Layer moduli were estimated at the FWD testing locations for a five layer pavement structure

consisting of the asphalt pavement, FDR, engineered soil, undisturbed soil, and a saturated soil layer. The values shown in Table 6.6 were used as MnPAVE inputs. Only the morning test drops at 9 kips (40 kN) were used for each test section to reduce temperature and load variability. These MnPAVE simulations showed how variations in the soil moduli influence surface deflections and therefore why it was not possible to determine the structural benefit of the geogrid from FWD surface measurements alone (Casanova and Siekmeier 2013).

Table 6.5 Descriptions of roadway test sections Q and R.

Section	Year	SP #	Asphalt	Agg. Base	Reinforcement
Q	2005	0413-30	4.5"	9" FDR	Geogrid @ 6"
R	2005	0413-30	4.5"	9" FDR	None

Table 6.6 MnPAVE input variables.

Material	Moduli (MPa)
Aggregate base (grid reinforced FDR)	400, 800, 1200
Engineered soil (compacted)	30, 60, 90
Undisturbed soil	15, 30, 45

6.3.4 Geogrid Types and Mechanisms

Geogrid is a petroleum product typically made of polypropylene or polyethylene that is punched and stretched, or woven, to create a planar structure. Geogrid can be further split into three broad categories: uniaxial, biaxial, and triaxial. Biaxial geogrid, which is the type of geogrid described in this paper, provides tensile stiffness and strength both longitudinally and laterally. The primary structural benefit of adding geogrid to the aggregate base layer of a flexible pavement is to provide lateral restraint, which results from interlocking and friction between the geogrid and the aggregate. Under repeated loads, the base layer tends to spread laterally and some of the shear stress in the base layer is transferred to tensile stress in the geogrid. A stiff geogrid will act to restrain the lateral spreading and result in a stiffer aggregate base. The lateral restraint mechanism is well described as "…restricting the ability of the aggregate particles to move by effectively fixing them into place via interaction with the geogrid." "If particles cannot move, then the modulus of the matrix will be maintained and the rate of accumulation of plastic deformation via shear and/or consolidation will be reduced" (Bagshaw et al 2015). This mechanism has been investigated and other important knowledge gained using the distinct element method (Konietzky et al 2008, McDowell et al 2006, Qian et al 2015, and Stahl and Konietzky, 2011).

<u>6.3.5 Geogrid Gain Factor</u>

The benefit of geogrid has been understood in Minnesota (Gale and Marti 2008, Leu and Tasa 2001, Skallman 2010), however MnPAVE does not account for the presence of a geogrid within the aggregate base layer. The geogrid gain factor is introduced as a means to modify the MnPAVE design modulus to account for the presence of geogrid within the aggregate base layer. The geogrid gain factor is defined as the ratio of resilient modulus of the aggregate base with geogrid to resilient modulus of the aggregate base without geogrid. The pavement design package is used to estimate the geogrid gain factors for typical geogrid reinforced aggregate roadway configurations (Potyondy et al 2016, Potyondy 2015, 2015a, 2015b). The MnPAVE design modulus of the aggregate base with geogrid is found by multiplying the design modulus of aggregate base without geogrid by the geogrid gain factor. MnPAVE can then be used to quantify geogrid's ability to reduce asphalt fatigue and rutting, and thereby estimate the performance of geogrid reinforced flexible pavements.

The pavement design package was used to estimate geogrid gain factors for typical geogrid reinforced aggregate roadway configurations in which the grain size distribution, initial specimen porosity, material moisture content, and confining stress were varied. For the models with geogrid, a single layer of biaxial geogrid was centered within the aggregate base and a hill material was used to represent a typical unsaturated aggregate base. The aggregate particles were modeled as spheres and grain size distributions were chosen within the MnDOT Class 5Q aggregate base grading designation (MnDOT 2016, Tutumluer et al 2015, Xiao and Tutumluer 2012, Xiao et al 2012). During compaction, the simulated aggregate was saturated but free draining (moisture surface tension between particles equaled zero) while being compacted at a stress of between 130 to 200 kPa (Mooney and Rinehart 2009, Rinehart and Mooney 2009). Next a moisture surface tension of 1 kPa to 60 kPa was added between the aggregate particles before performing the cyclic triaxial tests. Axial strains during the cyclic triaxial test simulations were similar to the vertical strains in the aggregate base layer calculated using MnPAVE for the expected traffic loads (Tanquist 2012). The confining stresses are similar to those defined by resilient modulus laboratory protocols (NCHRP 1-28A).

During the cyclic triaxial tests, six load-unload cycles were performed at axial strains of 0.02% (two cycles), 0.05% (two cycles) and 0.10% (two cycles) to estimate six moduli. The estimated geogrid gain factors resulting from the analyses at 0.05% strain are listed in Table 6.7. Note that moisture is defined in terms of suction stress based on measurements of typical natural and recycled aggregates in Minnesota (Gupta et al 2007, 2005). These moisture tensions are in the range measured for aggregates at gravimetric moisture contents of about 5 to 10 percent. The g1, g3, or g10 notation refers to test cases where moisture tension was extended to aggregate particles separated by a gap of up to 1, 3, or 10 mm in order to simulate smaller particles that partially fill the gaps between the larger aggregate particles.

Table 6.7 Estimated geogrid gain factors.

Case	Grain Size (mm)	Porosity & Friction	Moisture Suction (kPa)	Confining Stress (kPa)	Strain (%)	Gain Factor 2nd Cycle @ 0.05%
1	5-38	0.313 0.6	1 g1	50	0.05	1.73
			1 g10			2.07
			5 g1			1.54
			5 g10			1.73
			30 g1			1.45
			30 g10			1.62
2	5-38	0.313 0.6	1 g1	100	0.05	2.48
			1 g10			2.18
			5 g1			1.84
			5 g10			1.90
			30 g1			1.62
			30 g10			1.74
3	5-38	0.308 0.4	1 g1	50	0.05	1.89
			1 g3			1.98
			1 g10			1.92
			60 g1			1.50
			60 g3			1.58
			60 g10			1.70
4	5-38	0.308 0.4	1 g1	100	0.05	2.52
			1 g3			2.41
			1 g10			2.32
			60 g1			1.60
			60 g3			1.63
			60 g10			1.67

The dependence of the computed geogrid gain factors upon the system inputs is reasonable. All gain factors are greater than one, which confirms that the geogrid is increasing the stiffness. The gain factors increase with increasing confinement for an axial strain of 0.05%. The gain factors also increase with increasing moisture content (decreasing suction) meaning that the geogrid provides greater benefit when the unreinforced aggregate is weakest. It is recommended that additional simulations be performed to help interpret these initial results as well as provide greater understanding of the influence of grain size distribution, moisture content, and geogrid depth within the base layer.

CHAPTER 7: CONCLUSIONS

The pavement design package extends the capabilities of PFC3D to support triaxial testing of a synthetic unsaturated aggregate base containing geogrid. The geogrid provides lateral restraint to the aggregate base as a result of interlock and friction between the geogrid and the aggregate particles. The macroscopic system properties are affected by the microstructural system properties. Therefore, the modeled system was used to study and quantify the effect of microstructural properties on the macroscopic properties, which include the stress-strain curves produced during triaxial tests at different confinements. The microstructural properties of the aggregate base include: particle size, particle type (density, Young's modulus, and Poisson's ratio of each particle; and friction between particles), aggregate base moisture content (suction and gap), and initial aggregate base porosity. The microstructural properties of the geogrid include: geometry (aperture and rib dimensions), Young's modulus, bond stiffness, and grid-grain interface behavior. The pavement design package provides a mechanistically defensible model for aggregate-geogrid interaction, which was used to estimate geogrid gain factors for typical geogrid-reinforced aggregate roadways. It is anticipated that a simplified geogrid gain factor adjustment will be trialed during pavement design for projects where geogrid is being considered. As expected, this study concludes that geogrid provides benefit and that this benefit varies during the year. Therefore, it is recommended that the seasonal effects be included during implementation. This would allow the fatigue and rutting to be more accurately estimated over the expected pavement design life.

REFERENCES

1. Bagshaw, S., P. Herrington, P. Kathirgamanathan, and Cook S., (2015), Geosynthetics in Basecourse Reinforcement, Research Report 574, New Zealand Transport Agency, New Zealand.

2. Casanova, J. and J. Siekmeier, (2013), "Trunk Highway 72 Geogrid Analysis," Office of Materials and Road Research, Minnesota Department of Transportation, St. Paul, MN.

3. Clyne, T., (2011), Monitoring Geosynthetics in Local Roadways (LRRB 768) 10-Year Performance Summary, MnDOT 2011-20, Minnesota Department of Transportation, St. Paul, MN.

4. Cundall, P. and O. Strack, (1979), "A Discrete Numerical Model for Granular Assemblies," Geotechnique, 29(1):47-55.

5. Edil, T., J. Tinjum, and C. Benson, (2012), Recycled Unbound Materials, MnDOT 2012-35, Minnesota Department of Transportation, St. Paul, MN.

6. ELMOD, (2012), Evaluation of Layer Moduli and Overlay Design, Dynatest International, Glastrup, Denmark.

7. Erickson, H. and A. Drescher, (2001), Use of Geosynthetics to Reinforce Low Volume Roads, MnDOT 2001-15, Minnesota Department of Transportation, St. Paul, MN.

8. Gale, S. and M. Marti, (2008), Putting Research into Practice: Training Module for Designing and Constructing with Geosynthetics, MnDOT Technical Summary PP07GEO-TS, Minnesota Department of Transportation, St. Paul, MN.

9. Garcia-Rojo, R., S. McNamara, and H. Herrmann, (2008), "Influence of Contact Modeling on the Macroscopic Plastic Response of Granular Soils under Cyclic Loading," Mathematical Models of Granular Matter, 109-123.

10. Grading and Base Manual, (2015), Office of Materials and Road Research, Minnesota Department of Transportation, St. Paul, MN.

11. Gupta, S., and W. Larson, (1979), "Estimating Soil Water Retention Characteristics from Particle Size Distribution, Organic Matter Percent, and Bulk Density," *Water Resources Research*, 15, 1633-1635.

12. Gupta, S., A. Ranaivoson, T. Edil, C. Benson, and A. Sawangsuriya, (2007), Pavement Design Using Unsaturated Soil Technology, MnDOT 2007-11, Minnesota Department of Transportation, St. Paul, MN.

13. Gupta, S., A. Singh, and A. Ranaivoson, (2005), Moisture Retention Characteristics of Base and Sub-base Materials, MnDOT 2005-06, Minnesota Department of Transportation, St. Paul, MN.

14. Hart, D. and P. Cundall, (1992), "Microcomputer Programs for Explicit Numerical Analysis in Geotechnical Engineering," International Seminar on Numerical Methods in Geomechanics, Moscow, Russia.

15. Itasca Consulting Group, Inc., (2015), PFC3D 5.0, Particle Flow Code, Itasca Consulting Group, Inc., Minneapolis, MN.

16. Jas, H., M. Stahl, H. Konietzky, L. teKamp, and T. Oliver, (2015), "Discrete Element Modeling of a Trafficked Sub-Base Stabilized with Biaxial and Multi-Axial Geogrids to Compare Stabilization Mechanisms," Geosynthetics, Portland, OR.

17. Konietky, H., L. teKamp, T. Groeger, and C. Jenner, (2004), "Use of DEM to Model the Interlocking Effect of Geogrids Under Static and Cyclic Loading," Numerical Modeling in Micromechanics via Particle Methods, Taylor and Francis, London, England.

18. Konietzky, H., J. Kwon, and E. Tutumluer, (2008), "Aggregate Base Residual Stresses Affecting Geogrid Reinforced Flexible Pavement Response," *Int. J. of Pavement Eng.*, 9(4):275-285.

19. Lekarp, F., U. Isacsson, and A. Dawson, (2000), "State of the Art. I: Resilient Response of Unbound Aggregates," *J. Transp. Engrg.*, 126(1):66-75.

20. Lekarp, F., U. Isacsson, and A. Dawson, (2000), "State of the Art. II: Permanent Strain Response of Unbound Aggregates," *J. Transp. Engrg.*, 126(1):76-83.

21. Lemos, J., (2011), "Recent Developments and Future Trends in Distinct Element Methods UDEC/3DEC and PFC Codes," 10th Int. Conf. Discontinuous Deformation Analysis, Hawaii.

22. Leu, W. and L. Tasa, (2001), "Applications of Geotextiles, Geogrids, and Geocells in Northern Minnesota," Geosynthetics Conference, Portland, OR.

23. Lukanen, E., R. Stubstad, and R. Briggs, (2000), Temperature Predictions and Adjustment Factors for Asphalt Pavement, FHWA, McLean, VA.

24. McDowell, G., O. Harireche, H. Konietzky, S. Brown, and N. Tho, (2006), "Discrete Element Modeling of Geogrid-Reinforced Aggregates," *Geotech. Eng.*, 1(159):35-48.

25. McDowell, G. M. and Lu, (2006), "The Importance of Modelling Ballast Particle Shape in the Discrete Element Method," *Granular Matter*, doi: 10.1007/s10035-006-0021-3.

26. MnDOT Pavement Distress Identification Manual, (2011), Office of Materials and Road Research, Minnesota Department of Transportation, St. Paul, MN.

27. Mooney, M. and R. Rinehart, (2009), "In Situ Soil Response to Vibratory Loading and its Relationship to Roller-Measured Soil Stiffness," *Journal of Geotechnical and Geoenvironmental Engineering*, ASCE, Washington, D.C.

28. Nazzal, M., (2007), "Laboratory Characterization and Numerical Modeling of Geogrid Reinforced Bases in Flexible Pavements," PhD Thesis, Department of Civil and Environmental Engineering, Louisiana State University.

29. Newcomb, D., D. Van Deusen, Y. Jiang, and J. Mahoney, (1995), Considerations of Saturated Soil Conditions in Backcalculation of Pavement Layer Moduli, Transportation Research Board, Washington, D.C.

30. NCHRP, (2003), "Harmonized Test Methods for Laboratory Determination of Resilient Modulus for Flexible Pavement Design," National Cooperative Highway Research Program, Transportation Research Board, Washington, D.C.

31. Ng, T. and R. Dobry, (1992), "A Numerical Simulation of Monotonic and Cyclic Loading of Granular Soil," *J. Geotechnical Engineering*., 120(2):388-403.

32. Oman, M., (2013), Pavement Deflection Testing and Analysis, MnDOT Contract 03375, Braun Intertec Corporation, St. Paul, MN.

33. Ovik, J., B. Birgisson, and D. Newcomb, (2000), Characterizing Seasonal Variations in Pavement Material Properties for Use in a Mechanistic Empirical Design Procedure, MnDOT 2000-35, Minnesota Department of Transportation, St. Paul, MN.

34. Perkins, S. and M. Ismeik, (1997), "A Synthesis and Evaluation of Geosynthetic-Reinforced Base Layers in Flexible Pavements: Part I," *Geosynthetics International*, 4,6:549-605.

35. Perkins, S. and M. Ismeik, (1997), "A Synthesis and Evaluation of Geosynthetic-Reinforced Base Layers in flexible Pavements: Part II," *Geosynthetics International*, 4,6:605-621.

36. Potyondy, D., J. Siekmeier, and L. Petersen, (2016), "Aggregate-Geogrid Interaction Model Incorporating Moisture Effects," Proceedings, Transportation Research Board Annual Meeting, Washington, D.C.

37. Potyondy, D. (2016a) "Pavement Design Package for PFC3D," Technical Memorandum ICG16-8528-15TM, Itasca Consulting Group, Minneapolis, MN.

38. Potyondy, D. (2016b) "Hill Contact Model," Technical Memorandum ICG7795-L, Itasca Consulting Group, Minneapolis, MN.

39. Potyondy, D., (2015), PFC Pavement Design, MnDOT Contract 03772, Itasca Consulting Group, Minneapolis, MN.

40. Potyondy, D., (2015a), PFC Pavement Design (Hill Contact Model in PFC3D 5.0), Technical Memorandum ICG15-2845-06TM, MnDOT Contract 03772, Itasca Consulting Group, Minneapolis, MN.

41. Potyondy, D., (2015b), PFC Pavement Design (PFC3D Pavement Design Package)," Technical Memorandum ICG15-2845-43TM, MnDOT Contract 03772, Itasca Consulting Group, Minneapolis, MN.

42. Potyondy, D., (2015c), "The Bonded-Particle Model as a Tool for Rock Mechanics Research and Application: Current Trends and Future Directions," *Geosystem Engineering*, 18(1):1–28.

43. Potyondy, D. and P. Cundall, (2004), A Bonded-particle Model for Rock, Elsevier.

44. Qian, Y., D. Mishra, E. Tutumluer, and H. Kazmee, (2015), "Characterization of Geogrid Reinforced Ballast Behavior at Different Levels of Degradation through Triaxial Shear Strength Test and Discrete Element Modeling," *Geotextiles and Geomembranes*.

45. Qian Y., D. Mishra, E. Tutumluer, and J. Kwon, (2013), "Comparative Evaluation of Different Aperture Geogrids for Ballast Reinforcement through Triaxial Testing and Discrete Element Modeling," Proceedings, Geosynthetics 2013, Long Beach, CA.

46. Rinehart, R. and M. Mooney, (2009), "Measurement of Roller Compactor Induced Triaxial Soil Stresses and Strains," *Geotechnical Testing Journal*.

47. Schmalzer, P., (2006), LTPP Manual for Falling Weight Deflectometer Measurements, Version 4.1. MACTEC Engineering and Consulting, McLean, VA.

48. Skallman, J., (2010), Geogrids on CSAH and MSAS Routes General Specification, Granular Equivalent and Design Guidelines, Technical Memorandum 10-SA-03, Minnesota Department of Transportation, St. Paul, MN.

49. Skok, E., E. Johnson, and M. Brown, (2003), Special Practices for Design and Construction of Subgrades in Poor, Wet and/or Saturated Soil Conditions, MnDOT 2003-39, Minnesota Department of Transportation, St. Paul, MN.

50. Skok, E., D. Timm, M. Brown, T. Clyne, and E. Johnson, (2003), Best Practices for the Design and Construction of Low Volume Roads, MnDOT 2002-17REV, Minnesota Department of Transportation, St. Paul, MN.

51. Stahl, M., H. Konietzky, L. teKamp, and H. Jas, (2013), "Discrete Element Simulation of Geogrid-Stabilized Soil," *Acta Geotechnica*., doi: 10.1007/s11440-013-0265-0.

52. Stahl, M. and H. Konietzky, (2010), "Discrete Element Simulation of Ballast and Gravel under Special Consideration of Grain-Shape, Grain-Size, and Relative Density," *Granular Matter*.

53. Sun, L., c. Graves, l. Frank, and p. Looney, (2016), "Developing Flexible Pavement Design Aide Counting Geogrid Effect by Using Parametrical Study and Optimization Procedure," Proceedings, Geo-Americas, Miami Beach, FL.

54. Tanquist, B., (2012), MnPAVE User's Guide, Office of Materials and Road Research, Minnesota Department of Transportation, St. Paul, MN.

55. Tanquist, B., S. Dai, P. Davich, J. Siekmeier, and D. VanDeusen, (2002), Pavement Designer's Guide MnDOT Flexible Pavement Design MnPAVE Beta Version 5.1, Office of Materials and Road Research, Minnesota Department of Transportation, St. Paul, MN.

56. Tan, D., K. Hill, and L. Khazanovich, (2014), Quantifying Moisture Effects in DCP and LWD Tests Using Unsaturated Mechanics, MnDOT 2014-13, Minnesota Department of Transportation, St. Paul, MN.

57. Tutumluer, E., Y. Xiao, and W. Wilde, (2015), Cost Effective Base Type and Thickness for Long Life Concrete Pavements, MnDOT 2015-42, Minnesota Department of Transportation, St. Paul, MN.

58. Tutumluer, E., Y. Qian, Y. Hashash, J. Ghaboussi, and D. Davis, (2013), "Discrete Element Modelling of Ballasted Track Deformation Behavior," *Int. J. of Rail Trans.*, 1(1-2):57-73.

59. Van Cauwelaert, F., D. Alexander, T. White, and W. Barker, (1989), "Multilayer Elastic Program for Backcalculating Layer Moduli in Pavement Evaluation (WESLEA)," Nondestructive Testing of Pavements and Backcalculation of Moduli, ASTM STP1026, American Society for Testing and Materials, Philadelphia, PA.

60. Xiao, Y., E. Tutumluer, Y. Qian, and J. Siekmeier, (2012), Gradation Effects Influencing Mechanical Properties of Aggregate Base and Granular Subbase Materials in Minnesota, *Transportation Research Record 2267*, Transportation Research Board, Washington, D.C.

61. Xiao, Y., E. Tutumluer, and J. Siekmeier, (2011), Mechanistic-Empirical Evaluation Aggregate Base and Granular Subbase Quality Affecting Flexible Pavement Performance in Minnesota, *Transportation Research Record 2227*, Transportation Research Board, Washington, D.C.

62. Xiao, Y. and E. Tutumluer, (2012), Best Value Granular Material for Road Foundations, MnDOT 2012-01, Minnesota Department of Transportation, St. Paul, MN.

63. Yohannes, B., K. Hill, and L. Khazanovich, (2009), Mechanistic Modeling of Unbound Granular Materials, MnDOT 2009-21, Minnesota Department of Transportation, St. Paul, MN.

64. Zeghal, M., (2005), "Discrete-Element Method Investigation of the Resilient Behavior of Granular Materials," *Journal of Transportation Engineering*, 130(10):503-509.

APPENDIX A

MnDOT Trunk Highway 72 Geogrid Analysis (2013)

Trunk Highway 72 Geogrid Analysis

August 19, 2013

Prepared by:

Joseph Casanova
John Siekmeier

Table of Contents

LIST OF FIGURES

LIST OF TABLES

Executive Summary

Geosynthetics have been installed in northern Minnesota roadways for many years, with the expectation that they will provide additional reinforcement and life to the roadway. Although the use has been quite common in some areas, the pavement performance has not been well documented. This project will focus on a set of falling weight deflectometer (FWD) measurements collected by Braun Intertec under contract with MnDOT on two trunk highways (TH) in Lake of the Woods, Koochiching, and Beltrami Counties.

The objective of this project is to document any pavement structure benefits resulting from the use of biaxial geogrid placed in the base layer. FWD measurements are compared for two test sections on TH 72, one with geogrid in the base layer and one without. An analysis of the simulated and collected measurements was done to quantify the effect of geogrid on the road surface. To simulate the FWD deflections MnDOT's mechanistic empirical flexible pavement design program MnPAVE was used.

The data from Braun Intertec was collected using a Dynatest™ Model 8002E FWD. A proposed 1/4 mi (0.40 km) baseline subsection for each test section was selected to perform tests in 50 ft (15 m) intervals. Outside these baseline segments, tests were performed every 1/8 mi (0.20 km) to allow comparison of spatial variability. At each test point a total of 4 drops were applied, two on the order of 6 kips (26.7 kN) and two on the order of 9 kips (40.0 kN). The drops on the order of 9 kips were used for the analyses in this report. Due to tests being run in the morning and afternoon, the difference in road surface temperatures meant that the data had to be split to avoid applying temperature corrections to the data. The cooler temperatures were used because the test section without geogrid did not have enough data collected in the afternoon to perform any statistically valid analyses. This left 56 data points for the section with geogrid and 64 data points for the section without geogrid.

Given the constructed plans and some basic assumptions MnPAVE and ELMOD used a five layer system; HMA, full depth reclamation (FDR), engineered soil, undisturbed soil, and saturated water layer. Using MnPAVE and ELMOD an analysis matrix for the roadway layers was created. Using the values from the ELMOD backcalculation a range of values for FDR and soil were used as inputs into MnPAVE's FWD simulation. MnPAVE's FWD simulation deflection basins are plotted along with the test measurements to analyze the effect that the FDR and soil have on the roadway structure.

The analyses of the collected and simulated FWD measurements both conclude that it is not possible, given the current measurements, to determine the structural benefit of the geogrid due to the stiffness and variability in both the FDR and soil layers. It is recommended that testing be done shortly after the 2014 spring thaw and that FWD test drops be delivered at a higher load level.

CHAPTER 1: INTRODUCTION

Geogrid has been used in roadway projects for years with expectation that it provides additional reinforcement and life. The main implementation of geogrid is on roads that are built on poor soils with the anticipation of improved strength and reduced future maintenance. The two test sections analyzed in this report are built upon soil that is made up of predominately peat. Also, the FWD testing just after the spring thaw of the roadway was done to maximize the measured geogrid influence, because the pavement foundation layers are at their weakest during this period.

1.1 Geosynthetics Background

Geosynthetics can be grouped into two main categories: geotextile and geogrid. Geotextiles are not within the scope of this study so will not be discussed. Geogrid can provide lateral restraint, modified failure surface, and tensioned membrane. Lateral restraint is provided when the geogrid, placed properly, constrains the unbound materials. Modified failure surface happens when the geogrid reinforces a potential failure surface causing an increase in the bearing stress. Lastly, a tensioned membrane happens when rutting is countered by the tensile strength of the geogrid. All of these benefits result in a stronger and more resilient foundation for the pavement (Erickson and Drescher 2001).

Geogrid is a petroleum product typically made of polypropylene or polyethylene woven or bonded together to create a planar surface and used mostly as a reinforcing element. Geogrid can be further split up into two more categories: biaxial and uniaxial. Biaxial geogrid, which is what was used in one of the test sections analyzed, provides tensile strength in both planar directions, whereas uniaxial only provides strength in one planar direction. Geogrid is usually used on roadway construction where the underlying soil is of a very poor quality (Clyne 2011). This is because geogrid is intended to provide a stable construction platform to build on taking the load off of the poor soil.

Even though the use of geogrid in road construction is growing in popularity, its benefits are not well documented. The scope of this project is to quantify the benefit that geogrid provides to the unbound material modulus.

1.2 FWD Background

The Falling Weight Deflectometer (FWD) is a large trailer mounted device designed to simulate the deflection of a pavement surface under truck traffic. When the large mass is dropped a deflection basin is created. FWDs are particularly useful for estimating the in situ moduli of asphalt, aggregate base, granular subbase, and subgrade pavement layers through a method of backcalculation using the deflection measurements (Schmalzer 2006).

The primary sensors are the load cell which measures the force imparted to the road surface and geophones which measure the deflection basin. Some secondary sensors are the distance measurement instrument (DMI) and temperature sensors (air and infrared).

1.3 MnPAVE Background

MnPAVE (Tanquist 2012) is a mechanistic empirical flexible pavement design computer program that consists of three general inputs: climate, traffic, and structure; and three design levels: basic, intermediate, and advanced. Traffic loads are simulated in MnPAVE through a Layered Elastic Analysis (LEA) called WESLEA (Tanquist et al. 2002). This is a five-layer isotropic system program written in 1987 by Frans Van Cauwelaert and modified in 1989 by Donald R. Alexander (Van Cauwelaert et al. 1989). WESLEA assumes all layers are isotropic in all directions and infinite in the horizontal direction. However, the fifth layer is also assumed to be infinite in the vertical direction. Its inputs include layer thickness, modulus, Poisson's ratio, and an index indicating the degree of slip between layers. MnPAVE assumes zero slip between interfaces. This is all used with the final goal of finding the expected life of the pavement, which is calculated using a damage factor based on Miner's Hypothesis.

MnPAVE's climate moduli have five default seasons based on material properties. The five seasons are Summer, Fall, Winter, Early Spring, and Late Spring. Spring is split into two seasons because of the dramatic changes in the aggregate base and subgrade soil during the Spring thaw. The air temperature at the selected project location near TH 11 and TH 72 is based on a weighted average of data from weather stations in a 75 mile radius.

The expected traffic volume was not used in this project study because it is needed for pavement life expectancy and is not needed for the FWD simulation.

When first using the structure module, a window will open for the HMA mix where the user can adjust the HMA and include up to three lifts. From here the project worked in the intermediate level structure tab where the FDR, soil, and other layers were added to the pavement structure.

MnPAVE is being used to simulate the roadway because unlike other methods of, MnPAVE can take into account more variables. For instance the varying modulus values during different seasons (Skok et. al 2003).

1.4 Contract with Braun Intertec

Braun Intertec was contracted by MnDOT to perform FWD testing on test sections comparing geosynthetics on two trunk highways (TH), TH 11 and TH 72 in Lake of the Woods, Koochiching, and Beltrami Counties (Oman 2013). There were 18 different pavement sections and to simplify record keeping Braun Intertec labeled the sections "A" through "R". Figure 1.1 shows the general location of the test sections and Table 2.1 provides the general roadway structure. Along with naming the test sections Braun Intertec also grouped test sections together in order to isolate variables to compare the effects of geosynthetics, pavement thickness, and subgrade thickness. For the scope of this report only test sections "Q" and "R" have been compared.
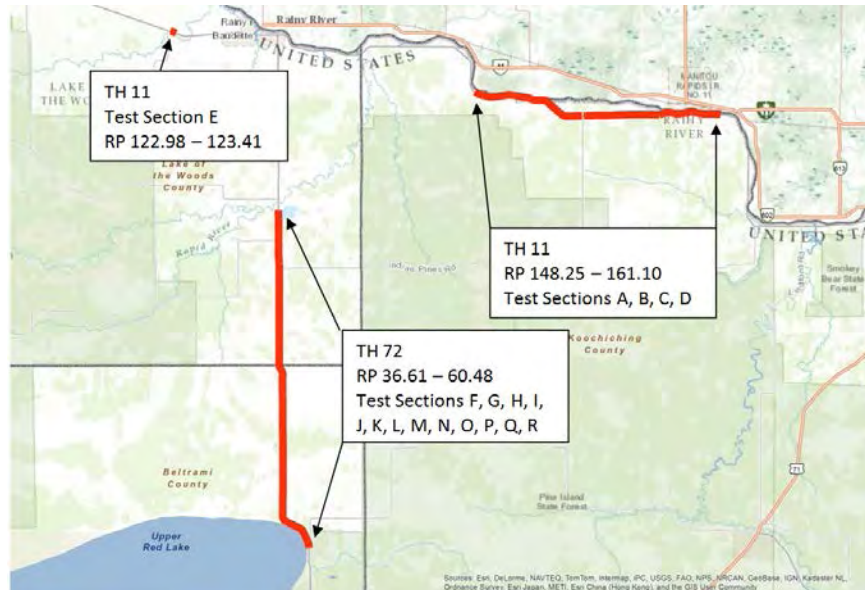
Figure 1.1 Location of test sections (MnDOT District 2)

The FWD testing was completed during the spring season of 2013 following complete thaw. Testing was initially set for April 23-25, 2013, but frost data collected from a MnDOT site on TH 11 in Koochiching County still showed frost in the ground. So the testing period was delayed to May 7 and 8, 2013. The frost depth from the MnDOT site on May 7, 2013 showed that frost was completely out of the pavement system (see Figure 1.2). Braun Intertec then took FWD measurements on all test sections during May 7 and 8, 2013. Taking tests this early after spring thaw has the potential of having residual frost in the soil allowing for some aspects of the roadway to be partially frozen and therefore have higher moduli than anticipated.
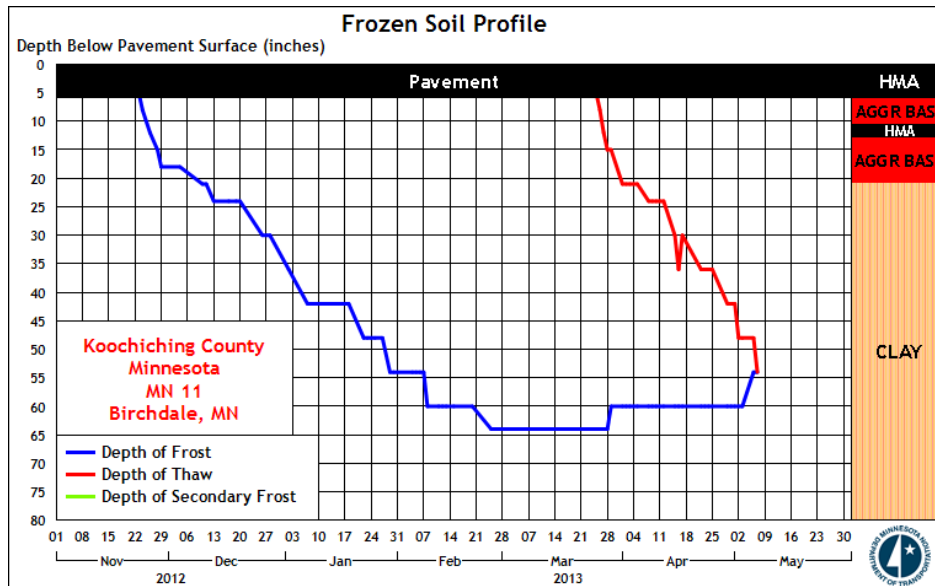
Figure 1.2 Frost depth indicator for Birchdale, MN

Each test section "A" through "R" was then split up into subsections and testing was done every 1/8th mile (0.20 km) except for one subsection in each test section, 1/4 mile (0.40 km) in length,

A-8

where tests were run in 50 ft (15 m) intervals. This was done to allow for statistically valid sample set and to account for spatial variability between test section measurements.

CHAPTER 2: SUMMARY OF MEASURED DATA

2.1 Discussion

Braun Intertec conducted FWD field measurements on test segments located on sections of TH 11 and 72. There were a total of 18 different pavement sections distinguished by varying length, year of construction, and constructed layers. To simplify record keeping Braun Intertec named the test sections "A" thru "R" (Table 2.1).

Table 2.1. Test sections summary

Test_Section	TH	Constructed	Project Number	RP_from	RP_to	Bituminous	Base	Subbase	Geosynthetic
A				148.25	166.72	6"	12" FDR	?	Geogrid @ 6" in FDR
B		2010	SP 3604-69	151.24	162.16	6"	12" CL 5	12" SGB	Type V fabric below SGB
C	11	2010	SP 3604-69	156.72	164.70	6"	12" FDR	?	Geogrid @ 6" in FDR
D				160.38	161.10	7"	12" FDR	?	Geogrid @ 6" in FDR
E		1997	SP 3901-34	122.98	123.41	5.5"	6" CL 6	bit & agg base	Geogrid @ 4" in CL 6
F		2011	SP 0413-33	36.61	45.00	5"	10" FDR	?	Geogrid @ 6" in FDR
G				42.45	42.70	6"	6" CL 5	8" SGB	Geogrid below SGB
H		1997	?	42.70	42.95	6"	6" CL 5	8" SGB	Type VI fabric below SGB
I				42.95	43.20	6"	6" CL 5	8" SGB	Geocell filled with SGB
J				43.20	43.45	6"	18" CL 6	?	Type V fabric below CL 5
K	72			45.00	45.50	5"	10" FDR	?	Geogrid @ 8" in FDR
L				45.50	46.00	5"	4" SFDR/6" FDR	?	Geogrid @ 8" in FDR
M		2011	SP 0413-33	46.00	46.50	4"	10" FDR	?	Geogrid @ 8" in FDR
N				46.50	47.00	4"	4" SFDR/6" FDR	?	Geogrid @ 8" in FDR
O				47.00	48.00	4"	4" SFDR/6" FDR	?	--
P				48.00	62.00	3"	mill & overlay		--
Q		2005	SP 0413-30	48.62	61.35	4.5"	9" FDR	?	Geogrid @ 6" in FDR
R				49.35	60.48	4.5"	9" FDR	?	--

FDR = Full-depth Reclamation   SFDR = Stabilized Full-depth Reclamation

CL 5/CL 6 = MnDOT Class 5/6 Aggregate Base   SGB = MnDOT Select Granular Borrow

The scope of the current MnPAVE analysis is limited to test sections Q and R and simulating the measured FWD data. As seen in the test section summary, the only difference in the constructed layers between test section Q and R, is that test section Q has Tensar™ Biaxial Geogrid 6 inches below the top of the FDR and test section R does not contain geogrid.

From the measurements provided by Braun Intertec, only the FWD measurements from test sections Q and R were selected. From this data set the tests around 9 kips were used in the MnPAVE analysis described in this report. The reasoning behind this is because pavement surface and subgrade interactions between load and deflection are not linear as seen in Figure 3.1. Also, as stated in the Braun Intertec report, even drops around 9 kips (40.0 kN) might not have been large enough to fully mobilize the geogrid in the FDR layer.
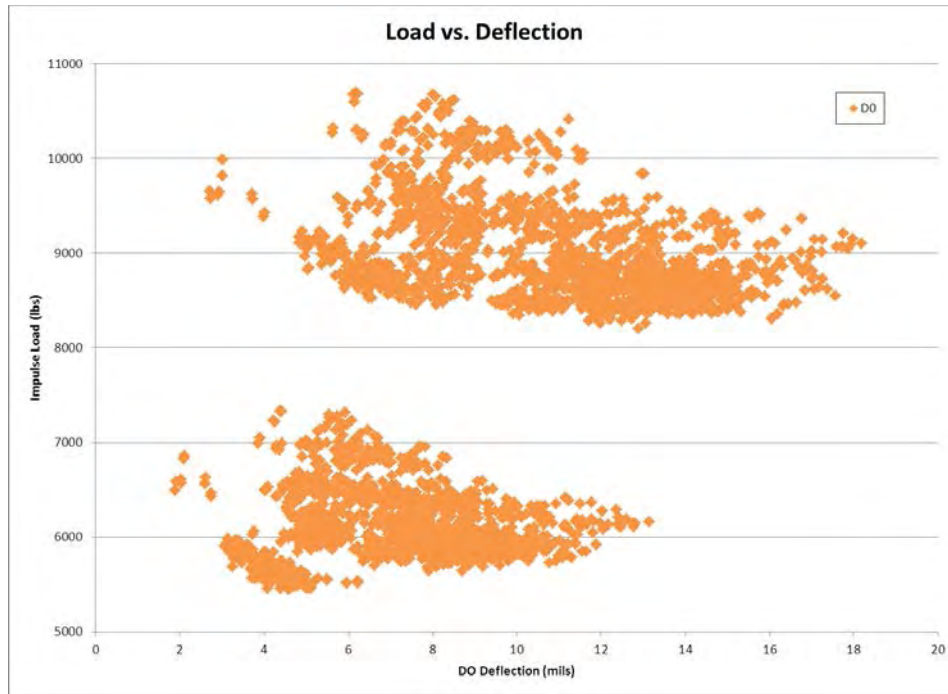
Figure 2.1 Load vs. D0 deflection for test sections A through R

The next consideration was pavement temperature measured by the FWD infrared temperature sensor at each test point. Tests were run on May 7 and 8 during the morning and afternoon. None of the afternoon times were used due to a lack of sufficient data from section R. Using this raw data, a mean value drop was chosen and then the rest of the data was normalized to this number. A summary of the data is shown in Table 2.2 and as can be seen the variable temperature has been reduced to an allowable tolerance.

Table 2.2 Data summary of test sections Q and R

Row Labels	Count of Drop #	Average of Pvmt Temp (C)	Average of Load (kN)				
Q	56	14.27	45.42				
R	64	14.33	45.42				
Grand Total	120	14.30	45.42				
	D0 (mm)	D8 (mm)	D12 (mm)	D18 (mm)	D24 (mm)	D36 (mm)	D60 (mm)
Average Q	224.7567	181.7033	152.6398	121.3220	100.4694	75.9709	53.3929
Average R	211.1982	171.4971	144.0826	113.8762	94.1470	71.0759	49.3324
Total Average	217.5255	176.2600	148.0759	117.3509	97.0975	73.3602	51.2273

The reason for not normalizing to the standard 9 kips was because the range of the drops was from 8.9 to 10.7 kips (39.6 to 47.6 kN). So it was decided to normalize to the mean value of the data, 10.2 kips (45.4 kN). In Figure 2.2 is a plot of the deflection basins for the two test sections adjusted linearly to 10.2 kips. This graph shows all 120 test points and from this it is uncertain if any differences between the two test sections are seen, because of the large amount of variability in the roadway.
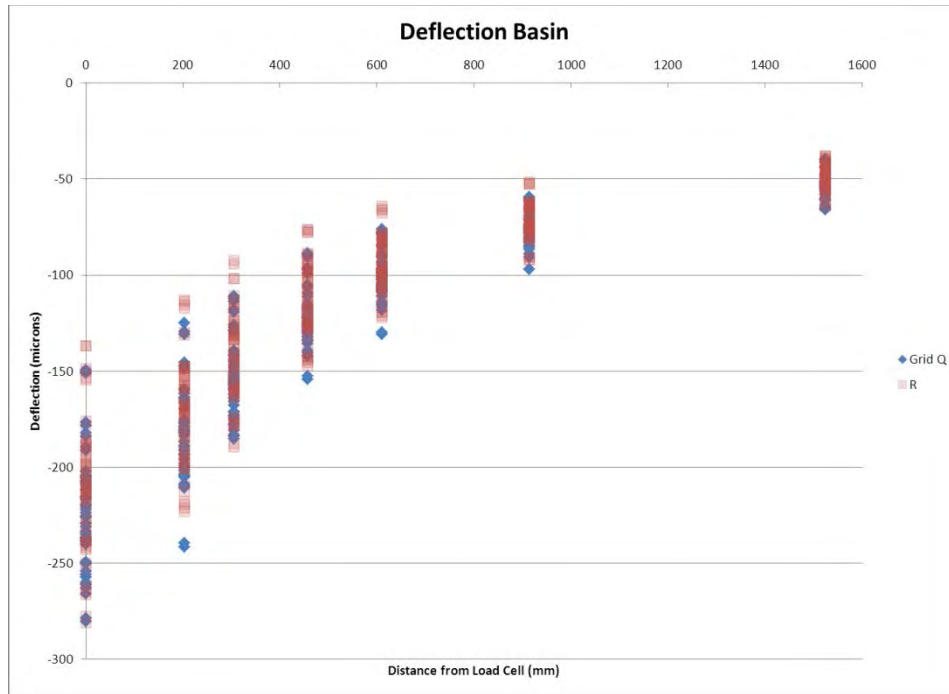
Figure 2.2 Deflection Basin for Test Sections Q and R

To reduce the variability and find trends in the measurements, the test sections were split into subsections (Table 2.3). From these subsections five were chosen Q3, Q4, Q6, R2, and R4. Soil logs were known for each test section and two subsections were chosen from each subsection to compare variability.

As seen in Figure 2.3 and Figure 2.4 a difference is measured when comparing grid reinforced to no grid sections. Also it can be seen from grid test sections Q3 and Q6 the variability in Q6 is greater than Q3 because subsection Q3 was only of length 0.08 miles as opposed to subsection Q6 which is 0.87 miles. This discovery unfortunately means that the test sections Q and R differ by more than just the grid. There is another difference in the test sections and that is the soil and can be seen in Appendix B. This difference in the deflections with and without the grid is actually a lower bound value because the soil underneath the grid (section Q) is made up mostly of peat as opposed to without grid (Section R) where peat is not as prevalent.

However, this does not definitively conclude that geogrid has an effect on this road surface. When comparing test sections Q4 and R2, which are both built on relatively the same type of soil no significant difference in their deflections are seen (Figure 2.5). The variability within R2 is not too great due to a length of only 0.25 miles, however Q4 is 1.69 miles long and the variability of this is seen. The conclusion is that the geogrid seems to have no effect on roadway, which contradicts what was seen in Figure 2.3 and 2.4. This analysis therefore is inconclusive and further field measurements need to be done.

Table 2.3 Detail of test sections and subsections

	2011	36.61	42.45	5.84	F	7.39	82	F1	
	2011	43.45	45.00	1.55				F2	
	2011	42.45	42.70	0.25	G	0.25	25	G	x
	2011	42.70	42.95	0.25	H	0.25	25	H	x
	2011	42.95	43.20	0.25	I	0.25	25	I	x
	2011	43.20	43.45	0.25	J	0.25	25	J	x
	2011	45.00	45.50	0.50	K	0.50	27	K	x
	2011	45.50	46.00	0.50	L	0.50	27	L	x
	2011	46.00	46.50	0.50	M	0.50	27	M	x
	2011	46.50	47.00	0.50	N	0.50	27	N	x
	2011	47.00	48.00	1.00	O	1.00	31	O	x
72	2005	48.00	48.62	0.62				P1	
	2005	51.86	57.80	5.94	P	7.21	81	P2	x
	2005	61.35	62.00	0.65				P3	
	2005	48.62	49.35	0.73				Q1	
	2005	49.63	51.86	2.23				Q2	
	2005	57.80	57.88	0.08	Q	5.74	69	Q3	x
	2005	58.15	59.84	1.69				Q4	
	2005	60.07	60.21	0.14				Q5	
	2005	60.48	61.35	0.87				Q6	
	2005	49.35	49.63	0.28				R1	
	2005	57.88	58.15	0.27	R	1.05	31	R2	x
	2005	59.84	60.07	0.23				R3	
	2005	60.21	60.48	0.27				R4	

Figure 2.3 Comparison of the test subsections Q3 with grid and R4
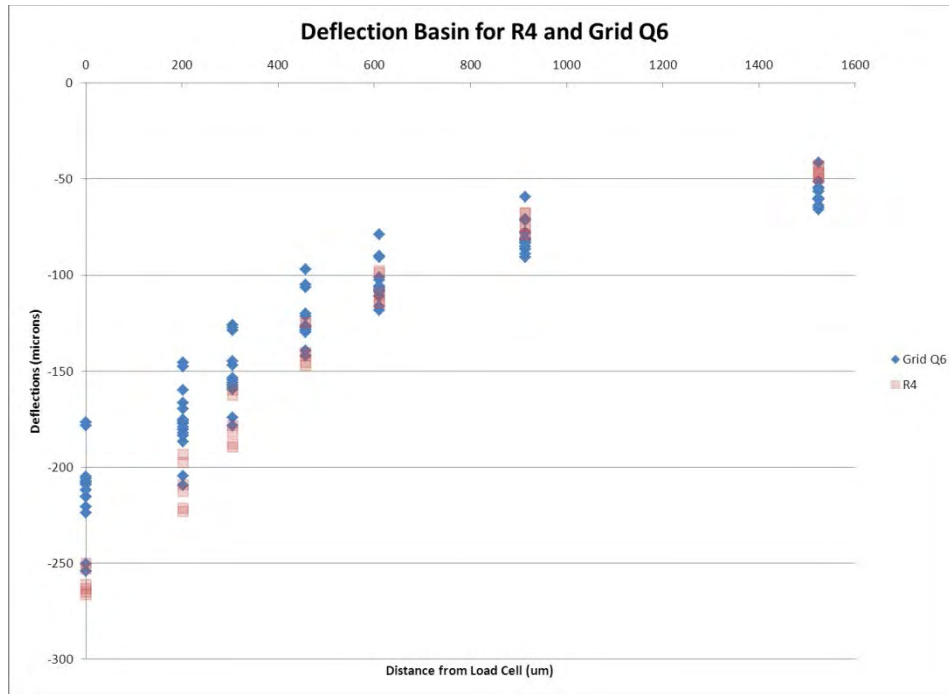
Figure 2.4 Comparison of the test subsections Q6 with grid and R4
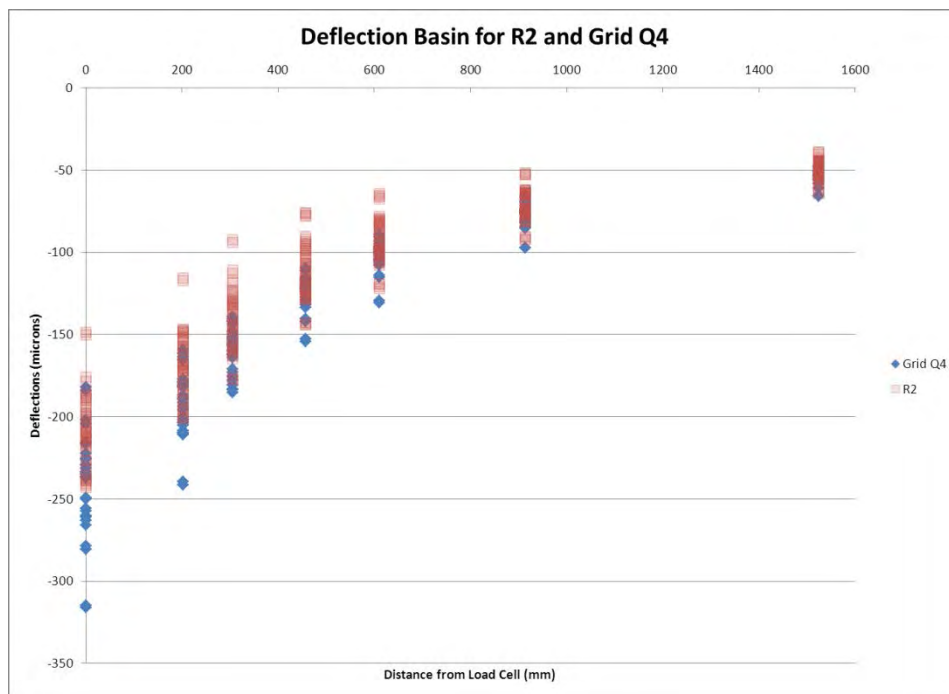
Figure 2.5 Comparison of the test subsections Q4 with grid and R2

2.2 Conclusions from Measured Data

The FWD measurements were collected by Braun Intertec on 18 different test sections. This project focused on two of these test sections in particular, Q and R. These two test sections were chosen because it was anticipated from the plans they only differed by the addition of geogrid in

the FDR. However, upon further inspection of the soil logs it was determined that subsections Q3, Q4, Q6, R2, and R4 were built on varying soil conditions.

A representative group of measurements were selected based on a set of criteria. First, was the selection of FWD measurements taken around 9 kips which was done mainly to mobilize the geogrid in the FDR layer. Second, was temperature which was around two different temperatures, a morning and an afternoon temperature, morning temperatures were chosen because section R had no afternoon temperature measurements. This was done to reduce the uncertainty that would result from temperature corrections.

From the entire set of FWD measurements it is hard to see any distinguishable difference between the test sections Q and R. So using the soil logs and the subsections an even more select group of points were chosen and plotted. From this selection of measurements, the amount of variability is reduced.

What can be drawn from this selection of data is that the grid does have an effect, but quantifying this effect will be harder than previously thought due to the large variability in the soil under the roadway. From the measurements selected the effect of the geogrid compared to no geogrid would be a lower bound estimate for subsections Q3, Q6, and R4. However, soil variability makes it difficult to quantify the effect of geogrid, as seen in subsections Q4 and R2 where no difference was found in the geogrid. Given the differences in soils beneath the two sections, determining the range of geogrid reinforcement benefit will require additional field measurements and analyses.

CHAPTER 3: MNPAVE FWD SIMULATIONS

3.1 Discussion

Analysis for the FWD data using MnPAVE was simulated during the late spring. The first input for MnPAVE was deciding the right location for the climate parameter. Since the data is only dealing with test sections Q and R, the climate location was picked to be approximately in the middle of the test section on TH 72 as seen in Figure 3.1. Climate is predicted from a 75 mile radius around the spot picked. Test sections Q and R are not far enough apart to be concerned with different climate temperatures.

By selecting this location MnPAVE inputs default seasonal lengths based on past research, which is only important towards the output of the pavement life cycle. Of more importance is the temperature input which is defined by a weighted average of data from weather stations in a 75 mile radius. This input goes into calculating seasonal values for structural inputs such as HMA, which is vital towards FWD simulation in MnPAVE.
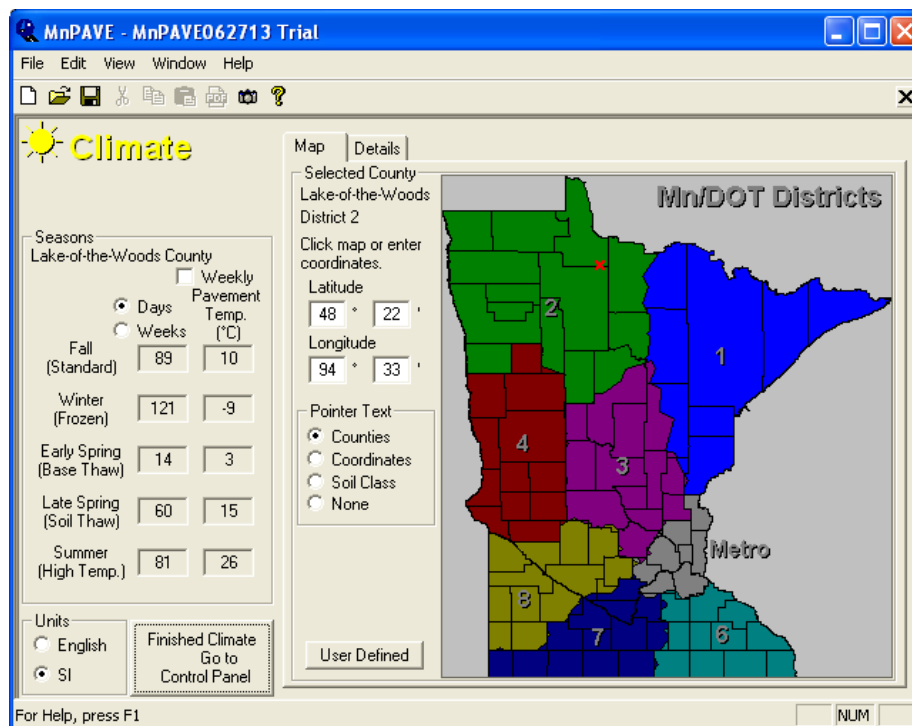
Figure 3.1 Overview of the climate input

The traffic input does not change the FWD simulation in MnPAVE and is only used when evaluating the roadway life expectancy. In the structure window the intermediate tab was chosen for designing the roadway. From the geotechnical exploration and construction data received from District 2, an analysis matrix was chosen to simulate the different variables affecting the road. It is noted that the HMA mix type and the thickness for the HMA, FDR, engineered soil, and undisturbed soil layers were held constant along with the climate and season.

The HMA mix provided by District 2 was SPWEB340C and was inputted into MnPAVE program as seen in Figure 3.2. This was assumed to accurately represent the actual asphalt on the roadway surface at the time of installation. From here the roadway structure was entered into the intermediate design level and then simulated using MnPAVE's FWD simulation. As seen in Figure 3.3 several inputs were needed for accurate representation of the data collected: the FWD load, plate diameter, season, and temperature. These all need to be entered before MnPAVE can estimate the deflections. From the data collected by Braun Intertec, only the I.R. pavement temperature at the surface was given so using MnPAVE's FWD data program, as seen in Figure 3.4, which uses the BELLS3 equation to equate the pavement temperature at a third of the depth, was used to find the temperature of the HMA layer (Lukanen et. al. 2000). This was done using the measured data from Braun and weather underground (www.wundground.com) to input the I.R. surface temp and previous day's high and low respectively. From this screen the only important information is the calculation of the pavement temperature at a third of the depth of the HMA layer which is needed for the FWD simulation.

Figure 3.2 HMA Specifications in MnPAVE

Figure 3.3 MnPAVE FWD test simulation

Figure 3.4 MnPAVE estimation of the HMA temperature

Using an ELMOD (Dynatest 2012) five layer analysis to backcalculate the moduli an idea of the range for the moduli of the HMA, FDR, and soil were found and simulated in MnPAVE's FWD simulation (Table 3.1). The ELMOD analysis used five layers HMA, FDR, engineered soil, undisturbed soil, and a stiff layer due to the water table (Newcomb et. al. 1995). The seed moduli were 4345, 1200, 90, 45, and 5000 MPa respectively (500, 138, 10, 5, and 575 kips). Deciding five layers and higher value moduli was determined through manipulation of MnPAVE and ELMOD structures and seed moduli till the MnPAVE simulation was within the range of the measured data. Running the ELMOD backcalculation on each analyzed subsection in chapter 2 (Table 3.2 – 3.6) gives a range of values for each layer. From these tables it can be seen that there is large variation in moduli between test subsections and even test measurements within subsections.

Table 3.1 Roadway structure for ELMOD backcalculation

	Thickness	Seed Modulus (MPa)
HMA	4.5"	4345
FDR	9"	1200
Eng. Soil	24"	90
Und. Soil	24"	45
Stiff Layer	N/A	5000

Table 3.2 Range of roadway backcalculation results for subsection Q3 with geogrid

Moduli in Mpa				
HMA	FDR	Eng. Soil	Und. Soil	Stiff Layer
14021.84	1043.15	257.00	29.63	3514.59
6272.66	622.86	451.98	23.43	2181.37

Table 3.3 Range of roadway backcalculation results for subsection Q4 with geogrid

Moduli in Mpa				
HMA	FDR	Eng. Soil	Und. Soil	Stiff Layer
7392.28	654.55	221.17	25.49	2645.76
5388.67	1018.34	223.93	20.67	2157.26
5430.70	551.20	249.42	23.43	2086.29
4760.30	535.35	294.89	24.12	2415.63
13718.68	775.81	202.57	19.29	3469.80
8923.93	528.46	216.35	20.67	5541.63
4021.00	460.94	274.91	22.74	2367.40

Table 3.4 Range of roadway backcalculation results for subsection Q6 with geogrid

Moduli in Mpa				
HMA	FDR	Eng. Soil	Und. Soil	Stiff Layer
3779.17	629.75	327.96	28.94	2988.88
8706.20	797.86	177.07	21.36	2414.26
6637.83	1290.50	237.71	21.36	2995.77
4337.94	1170.61	208.77	22.05	6884.49
7211.76	1075.53	186.03	20.67	3314.78
5236.40	627.68	206.70	17.91	2300.57
7127.71	663.51	216.35	17.91	2357.76
8310.72	731.72	214.28	16.54	2543.79

Table 3.5 Range of roadway backcalculation results for subsection R2 without geogrid
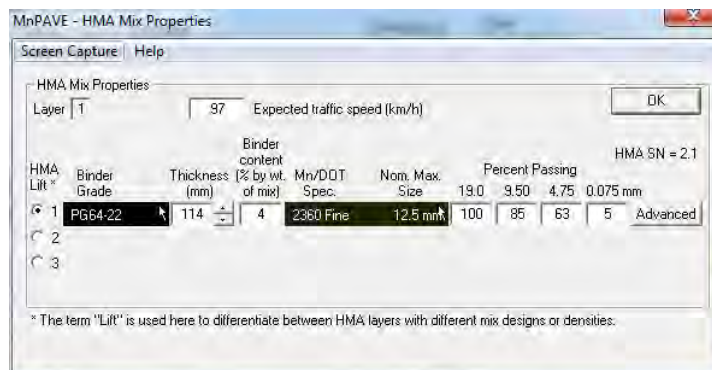
Moduli in Mpa				
HMA	FDR	Eng. Soil	Und. Soil	Stiff Layer
5498.22	866.76	302.47	22.74	2602.35
5828.25	710.36	421.67	23.43	2655.41
6563.41	323.14	803.37	23.43	2781.49
5997.75	1297.39	484.37	26.18	2986.82
7589.34	443.03	383.77	25.49	2420.46
6540.68	503.66	416.85	23.43	2518.30
5166.12	717.94	378.95	23.43	2253.03
6048.04	903.28	315.56	26.87	6097.65

Table 3.6 Range of roadway backcalculation results for subsection R4 without geogrid
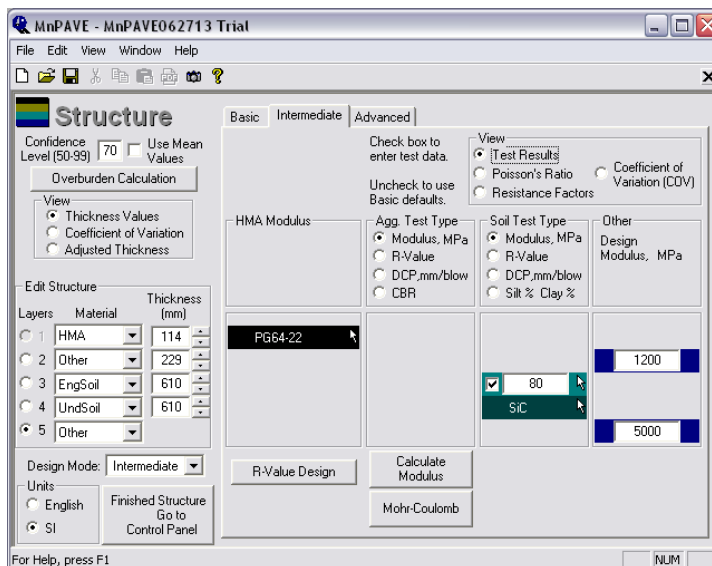
Moduli in Mpa				
HMA	FDR	Eng. Soil	Und. Soil	Stiff Layer
6400.12	465.76	134.36	35.83	2681.59
4523.29	575.32	151.58	34.45	4809.22
3701.31	632.50	186.03	33.76	3307.20
4874.90	**557.86**	**157.32**	**34.68**	**3599.34**

It was found from this backcalculation that the HMA and FDR were a lot stiffer than expected. Since HMA stiffens as it ages it is very likely that the original HMA default layer modulus in MnPAVE is too low, so a PG64-22 binder was used to increase the moduli of the HMA. Also, due to the large range of possible FDR values, which are due in part by the current specifications for FDR and the time of year, the higher values 400 to 1200 MPa were determined to be a reasonable range. This FDR was represented using the "Other" option in MnPAVE. For the soil there was large variability from soil samples taken by District 2 though the soil is made up predominantly of peat at varying amounts mixed with other poor soils. So a range for the soil

was decided to be between 30- 90 MPa, please note that MnPAVE puts a seasonal correction factor of 0.68 on these values due to it being inputted as engineered soil during the Late Spring. Then a fourth layer of undisturbed soil was set and MnPAVE gives this soil a value half the value of the engineered soil. Finally, estimates from the District 2 office indicate that groundwater saturation is like between five to nine feet below the road surface. From past studies and reports this groundwater can act like a stiff layer with a modulus of approximately 5000 MPa.

Figure 3.5 Analysis matrix HMA specifications

Figure 3.6 Sample of roadway structure for analysis matrix

An analysis matrix was put together changing only the reclaim, denoted as "Other" to allow manipulation of the strength to high values, and the engineered soil. An overview of the variables is seen in Table 3.7 and some results of the simulations are shown in Table 3.8. The thickness of each layer was kept fixed at the values shown in Figure 3.8. The coefficient of variation was set to zero percent so that the thicknesses shown were the actual thicknesses the program used for the FWD simulation and the confidence level was not adjusted and does not affect the FWD simulation.

Table 3.7 MnPAVE input matrix

Input Category	Input Variables	Number of Variables
Asphalt Layer	PG 64-22	1
FDR	Modulus Value (MPa) 400, 800, 1200	3
Engineered Soil	*Modulus Value (MPa) 30, 60, 90	3
Undist. Soil	Modulus Value (MPa) 1/2 Engineered Soil	1
Water Table	Modulus Value (MPa) 5000	1
	Total:	9

*late spring seasonal factor of 0.68 applied to these

Table 3.8 Simulated FWD measurements from analysis matrix

	FWD Deflections (μm) at top of Surface Material						
	0	203	305	457	610	914	1524
AD	629	565	515	441	371	251	87
AE	459	399	354	290	233	143	36
AF	380	322	280	223	174	100	20
BD	498	448	411	359	309	221	92
BE	369	321	288	242	200	132	42
BF	308	262	231	189	152	94	25
CD	426	384	355	313	274	202	92
CE	318	278	251	214	181	123	44
CF	268	228	203	169	139	90	28

Legend:

	A	B	C
Reclaim	400	800	1200
	D	E	F
Eng Soil*	30	60	90

*seasonal factor of 0.68 applied

Comparing the different values of the FDR and soil against subsections Q3, Q6, and R4 several conclusions can be made (Figure 3.9 – 3.12). First, the predicted values from MnPAVE have a predicted greater deflection than what was measured by the FWD. This along with the ELMOD backcalculation shows that this roadway is very stiff. Another observation that can be seen from changing either the FDR or soil moduli large variations in the deflection curve can appear. Further agreeing with the results found in the data summary analysis that the variation in the FDR and soil makes drawing any conclusions from the data measured by the FWD inconclusive.
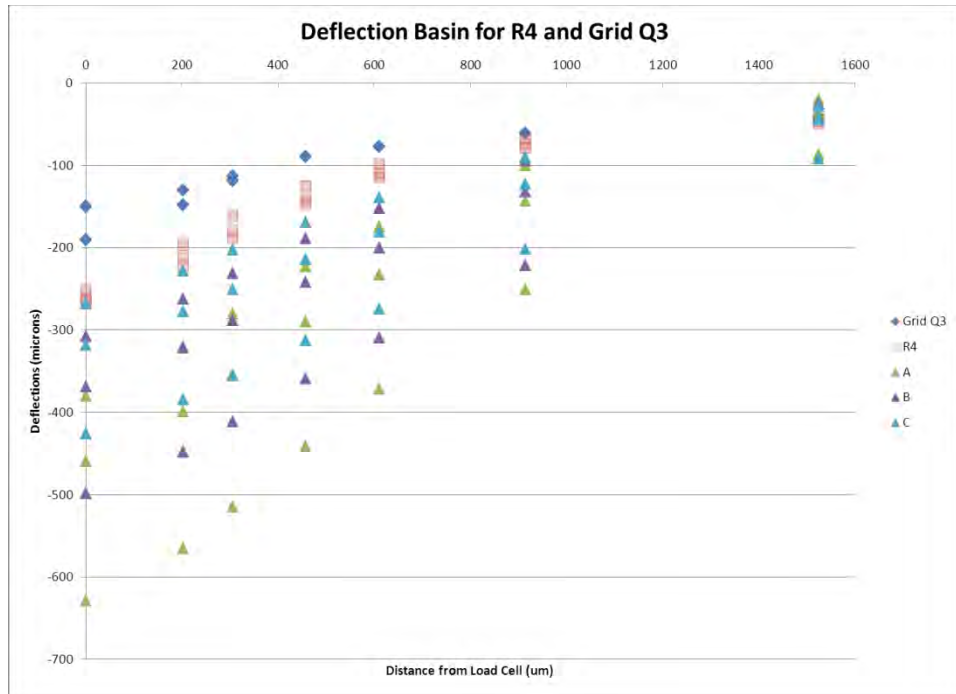
Figure 3.7 Simulated FWD measurements keeping FDR values fixed against Q3 and R4
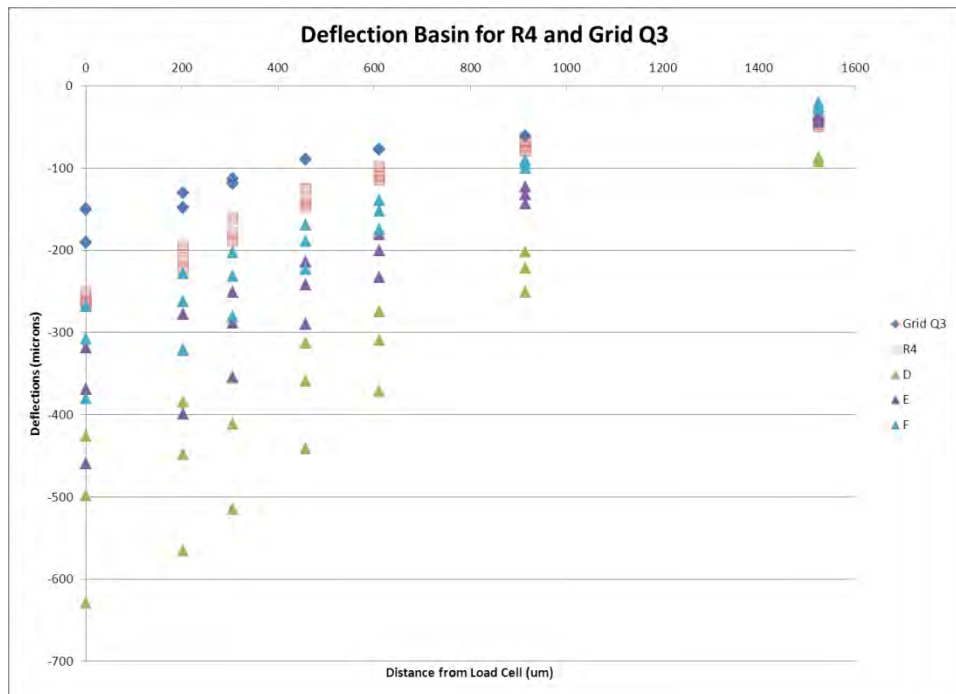
Figure 3.8 Simulated FWD measurements keeping soil values fixed against Q3 and R4
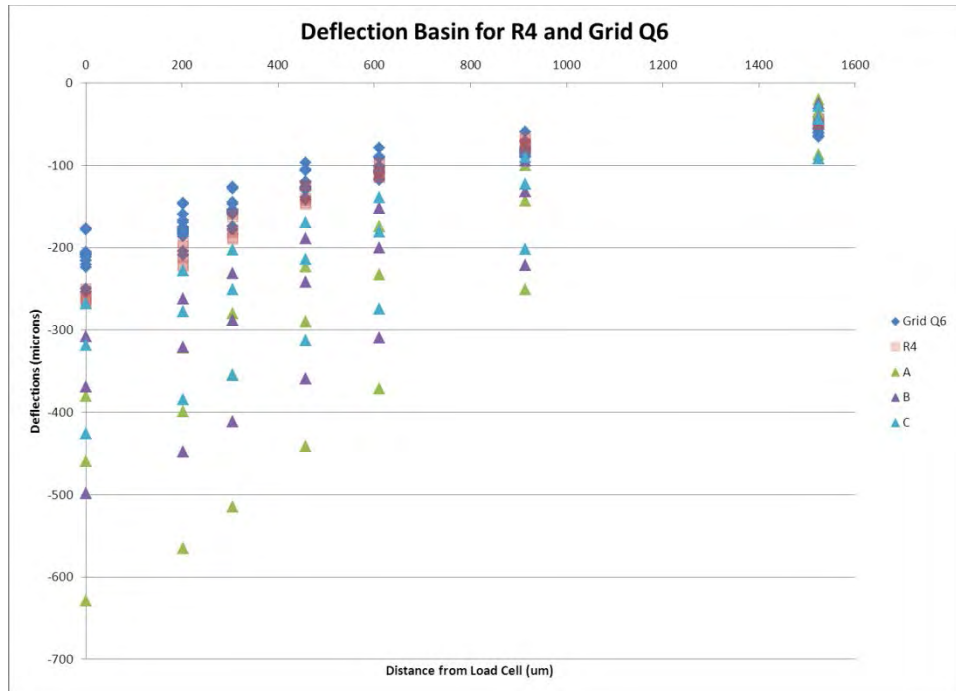
Figure 3.9 Simulated FWD measurements keeping FDR values fixed against Q6 and R4
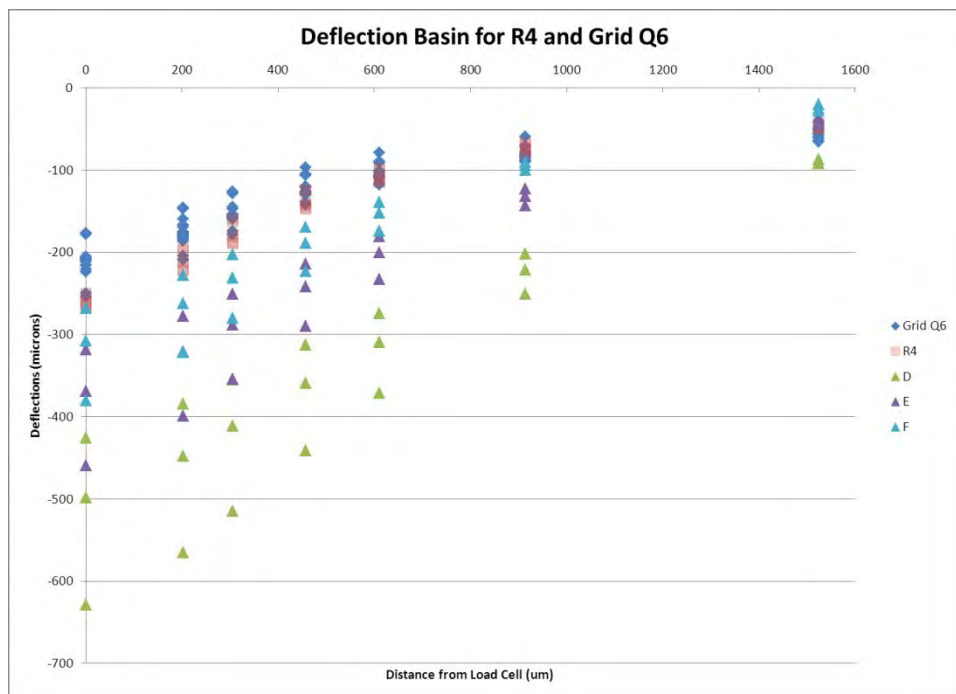
Figure 3.10 Simulated FWD measurements keeping soil values fixed against Q6 and R4

3.2 Conclusion of MnPAVE FWD Simulations

Drawing from both the ELMOD backcalculation analyses and MnPAVE FWD simulations, the roadway layer properties appear stiffer road than anticipated. This can be attributed to the age of the roadway, which stiffens the HMA and potentially the FDR. Also, the current specifications

for FDR allow very large variations in its moduli. Not only are these variations apparent, but soil variations are also apparent and when comparing differences in FDR and soil moduli for the range of values the ELMOD simulation provided shows that due to the large variation any conclusions are difficult at this time.

CHAPTER 4: CONCLUSION

The FWD data measured by Braun Intertec was simulated using MnPAVE to compare test sections Q and R. As the data was analyzed it was found that there was too much variability in each test section to draw any definitive conclusions.

Only the morning test drops from 9 kips (40 kN) were used from each test section. This was done in an effort to reduce variability. The 120 test points were split up into their perspective subsections and plotted against one another. When comparing test subsections Q6 and Q3 against subsection R4 it appears the geogrid has an advantage. However, when comparing test subsections Q4 against R2 the data does not seem to have any difference amongst subsections. This means that the results are inconclusive, there may be a benefit due to the geogrid, but further test measurements and analyses will be needed.

The conclusion from looking at the test measurements were further backed up by the MnPAVE simulation and ELMOD backcalculation for the roadway. From MnPAVE's FWD simulation it was found that the stiffness of the HMA and FDR were higher than anticipated, which makes it difficult to get readings as far down as the geogrid. As well by changing the soil or FDR moduli within the range found in ELMOD the large variations in the soil and FDR could explain the differences seen in test subsections Q6, Q3, and R4.

REFERENCES

Clyne, Timothy R. (2011) *Monitoring Geosynthetics in Local Roadways (LRRB 768) 10-Year Performance Summary,* MN/RC 2011-20, Office of Materials, Minnesota, Department of Transportation, Maplewood, MN, USA.

Edil, Tuncer B., James M. Tinjum, and Craig H. Benson. (2012) *Recycled Unbound Materials,* MN/RC 2012-35, Department of Civil and Environmental Engineering Geological Engineering Program University of Wisconsin – Madison.

Erickson, Hans, Andrew Drescher. (2001) *The Use of Geosynthetics to Reinforce Low Volume Roads,* MN/RC 2001-15, University of Minnesota Department of Civil Engineering, Minneapolis, MN, USA.

ELMOD 6.1.53 (2012) *Evaluation of Layer Moduli and Overlay Design*, Dynatest International, Glastrup, Denmark.

Gale, Steve, and Michael Marti. (2008) *Putting Research into Practice: Training Module for Designing and Constructing with Geosynthetics,* PP07GEO-TS, Minnesota Department of Transportation, Minneapolis, MN, USA.

Grading and Base Unit (2002) *Grading and Base Manual*, Office of Materials, Minnesota Department of Transportation, Maplewood, MN, USA.

Lukanen, Erland O., Richard Stubstad, and Robert Briggs (2000) *Temperature Predictions and Adjustment Factors for Asphalt Pavement,* FHWA-RD-98-085, Office of Infrastructure Research and Development, Mclean, VA, USA.

Newcomb, David E., David A. Van Deusen, Yan Jiang, and Joe P. Mahoney. (1995) *Considerations of Saturated Soil Conditions in Backcalculation of Pavement Layer Moduli,* Transportation Research Record 1473.

Oman, Mathew S., (2013) *Pavement Evaluation Report,* BL-13-01691, Braun Intertec Corp, St. Paul, MN, USA.

Robert, D. Holtz, Barry R. Christopher, and Ryan R. Berg. (1998) *Geosynthetics Design and Construction Guideline*, Ryan R. Berg and Associates, Inc. Maplewood, MN, USA.

Schmalzer, Peter N. (2006) *LTPP Manual for Falling Weight Deflectometer Measurements, 4.1,* FHWA-HRT-06-132, Federal Highway Administration Office of Infrastructure Research and Development, McLean, VA, USA.

Skok, Eugene L., David H. Timm, Marcus L. Brown, Timothy R. Clyne, and Eddie Johnson. (2003) *Best Practices for the Design and Construction of Low Volume Roads Revised.* Office of Materials, Minnesota Department of Transportation, Maplewood, MN, USA.

Tanquist, Bruce. (2012) *MnPAVE User's Guide,* Office of Materials, Minnesota Department of Transportation, Maplewood, MN, USA.

Tanquist, Bruce, Shangtao Dai, Peter Davich, John Siekmeier, and David VanDeusen. (2002) *Pavement Designer's Guide MnDOT Flexible Pavement Design MnPAVE Beta Version 5.1*, Office of Materials, Minnesota Department of Transportation, Maplewood, MN, USA.

Van Cauwelaert, F.J., Alexander, D.R., White T.D., and Barker, W.R., (1989) *Multilayer Elastic Program for Backcalculating Layer Moduli in Pavement Evaluation*, American Society for Testing and Materials, Philadelphia, PA, USA.

APPENDIX B

Braun Intertec Pavement Evaluation Report (2013)

Pavement Evaluation Report

Pavement Deflection Testing and Analysis
TH 11 and TH 72
Lake of the Woods, Beltrami and Koochiching Counties, Minnesota

Prepared for

Minnesota Department of Transportation
Office of Materials

Professional Certification

I hereby certify that this plan, specification or report
was prepared by me or under my direct supervision
and that I am a duly Licensed Professional Engineer
under the laws of the State of Minnesota.

Matthew S. Oman, PE
Senior Engineer / Associate Principal
License Number: 43893
June 28, 2013

Project BL-13-01691

Braun Intertec Corporation

B-1

June 28, 2013   Project BL-13-01691

John Siekmeier, PE
MnDOT Office of Materials
1400 Gervais Avenue
Maplewood, MN 55109

Re: FWD Testing for Geosynthetic Reinforced Pavements
      TH 11 and TH 72
      Lake of the Woods/Koochiching/Beltrami Counties, Minnesota

Dear Mr. Siekmeier:
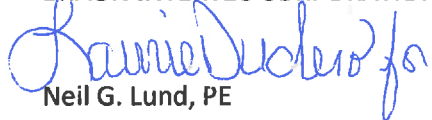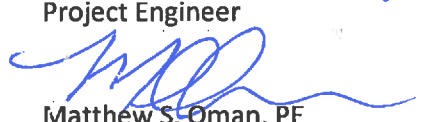
As authorized, we have completed our Falling Weight Deflectometer (FWD) testing and analyses for two
Trunk Highways (TH) in Lake of the Woods, Koochiching, and Beltrami Counties. The purpose of our
testing was to provide deflection measurements for pavement sections that utilize geosynthetics.

FWD testing was accomplished within the appropriate time frame, the first week following complete
thaw through the sixth week following complete thaw of the highway foundation. We completed this
work under the terms of Contract 03375 executed by the State of Minnesota on April 8, 2013.

We performed FWD tests on each test segment in a single direction of travel at an approximate rate of
eight tests per mile. Additionally, tests were conducted approximately every fifty feet for a length of
approximately 1,320 feet within each test section. A summary of this latter data is reported in Table 2 of
the report showing average effective subgrade R-value (average and standard deviation) and Effective
Granular Equivalent (GE) of the pavement section (average and standard deviation).

Please refer to the attached report for detailed for additional information and discussion. Thank you for
the opportunity to be of service on this project. If we can provide additional assistance, please call Neil
Lund at 952.995.2284 or Matt Oman at 651.487.7009.

Sincerely,

BRAUN INTERTEC CORPORATION

Neil G. Lund, PE
Project Engineer

Matthew S. Oman, PE
Senior Engineer / Associate Principal

Attachment:
Pavement Evaluation Report

B-2

AA/EOE   *Providing engineering and environmental solutions since 1957*

Table of Contents

Description   **Page**

Appendix

A. Introduction

A.1. Project Description

State highway projects have been constructed using geosynthetics with the assumption that the addition of the geosynthetics provides benefits that lead to more sustainable pavements. In order to provide further justification for similar projects in the future, quantitative measurements are needed to verify certain properties of the constructed pavement sections. This research promises a large return on investment due to the Minnesota Department of Transportation's (MnDOT) proactive approach of implementation of innovative materials and methods.

Braun Intertec was contracted by MnDOT to perform Falling Weight Deflectometer (FWD) testing on geosynthetic test sections on two Trunk Highway (TH) routes, TH 11 and TH 72 in Lake of the Woods, Koochiching, and Beltrami Counties.

A.2. Purpose

The purpose of this FWD testing was to provide deflection data to MnDOT in order to describe various parameters of pavements that utilize geosynthetics during spring thaw. This test data will be used by MnDOT to evaluate the usefulness of geosynthetics in additional TH construction projects.

A.3. Scope

The Contractor will perform Falling Weight Deflectometer (FWD) testing on highways identified by MnDOT. This testing will be completed during the spring season of 2013 between the first week following complete thaw to the sixth week following complete thaw of the highway foundation. Tasks performed in accordance with our authorized scope of services included:

- Develop and submit testing plan for approval by State.

- Collecting FWD data on the identified test segments and submitting the results electronically.

- Complete Final Report including:
  - Detailed description of the field work;
  - Falling weight deflectometer test results and comparison of measurements;
  - Discussion of factors influencing results;
  - Discussion of sources of error, accuracy, precision, and any test bias.

A.4.   Support Provided by MnDOT

Planned and/or as-built pavement thicknesses, pavement cross-sections, including types of the geosynthetics, and traffic data were provided by MnDOT. The MnDOT District 2 Offices provided traffic control during FWD testing.

Temperature data was retrieved from www.wunderground.com.

B.   Test Plan and Data Collection

B.1.   Test Sections

The segments on TH 11 and TH 72 were provided by MnDOT. A total of 18 different pavement sections of varying length and year of construction were identified by MnDOT. To simply record keeping and presentation of the data, we have named the sections "A" thru "R". Test section details are attached to this report and were provided by MnDOT District 2 staff. Table 1 presents a summary of the test sections Figure 1 shows the general location of all test sections and routes.

Table 1. Test Section Summary.

Test_Section	TH	Constructed	Project Number	RP_from	RP_to	Bituminous	Base	Subbase	Geosynthetic
A				148.25	166.72	6"	12" FDR	?	Geogrid @ 6" in FDR
B		2010	SP 3604-69	151.24	162.16	6"	12" CL 5	12" SGB	Type V fabric below SGB
C	11			156.72	164.70	6"	12" FDR	?	Geogrid @ 6" in FDR
D				160.38	161.10	7"	12" FDR	?	Geogrid @ 6" in FDR
E		1997	SP 3901-34	122.98	123.41	5.5"	6" CL 6	bit & agg base	Geogrid @ 4" in CL 6
F		2011	SP 0413-33	36.61	45.00	5"	10" FDR	?	Geogrid @ 6" in FDR
G				42.45	42.70	6"	6" CL 5	8" SGB	Geogrid below SGB
H		1997	?	42.70	42.95	6"	6" CL 5	8" SGB	Type VI fabric below SGB
I				42.95	43.20	6"	6" CL 5	8" SGB	Geocell filled with SGB
J				43.20	43.45	6"	18" CL 6	?	Type V fabric below CL 5
K				45.00	45.50	5"	10" FDR	?	Geogrid @ 8" in FDR
L	72			45.50	46.00	5"	4" SFDR/6" FDR	?	Geogrid @ 8" in FDR
M		2011	SP 0413-33	46.00	46.50	4"	10" FDR	?	Geogrid @ 8" in FDR
N				46.50	47.00	4"	4" SFDR/6" FDR	?	Geogrid @ 8" in FDR
O				47.00	48.00	4"	4" SFDR/6" FDR	?	--
P				48.00	62.00	3"	mill & overlay		--
Q		2005	SP 0413-30	48.62	61.35	4.5"	9" FDR	?	Geogrid @ 6" in FDR
R				49.35	60.48	4.5"	9" FDR	?	--

FDR = Full-depth Reclamation   SFDR = Stabilized Full-depth Reclamation

CL 5/CL 6 = MnDOT Class 5/6 Aggregate Base   SGB = MnDOT Select Granular Borrow

Figure 1. Overall test section map (MnDOT District 2).

B.2. Test Plan

The intent of this project was to collect FWD data during the spring thaw. Testing was initially set up for April 23-25, 2013, but frost data from a MnDOT site on TH 11 in Koochiching County indicated significant frost in the ground. The proposed dates were pushed back based on 10-day forecasts with highs in the low 40s and nightly freezing temperatures. We followed the frost monitoring data, and based on forecasts, scheduled testing for May 7-8, 2013. The frost depth graph shown in Figure 2 indicates that all frost was completely out of the pavement system on May 7, 2013.

The shortest continuous segment is 0.25 mi in length (with the exception of Test Section C on TH 11 – 0.10 mi + 0.18 mi). As a result, we proposed to use **0.25 mi** as the **baseline segment** in each test section. **Within this baseline segment in each test section ("A" through "R"), we collected 25 FWD drops at approximately 50 foot intervals.** The idea was to produce statistically valid sample sets across all sections. **Outside the baseline segments, FWD testing was conducted at approximately 1/8th mile intervals**. This will allow for advanced spatial analysis into variability.
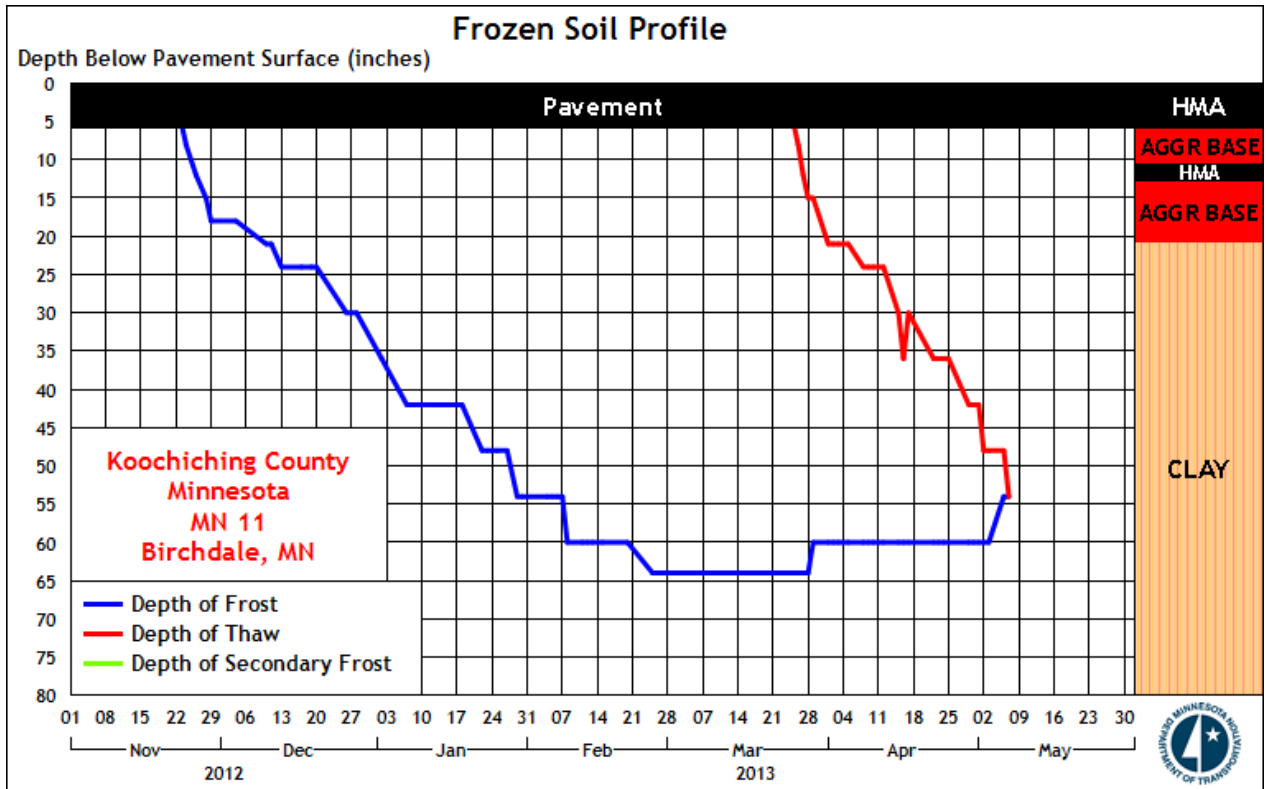
Figure 2. Frost depth on TH 11 in Birchdale in Koochiching County. Data from MnDOT
(www.mrr.dot.state.mn.us/research/seasonal_load_limits/thawindex/frost_thaw_graphs.asp).

C.   Results

C.1.   FWD Data Tabulation

Deflection data at each of the test points was submitted electronically in raw format and analyzed by
Braun Intertec. The analyzed data tabulation sheets contain a header section and tabulated data,
including some raw data, gathered data related to temperature, and analysis results.

MnDOT Contract No. 03375
Project BL-13-01691
June 26, 2013
Page 5

C.2.   FWD Results

All of the test sections are rated as 10-ton routes, according to the TONN procedures used for analysis.

The deflection data analysis results are statistical estimates representing values calculated for the test locations along each roadway. Parameters chosen for test section comparison are effective subgrade R-Value, effective Granular Equivalent (GE), ISM (Impulse Stiffness Modulus --normalized test load divided by the center deflection) and AREA, as defined in Equation 1.

$$AREA = 6 \left[\frac{D_0 + 2D_1 + 2D_2 + D_3}{D_0} \right] \qquad\qquad \text{Equation 1}$$

Where: d_i = Deflection of the ith FWD sensor (0, 12, 24, and 36 inches) [mils]

All lettered test sections have one subsection in which FWD tests were performed at intervals of approximately 50 feet, with the balance of the section tested approximately every $1/8^{th}$ mile. These subsections were utilized for the section-to-section comparisons presented in the tables below. The Excel data sheets were truncated to include only twenty-two drop locations, eliminating the FWD data from the beginning and end of the baseline test segment. This was done to ensure that all test points fell within the actual portion constructed as identified in the cross-sections.

Table 2 provides an overall summary of each test section and presents the average and standard deviation for the effective subgrade R-value and effective pavement system GE.

B-8

Table 1: Average FWD-derived Pavement Characteristics

Test Section	Pavement Section	Ave R-value	StdDev of Ave Eff R-value	Ave Eff GE (in)	StdDev of Ave Eff GE (in)
A	6" Bit, 12" Reclaim, Grid @ 6"	30.7	2.8	34.3	0.8
B	6" Bit, 12" CL 5, 12" SGB, fabric @ 24"	29.2	4.5	32.3	0.9
C	6" Bit, 12" Reclaim, Grid @ 6"	29.0	5.5	34.4	1.1
D	7" Bit, 12" Reclaim, Grid @ 6"	19.0	1.1	39.6	1.2
E	5.5" Bit, 6' CL 6 base, Grid @ 4" in base, existing Bituminous	59.6	10.6	32.2	2.3
F	5" Bit, 10" Reclaim, Grid @ 6"	50.3	3.9	29.7	1.3
G	6" Bit, 6" CL 5 base, 8" SGB, Grid @14"	39.6	2.7	40.2	1.0
H	6" Bit, 6" CL 5 base, 8" SGB,fabric @14"	34.7	3.5	40.2	1.0
I	6" Bit, 6" CL 5, 8" Geocell w/ SGB below base	39.2	4.0	37.9	1.1
J	6" Bit, 18" CL 5, fabric under base	35.4	4.5	37.5	1.5
K	5" Bit, 10" Reclaim, Grid @ 8"	31.4	3.9	31.0	1.1
L	5" Bit, 10" Reclaim, Grid @ 8" (4" stab, 6" non-stab)	36.2	2.9	38.6	0.7
M	4" Bit, 10" Reclaim, Grid @ 8"	26.5	3.4	34.8	1.1
N	4" Bit, 10" Reclaim, Grid @ 8" (4" stab, 6" non-stab)	26.1	3.3	36.5	1.0
O	4" Bit, 10" Reclaim, (4" stab, 6" non-stab)	32.1	2.6	37.1	0.8
P	3" Bit, CL 5 base, no geo	27.6	2.6	34.6	1.7
Q	4.5" Bit, 9" Reclaim, Grid @ 6"	34.0	3.3	36.9	0.9
R	4.5" Bit, 9" Reclaim	46.9	8.8	31.6	2.0

Comparisons shown in Table 3 are those which contain only one variable (geosynthetic type/depth, pavement surface layer thickness, etc.).

Table 2: Test Section Comparisons with Isolated Design Variable

Test Section	Pavement Section	Ave R-value	StdDev of Ave Eff R-value	Ave Eff GE (in)	StdDev of Ave Eff GE (in)
Q	4.5" Bit, 9" Reclaim, Grid @ 6"	34.0	3.3	36.9	0.9
R	4.5" Bit, 9" Reclaim	46.9	8.8	31.6	2.0
G	6" Bit, 6" CL 5 base, 8" SGB, Grid @14"	39.6	2.7	40.2	1.0
I	6" Bit, 6" CL 5, 8" Geocell w/ SGB below base	39.2	4.0	37.9	1.1
F	5" Bit, 10" Reclaim, Grid @ 6"	50.3	3.9	29.7	1.3
K	5" Bit, 10" Reclaim, Grid @ 8"	31.4	3.9	31.0	1.1
G	6" Bit, 6" CL 5 base, 8" SGB, Grid @14"	39.6	2.7	40.2	1.0
H	6" Bit, 6" CL 5 base, 8" SGB,fabric @14"	34.7	3.5	40.2	1.0
H	6" Bit, 6" CL 5 base, 8" SGB,fabric @14"	34.7	3.5	40.2	1.0
I	6" Bit, 6" CL 5, 8" Geocell w/ SGB below base	39.2	4.0	37.9	1.1
H	6" Bit, 6" CL 5 base, 8" SGB,fabric @14"	34.7	3.5	40.2	1.0
J	6" Bit, 18" CL 5, fabric under base	35.4	4.5	37.5	1.5
C	6" Bit, 12" Reclaim, Grid @ 6"	29.0	5.5	34.4	1.1
D	7" Bit, 12" Reclaim, Grid @ 6"	19.0	1.1	39.6	1.2
L	5" Bit, 10" Reclaim, Grid @ 8" (4" stab, 6" non-stab)	36.2	2.9	38.6	0.7
N	4" Bit, 10" Reclaim, Grid @ 8" (4" stab, 6" non-stab)	26.1	3.3	36.5	1.0
K	5" Bit, 10" Reclaim, Grid @ 8"	31.4	3.9	31.0	1.1
M	4" Bit, 10" Reclaim, Grid @ 8"	26.5	3.4	34.8	1.1
A	6" Bit, 12" Reclaim, Grid @ 6"	30.7	2.8	34.3	0.8
C	6" Bit, 12" Reclaim, Grid @ 6"	29.0	5.5	34.4	1.1
K	5" Bit, 10" Reclaim, Grid @ 8"	31.4	3.9	31.0	1.1
L	5" Bit, 10" Reclaim, Grid @ 8" (4" stab, 6" non-stab)	36.2	2.9	38.6	0.7
M	4" Bit, 10" Reclaim, Grid @ 8"	26.5	3.4	34.8	1.1
N	4" Bit, 10" Reclaim, Grid @ 8" (4" stab, 6" non-stab)	26.1	3.3	36.5	1.0

C.3.   Discussion and Conclusions

From a quick review of the results shown in Table 3, the following observations can be made:

- A layer of geogrid provides an average increase in GE of 5.3" (Q vs R).
- A layer of geogrid provides an additional 2.2" of GE compared to Geocell (G vs I).
- Geogrid at a depth of 8-inches in a 10-inch reclaim layer provides an increase of 1.3" of GE compred to a depth of 6-inches (F vs K).
- There is no apparent difference in effective GE between geogrid or type V geotextile fabric at a total depth of 20-inches (G vs H).
- Type V geotextile fabric provides an approximate increase in GE of 2.3" compared to geocell (H vs I).
- Type V geotextile fabric at a depth of 14-inches compared to 24-inches, provides an apparent increase in GE of 2.7" (H vs J).
- 1-inch of bituminous surfacing provides an increase in GE ranging from 2.0" to 5.3" (L vs N and C vs D).
- 4-inches of stabilized full-depth reclamation provides an increase in GE ranging from 1.7" to 7.6" (M vs N and K vs L).

We have the following conclusions and recommendations:

- It appears that geogrid properly placed within the pavement section provides a structural benefit. We suggest that MnDOT perform advanced modeling using layered elastic models or disrete element to further investigate the data collected under this project.
- After MnDOT evaluates the data and/or performs modeling, MnDOT could consider expanding the use of Tech Memo 10-SA-03 from State Aid routes only to use on Trunk Highways.
- The approximate FWD load magnitude was on the order of 9,000 lbs. It is conceptually possible that the deflections were not great enough to fully mobilize the benefits of the various geosynthetic components. Any future FWD testing to evaluate geotextiles within pavement structures should consider several load levels with a 15,000 lbs maximum.

D. Factors Influencing FWD Test Results

D.1. Pavement Section Details

Several pavement material types and dimensions were part of the tested sections. The analysis contains three variables -- surface layer thickness, base layer thickness, and presence/depth of geosynthetic material – that may have an effect on the deflections measured by FWD testing.

D.1.a. Tensar™ Biaxial Geogrid

Tensar ™ biaxial geogrid was placed in several pavement structures at varying depths within the base layer. Intuitively multi-axial geogrid provides benefits pavement service life including a more sustainable pavement and possibly reduced maintenance costs. MnDOT Technical Memorandum 10-SA-03 published on December 21, 2010, outlines the use of multiaxial geogrids and assigns a granular equivalent (GE) equal to 2.0 to a layer of geogrid.

D.1.b. Type V/VI Geotextile Fabric

Geotextiles are polymer fabrics that may also provide some reinforcement, but are used primarily to:

- Facilitate filtration and water drainage through road foundation soils without the loss of soil particles.
- Provide separation between dissimilar base materials, improving their integrity and function.
- Provide a stable construction platform over soft or wet soils, facilitating the movement of equipment and the process of soil compaction.[1]

D.1.c. Geocell

Cellular Confinement Systems (CCS, also known as geocells) are widely used in construction for erosion control, soil stabilization on flat ground and steep slopes, channel protection, and structural reinforcement for load support and earth retention. Typical cellular confinement systems are made with ultrasonically-welded high-density polyethylene (HDPE) expanded on-site to form a honeycomb-like structure which may be filled with sand, soil, rock or concrete.[2]

Test section I on TH 72 contains an eight inch thick geocell filled with select granular borrow.

---

[1] http://www.dot.state.mn.us/research/TS/2011/201120TS.pdf

[2] State of California Department of Transportation, Division of Environmental Analysis, Stormwater Program. Sacramento, CA."Cellular Confinement System Research." 2006.

D.2. Temperature

Daily variations in air temperature can significantly affect the stiffness of the bituminous layer. The previous day's average air temperature is also used during some of the analysis procedures.

E.   Sources of Error, Accuracy, Precision and Test Bias

E.1.   Test Sections

Test error can be caused by many factors and extreme care has been taken to minimize these effects. The following are possible sources of error:

- We did not review and field construction note or construction plans for any of the projects including in this testing. We used the values as provided by MnDOT District 2 for the various sections.

- Pavement structure analysis assumes constant layer thickness for the bituminous and aggregate base. Although the average values may very well be equal to the design values (taken from plans, we presume), variation is anticipated. There is likely additional variation at the transitions to other design sections.

- Test sections termini provided by MnDOT District 2 were presented with an accuracy of 0.01 mile, or just over 50 feet. We used GIS data to layout the test sections based on the beginning and ending point definitions. We used these locations to produce GPS coordinates for locating the test sections in the field. That means that some the beginning locations could be off by up to 50 feet based on the accuracy of the test section termini. As a result, it is possible that a test result labeled section "A" might actually fall into the area that was actually constructed as "B". To minimize this effect, the comparisons shown in Table 2 and 3 were made using deflection data from twenty-two FWD drop locations, or trimmed at the beginning and end points.

E.2.   Data Collection[3]

E.2.a. GPS

FWD trailer placement relative to the section was checked using GPS with MnCORS corrections. Although accuracy of less than one centimeter is possible, GPS inputs can contribute to error during certain adverse conditions

E.2.b. FWD Seating

When the trailer is positioned to collect data, many factors can affect the accuracy of deflection data. Of main concern is that the sensors and load plate are not firmly seated on the pavement surface. This error source is minimized by dropping the load at least one time prior to actual data collection for proper plate and sensor seating; Braun Intertec follows testing procedures to minimize this potential source of error.

E.2.c. Random Error

Due to the unpredictable nature of random errors such as electrical signals or weather conditions, we conduct four test drops at each location. These replicates are averaged which can reduce this random error. Although it is not possible to remove all error, AMRL cites a reduction in the range of 0.04 to 0.08 [mils].

E.2.d. Calibration

FWD System calibration is performed on a yearly basis at the AMRL-accredited FWD Calibration Center at MnDOT in Maplewood, Minnesota. Calibration records are available upon request.

F.   Procedures

F.1.   Falling Weight Deflectometer

F.1.a. Field Testing

A Dynatest[TM] Model 8002E FWD was used for deflection testing. This equipment is a trailer-mounted device that measures pavement deflections induced by an applied impulse load. Four impulse loads were applied at each test point in a single direction of travel at an approximate interval of eight tests per mile and approximately every 50 feet in the test subsections.

---

[3] http://amrl.net/AmrlSitefinity/default/aboutus/newsletter/Newsletter_Spring2013/8.aspx

Field testing was conducted on May 7 and May 8, 2013. Data collected by the FWD during testing include the measured surface deflections, applied impulse load levels, pavement surface temperature, and ambient air temperature.

The equipment operator observes and records features such as bridges and intersections along the roadway as well as distresses on the pavement surfaces. These observation notes are recorded in the comment column of the data tabulation sheets in the Appendix.

F.1.b. Deflection Data Analysis

F.1.b.1. Input Data
The following data are required inputs into the analysis program used to generate the structural information from the deflection data:

- Traffic loadings (MnDOT)
- Pavement layer thicknesses (MnDOT)
- Base and subgrade soil type (MnDOT)
- Pavement temperatures (Braun Intertec)
- Previous day temperature (Weather Underground website)
- Pavement deflection data (Braun Intertec)

F.1.b.2. Adjustment Factors
Flexible pavement systems consisting of bituminous layers, aggregate bases, and subgrade soils are normally frozen during winter and very weak during early spring thaw. Deflection testing is normally not recommended during either extreme season due to the presence of subsurface frost. Measured deflections during summer and fall seasons are adjusted to reflect a spring condition when the pavement system is in its weakest state. Seasonal correction factors recommended by MnDOT are used for this purpose. A seasonal correction factor of 1.0 was used for all data. This is a result of the data collection taking place after complete thaw of the pavement foundation.

Surface deflection is inversely proportional to the stiffness of flexible pavements. Since stiffness in flexible pavements is temperature dependent, measured deflections are adjusted to the MnDOT standard of 80 degrees Fahrenheit for deflection data analysis.

The FWD equipment is equipped with an infrared temperature sensor for measuring pavement surface temperature. Based on ASTM D7228 from the Federal Highway Administration's Long Term Pavement Performance Seasonal Monitoring Program (FHWA-LTPP), the mid-depth bituminous temperature for test sections is estimated from the surface temperature and the previous day average air temperature, as obtained from the Weather Underground website located at *http://www.wunderground.com*. The resulting factor is used to convert the estimated mid-depth temperature to the standard 80 degrees Fahrenheit mid-depth temperature.

The Temperature Adjustment Factor (TAF) and Seasonal Correction Factor (SCF) are then used to adjust the measured deflection to an equivalent spring deflection at the reference temperature of 80 degrees Fahrenheit.

F.1.b.3. Analyses

The Braun Intertec Non-Destructive Testing (NDT) program is used for analysis of the deflection data to estimate various factors pertaining to pavement structure. NDT incorporates flexible pavement thickness design relationships from MnDOT, along with those from the 1993 *Guide for Design of Pavement Structures*, published by AASHTO. The following briefly defines the parameters presented in this report:

TONN Spring Load Capacity and 10-ton Overlay - The MnDOT TONN method (revised from MnDOT Investigation 603) is used for spring load capacity estimations. The TONN method uses pavement section information (bituminous thickness), FWD center deflections (normalized to 9 kips), and seasonal and temperature adjustment factors to provide an estimate of load capacity for a given pavement segment. The required 10 ton overlay is computed iteratively at half-inch intervals assuming an equal contribution to roadway load capacity from each incremental addition.

Effective R-value - Effective R-value provides a measure of the stiffness of the pavement subgrade soil. R-value calculations are computed using the Hogg Model, which represents the subgrade as a soil mass of finite depth over a stiff layer. Hogg Model resilient modulus values are corrected for seasonal effects and for congruence to back calculated resilient modulus values. Finally, the results are converted to R-value by the method described in MnDOT Investigation 201.

Because Hogg Model-calculated R-values are relatively conservative compared to methods where an infinite half-space is considered, and seasonal adjustments are also used, we make no further reduction of the results for design or evaluation purposes.

Effective Granular Equivalent (GE) - Effective GE provides values for the design of pavement structures in inches of MnDOT Class 5 aggregate base equivalent and is determined using relationships from the MnDOT Investigation 195 interim report.

The Braun Intertec Non-Destructive Testing (NDT) program is used for analysis of the deflection data to estimate various factors pertaining to pavement structure. NDT incorporates flexible pavement thickness design relationships from MnDOT, along with those from the 1993 *Guide for Design of Pavement Structures*, published by AASHTO. The following briefly defines the parameters presented in this report:

G.   Qualifications

G.1.   Use of Report

This report is for the exclusive use of the parties to which it has been addressed. Without written approval, we assume no responsibility to other parties regarding this report. Our evaluation, analyses and recommendations may not be appropriate for other parties or projects.

G.2.   Standard of Care

In performing its services, Braun Intertec used that degree of care and skill ordinarily exercised under similar circumstances by reputable members of its profession currently practicing in the same locality. No warranty, express or implied, is made.

Appendix

Project Limits ---> 148.22 - 166.69

TEST SECTION A
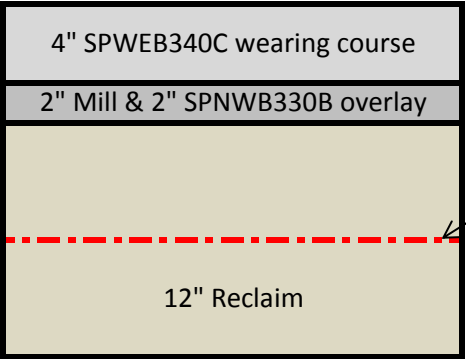
4" SPWEB340C wearing course
2" Mill & 2" SPNWB330B overlay
12" Reclaim

Tensar Bixial Geogrid @ 6" deep in reclaim

Station		Reference Point		
From	To	From	To	Length
990+75	1149+00	148.25	151.24	2.99
1208+00	1419+00	152.36	156.37	4.01
1442+00	1631+00	156.82	160.38	3.56
1669+20	1720+13	161.10	162.06	0.96
1725+60	1849+00	162.16	164.52	2.36
1859+00	1946+00	164.70	166.72	2.02
				15.9

TEST SECTION B

4" SPWEB340C wearing course
2" SPNWB330B non wearing course
12" Class VI aggregate base
12" select granular borrow
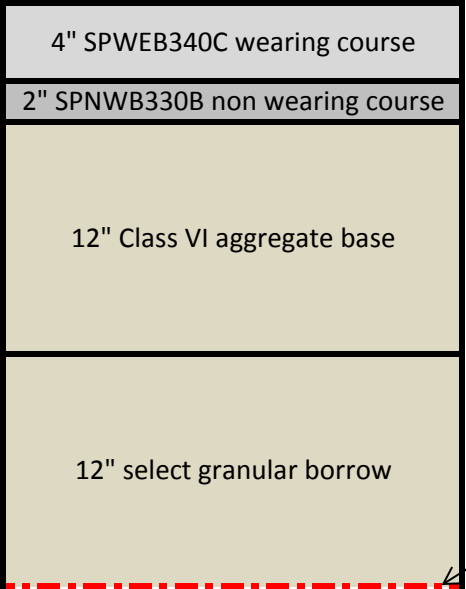
Type 5 Geotextile Fabric

Station		Reference Point		
From	To	From	To	Length
1149+00	1208+00	151.24	152.36	1.12
1419+00	1429+00	156.37	156.57	0.20
1434+00	1437+00	156.66	156.72	0.06
1720+13	1725+60	162.06	162.16	0.10
				1.48

TEST SECTION C
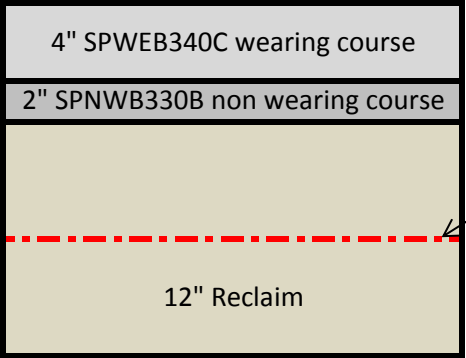
4" SPWEB340C wearing course
2" SPNWB330B non wearing course
12" Reclaim

Tensar Bixial Geogrid @ 6" deep in reclaim

Station		Reference Point		
From	To	From	To	Length
1437+00	1442+00	156.72	156.82	0.1
1849+00	1859+00	164.52	164.70	0.18
				0.28

TEST SECTION D

4" SPWEB340C wearing course
3" Mill & 3" SPNWB330B overlay
12" Reclaim

Tensar Bixial Geogrid @ 6" deep in reclaim
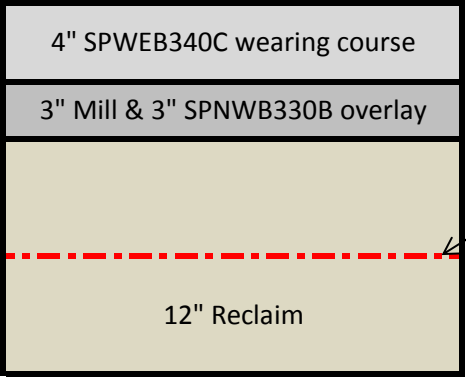
Station		Reference Point		
From	To	From	To	Length
1631+00	1669+20	160.38	161.10	0.72

TEST SECTION E

| 1.5" 41WEA50055 wearing course |
| 2" 41LVB50055 leveling course mix |
| 2" 3188850000 base course mix |
| 6" Class VI aggregate Base |

Tensar Bixial Geogrid @ 4" deep in aggregate base

Inplace Bituminous   Inplace
            Aggregate Base

Station		Reference Point		
From	To	From	To	Length
197+927	198+628	122.98	123.41	0.43

Project Limits ---> 36.61 - 48.00

TEST SECTION F
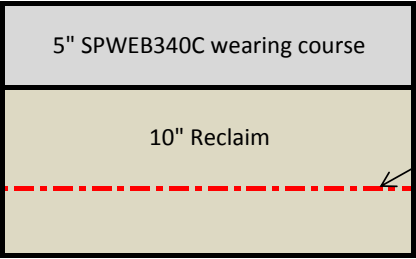
5" SPWEB340C wearing course
10" Reclaim

Tensar Bixial Geogrid @ 6" deep in reclaim

	Station		Reference Point		
	From	To	From	To	Length
	45+26	350+20	36.61	42.45	5.84
	403+00	484+10	43.45	45.00	1.55
					7.39

TEST SECTION G and TEST SECTION H

2" MVWE25035A wearing course
2" MVNW25030 non wearing course
2" 3188850000 base course mix
6" Class V aggregate base
8" select granular borrow
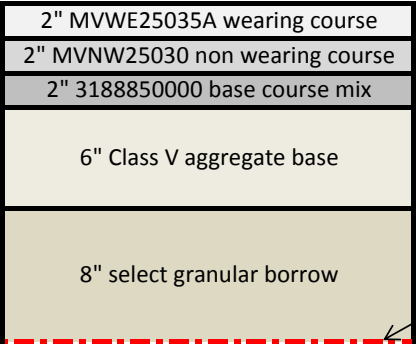
1997 Test Section

see table to right
(both geosynthetics
on bottom of select
granular borrow)

Geosynthetic Type		Station		Reference Point		
		From	To	From	To	Length
G	Biaxial Geogrid	68+275.020	68+677.356	42.45	42.70	0.25
H	Type VI Geotextile Fabric	68+677.356	69+079.692	42.70	42.95	0.25
						0.5

TEST SECTION I

2" MVWE25035A wearing course
2" MVNW25030 non wearing course
2" 3188850000 base course mix
6" Class V aggregate base
8" Geocell filled with select granular borrow
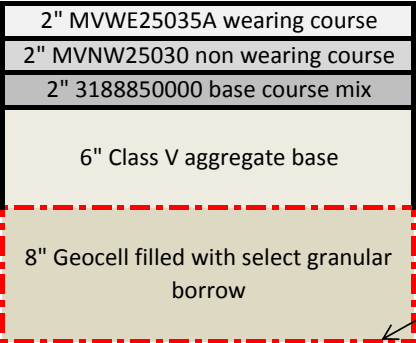
1997 Test Section

Geocell

	Station		Reference Point		
	From	To	From	To	Length
	69+079.692	69+482.027	42.95	43.20	0.25
					0.25

TEST SECTION J

2" MVWE25035A wearing course
2" MVNW25030 non wearing course
2" 3188850000 base course mix
18" Class V aggregate base

1997 Test Section

Type V Geotextile Fabric

	Station		Reference Point		
	From	To	From	To	Length
	69+482.027	69+884.363	43.20	43.45	0.25
					0.25

TEST SECTION K

5" SPWEB340C wearing course
10" Reclaim

Tensar Bixial Geogrid @ 8" deep in reclaim
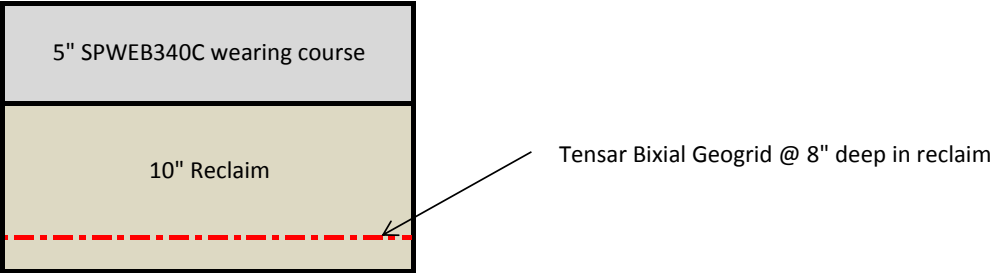
	Station		Reference Point		
From	**To**	**From**	**To**	**Length**
484+10	510+40	45.00	45.50	0.5
				0.5

TEST SECTION L

5" SPWEB340C wearing course
4" stabalized reclaim
6" Non-Stabalized Reclaim

Tensar Bixial Geogrid @ 8" deep in reclaim
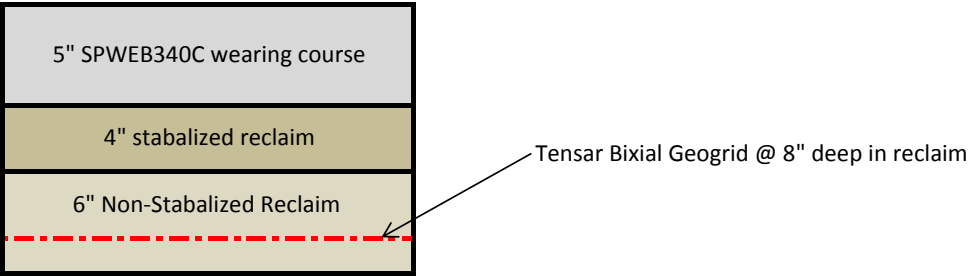
	Station		Reference Point		
From	**To**	**From**	**To**	**Length**
510+40	536+70	45.50	46.00	0.5
				0.5

TEST SECTION M

4" SPWEB340C wearing course
10" Reclaim

Tensar Bixial Geogrid @ 8" deep in reclaim
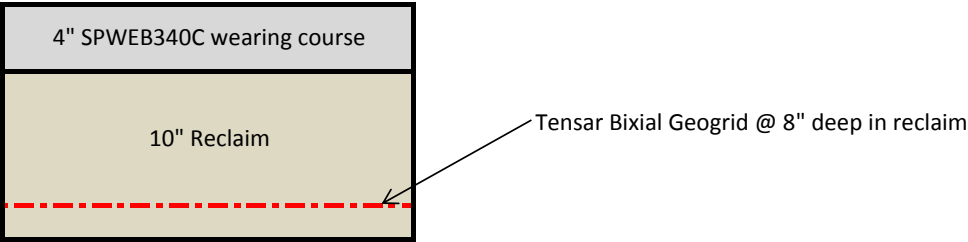
	Station		Reference Point		
From	**To**	**From**	**To**	**Length**
536+70	563+67.5	46.00	46.50	0.5
				0.5

TEST SECTION N

4" SPWEB340C wearing course
4" stabalized reclaim
6" Non-Stabalized Reclaim

Tensar Bixial Geogrid @ 8" deep in reclaim
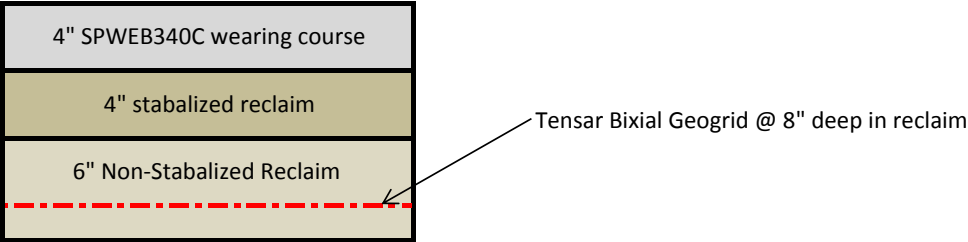
	Station		Reference Point		
From	**To**	**From**	**To**	**Length**
563+67.5	590+65	46.50	47.00	0.5
				0.5

TEST SECTION O

4" SPWEB340C wearing course
4" stabalized reclaim
6" Non-Stabalized Reclaim
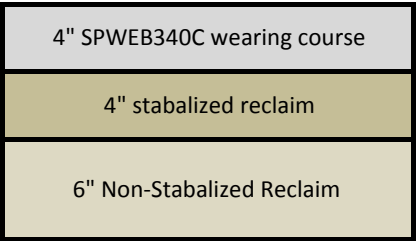
	Station		Reference Point		
From	**To**	**From**	**To**	**Length**
590+65	643+41	47.00	48.00	1.0
				1.0

TEST SECTION P

1.5" SPWEB340C wearing course
1.5" mill/1.5" SPWEB340C overlay
Inplace Bituminous

Station		Reference Point		
From	To	From	To	Length
643+41	676+00	48.00	48.62	0.62
848+00	1161+50	51.86	57.80	5.94
1349+50	1383+75	61.35	62.00	0.65
				7.21

TEST SECTION Q

4.5" SPWEB340C wearing course
9" Reclaim

Tensar Bixial Geogrid @ 6" deep in reclaim

Station		Reference Point		
From	To	From	To	Length
676+25	714+75	48.62	49.35	0.73
729+50	847+75	49.63	51.86	2.23
1161+50	1165+75	57.80	57.88	0.08
1179+50	1269+50	58.15	59.84	1.69
1282+00	1289+50	60.07	60.21	0.14
1303+75	1349+50	60.48	61.35	0.87
				5.74

TEST SECTION R

4.5" SPWEB340C wearing course
9" Reclaim

Station		Reference Point		
From	To	From	To	Length
676+00	676+25	48.62	48.62	0
714+75	729+50	49.35	49.63	0.28
1165+75	1179+50	57.88	58.15	0.27
1269+50	1282+00	59.84	60.07	0.23
1289+50	1303+75	60.21	60.48	0.27
				1.05

MnDOT District 2 FWD Testing Key

*Tested based on linear distance from start to end according to the attached chart. Cross-referenced with the apparent lat/long at RP locations of section breaks (per MnDOT).
*QC on 5/10/2013: Checked apparent lengths and number of tests, deleted repeat stations, replaced output files for broken test sessions

TH	Constructed	RP_from	RP_to	Length	Test_Section	Test Section Length	Total FWD Tests	FWD FILE NAME	LOCATION OF 25x50' TEST SECTION
	2010	148.25	151.24	2.99				A1	x
	2010	152.36	156.37	4.01				A2	
	2010	156.82	160.38	3.56	A	15.90	150	A3	
	2010	161.10	162.06	0.96				A4	
	2010	162.16	164.52	2.36				A5	
	2010	164.70	166.72	2.02				A6	
11	2010	151.24	152.36	1.12				B1	x
	2010	156.37	156.57	0.20	B	1.48	35	B2	
	2010	156.66	156.72	0.06				B3	
	2010	162.06	162.16	0.10				B4	
	2010	156.72	156.82	0.10	C	0.28	25	C1	
	2010	164.52	164.70	0.18				C2	
	2010	160.38	161.10	0.72	D	0.72	29	D	
	1997	122.98	123.41	0.43	E	0.43	26	E	x
	2011	36.61	42.45	5.84	F	7.39	82	F1	
	2011	43.45	45.00	1.55				F2	
	2011	42.45	42.70	0.25	G	0.25	25	G	x
	2011	42.70	42.95	0.25	H	0.25	25	H	x
	2011	42.95	43.20	0.25	I	0.25	25	I	x
	2011	43.20	43.45	0.25	J	0.25	25	J	x
	2011	45.00	45.50	0.50	K	0.50	27	K	x
	2011	45.50	46.00	0.50	L	0.50	27	L	x
	2011	46.00	46.50	0.50	M	0.50	27	M	x
	2011	46.50	47.00	0.50	N	0.50	27	N	x
	2011	47.00	48.00	1.00	O	1.00	31	O	x
72	2005	48.00	48.62	0.62				P1	
	2005	51.86	57.80	5.94	P	7.21	81	P2	x
	2005	61.35	62.00	0.65				P3	
	2005	48.62	49.35	0.73				Q1	
	2005	49.63	51.86	2.23				Q2	
	2005	57.80	57.88	0.08	Q	5.74	69	Q3	x
	2005	58.15	59.84	1.69				Q4	
	2005	60.07	60.21	0.14				Q5	
	2005	60.48	61.35	0.87				Q6	
	2005	49.35	49.63	0.28				R1	
	2005	57.88	58.15	0.27	R	1.05	31	R2	x
	2005	59.84	60.07	0.23				R3	
	2005	60.21	60.48	0.27				R4	
						Approx Total Tests	767		

Segment	SegPntID	Name	Dist From Start	Dist From End	DD_LAT	DD_LONG
TH11East	15	TH11 East, End	18.492	0.000	48.62903835580	-93.86110174530
TH11East	14		16.476	2.016	48.63173214020	-93.90472169720
TH11East	13		16.296	2.196	48.63191210950	-93.90860057920
TH11East	12		13.939	4.553	48.62856122110	-93.95863235050
TH11East	11		13.838	4.654	48.62845658040	-93.96081735150
TH11East	10		12.879	5.613	48.62862361040	-93.98176121240
TH11East	9		12.160	6.332	48.62866533210	-93.99746115900
TH11East	8		8.608	9.884	48.62740099030	-94.07499019160
TH11East	7		8.508	9.983	48.62735209630	-94.07716519960
TH11East	6		8.449	10.043	48.62732274020	-94.07847020210
TH11East	5		8.313	10.179	48.62728722640	-94.08043265150
TH11East	4		8.113	10.379	48.62722533530	-94.08480356820
TH11East	3		4.105	14.387	48.64544115400	-94.16290283120
TH11East	2		2.981	15.511	48.64861786880	-94.18691338810
TH11East	1	TH11 East, Start	0.000	18.492	48.65244744540	-94.25006951900

-93.861102, 48.629038 (18.492) #15 **#15.(0.)**

A (2.02 miles)

-93.904722, 48.631732 (16.476) #14 **#14 (2.016)**
-93.908601, 48.631912 (16.296) #13 **#13 (2.196)**

C (0.18 miles)

A (2.36 miles)

B (0.1 miles)

-93.958632, 48.628561 (13.939) #12 **#12 (4.553)**
-93.960817, 48.628457 (13.838) #11 **#11 (4.654)**

A (0.96 miles)

-93.981761, 48.628624 (12.879) #10 **#10 (5.613)**

D (0.72 miles)

-93.997461, 48.628665 (12.16) #9 **#9 (6.332)**

A (3.56 miles)

C (0.1 miles)
-94.07499, 48.627401 (8.608) #8 **#8 (9.884)**
-94.077103, 48.627352 (8.508) #7 **#7 (9.983)**
-94.080433, 48.627257 (8.313) #5 **#5 (10.179)**
-94.084804, 48.627225 (8.113) #4 **#4 (10.379)**

B (0.06 miles)
B (0.2 miles)

339.4' East of CR 86
&
377.6' West of CR 86

Koochiching County

A (4.01 miles)
-94.162903, 48.645441 (4.105) #3 **#3 (14.387)**

B (1.12 miles)
-94.186913, 48.648618 (2.981) #2 **#2 (15.511)**

A (2.99 miles)

-94.25007, 48.652447 (0) #1 **#1 (18.492)**

Project No.	
Drawing No.	field_TH11 East of Baudette
Scale:	1 inch = 14,186 feet
Drawn By:	RHD
Date Drawn:	04/22/2013
Checked By:	XXX
Last Modified:	5/6/2013, 2:15:54 PM

Proposed FWD Test Segments
TH 11, East of Baudette

FWD Testing Project
Minnesota Department of Transportation
Baudette, MN

BRAUN INTERTEC

11001 Hampshire Avenue So. Minneapolis, MN 55438
PH. (952) 995-2000 FAX (952) 995-2020

D:\ArcGIS One-offs\FWD Analysis2\field_TH11 East of Baudette.mxd

1711.7' South of CR 16 intersection

-94.560746, 48.529074 (25.38) #25 — #25 (0)

P (0.65 miles)

#24 (0.649)

Q (0.87 miles)

-94.560358, 48.507122 (23.863) #23 — #23 (1.517)

R (0.27 miles)

#22 (1.786)

-94.560433, 48.501205 (23.454) #21 — #21 (1.925)

Q (0.14 miles)

-94.560475, 48.497886 (23.225) #20 — #20 (2.155)

R (0.23 miles)

Q (1.69 miles)

-94.559478, 48.473449 (21.535) #19 — #19 (3.844)

R (0.27 miles)

-94.559396, 48.468376 (21.185) #17 — #17 (4.195)

Q (0.08 miles)

Lake of the Woods County

P (5.94 miles)

Red Lake Indian Reservation

-94.559455, 48.382323 (15.24) #16 — #16 (10.139)

72

Koochiching County

Q (2.23 miles)

-94.554113, 48.350907 (13.012) #15 — #15 (12.368)

R (0.28 miles)

-94.554091, 48.34686 (12.732) #14 — #14 (12.647)

Q (0.73 miles)

-94.554025, 48.336309 (12.003) #13 — #13 (13.376)

P (0.62 miles)

-94.553925, 48.327348 (11.384) #12 — #12 (13.995)

O (1 miles)

-94.553854, 48.312882 (10.385) #11 — #11 (14.994)

N (0.5 miles)

-94.553792, 48.30565 (9.885) #10 — #10 (15.494)

M (0.5 miles)

-94.553676, 48.29842 (9.386) #9 — #9 (15.993)

L (0.5 miles)

-94.553561, 48.291191 (8.887) #8 — #8 (16.493)

K (0.5 miles)

-94.553446, 48.28396 (8.387) #7 — #7 (16.992)

Beltrami County

F (1.55 miles)

-94.553449, 48.26155 (6.839) #6 — #6 (18.54)

J (0.25 miles)

-94.553462, 48.257936 (6.589) #5 — #5 (18.79)

I (0.25 miles)

-94.553475, 48.254322 (6.34) #4 — #4 (19.04)

H (0.25 miles)

-94.553488, 48.250708 (6.09) #3 — #3 (19.289)

G (0.25 miles)

-94.553501, 48.247094 (5.84) #2 — #2 (19.539)

F (5.84 miles)

Upper Red Lake

-94.512696, 48.175876 (0) #1 — #1 (25.38)

D:\ArcGIS One-offs\FWD Analysis2\field_TH72 South of Baudette.mxd

Map labels:
- Lake Of The Woods
- UNITED STATES
- Zippel Bay
- State Park
- Rainy River
- Baudette
- Red Lake Indian Reservation
- #1 (0.431)
- #2 (0) #1
- -94.731426, 48.71532 (0) #1
- -94.72445, 48.73453 (0.431) #2
- E (0.43 miles)
- 1825.4' West of CR 6

Proposed FWD Test Segments
TH 11, West of Baudette
FWD Testing Project
Minnesota Department of Transportation
Baudette, MN

BRAUN
INTERTEC

B-30

APPENDIX C

MnPAVE Input Parameters and Results

Table C.1 Raw Data with 40 MPa Base and 4 in. HMA

Modulus						Thickness				Damage Index		Stress (kPa)				Vertical Deflection (µm)			
Base		Eng Soil		Und Soil		Base		Eng Soil		Fatigue	Rutting	Top Base	Mid Base	Bottom Base	Bottom Eng Soil	Top Base	Mid Base	Bottom Base	Bottom Eng Soil
MPa	ksi	MPa	ksi	MPa	ksi	mm	in	mm	in										
40	5.80	20	2.90	5	0.73	203	8	203	8	2.42	5.21	64	37	24	17	3633	3480	3350	3046
40	5.80	30	4.35	8	1.09	203	8	203	8	2.02	2.8	68	43	28	19	2640	2488	2370	2134
40	5.80	40	5.80	10	1.45	203	8	203	8	1.82	1.72	71	46	31	20	2252	2099	1986	1788
40	5.80	20	2.90	5	0.73	254	10	203	8	2.17	4.05	67	36	22	18	3437	3252	3105	2830
40	5.80	30	4.35	8	1.16	254	10	203	8	1.87	2.17	70	41	26	19	2521	2337	2203	1990
40	5.80	40	5.80	10	1.45	254	10	203	8	1.72	1.33	73	44	29	20	2162	1977	1850	1671
40	5.80	20	2.90	5	0.73	305	12	203	8	1.98	3.15	70	35	21	18	3259	3044	2885	2636
40	5.80	30	4.35	8	1.16	305	12	203	8	1.76	1.69	72	39	24	19	2414	2200	2054	1861
40	5.80	40	5.80	10	1.45	305	12	203	8	1.64	1.04	74	42	27	20	2082	1867	1728	1566
40	5.80	20	2.90	5	0.73	203	8	610	24	1.93	4.38	68	43	31	21	2934	2783	2658	2092
40	5.80	30	4.35	8	1.09	203	8	610	24	1.63	2.4	73	49	36	22	2125	1971	1853	1420
40	5.80	40	5.80	10	1.45	203	8	610	24	1.47	1.5	76	53	40	22	1790	1634	1517	1160
40	5.80	20	2.90	5	0.73	254	10	610	24	1.8	3.34	70	41	28	22	2814	2630	2489	1975
40	5.80	30	4.35	8	1.16	254	10	610	24	1.57	1.81	74	46	33	23	2059	1873	1739	1346
40	5.80	40	5.80	10	1.45	254	10	610	24	1.44	1.11	77	50	36	23	1747	1558	1427	1104
40	5.80	20	2.90	5	0.73	305	12	610	24	1.7	2.55	72	40	27	23	2704	2489	2337	1869
40	5.80	30	4.35	8	1.16	305	12	610	24	1.52	1.37	75	44	31	23	1998	1782	1637	1280
40	5.80	40	5.80	10	1.45	305	12	610	24	1.42	0.84	78	47	33	24	1707	1488	1346	1053
40	5.80	20	2.90	5	0.73	203	8	914	36	1.83	4.28	69	44	32	26	2628	2476	2353	1679
40	5.80	30	4.35	8	1.09	203	8	914	36	1.56	2.39	73	50	38	26	1912	1758	1639	1124
40	5.80	40	5.80	10	1.45	203	8	914	36	1.4	1.52	77	55	42	26	1606	1449	1332	908.3
40	5.80	20	2.90	5	0.73	254	10	914	36	1.72	3.26	71	43	30	26	2537	2353	2214	1600
40	5.80	30	4.35	8	1.16	254	10	914	36	1.51	1.8	75	48	35	27	1865	1678	1544	1076
40	5.80	40	5.80	10	1.45	254	10	914	36	1.39	1.13	77	51	38	27	1579	1389	1257	872.5
40	5.80	20	2.90	5	0.73	305	12	914	36	1.64	2.49	73	41	28	27	2453	2239	2087	1528
40	5.80	30	4.35	8	1.16	305	12	914	36	1.47	1.37	76	45	32	28	1821	1604	1458	1032
40	5.80	40	5.80	10	1.45	305	12	914	36	1.37	0.85	77	48	35	28	1553	1333	1189	839.3

Table C.2 Raw Data with 60 MPa Base and 4 in. HMA

Modulus						Thickness				Damage Index		Stress (kPa)				Vertical Deflection (μm)			
Base		Eng Soil		Und Soil		Base		Eng Soil		Fatigue	Rutting	Top Base	Mid Base	Bottom Base	Bottom Eng Soil	Top Base	Mid Base	Bottom Base	Bottom Eng Soil
MPa	ksi	MPa	ksi	MPa	ksi	mm	in	mm	in										
60	8.70	20	2.90	5	0.73	203	8	203	8	1.84	5.15	79	41	23	17	3461	3329	3213	2921
60	8.70	30	4.35	8	1.09	203	8	203	8	1.55	3.03	84	46	28	18	2511	2381	2277	2044
60	8.70	40	5.80	10	1.45	203	8	203	8	1.39	2.01	87	50	31	19	2137	2007	1908	1710
60	8.70	20	2.90	5	0.73	254	10	203	8	1.58	3.81	85	40	21	17	3231	3072	2944	2684
60	8.70	30	4.35	8	1.16	254	10	203	8	1.38	2.24	88	45	25	19	2367	2211	2094	1887
60	8.70	40	5.80	10	1.45	254	10	203	8	1.28	1.49	90	48	28	19	2026	1870	1760	1583
60	8.70	20	2.90	5	0.73	305	12	203	8	1.41	2.83	88	39	20	17	3027	2845	2708	2477
60	8.70	30	4.35	8	1.16	305	12	203	8	1.27	1.67	91	43	24	19	2239	2059	1934	1749
60	8.70	40	5.80	10	1.45	305	12	203	8	1.19	1.11	92	45	26	19	1928	1747	1630	1471
60	8.70	20	2.90	5	0.73	203	8	610	24	1.49	4.39	83	47	30	21	2816	2686	2578	2032
60	8.70	30	4.35	8	1.09	203	8	610	24	1.27	2.6	88	53	35	22	2030	1900	1799	1375
60	8.70	40	5.80	10	1.45	203	8	610	24	1.14	1.72	92	57	40	22	1703	1573	1475	1120
60	8.70	20	2.90	5	0.73	254	10	610	24	1.35	3.22	88	45	27	22	2669	2513	2394	1904
60	8.70	30	4.35	8	1.16	254	10	610	24	1.18	1.9	91	50	32	22	1944	1788	1676	1295
60	8.70	40	5.80	10	1.45	254	10	610	24	1.09	1.25	94	54	36	23	1642	1485	1377	1059
60	8.70	20	2.90	5	0.73	305	12	610	24	1.24	2.38	91	43	25	23	2538	2358	2230	1790
60	8.70	30	4.35	8	1.16	305	12	610	24	1.12	1.4	93	47	30	23	1866	1686	1566	1223
60	8.70	40	5.80	10	1.45	305	12	610	24	1.05	0.92	95	51	33	23	1587	1406	1290	1004
60	8.70	20	2.90	5	0.73	203	8	914	36	1.42	4.25	84	48	31	25	2525	2397	2291	1642
60	8.70	30	4.35	8	1.09	203	8	914	36	1.22	2.55	89	54	37	26	1828	1699	1598	1096
60	8.70	40	5.80	10	1.45	203	8	914	36	1.1	1.7	92	59	42	26	1529	1399	1302	883.9
60	8.70	20	2.90	5	0.73	254	10	914	36	1.29	3.12	88	46	29	26	2412	2257	2139	1555
60	8.70	30	4.35	8	1.16	254	10	914	36	1.14	1.86	92	51	34	27	1762	1607	1495	1043
60	8.70	40	5.80	10	1.45	254	10	914	36	1.05	1.24	94	55	37	27	1485	1329	1220	844.2
60	8.70	20	2.90	5	0.73	305	12	914	36	1.2	2.3	91	44	27	27	2308	2129	2003	1477
60	8.70	30	4.35	8	1.16	305	12	914	36	1.09	1.37	94	48	31	28	1703	1523	1403	995.1
60	8.70	40	5.80	10	1.45	305	12	914	36	1.02	0.91	96	52	34	28	1445	1264	1147	807.9

Table C.3 Raw Data with 80 MPa Base and 4 in. HMA

Modulus						Thickness				Damage Index		Stress (kPa)				Vertical Deflection (µm)			
Base		Eng Soil		Und Soil		Base		Eng Soil		Fatigue	Rutting	Top Base	Mid Base	Bottom Base	Bottom Eng Soil	Top Base	Mid Base	Bottom Base	Bottom Eng Soil
MPa	ksi	MPa	ksi	MPa	ksi	mm	in	mm	in										
80	11.60	20	2.90	5	0.73	203	8	203	8	1.44	4.77	93	44	22	16	3327	3208	3102	2824
80	11.60	30	4.35	8	1.09	203	8	203	8	1.22	2.97	98	49	27	18	2414	2298	2202	1977
80	11.60	40	5.80	10	1.45	203	8	203	8	1.11	2.06	101	53	30	19	2053	1938	1848	1653
80	11.60	20	2.90	5	0.73	254	10	203	8	1.21	3.4	100	43	20	17	3075	2933	2818	2574
80	11.60	30	4.35	8	1.16	254	10	203	8	1.07	2.13	103	48	24	18	2253	2114	2010	1812
80	11.60	40	5.80	10	1.45	254	10	203	8	0.99	1.48	105	51	27	19	1928	1790	1691	1520
80	11.60	20	2.90	5	0.73	305	12	203	8	1.06	2.43	104	42	19	17	2856	2694	2573	2360
80	11.60	30	4.35	8	1.16	305	12	203	8	0.96	1.53	107	46	23	18	2113	1954	1843	1669
80	11.60	40	5.80	10	1.45	305	12	203	8	0.91	1.07	108	48	25	19	1818	1660	1556	1404
80	11.60	20	2.90	5	0.73	203	8	610	24	1.19	4.12	97	49	28	21	2726	2611	2513	1989
80	11.60	30	4.35	8	1.09	203	8	610	24	1.02	2.56	102	56	34	21	1961	1847	1757	1345
80	11.60	40	5.80	10	1.45	203	8	610	24	0.92	1.77	105	60	39	22	1643	1528	1442	1095
80	11.60	20	2.90	5	0.73	254	10	610	24	1.05	2.93	103	48	26	22	2563	2425	2318	1854
80	11.60	30	4.35	8	1.16	254	10	610	24	0.93	1.82	106	53	31	22	1862	1725	1626	1260
80	11.60	40	5.80	10	1.45	254	10	610	24	0.86	1.25	108	57	35	22	1570	1433	1338	1030
80	11.60	20	2.90	5	0.73	305	12	610	24	0.95	2.11	106	46	24	22	2418	2259	2146	1753
80	11.60	30	4.35	8	1.16	305	12	610	24	0.86	1.31	109	50	28	23	1773	1615	1511	1185
80	11.60	40	5.80	10	1.45	305	12	610	24	0.81	0.9	111	53	32	23	1506	1348	1247	971.7
80	11.60	20	2.90	5	0.73	203	8	914	36	1.13	3.98	98	51	30	25	2449	2334	2239	1616
80	11.60	30	4.35	8	1.09	203	8	914	36	0.98	2.5	102	57	36	26	1767	1654	1565	1078
80	11.60	40	5.80	10	1.45	203	8	914	36	0.89	1.73	106	62	41	26	1476	1362	1276	868.6
80	11.60	20	2.90	5	0.73	254	10	914	36	1.01	2.83	103	49	27	26	2319	2182	2078	1525
80	11.60	30	4.35	8	1.16	254	10	914	36	0.9	1.77	106	54	32	27	1690	1553	1456	1022
80	11.60	40	5.80	10	1.45	254	10	914	36	0.83	1.23	109	58	36	27	1421	1284	1190	826.2
80	11.60	20	2.90	5	0.73	305	12	914	36	0.92	2.03	107	47	25	27	2204	2046	1936	1442
80	11.60	30	4.35	8	1.16	305	12	914	36	0.84	1.27	109	51	30	27	1620	1463	1359	970.9
80	11.60	40	5.80	10	1.45	305	12	914	36	0.79	0.88	111	54	33	28	1372	1214	1114	787.8

Table C.4 Raw Data with 120 MPa Base and 4 in. HMA

| Modulus | | | | | | Thickness | | | | Damage Index | | Stress (kPa) | | | | Vertical Deflection (μm) | | | |
| Base | | Eng Soil | | Und Soil | | Base | | Eng Soil | | Fatigue | Rutting | Top Base | Mid Base | Bottom Base | Bottom Eng Soil | Top Base | Mid Base | Bottom Base | Bottom Eng Soil |
MPa	ksi	MPa	ksi	MPa	ksi	mm	in	mm	in										
120	17.40	20	2.90	5	0.73	203	8	203	8	0.94	3.9	118	49	21	16	3120	3018	2927	2675
120	17.40	30	4.35	8	1.09	203	8	203	8	0.82	2.61	121	54	25	17	2267	2168	2086	1878
120	17.40	40	5.80	10	1.45	203	8	203	8	0.75	1.92	124	58	29	18	1929	1832	1755	1571
120	17.40	20	2.90	5	0.73	254	10	203	8	0.76	2.62	126	48	19	16	2843	2724	2627	2412
120	17.40	30	4.35	8	1.16	254	10	203	8	0.69	1.77	129	52	23	17	2086	1970	1882	1703
120	17.40	40	5.80	10	1.45	254	10	203	8	0.65	1.31	131	56	25	18	1786	1671	1588	1430
120	17.40	20	2.90	5	0.73	305	12	203	8	0.65	1.79	132	47	18	16	2609	2475	2375	2191
120	17.40	30	4.35	8	1.16	305	12	203	8	0.61	1.22	133	50	21	18	1933	1801	1709	1555
120	17.40	40	5.80	10	1.45	305	12	203	8	0.58	0.91	135	53	23	18	1665	1534	1447	1310
120	17.40	20	2.90	5	0.73	203	8	610	24	0.8	3.46	121	54	27	21	2590	2493	2409	1927
120	17.40	30	4.35	8	1.09	203	8	610	24	0.7	2.29	125	60	32	21	1861	1765	1688	1303
120	17.40	40	5.80	10	1.45	203	8	610	24	0.63	1.66	128	65	37	21	1557	1462	1389	1061
120	17.40	20	2.90	5	0.73	254	10	610	24	0.68	2.34	128	52	24	21	2406	2290	2201	1782
120	17.40	30	4.35	8	1.16	254	10	610	24	0.61	1.56	131	57	29	22	1745	1631	1548	1212
120	17.40	40	5.80	10	1.45	254	10	610	24	0.57	1.13	133	61	33	22	1470	1357	1278	990.8
120	17.40	20	2.90	5	0.73	305	12	610	24	0.6	1.61	133	50	22	22	2246	2114	2022	1656
120	17.40	30	4.35	8	1.16	305	12	610	24	0.56	1.07	135	54	26	23	1644	1513	1428	1133
120	17.40	40	5.80	10	1.45	305	12	610	24	0.53	0.78	137	57	29	23	1394	1264	1183	929.3
120	17.40	20	2.90	5	0.73	203	8	914	36	0.77	3.34	121	55	28	25	2333	2236	2155	1580
120	17.40	30	4.35	8	1.09	203	8	914	36	0.67	2.22	126	61	34	26	1679	1584	1509	1054
120	17.40	40	5.80	10	1.45	203	8	914	36	0.61	1.61	129	66	39	26	1400	1306	1234	848.8
120	17.40	20	2.90	5	0.73	254	10	914	36	0.66	2.26	129	53	25	26	2184	2070	1983	1481
120	17.40	30	4.35	8	1.16	254	10	914	36	0.6	1.51	132	58	30	26	1586	1473	1393	993
120	17.40	40	5.80	10	1.45	254	10	914	36	0.56	1.1	134	62	34	27	1332	1219	1142	802.9
120	17.40	20	2.90	5	0.73	305	12	914	36	0.59	1.56	133	51	23	27	2055	1924	1834	1393
120	17.40	30	4.35	8	1.16	305	12	914	36	0.55	1.04	136	55	28	27	1505	1375	1291	938.6
120	17.40	40	5.80	10	1.45	305	12	914	36	0.52	0.76	137	58	31	27	1272	1143	1062	761.7

Table C.5 Raw Data with 160 MPa Base and 4 in. HMA

Modulus						Thickness				Damage Index		Stress (kPa)				Vertical Deflection (µm)			
Base		Eng Soil		Und Soil		Base		Eng Soil		Fatigue	Rutting	Top Base	Mid Base	Bottom Base	Bottom Eng Soil	Top Base	Mid Base	Bottom Base	Bottom Eng Soil
MPa	ksi	MPa	ksi	MPa	ksi	mm	in	mm	in										
160	23.20	20	2.90	5	0.73	203	8	203	8	0.65	3.18	138	53	19	15	2962	2873	2792	2563
160	23.20	30	4.35	8	1.09	203	8	203	8	0.58	2.22	142	58	24	17	2156	2070	1996	1804
160	23.20	40	5.80	10	1.45	203	8	203	8	0.53	1.7	144	62	27	17	1837	1752	1683	1512
160	23.20	20	2.90	5	0.73	254	10	203	8	0.51	2.05	148	53	18	16	2674	2570	2486	2294
160	23.20	30	4.35	8	1.16	254	10	203	8	0.47	1.45	150	56	21	17	1965	1864	1786	1624
160	23.20	40	5.80	10	1.45	254	10	203	8	0.45	1.11	152	59	24	17	1684	1584	1511	1366
160	23.20	20	2.90	5	0.73	305	12	203	8	0.43	1.35	154	51	17	16	2436	2319	2233	2071
160	23.20	30	4.35	8	1.16	305	12	203	8	0.41	0.96	156	54	20	17	1806	1691	1613	1474
160	23.20	40	5.80	10	1.45	305	12	203	8	0.4	0.75	157	56	22	18	1557	1443	1369	1244
160	23.20	20	2.90	5	0.73	203	8	610	24	0.57	2.88	141	58	25	20	2487	2402	2328	1880
160	23.20	30	4.35	8	1.09	203	8	610	24	0.5	1.98	145	64	30	21	1786	1702	1635	1274
160	23.20	40	5.80	10	1.45	203	8	610	24	0.46	1.48	148	68	35	21	1495	1412	1348	1038
160	23.20	20	2.90	5	0.73	254	10	610	24	0.47	1.88	150	56	22	21	2291	2190	2112	1730
160	23.20	30	4.35	8	1.16	254	10	610	24	0.43	1.3	152	61	27	22	1660	1561	1490	1179
160	23.20	40	5.80	10	1.45	254	10	610	24	0.4	0.98	154	64	31	22	1399	1301	1233	964.4
160	23.20	20	2.90	5	0.73	305	12	610	24	0.41	1.25	155	54	21	22	2123	2009	1929	1600
160	23.20	30	4.35	8	1.16	305	12	610	24	0.38	0.87	157	58	25	22	1553	1440	1366	1096
160	23.20	40	5.80	10	1.45	305	12	610	24	0.37	0.66	159	61	28	23	1317	1205	1135	900.6
160	23.20	20	2.90	5	0.73	203	8	914	36	0.54	2.78	142	59	26	25	2245	2160	2089	1553
160	23.20	30	4.35	8	1.09	203	8	914	36	0.48	1.92	145	65	32	25	1614	1531	1465	1037
160	23.20	40	5.80	10	1.45	203	8	914	36	0.45	1.44	148	70	37	26	1346	1263	1200	835.6
160	23.20	20	2.90	5	0.73	254	10	914	36	0.45	1.82	150	57	24	26	2086	1986	1911	1449
160	23.20	30	4.35	8	1.16	254	10	914	36	0.42	1.26	153	62	28	26	1512	1414	1344	973.1
160	23.20	40	5.80	10	1.45	254	10	914	36	0.4	0.95	155	66	32	26	1269	1172	1105	787.4
160	23.20	20	2.90	5	0.73	305	12	914	36	0.4	1.21	156	55	22	27	1949	1836	1758	1357
160	23.20	30	4.35	8	1.16	305	12	914	36	0.38	0.85	158	58	26	27	1424	1312	1241	916.4
160	23.20	40	5.80	10	1.45	305	12	914	36	0.36	0.64	159	62	29	27	1203	1092	1023	744.4

Table C.6 Raw Data with 40 MPa Base and 6 in. HMA

Modulus						Thickness				Damage Index		Stress (kPa)				Vertical Deflection (µm)			
Base		Eng Soil		Und Soil		Base		Eng Soil		Fatigue	Rutting	Top Base	Mid Base	Bottom Base	Bottom Eng Soil	Top Base	Mid Base	Bottom Base	Bottom Eng Soil
MPa	ksi	MPa	ksi	MPa	ksi	mm	in	mm	in										
40	5.80	20	2.90	5	0.73	203	8	203	8	0.43	1.3	29	21	16	16	2769	2688	2617	2441
40	5.80	30	4.35	8	1.09	203	8	203	8	0.36	0.74	32	24	19	17	2005	1925	1860	1720
40	5.80	40	5.80	10	1.45	203	8	203	8	0.32	0.47	34	26	21	18	1709	1629	1567	1448
40	5.80	20	2.90	5	0.73	254	10	203	8	0.4	1.11	31	21	17	17	2664	2566	2482	2317
40	5.80	30	4.35	8	1.16	254	10	203	8	0.33	0.62	33	24	19	18	1938	1841	1765	1634
40	5.80	40	5.80	10	1.45	254	10	203	8	0.3	0.4	35	25	20	18	1657	1560	1488	1376
40	5.80	20	2.90	5	0.73	305	12	203	8	0.37	0.94	33	21	17	17	2562	2447	2354	2199
40	5.80	30	4.35	8	1.16	305	12	203	8	0.32	0.52	35	24	19	18	1874	1760	1676	1553
40	5.80	40	5.80	10	1.45	305	12	203	8	0.29	0.33	36	25	20	19	1608	1494	1414	1310
40	5.80	20	2.90	5	0.73	203	8	610	24	0.34	1.08	32	25	20	21	2333	2253	2185	1826
40	5.80	30	4.35	8	1.09	203	8	610	24	0.28	0.61	35	28	24	22	1673	1591	1526	1249
40	5.80	40	5.80	10	1.45	203	8	610	24	0.25	0.38	38	31	26	22	1405	1322	1259	1027
40	5.80	20	2.90	5	0.73	254	10	610	24	0.32	0.89	34	24	20	22	2256	2158	2079	1743
40	5.80	30	4.35	8	1.16	254	10	610	24	0.27	0.49	36	28	23	23	1627	1528	1454	1195
40	5.80	40	5.80	10	1.45	254	10	610	24	0.25	0.3	38	30	25	23	1373	1273	1200	985.1
40	5.80	20	2.90	5	0.73	305	12	610	24	0.3	0.74	35	24	20	23	2182	2067	1980	1665
40	5.80	30	4.35	8	1.16	305	12	610	24	0.26	0.4	37	27	22	24	1585	1469	1387	1145
40	5.80	40	5.80	10	1.45	305	12	610	24	0.24	0.25	39	29	24	24	1343	1227	1146	946
40	5.80	20	2.90	5	0.73	203	8	914	36	0.32	1.05	33	26	22	26	2104	2024	1956	1548
40	5.80	30	4.35	8	1.09	203	8	914	36	0.26	0.6	36	29	25	26	1509	1427	1362	1023
40	5.80	40	5.80	10	1.45	203	8	914	36	0.24	0.39	39	32	27	27	1262	1178	1114	832.3
40	5.80	20	2.90	5	0.73	254	10	914	36	0.3	0.86	34	25	21	27	2043	1945	1867	1456
40	5.80	30	4.35	8	1.16	254	10	914	36	0.26	0.48	37	29	24	27	1475	1376	1301	985.2
40	5.80	40	5.80	10	1.45	254	10	914	36	0.23	0.31	39	31	26	28	1239	1138	1064	803.2
40	5.80	20	2.90	5	0.73	305	12	914	36	0.29	0.71	35	25	21	28	1985	1871	1783	1399
40	5.80	30	4.35	8	1.16	305	12	914	36	0.25	0.39	38	28	24	28	1443	1327	1244	949.6
40	5.80	40	5.80	10	1.45	305	12	914	36	0.23	0.25	39	30	25	29	1218	1101	1019	775.9

Table C.7 Raw Data with 60 MPa Base and 6 in. HMA

Modulus						Thickness				Damage Index		Stress (kPa)				Vertical Deflection (μm)			
Base		Eng Soil		Und Soil		Base		Eng Soil		Fatigue	Rutting	Top Base	Mid Base	Bottom Base	Bottom Eng Soil	Top Base	Mid Base	Bottom Base	Bottom Eng Soil
MPa	ksi	MPa	ksi	MPa	ksi	mm	in	mm	in										
60	8.70	20	2.90	5	0.73	203	8	203	8	0.36	1.35	37	23	16	16	2685	2613	2547	2373
60	8.70	30	4.35	8	1.09	203	8	203	8	0.3	0.83	40	26	19	17	1942	1871	1811	1670
60	8.70	40	5.80	10	1.45	203	8	203	8	0.27	0.57	42	28	21	17	1653	1582	1526	1404
60	8.70	20	2.90	5	0.73	254	10	203	8	0.32	1.11	40	23	16	16	2557	2470	2394	2232
60	8.70	30	4.35	8	1.16	254	10	203	8	0.27	0.67	42	26	19	17	1858	1773	1705	1574
60	8.70	40	5.80	10	1.45	254	10	203	8	0.25	0.46	44	28	20	18	1586	1502	1437	1324
60	8.70	20	2.90	5	0.73	305	12	203	8	0.29	0.9	42	23	16	17	2434	2333	2250	2101
60	8.70	30	4.35	8	1.16	305	12	203	8	0.25	0.55	44	26	18	18	1780	1681	1606	1485
60	8.70	40	5.80	10	1.45	305	12	203	8	0.23	0.37	45	27	20	18	1525	1426	1355	1251
60	8.70	20	2.90	5	0.73	203	8	610	24	0.29	1.15	40	26	20	21	2271	2200	2138	1785
60	8.70	30	4.35	8	1.09	203	8	610	24	0.24	0.7	43	30	23	22	1622	1552	1495	1217
60	8.70	40	5.80	10	1.45	203	8	610	24	0.21	0.47	46	33	26	22	1358	1287	1232	997.9
60	8.70	20	2.90	5	0.73	254	10	610	24	0.26	0.93	42	26	20	22	2176	2091	2020	1693
60	8.70	30	4.35	8	1.16	254	10	610	24	0.22	0.55	45	30	23	23	1564	1479	1414	1157
60	8.70	40	5.80	10	1.45	254	10	610	24	0.2	0.37	47	32	25	23	1316	1230	1168	851.2
60	8.70	20	2.90	5	0.73	305	12	610	24	0.24	0.74	44	26	20	23	2087	1988	1911	1607
60	8.70	30	4.35	8	1.16	305	12	610	24	0.21	0.44	46	29	22	24	1511	1412	1340	1103
60	8.70	40	5.80	10	1.45	305	12	610	24	0.19	0.29	48	31	24	24	1276	1177	1108	908.4
60	8.70	20	2.90	5	0.73	203	8	914	36	0.27	1.11	40	27	21	26	2050	1981	1920	1489
60	8.70	30	4.35	8	1.09	203	8	914	36	0.22	0.68	44	31	25	26	1465	1395	1338	1001
60	8.70	40	5.80	10	1.45	203	8	914	36	0.2	0.46	46	34	28	26	1220	1149	1094	812.1
60	8.70	20	2.90	5	0.73	254	10	914	36	0.25	0.89	43	27	21	27	1975	1890	1821	1421
60	8.70	30	4.35	8	1.16	254	10	914	36	0.21	0.53	46	31	24	27	1420	1335	1270	958.7
60	8.70	40	5.80	10	1.45	254	10	914	36	0.19	0.36	48	33	26	27	1188	1103	1040	779.5
60	8.70	20	2.90	5	0.73	305	12	914	36	0.23	0.71	45	27	21	28	1904	1805	1729	1359
60	8.70	30	4.35	8	1.16	305	12	914	36	0.2	0.42	47	30	23	28	1378	1279	1208	919.3
60	8.70	40	5.80	10	1.45	305	12	914	36	0.19	0.28	48	32	25	28	1159	1060	990.8	749.4

Table C.8 Raw Data with 80 MPa Base and 6 in. HMA

Modulus						Thickness				Damage Index		Stress (kPa)				Vertical Deflection (μm)			
Base		Eng Soil		Und Soil		Base		Eng Soil		Fatigue	Rutting	Top Base	Mid Base	Bottom Base	Bottom Eng Soil	Top Base	Mid Base	Bottom Base	Bottom Eng Soil
MPa	ksi	MPa	ksi	MPa	ksi	mm	in	mm	in										
80	11.60	20	2.90	5	0.73	203	8	203	8	0.3	1.31	44	24	16	15	2615	2549	2487	2318
80	11.60	30	4.35	8	1.09	203	8	203	8	0.25	0.84	47	28	19	16	1891	1826	1771	1631
80	11.60	40	5.80	10	1.45	203	8	203	8	0.23	0.6	49	30	20	17	1609	1545	1493	1370
80	11.60	20	2.90	5	0.73	254	10	203	8	0.26	1.04	48	25	16	16	2469	2390	2320	2165
80	11.60	30	4.35	8	1.16	254	10	203	8	0.22	0.67	50	28	18	17	1796	1718	1655	1527
80	11.60	40	5.80	10	1.45	254	10	203	8	0.21	0.48	51	29	20	18	1533	1456	1396	1285
80	11.60	20	2.90	5	0.73	305	12	203	8	0.23	0.82	51	25	16	17	2333	2241	2165	2024
80	11.60	30	4.35	8	1.16	305	12	203	8	0.2	0.53	52	27	18	18	1707	1617	1549	1432
80	11.60	40	5.80	10	1.45	305	12	203	8	0.19	0.38	54	29	19	18	1462	1373	1309	1207
80	11.60	20	2.90	5	0.73	203	8	610	24	0.25	1.14	47	28	20	21	2221	2157	2100	1755
80	11.60	30	4.35	8	1.09	203	8	610	24	0.2	0.72	50	32	23	22	1585	1521	1469	1195
80	11.60	40	5.80	10	1.45	203	8	610	24	0.18	0.5	52	35	26	22	1325	1262	1212	978.6
80	11.60	20	2.90	5	0.73	254	10	610	24	0.22	0.89	50	28	19	22	2115	2037	1973	1656
80	11.60	30	4.35	8	1.16	254	10	610	24	0.19	0.56	52	31	22	23	1518	1442	1382	1131
80	11.60	40	5.80	10	1.45	254	10	610	24	0.17	0.39	54	34	25	23	1275	1199	1142	928.6
80	11.60	20	2.90	5	0.73	305	12	610	24	0.2	0.7	52	28	19	23	2015	1926	1856	1565
80	11.60	30	4.35	8	1.16	305	12	610	24	0.17	0.44	54	30	22	23	1456	1368	1304	1073
80	11.60	40	5.80	10	1.45	305	12	610	24	0.16	0.3	56	33	24	24	1229	1141	1079	883.1
80	11.60	20	2.90	5	0.73	203	8	914	36	0.23	1.09	47	29	21	26	2009	1945	1890	1469
80	11.60	30	4.35	8	1.09	203	8	914	36	0.19	0.7	51	33	25	26	1432	1369	1318	986.6
80	11.60	40	5.80	10	1.45	203	8	914	36	0.17	0.49	53	36	27	26	1191	1128	1079	799.2
80	11.60	20	2.90	5	0.73	254	10	914	36	0.21	0.86	50	29	20	27	1923	1846	1784	1397
80	11.60	30	4.35	8	1.16	254	10	914	36	0.18	0.54	53	32	23	27	1380	1304	1245	941
80	11.60	40	5.80	10	1.45	254	10	914	36	0.16	0.37	55	35	26	27	1153	1077	1021	764.3
80	11.60	20	2.90	5	0.73	305	12	914	36	0.19	0.67	53	28	20	28	1842	1754	1685	1330
80	11.60	30	4.35	8	1.16	305	12	914	36	0.17	0.42	55	31	23	28	1331	1243	1179	899.1
80	11.60	40	5.80	10	1.45	305	12	914	36	0.15	0.29	57	34	25	28	1117	1029	968.3	732.1

Table C.9 Raw Data with 120 MPa Base and 6 in. HMA

Modulus						Thickness				Damage Index		Stress (kPa)				Vertical Deflection (μm)			
Base		Eng Soil		Und Soil		Base		Eng Soil		Fatigue	Rutting	Top Base	Mid Base	Bottom Base	Bottom Eng Soil	Top Base	Mid Base	Bottom Base	Bottom Eng Soil
MPa	ksi	MPa	ksi	MPa	ksi	mm	in	mm	in										
120	17.40	20	2.90	5	0.73	203	8	203	8	0.22	1.16	56	27	16	15	2500	2441	2385	2227
120	17.40	30	4.35	8	1.09	203	8	203	8	0.19	0.79	59	30	18	16	1810	1753	1703	1570
120	17.40	40	5.80	10	1.45	203	8	203	8	0.17	0.6	61	33	20	17	1541	1485	1437	1320
120	17.40	20	2.90	5	0.73	254	10	203	8	0.19	0.88	62	28	15	16	2331	2261	2199	2058
120	17.40	30	4.35	8	1.16	254	10	203	8	0.16	0.6	64	30	18	17	1698	1630	1574	1455
120	17.40	40	5.80	10	1.45	254	10	203	8	0.15	0.45	65	32	19	17	1450	1384	1331	1225
120	17.40	20	2.90	5	0.73	305	12	203	8	0.16	0.66	66	28	16	16	2177	2098	2032	1906
120	17.40	30	4.35	8	1.16	305	12	203	8	0.14	0.45	67	30	17	17	1596	1519	1459	1353
120	17.40	40	5.80	10	1.45	305	12	203	8	0.13	0.34	68	32	19	18	1369	1292	1236	1141
120	17.40	20	2.90	5	0.73	203	8	610	24	0.18	1.04	59	31	19	21	2143	2086	2035	1709
120	17.40	30	4.35	8	1.09	203	8	610	24	0.16	0.69	62	34	22	21	1528	1473	1426	1163
120	17.40	40	5.80	10	1.45	203	8	610	24	0.14	0.51	64	37	25	22	1277	1222	1178	952.4
120	17.40	20	2.90	5	0.73	254	10	610	24	0.16	0.78	64	31	19	22	2019	1952	1895	1600
120	17.40	30	4.35	8	1.16	254	10	610	24	0.14	0.52	66	34	21	22	1449	1383	1331	1094
120	17.40	40	5.80	10	1.45	254	10	610	24	0.13	0.38	68	36	24	23	1216	1151	1102	897.8
120	17.40	20	2.90	5	0.73	305	12	610	24	0.14	0.59	67	30	18	23	1906	1829	1768	1502
120	17.40	30	4.35	8	1.16	305	12	610	24	0.13	0.39	69	33	21	23	1377	1301	1246	1031
120	17.40	40	5.80	10	1.45	305	12	610	24	0.12	0.28	70	35	23	23	1161	1086	1034	848.5
120	17.40	20	2.90	5	0.73	203	8	914	36	0.17	1	59	31	20	26	1944	1888	1839	1440
120	17.40	30	4.35	8	1.09	203	8	914	36	0.15	0.67	63	35	24	26	1384	1329	1284	966.5
120	17.40	40	5.80	10	1.45	203	8	914	36	0.13	0.49	65	38	27	26	1150	1096	1053	782.4
120	17.40	20	2.90	5	0.73	254	10	914	36	0.15	0.75	64	31	20	27	1843	1776	1722	1360
120	17.40	30	4.35	8	1.16	254	10	914	36	0.13	0.5	67	35	23	27	1320	1255	1205	916.7
120	17.40	40	5.80	10	1.45	254	10	914	36	0.12	0.36	69	37	25	27	1102	1037	989.6	744.1
120	17.40	20	2.90	5	0.73	305	12	914	36	0.13	0.56	67	31	19	28	1750	1674	1615	1288
120	17.40	30	4.35	8	1.16	305	12	914	36	0.12	0.38	69	34	22	28	1262	1187	1133	871.1
120	17.40	40	5.80	10	1.45	305	12	914	36	0.11	0.27	71	36	24	28	1058	984	932.6	709.2

Table C.10 Raw Data with 160 MPa Base and 6 in. HMA

Modulus						Thickness				Damage Index		Stress (kPa)				Vertical Deflection (µm)			
Base		Eng Soil		Und Soil		Base		Eng Soil		Fatigue	Rutting	Top Base	Mid Base	Bottom Base	Bottom Eng Soil	Top Base	Mid Base	Bottom Base	Bottom Eng Soil
MPa	ksi	MPa	ksi	MPa	ksi	mm	in	mm	in										
160	23.20	20	2.90	5	0.73	203	8	203	8	0.17	1.01	68	30	15	15	2406	2352	2301	2154
160	23.20	30	4.35	8	1.09	203	8	203	8	0.15	0.72	70	33	18	16	1744	1693	1647	1521
160	23.20	40	5.80	10	1.45	203	8	203	8	0.13	0.56	72	35	19	16	1486	1436	1392	1280
160	23.20	20	2.90	5	0.73	254	10	203	8	0.14	0.73	74	30	15	15	2222	2160	2104	1975
160	23.20	30	4.35	8	1.16	254	10	203	8	0.12	0.52	76	33	17	16	1621	1561	1511	1400
160	23.20	40	5.80	10	1.45	254	10	203	8	0.11	0.4	77	35	19	17	1387	1327	1280	1180
160	23.20	20	2.90	5	0.73	305	12	203	8	0.11	0.53	79	30	15	16	2059	1989	1931	1816
160	23.20	30	4.35	8	1.16	305	12	203	8	0.1	0.38	80	33	17	17	1512	1444	1391	1293
160	23.20	40	5.80	10	1.45	305	12	203	8	0.1	0.3	81	34	18	17	1298	1231	1181	1092
160	23.20	20	2.90	5	0.73	203	8	610	24	0.14	0.92	70	33	18	21	2079	2028	1982	1673
160	23.20	30	4.35	8	1.09	203	8	610	24	0.12	0.64	73	36	22	21	1483	1434	1391	1140
160	23.20	40	5.80	10	1.45	203	8	610	24	0.11	0.48	75	39	24	22	1240	1191	1151	933.9
160	23.20	20	2.90	5	0.73	254	10	610	24	0.12	0.67	76	33	18	22	1944	1884	1833	1558
160	23.20	30	4.35	8	1.16	254	10	610	24	0.11	0.46	78	36	21	22	1396	1337	1291	1066
160	23.20	40	5.80	10	1.45	254	10	610	24	0.1	0.35	80	38	23	22	1172	1114	1071	876
160	23.20	20	2.90	5	0.73	305	12	610	24	0.1	0.49	80	33	18	23	1822	1754	1700	1455
160	23.20	30	4.35	8	1.16	305	12	610	24	0.09	0.34	82	35	20	23	1317	1250	1201	1001
160	23.20	40	5.80	10	1.45	305	12	610	24	0.09	0.25	83	37	22	23	1112	1045	999.1	824.3
160	23.20	20	2.90	5	0.73	203	8	914	36	0.13	0.88	70	34	19	26	1891	1841	1796	1417
160	23.20	30	4.35	8	1.09	203	8	914	36	0.12	0.61	73	37	23	26	1346	1297	1256	952
160	23.20	40	5.80	10	1.45	203	8	914	36	0.1	0.46	76	41	26	26	1118	1070	1031	770.9
160	23.20	20	2.90	5	0.73	254	10	914	36	0.11	0.64	76	34	19	27	1780	1721	1672	1333
160	23.20	30	4.35	8	1.16	254	10	914	36	0.1	0.44	78	37	22	27	1275	1217	1172	899.2
160	23.20	40	5.80	10	1.45	254	10	914	36	0.09	0.33	80	40	24	27	1064	1007	964.4	730.4
160	23.20	20	2.90	5	0.73	305	12	914	36	0.1	0.47	80	33	18	28	1679	1612	1560	1257
160	23.20	30	4.35	8	1.16	305	12	914	36	0.09	0.33	82	36	21	28	1210	1144	1097	851.3
160	23.20	40	5.80	10	1.45	305	12	914	36	0.09	0.25	83	38	23	28	1016	949.9	904.7	693.5

APPENDIX D

Itasca Consulting Group Technical Memorandums

Technical Memorandum

ITASCA
Consulting Group, Inc.

Date: June 23, 2016

To: PFC 5 Documentation Set

From: David Potyondy

Re: Pavement-Design Package for PFC3D [pdPkg10]

Ref: ICG16-8528-15TM

This memo describes the pavement-design package for the Particle Flow Code in 3 Dimensions (*PFC3D*, Itasca [2016]).[1] The package supports creation and triaxial testing of a synthetic unsaturated granular material containing geogrid (see Figure 3). The geogrid provides lateral restraint to the granular material as a result of interlocking and friction between the geogrid and the granular material, and this is believed to be the primary structural benefit of adding geogrid to the aggregate base layer of a pavement structure. The package can be used to study and quantify the effect of microstructural properties on macroscopic response, which includes the stress-strain curves produced during triaxial tests. The microstructural properties of the granular material include: grain size distribution of spherical grains, grain material type, moisture content and initial specimen porosity. The microstructural properties of the geogrid include: geometry, structural stiffness and grid-grain interface behavior. The package is being used to improve pavement-design methodology in Minnesota by estimating geogrid gain factors (defined as the ratio of resilient modulus of the aggregate base with geogrid to resilient modulus of the aggregate base without geogrid) for typical geogrid-reinforced aggregate roadway configurations in which the grain-size distribution, initial specimen porosity, moisture content and confining stress are varied (Potyondy et al., 2016; Siekmeier et al., 2016). The package could be extended to investigate the behavior of other aggregate-geogrid systems such as a geogrid pull-out or wheel-load test.

Pavement-design methodology is summarized in the first major section. The pavement-design package is described in the second major section, with a particular emphasis on the geogrid-modeling methodology. Pavement-design examples are given in the third major section. A typical aggregate base layer of an asphalt-surface roadway is modeled. The resilient modulus is measured, for dry and wet conditions both with and without a geogrid, by performing triaxial tests on the modeled systems.

---

[1] The pavement-design package is provided in the form of a consistent set of FISH functions that operate within *PFC3D* version 5.0. FISH is a programming language embedded within *PFC3D*. The *PFC3D* code can be obtained from http://www.itascacg.com/software/pfc, and it is planned that the pavement-design package will be obtained from the Material Modeling Support link on this page.

TABLE OF CONTENTS

1.0   PAVEMENT-DESIGN METHODOLOGY

The first subsection outlines the layered elastic analysis that is used to support pavement design via *MnPAVE* (Tanquist, 2012). The second subsection introduces the geogrid gain factor as a means to modify the *MnPAVE* design modulus to account for the presence of geogrid within the aggregate base layer. And the final subsection discusses the unsaturated condition of pavement materials.

1.1   Layered Elastic Analysis

The mechanistic-empirical flexible pavement design program *MnPAVE* embodies an accepted procedure for the design of flexible pavements in Minnesota. *MnPAVE* simulates traffic loads on a pavement using a layered elastic analysis (LEA). The LEA is an axisymmetric, isotropic, elastic-layer model with bottom and sides at infinity, wheel load at the top, parameterized by thickness, Young's modulus and Poisson's ratio for each of the five layers, and allowing full to zero slip interface conditions. *MnPAVE* enforces the zero-slip condition to compute normal and shear stress, normal strain and displacement within the system shown in Figure 1. Of particular importance is the horizontal tensile strain at the bottom of the asphalt layer (ε_h), and the vertical compressive strain at the top of the compacted soil layer (ε_v). An excessive value of ε_h can result in a fatigue crack forming and continuing upwards to the pavement surface, and an excessive vertical stress associated with ε_v can result in permanent deformation in the compacted soil layer, which over time will be visible at the pavement surface as rutting. Estimates of fatigue and rutting life are obtained via empirical relations that employ these quantities (ε_h for fatigue and ε_v for rutting). Both life estimates must be greater than twenty years for the design to be acceptable. The inputs to *MnPAVE* include the thickness and material type of each layer, climate and traffic. The parameters are tied to one another via empirical relations. For example, life predictions require integrating the damage effects of wheel loading over time, and the climate dictates moisture conditions, which affect the elastic constants.
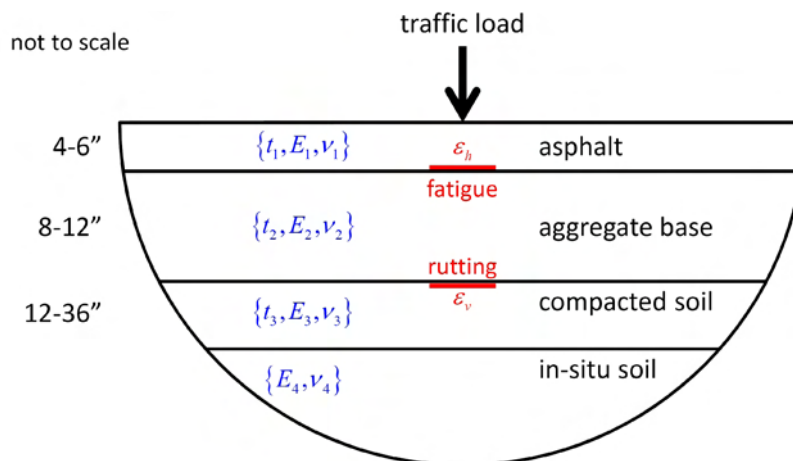
Figure 1   *Layered elastic analysis showing inputs (blue), typical layer names and thicknesses, and outputs (red) used to estimate fatigue and rutting life of flexible pavements.*

Traffic loading in pavement analysis is conventionally simplified as a cyclic deviator stress (σ_d). The repeated application of the deviator stress results in permanent strain (ε_p) and resilient strain (ε_r) within pavement materials, as shown in Figure 2. The resilient modulus (M_R) is defined as the ratio of applied deviator stress to recoverable or "resilient" strain. It is a granular material characterization parameter that is stress dependent. The resilient modulus is used as the design modulus for the layered elastic analysis shown in Figure 1. LEA is utilized extensively for pavement system evaluation and is a means of calculating pavement response under loading. Each pavement layer is defined by its resilient modulus and Poisson's ratio, even though granular bases exhibit nonlinear elastoplastic behavior in laboratory and field applications. LEA is used because it is a relatively simple analysis procedure and, more importantly, pavement loading is generally of low enough magnitude that a linear-elastic approximation of pavement material behavior is deemed suitable. According to Han and Vanapalli (2016), the resilient modulus is "…the key soil property in the mechanistic pavement design methods to rationally characterize the resilient behavior of the pavement materials, analyze the fatigue failure of the surface layer, and dimension the multi-layer system of the pavement structure."
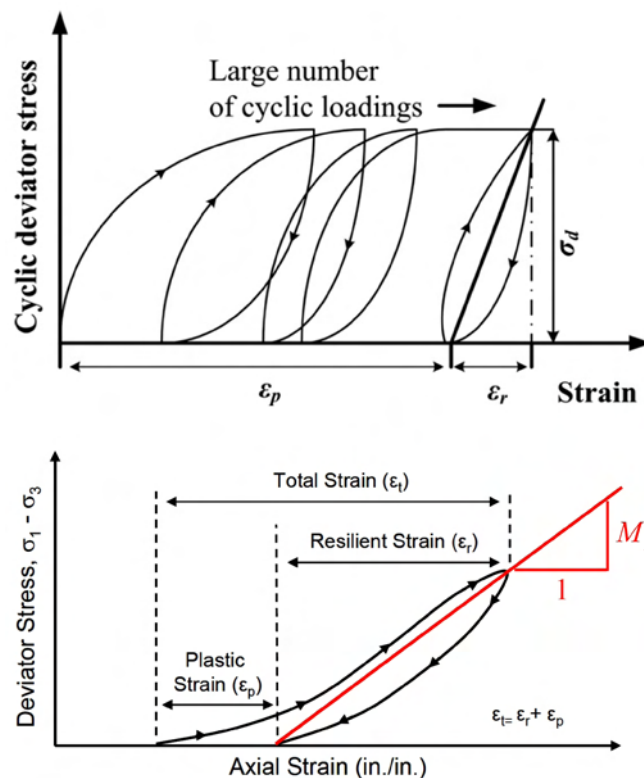
Figure 2   ***Response of granular material to cyclic deviator stress (top), and measurement of resilient modulus (bottom).*** (From Fig. 2 of Han and Vanapalli [2016], and Fig. 1 of Buchanan [2007].)

1.2   Geogrid Gain Factor

The material in this subsection is a summary of the more extensive presentation in Potyondy et al. (2016). The traditional reason to use geogrid in Minnesota has been to provide a more stable construction platform by improving the strength of the pavement foundation when weak soils are present (Clyne, 2001). A more recent reason to use geogrid has been to provide additional stiffness to the aggregate base layer. Geogrid use is known to increase aggregate compaction during construction, thereby allowing the aggregate base to more effectively protect the underlying soil layers from traffic loads. Geogrid use is also expected to improve both the short- and long-term performance of roadways; however, greater justification and quantification of this expectation is desired.

The primary structural benefit of adding geogrid to the aggregate base layer of a flexible pavement is to provide lateral restraint. Lateral restraint is provided for the base layer as the result of interlocking and friction between the geogrid and the aggregate. Under repeated loads, the base layer tends to spread laterally, and some of the shear stress in the base layer can be transferred to tensile stress in the geogrid. A stiff geogrid will act to restrain the lateral spreading and result in a stiffer aggregate base. The lateral-restraint mechanism (as summarized in Bagshaw et al. [2015]) ". . .is that by

restricting the ability of the aggregate particles to move, and by effectively fixing them into place via interaction with the geogrid, mass transfer through the pavement will be restricted. If particles cannot move, then the modulus of the matrix will be maintained, and the rate of accumulation of plastic deformation via shear and/or consolidation will be reduced."

It is understood that the use of geogrids in roadway aggregate base layer construction is beneficial (Skallman, 2010); however, *MnPAVE* does not account for the presence of a geogrid within the aggregate base layer. The geogrid gain factor is introduced as a means to modify the *MnPAVE* design modulus to account for the presence of geogrid within the aggregate base layer. The geogrid gain factor is defined as the ratio of resilient modulus of the aggregate base with geogrid to resilient modulus of the aggregate base without geogrid. The pavement-design package is used to estimate the geogrid gain factors for typical aggregate-geogrid roadway configurations (Siekmeier et al, 2016). Triaxial tests of an aggregate base, both with and without geogrid, are modeled, and the resilient moduli are measured in these tests to estimate the geogrid gain factor. The *MnPAVE* design modulus for the aggregate base with geogrid is found by multiplying the design modulus for the aggregate base without geogrid by the gain factor.

1.3   Unsaturated Condition of Pavement Materials

Han and Vanapalli (2016) describe the unsaturated condition of pavement materials, and argue for the use of soil suction to predict their mechanical behavior.

> Compacted pavement base/subbase materials and subgrade soils stay in an unsaturated condition and are subjected to environmental influences. Environmental factors contribute to moisture regime and soil suction (ψ) variations within the pavement structure which, in turn, influence strength and stiffness of pavement materials. Several research studies in recent years have demonstrated the strong correlations between the mechanical properties of unsaturated soils and the ψ. It is therefore recommended to use ψ as a key parameter to interpret and predict the response of the mechanical behavior of unsaturated soils to the soil moisture regime fluctuations. (Han and Vanapalli, 2016, p. 1)

The pavement-design package provides a means to predict the $M_R - \psi$ correlations for typical pavement materials both with and without geogrid.

2.0   PAVEMENT-DESIGN PACKAGE

The pavement-design package supports creation and triaxial testing of a synthetic unsaturated granular material containing geogrid (see Figure 3). The mechanical behavior of this discrete system is simulated by the three-dimensional discrete-element program *PFC3D*. The model can simulate the movement and interaction of hundreds of thousands of finite-sized particles. The particles are rigid bodies with finite mass that move independently of one another and can both translate and rotate. Particles interact at pair-wise contacts by means of an internal force and moment. Contact mechanics is embodied in particle-interaction laws (called contact models) that update the internal forces and moments. The time evolution of this system is computed via the distinct-element method, which provides an explicit dynamic solution to Newton's laws of motion. The PFC model can be envisioned as a synthetic material that encompasses a vast microstructural space spanning from the granular material described here to the rich variety of solid materials provided by the bonded-particle modeling methodology (Potyondy, 2015). The synthetic system described here consists of unsaturated granular material and geogrid. The unsaturated granular material is modeled as spherical grains that interact with one another via the hill contact model. The synthetic material is denoted as a hill material and described in Potyondy (2016b). The geogrid is modeled as strings of overlapping spherical balls joined by parallel bonds. The parallel bonds provide the structural properties of the grid, and the spherical balls provide the grid surface for grid-grain interaction.

granular material
(spherical balls and
hill contact model)

geogrid
(strings of overlapping bonded spherical balls)

parallel bonds (gold)
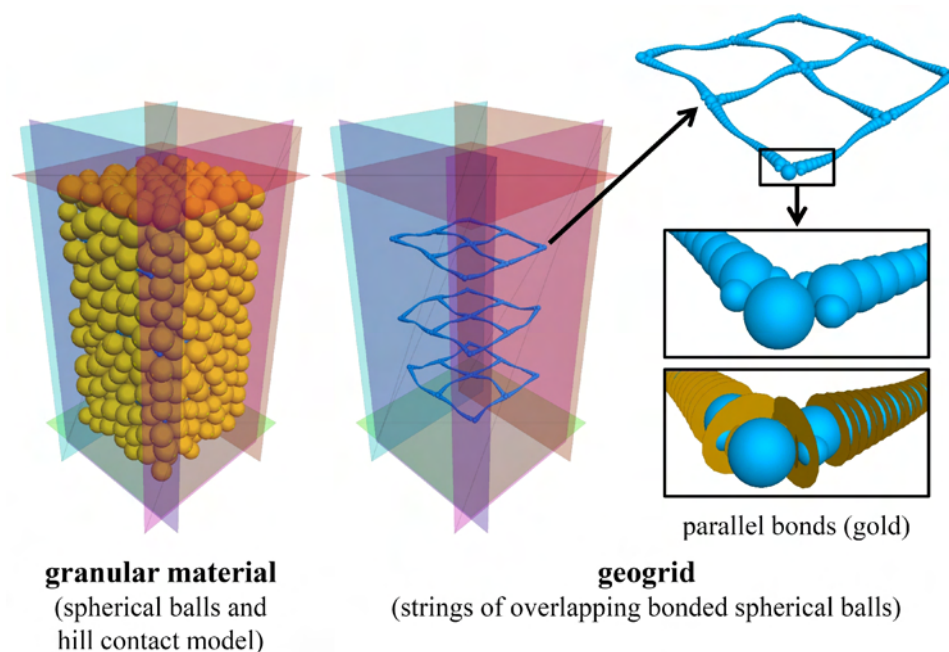
Figure 3   Pavement-design package supports creation and triaxial testing of synthetic unsaturated granular material containing geogrid, and measurement of resilient modulus for grid and no grid.

The grid-modeling methodology is described in the first subsection. The geogrids are specified as a grid set consisting of identical flat geogrids oriented perpendicular to the specimen axis and spaced evenly in the axial direction (see Figure 4). The grid-set description includes a definition of the grid-set parameters as well as the closed-form expressions defining the sizes and locations of the balls and the radii of the parallel bonds. The grid-set properties are chosen to match the geogrid geometry (which includes the aperture size, junction height and mid-rib thickness), the rib tensile stiffness from a Single Rib Tensile test, and the junction torsional stiffness from an Aperture Stability Modulus test. These two grid-calibration tests are described in the next two subsections. The descriptions include demonstrations that the Tensar SS20 biaxial geogrid used in the pavement-design example matches the laboratory-test responses. The material-genesis procedure to embed a geogrid within the granular material is described in the final subsection.

2.1 Grid-Modeling Methodology: Grid Set

The grid-modeling methodology draws upon the work of Stahl and co-workers (Jas et al. [2015a, 2015b]; Stahl and te Kamp [2013, 2012]; Stahl et al. [2014]; Stahl and Konietzky [2011]; Stahl [2011]; Konietzky et al. [2004]), with the primary contribution being the closed-form expressions defining the sizes and locations of the balls and the radii of the parallel bonds as summarized by Stille (2015).[2] McDowell and co-workers (McDowell et al. [2006]; Chen et al. [2013]) describe a similar grid-modeling methodology in which the geogrid consists of spherical balls joined by parallel bonds. Qian and co-workers (Qian et al. [2015]) describe the modeling of granular material as discrete polyhedral grains in which rigid geogrids may be embedded, with the mechanical behavior of the discrete system being simulated by the three-dimensional discrete-element program BLOKS3D.

The grid-modeling methodology is summarized as follows. The grid consists of strings of overlapping spherical balls joined by parallel bonds. The parallel bonds provide the structural properties of the grid, and the spherical balls provide the grid surface for grid-grain interaction, which occurs at the grid-grain contacts. Each grid junction (see Figure 5) consists of two intersecting ribs and additional material in the form of join balls that increases the junction stiffness.

There are five types of contacts in the modeled system: grain-grain, grid-grid, grid-grain, grid-wall and grain-wall. The grain-grain contacts employ the hill contact model, the grid-grid contacts employ the linear parallel bond contact model, and the remaining three contact types employ the linear contact model. The hill contact model provides the behavior of an infinitesimal, nonlinear elastic (no tension) and frictional interface that carries a compressive surface-interaction force and may carry a tensile moisture force. The parallel-bond contact model provides the behavior of a

---

[2] Tensar International Limited is acknowledged for its research efforts modeling geogrids and granular soils, and in particular, for granting access to the grid-modeling methodology developed on its behalf by Itasca Consultants GmbH. Tensar is commended for its willingness to grant this access, fostering development of these models to benefit the wider industry.

finite-size, linear elastic and bonded interface that carries a force and moment. The linear contact model provides the behavior of an infinitesimal, linear elastic (no tension) and frictional interface that carries a force. The hill contact model is described in Potyondy (2016b), and the parallel-bond and linear contacts models are described in Itasca (2016).

Each grid rib behaves as a beam of circular cross section with varying radius along its length. The grid behaves as an elastic body; it will not break, and it will return to its original shape when unloaded. The grid methodology of Stahl and te Kamp (2013) employed a parallel-bond radius and stiffness decreasing law to allow the grid to exhibit nonlinear and plastic behavior. The stiffness decreasing law is excluded from the present methodology, which is believed to be sufficient for cases in which the grid experiences small-deformation loading for which rib tensile strains remain less than three percent and junction rotations remain less than two degrees.

The geogrids are specified as a grid set that consists of identical flat geogrids oriented perpendicular to the global *z*-axis, and spaced evenly in the *z*-direction. When embedding the grid set within a granular material, the grid set is aligned with the specimen axis and positioned within either a polyaxial or cylindrical cell. The grid-set parameters are listed in Table 1, and the modeled system is shown in Figures 4 and 5. Grid deformation causes strain energy to be stored in the parallel bonds that join the grid balls to one another — expressions for the strain energy are given in Itasca (2016).[3] The strain energy stored in the grid set (E_g , $E_g \geq 0$) is given by the FISH variable **gd_Estr**, and provides a scalar index of the load being carried by the grid.

Table 1 Grid Set Parameters

Parameter	Type	Range	Default	Description
Grid set group:				
n_g , **gd_ng**	INT	$[1,\infty)$	1	number of grids
s_z , **gd_sz**	FLT	$(0.0,\infty)$	NA	grid spacing (in *z*-direc.)
$\{n_x, n_y\}$, **gd_n{x,y}**	INT	$[1,\infty)$	$\{1,1\}$	number of cross elements in *x* and *y* direcs.
c , **gd_c**	VEC	$[\mathbb{R},\mathbb{R},\mathbb{R}]$	**0**	position of node ball of bottom-left cross element
C_t , **gd_tips**	INT	$\{0,1\}$	0	grid-tip code $\begin{cases} 0, & \text{remove grid tips} \\ 1, & \text{keep grid tips} \end{cases}$
D_n , **gd_Dn**	FLT	$(0.0,\infty)$	NA	diameter of node ball

---

[3] In documentation set at PFC Model Components: Contacts and Contact Models: Contact Models: Built-in Contact Models: Linear Parallel Bond Model: Energy Partitions.

κ_r , **gd_Drat**	FLT	$(0.0, 1.0)$	0.9	diameter ratio of first rib ball $\left(\kappa_r = D_c^{(1)} / D_n \right)$
l_r , **gd_lr**	FLT	$(0.0, \infty)$	NA	length of rib
n_c , **gd_nc**	INT	$[1, \infty)$	7	core balls per half rib
$\bar{R}_n$, **gd_pbRadNd**	FLT	$(0.0, \infty)$	NA	parallel-bond radius at node ball
$\bar{R}_m$, **gd_pbRadMid**	FLT	$(0.0, \infty)$	NA	parallel-bond radius at mid rib $\left(\bar{R}_m \le \bar{R}_n \right)$
$\bar{\lambda}_j$, **gd_pbRmulJn**	FLT	$(0.0, \infty)$	1.0	parallel-bond radius multiplier of join balls
C_e , **gd_latExtent**	INT	$\{0, 1\}$	0	exclusion region lateral-extent existence code $\begin{cases} 0, & \text{exists} \\ 1, & \text{does not exist} \end{cases}$
Material properties group:				
α_g , **gd_dampFac**	FLT	$[0.0, 0.7]$	1.0	grid local-damping factor
ρ_g , **gd_density**	FLT	$(0.0, \infty)$	NA	grid density (set grid-ball density: $\rho_b = \rho_g$, does not account for grid-ball overlap)
E_g^* , **gd_emod**	FLT	$[0.0, \infty)$	0.0	grid effective modulus
κ_g^* , **gd_krat**	FLT	$[0.0, \infty)$	0.0	grid stiffness ratio
E_{gg}^* , **gd_ggemod**	FLT	$[0.0, \infty)$	0.0	grid-grain effective modulus
κ_{gg}^* , **gd_ggkrat**	FLT	$[0.0, \infty)$	0.0	grid-grain stiffness ratio
μ_{gg} , **gd_ggfric**	FLT	$[0.0, \infty)$	0.0	grid-grain friction coefficient
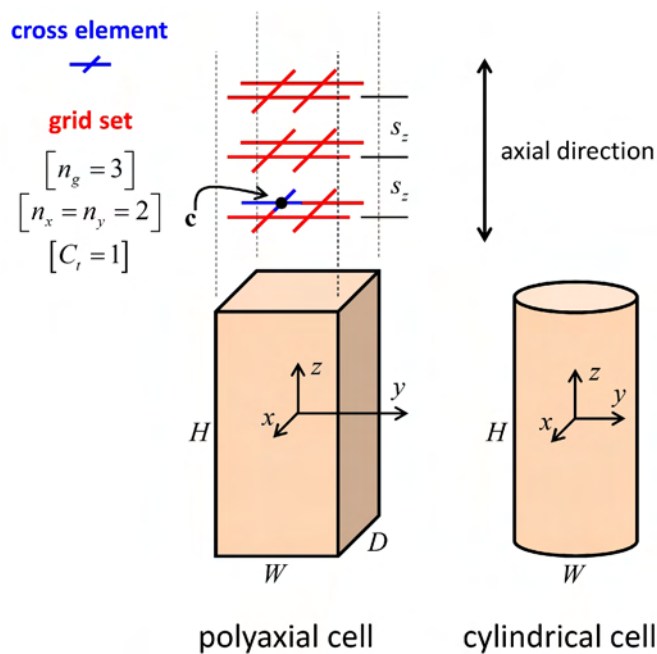
Figure 4   *Material vessels and grid set consisting of three grids, each of which has four cross elements that are shown in Figure 5.*
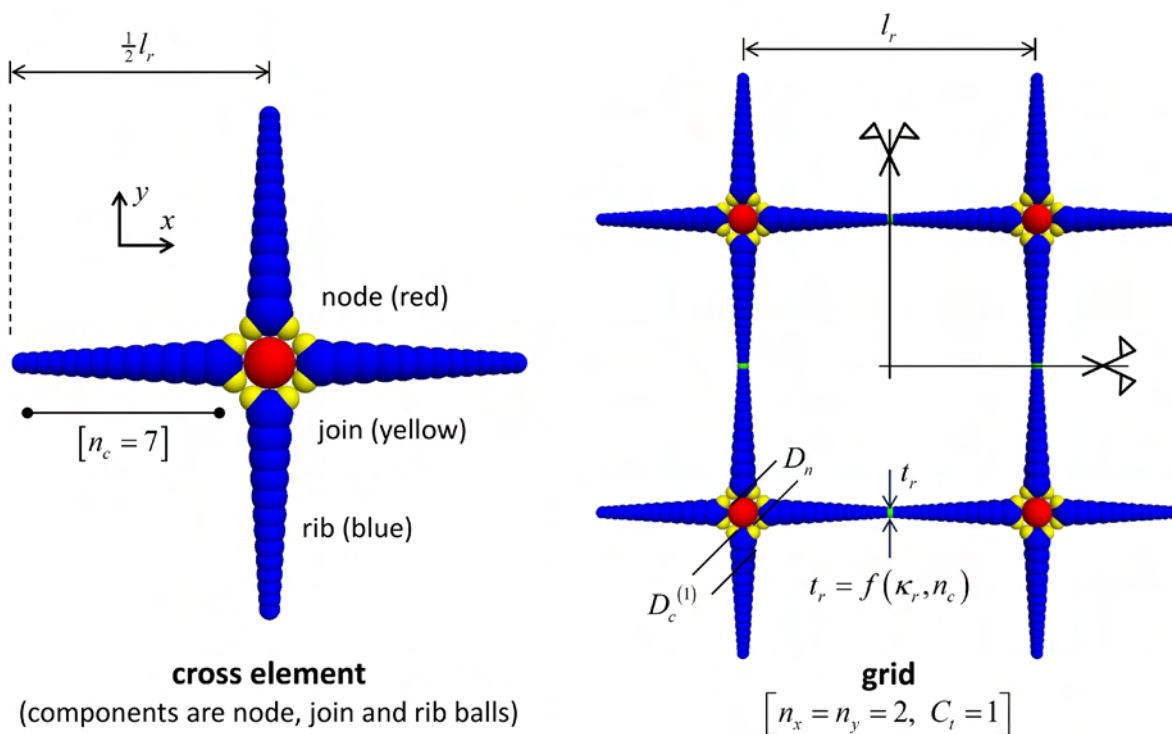
Figure 5   *Cross element and grid consisting of four cross elements.*

The grid set consists of n_g identical grids. Each grid is flat and lies in the *xy*-plane, and the grids are spaced evenly along the *z*-axis at a distance of s_z. A grid consists of identical cross elements, with n_x and n_y cross elements in the *x*- and *y*-directions, respectively. A cross element consists of one node ball with a half rib in both directions (see Figure 5).[4] The bottom-left cross element of the grid set is centered at **c** . The presence of cross-element tips at the outside edge of the grid set is controlled by the grid-tip code C_t.

The geometry of a cross element is defined by the node-ball diameter (D_n), the diameter ratio of the first rib ball $\left(\kappa_r = D_c^{(1)}/D_n\right)$, the rib length (l_r), and the number of core balls per half rib (n_c). The minimum rib thickness (t_r) is a function of κ_r and n_c. The parallel-bond radii in the grid are defined by the parallel-bond radii at the node and mid rib ($\bar{R}_n$ and $\bar{R}_m$ along with an exponential variation along each half rib) and the parallel-bond radius multiplier of the join balls $\left(\bar{\lambda}_j\right)$. The material properties of the grid are defined by the local-damping factor, density, effective modulus and stiffness ratio (α_g, ρ_g, E_g^* and κ_g^*). The material properties of the grid-grain interface are defined by the grid-grain effective modulus, stiffness ratio and friction coefficient (E_{gg}^*, κ_{gg}^* and μ_{gg}).[5]

The parallel bonds in the grid are assigned infinite strengths to preclude bond breakage, the parallel-bond stiffnesses are set based on E_g^* and κ_g^*, the parallel-bond radii at each join ball are set based on $\bar{\lambda}_j$ and join-ball diameter, and the parallel-bond radii along each half rib are set via Eq. (6).[6]

The closed-form expressions defining the sizes and locations of the balls and the radii of the parallel bonds are provided in the remainder of this subsection. The balls of a cross element half rib are shown in Figure 6. The half rib consists of one node ball, two join balls, and a string of rib balls,

---

[4] Each cross element is symmetric; thus, there is no differentiation between the transverse (TD) and longitudinal (LD) directions. Such a differentiation was employed by Stahl and te Kamp (2013). The pavement-design package can be modified to account for this by making the TD and LD directions correspond with the *x*- and *y*-directions, and replacing l_r and n_c with $\{l_{rx}, l_{ry}\}$ and $\{n_{cx}, n_{cy}\}$, respectively.

[5] The linear contact model is installed at the grid-grain and grid-grid contacts that may form after grid creation; the stiffnesses and friction coefficient of these contacts are set based on E_{gg}^* and κ_{gg}^*. The linear contact model is also installed at the grid-wall contacts that may form after grid creation; the walls are frictionless, and the normal stiffness of these contacts is set based on the effective modulus of the material vessel. [The linear contact bond model is installed at grid-grain contacts to facilitate visual inspection of the grid-grain contacts via the contact plot item (using Color By: Text Val: model name). The linear contact bond model is unbonded, and thus, its behavior is identical to that of the linear contact model.]

[6] The stiffnesses of the linear component of the linear parallel bond contact model are set to zero such that all load is carried in the bond — i.e., the linear force arising from ball-ball overlap always remains equal to zero.

with the rib balls being divided into core-rib balls, mid-rib balls and a tip-rib ball. The sizes of the core-rib balls satisfy the relation:

$$\tfrac{1}{2}l_r = \tfrac{1}{2}D_n + \sum_{b=1}^{n_c} \alpha^{(b-1)}\kappa_r D_n. \tag{1}$$

This relation is rewritten in the form:

$$f(\alpha) = \frac{D_n - l_r}{2\kappa_r D_n} + \sum_{b=1}^{n_c} \alpha^{(b-1)} = 0. \tag{2}$$

The constant, α, is found by solving the above expression via Newton-Raphson iteration. The diameters and positions of the rib balls are expressed in terms of alpha as follows. The diameters and positions of the core-rib balls:

$$D_c^{(b)} = \alpha^{(b-1)}\kappa_r D_n, \; b \in \{1, 2, \ldots, n_c\}$$
$$s_c^{(b)} = s_c^{(b-1)} + \tfrac{1}{2}D_c^{(b-1)} + \tfrac{1}{2}D_c^{(b)}, \; D_c^{(0)} = D_n, \; s_c^{(0)} = 0, \; b \in \{1, 2, \ldots, n_c\}. \tag{3}$$

The diameters and positions of the mid-rib balls:

$$D_m^{(b)} = \frac{2\alpha}{(1+\alpha)^2}\left(D_c^{(b)} + D_c^{(b+1)}\right), \quad D_m^{(n_c)} = 2D_c^{(n_c)} - D_m^{(n_c-1)}, \quad b \in \{1, 2, \ldots, n_c - 1\}$$
$$s_m^{(b)} = s_c^{(b)} + \tfrac{1}{2}D_c^{(b)}, \; b \in \{1, 2, \ldots, n_c\}. \tag{4}$$
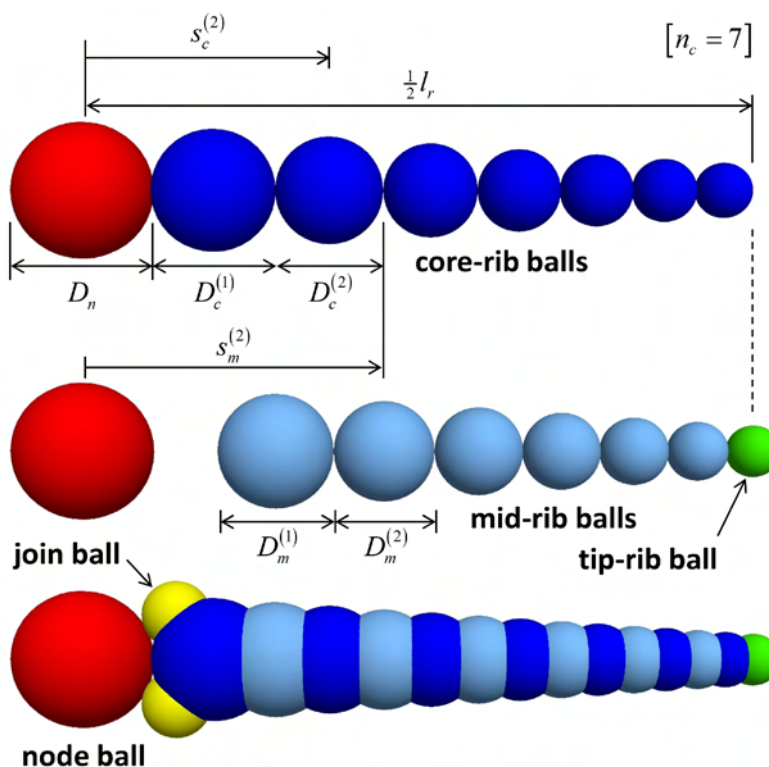
Figure 6   ***Cross element half rib showing node ball, join balls and rib balls.***

There is also a tip-rib ball that lies between adjoining cross elements, and its diameter and position are obtained by treating it as a mid-rib ball. The diameters and positions of the join balls (with reference to Figure 7):

$$D_j = \tfrac{1}{2} D_n$$

$$\beta = \frac{\pi}{4} - \varphi, \quad \varphi = \sin^{-1}\left(\frac{D_j}{D_n + D_j}\right). \tag{5}$$
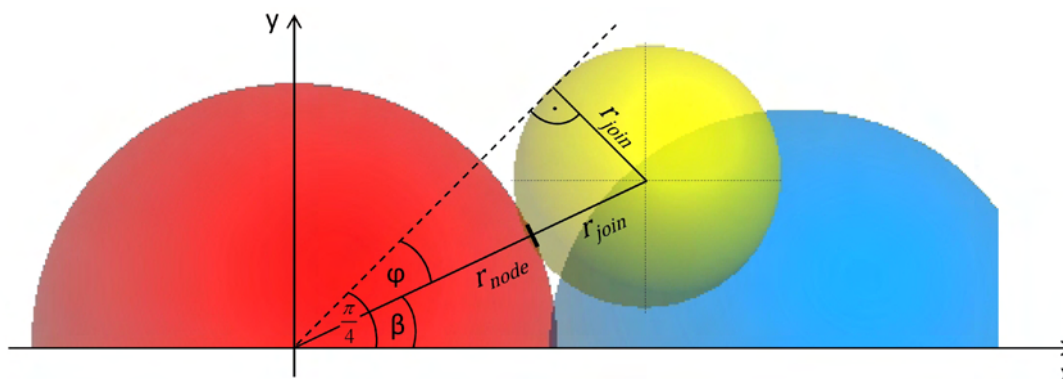
Figure 7   ***Cross element half rib showing location of the top join ball.***

The parallel-bond radii in the geogrid vary exponentially along each half rib (see Figure 8):

$$\bar{R} = ae^{bs}, \quad \tfrac{1}{2}D_n \leq s \leq \tfrac{1}{2}l_r$$

$$\text{with} \quad a = \bar{R}_n \exp\left(\frac{-bD_n}{2}\right) \tag{6}$$

$$b = \ln\left(\frac{\bar{R}_n}{\bar{R}_m}\right)\frac{2}{D_n - l_r}$$

where s is measured from the node-ball center. Each join ball has four parallel bonds joining it to the node ball, the adjacent join ball, and the first two rib balls (see Figure 9).
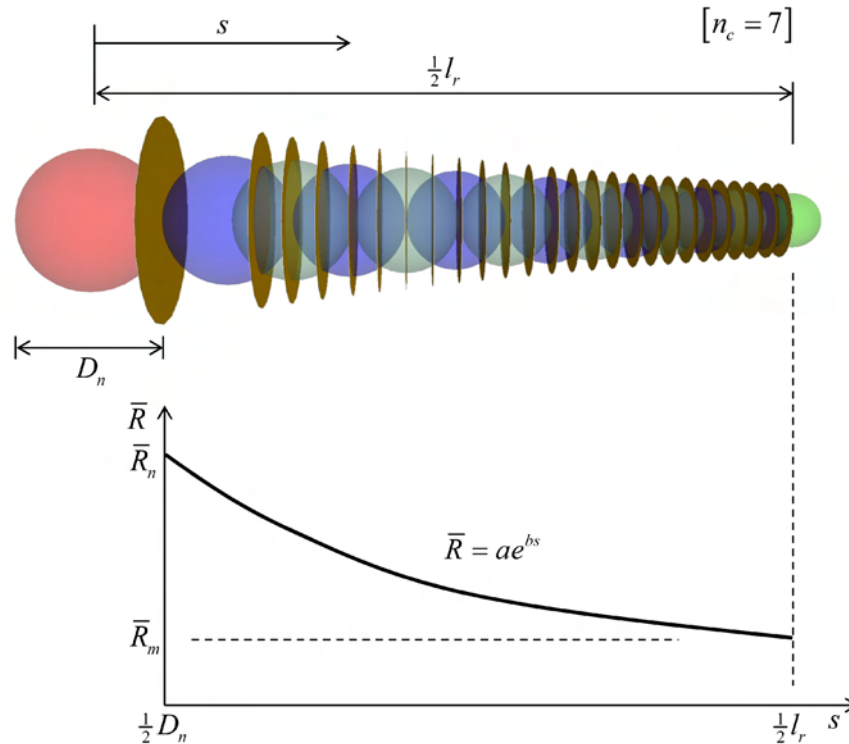
Figure 8   *Cross-element half rib showing variation of parallel-bond radius from node ball to mid rib. Each parallel-bonded interface is drawn as a disk with radius equal to parallel-bond radius.*
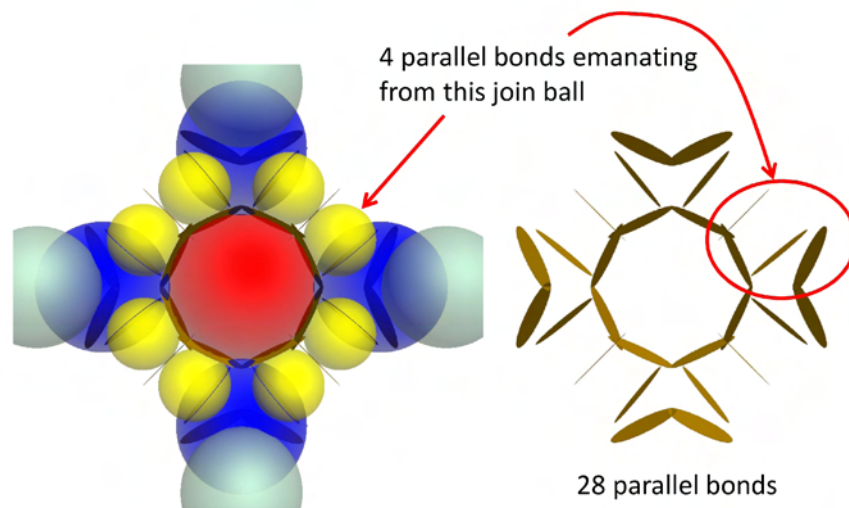
Figure 9   Parallel bonds emanating from the join balls at a cross-element node.

2.2   Grid Calibration: Single Rib Tensile Test

The rib tensile stiffnesses of a biaxial geogrid are measured by performing Single Rib Tensile (SRT) tests in the transverse (TD) and longitudinal (LD) directions. The two ribs emanating from a grid junction and aligned in the desired direction are clamped at the junctions at their ends (as shown in Figure 10). One end is fixed, and a constant velocity is applied to the other end while monitoring the applied displacement and associated force. The displacement is expressed as a strain using the length between clamps as the gauge length. The force-extension curves for a Tensar SS20 biaxial geogrid are shown in Figure 11, in which the black line is the average curve from five laboratory tests. The force-extension behaviors are similar in the TD and LD directions. The force-extension curve is linear for extension of less than three percent, at which point the slope begins to decrease. The slope of the force-extension curve is a measure of stiffness. The stiffness decrease indicates material softening, perhaps as the result of plastic yielding of the material at the rib center. A permanent rib extension would be associated with plastic yielding — it is not known to the author if a permanent rib extension has occurred.
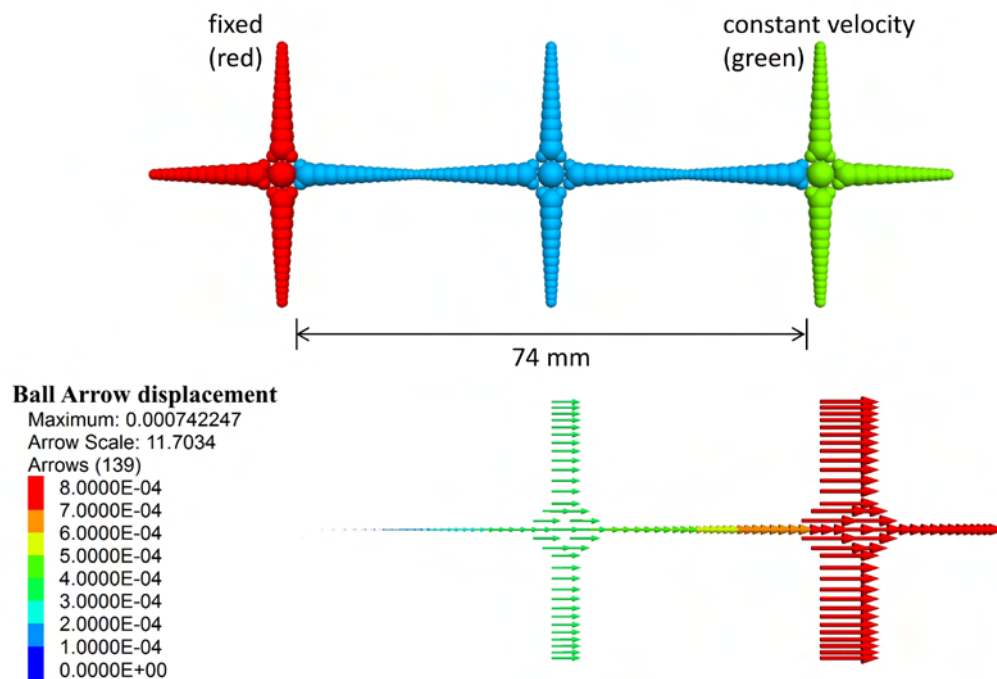
Figure 10 ***The undeformed SS20 grid at the start of the SRT test (above) and the grid displacement field at the end of the SRT test (below).***
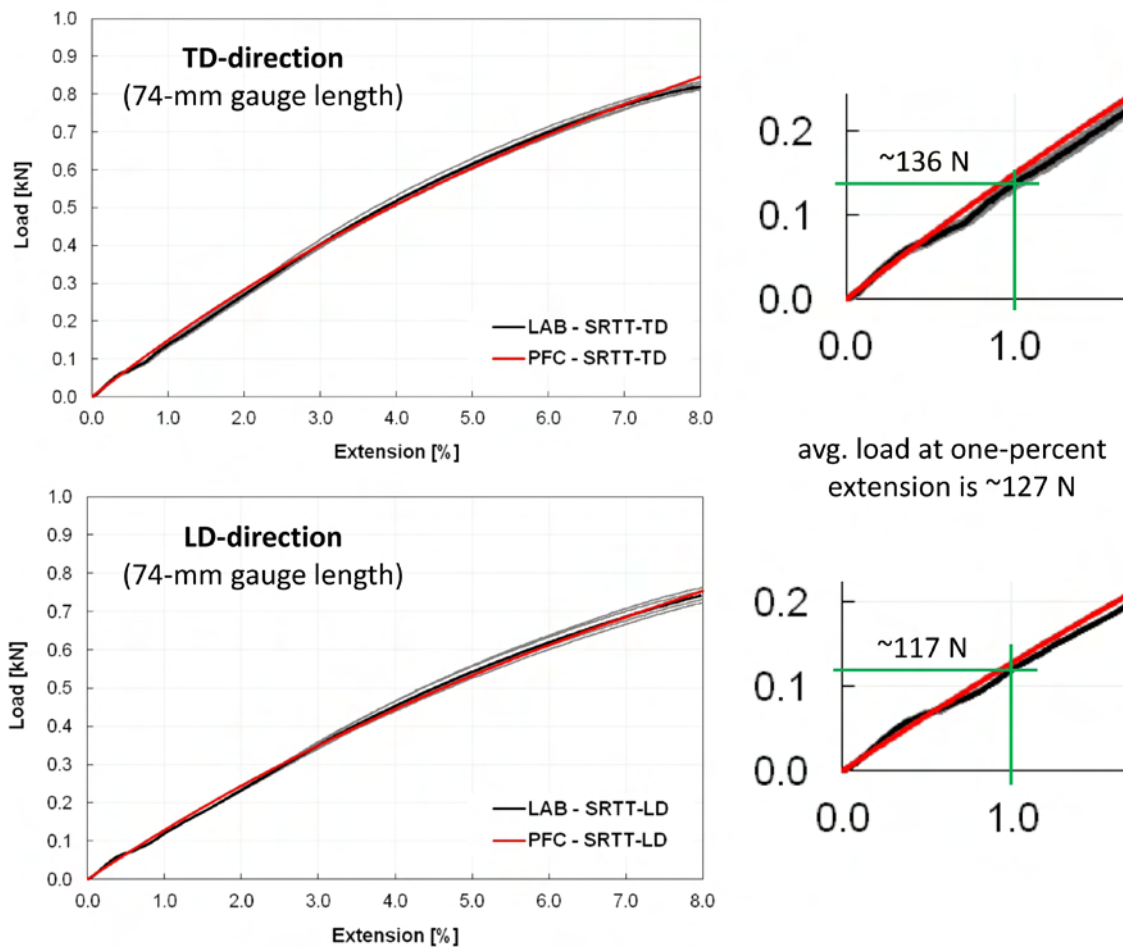
Figure 11   ***Force versus extension for a Tensar SS20 biaxial geogrid loaded in***
the TD and LD directions during SRT tests. (From Figs. 8 and 9 of
Stahl and te Kamp [2013] in which force is denoted as load.)

The Tensar SS20 biaxial geogrid is modeled in the pavement-design example using the grid-set properties in Table 3. The synthetic geogrid is symmetric, with no differentiation between the TD and LD directions; therefore, the grid-set properties are chosen to match the average stiffness for extension less than three percent. The modeled system at the start and end of the SRT test is shown in Figure 10. The applied force is obtained by summing the out-of-balance forces of the balls that are assigned a constant velocity. The force-extension curve for quasi-static loading is shown in Figure 12. The modeled system matches the average force of 127 N at one-percent extension.
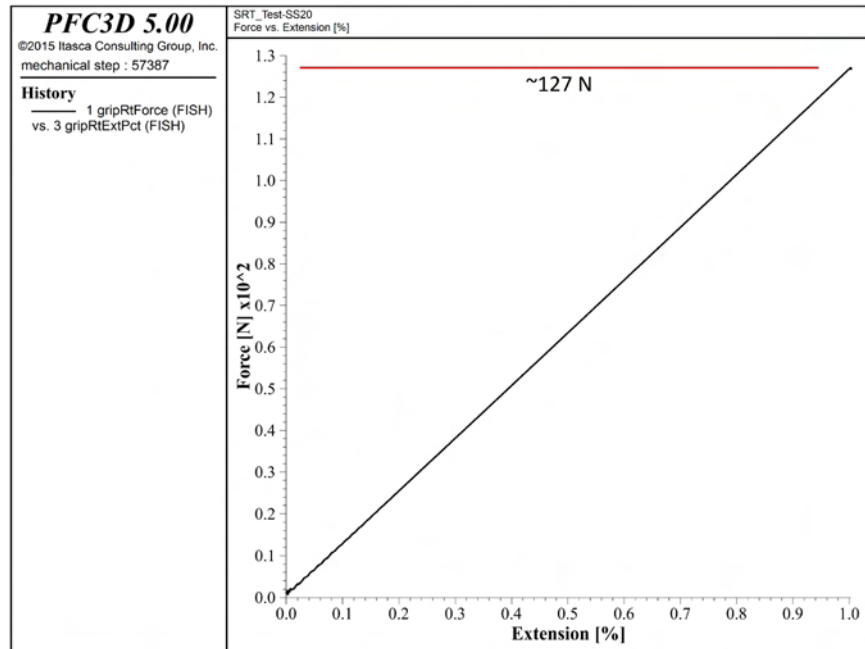
Figure 12 **Force versus extension for the SS20 grid during the SRT test and measurement of force for a one-percent extension.**

2.3   Grid Calibration: Aperture Stability Modulus Test

The junction torsional stiffness of a biaxial geogrid is measured by performing an Aperture Stability Modulus (ASM) test. A grid consisting of six by six apertures is clamped along its boundary as shown in Figure 13. The central junction is subjected to a twisting moment (M_t) by applying a force (F) to each of the four ribs emanating from the junction. The force is applied orthogonal to each rib at a fixed radial distance (r) such that $M_t = 4rF$. The rotation of the central junction (θ_t) is measured. The torsional stiffness of the junction is given by

$$k_t = \frac{M_t}{\theta_t}. \tag{7}$$

The concept of torsional stiffness is embodied in the following structural system. The torsional stiffness of a twisted elastic shaft of length L loaded at its ends by equal and opposite twisting moments is given by Crandall et al. (1978, Eq. 6.10):

$$M_t = k_t\theta_t, \quad k_t = \frac{GJ}{L} \tag{8}$$

where G is the shear modulus, and J is the polar moment of inertia of the cross-sectional area about the axis of the shaft.
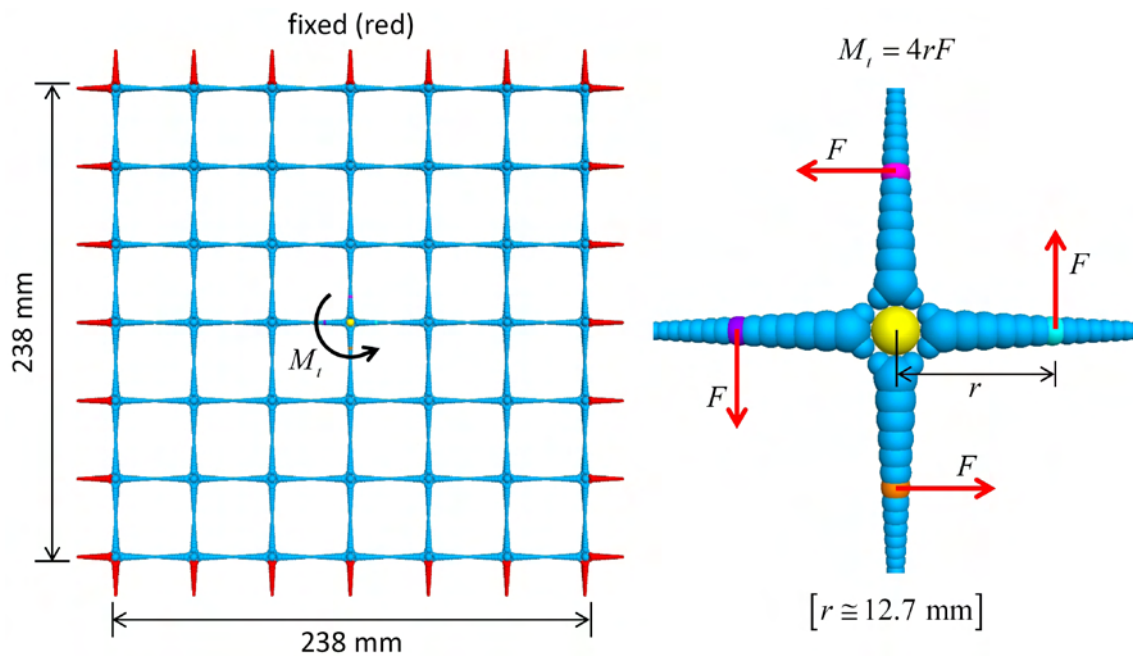
Figure 13   The SS20 grid showing the boundary conditions for the ASM test.

The moment-rotation curve for a Tensar SS20 biaxial geogrid is shown in Figure 14, in which the black line is the average curve from three laboratory tests. The moment-rotation curve is linear for rotation of less than two degrees, at which point the slope begins to increase. The slope of the moment-rotation curve is the torsional stiffness. The torsional stiffness increases with increasing rotation. This is a geometrically nonlinear effect denoted as stress stiffening.[7]

---

[7] The effect whereby the tensile membrane forces in a shell effectively increase the bending stiffness of the shell is called stress stiffening (Cook et al., 1989, p. 429). The tensile forces in the grid are similar to membrane forces in a shell. As the tensile forces in the grid are increased, the bending *and* torsional stiffnesses of the grid increase. The increase in torsional stiffness is described in the following analogous fashion. The geogrid provides a torsional elastic resistance to the deformation induced by the twisting moment, which aids in supporting the moment. The elastic resistance increases with increasing applied rotation.

$$k_t \cong \frac{0.33 \text{ Nm}}{2.0 \text{ deg}} \cong 0.17 \text{ Nm/deg}$$
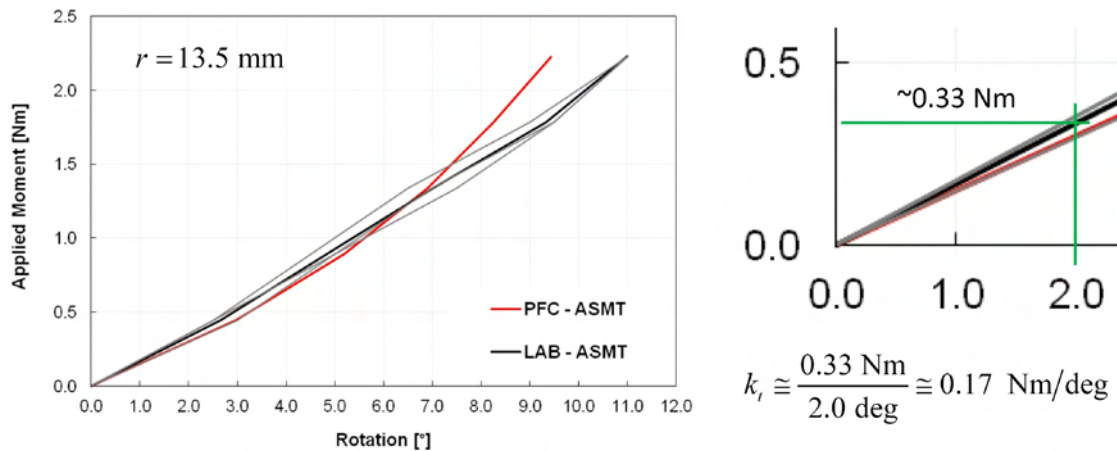
Figure 14   *Moment versus rotation for a Tensar SS20 biaxial geogrid during an ASM test.* (From Fig. 12 of Stahl and te Kamp [2013].)

The Tensar SS20 biaxial geogrid is modeled in the pavement-design example using the grid-set properties of Table 3. The modeled system is shown in Figure 13. A force of 5.9 N is applied to four grid balls, each of which is 12.7 mm from the central junction, such that the twisting moment is 0.30 Nm. Each force remains oriented in its initial global direction throughout the test. The model is run until the state of static equilibrium shown in Figure 15 has been obtained. The rotation is given by

$$\theta = \tan^{-1}\left(\frac{\Delta_y}{r}\right), \quad \text{valid for small-deformation} \tag{9}$$

where Δ_y is the y-displacement of the loaded ball to the right of the central junction. The rotational stiffness is found to be 0.15 Nm/deg, which is 12 percent less than the experimental data. This match is deemed to be sufficient for the purposes of this study. It should be possible to obtain a better match, without sacrificing the match of the rib tensile stiffness, by adjusting the parallel-bond radius multiplier of the join balls ($\overline{\lambda}_j$). Additional runs with applied forces of 20 and 40 N give rotations of 5.9 and 9.5 deg, respectively, and rotational stiffnesses of 0.17 and 0.22 Nm/deg, respectively, which demonstrate that the model is exhibiting a stress-stiffening effect similar to that of the physical grid (see Figure 16).
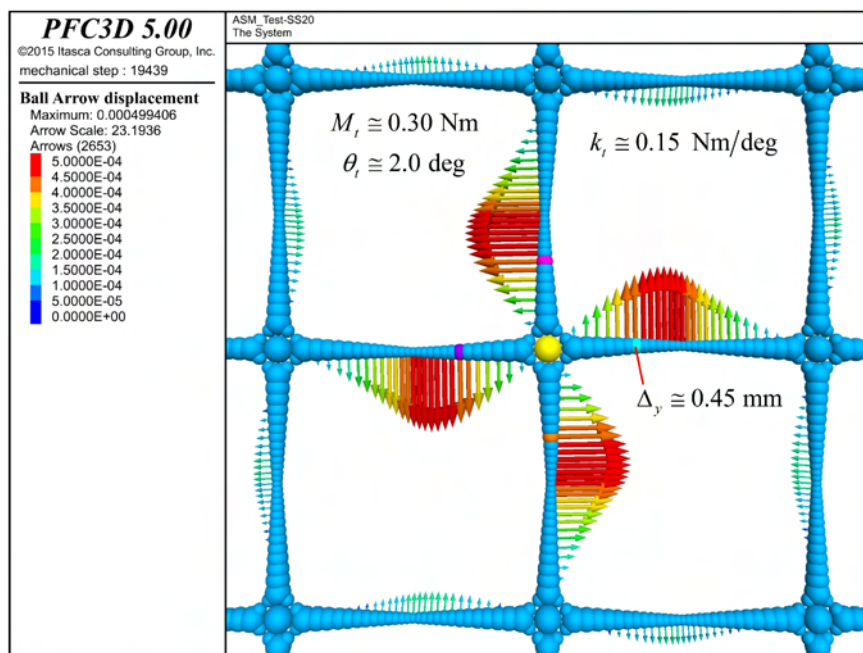
***Figure 15   Deformed grid and displacement field near the central junction of the
SS20 grid at the end of the ASM test with applied moment of 0.30 Nm.***
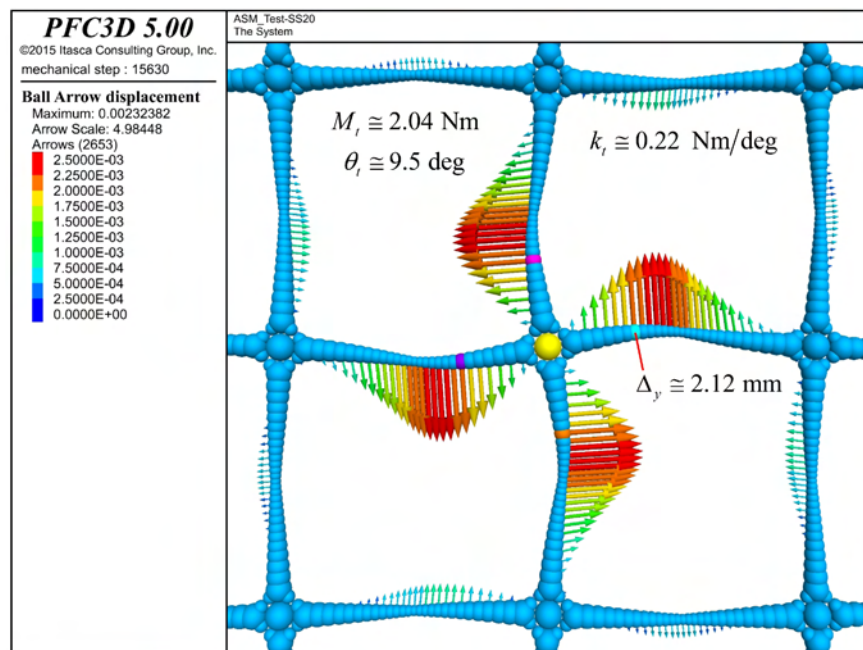
***Figure 16   Deformed grid and displacement field near the central junction of the
SS20 grid at the end of the ASM test with applied moment of 2.04 Nm.***

2.4   Grid-Embedment Procedure

The material-genesis procedure of Potyondy (2016a) is modified to embed a geogrid in a granular material. The procedure occurs within a material vessel (in the form of either a polyaxial or cylindrical cell with frictionless walls) and produces a specimen consisting of a homogeneous, isotropic and well-connected grain assembly at a user-defined material pressure (P_m) with an embedded and well-interlocked grid. The procedure consists of a packing phase followed by a finalization phase. During the packing phase, the grain assembly is subjected to the boundary-contraction packing procedure during which the friction coefficient is set to μ_{CA} — typically chosen as zero to obtain a dense packing. During the finalization phase, the friction coefficient is set to its final value, μ, which is assigned to existing grain-grain contacts and new grain-grain contacts that may form during subsequent motion.

The boundary-contraction packing procedure as modified to support grid embedment consists of the following five steps (see Figure 17).

1. Create the grid set in its initial, undeformed configuration within the material vessel, and constrain the grid by fixing the grid balls so that they cannot translate or rotate. The grid remains constrained during the next three steps, during which the grid does not move or deform while the grains flow around the grid.

2. Generate a cloud of grains with grain-cloud porosity of n_c. The grains are drawn from a specified size distribution, and then placed at arbitrarily chosen positions that lie fully within the material vessel and do not overlap an exclusion region that surrounds each grid. The exclusion region is a thin layer with a normal extent that just touches the node balls; and if the lateral extent exists ($C_e = 0$), then it just touches either the protruding half ribs or the outer node balls. There are large grain-grain overlaps in the grain cloud, but there are no grain-vessel or grain-grid overlaps. Typically, n_c is chosen equal to n_l, where n_l corresponds with the loose state for which grains are just in contact at a mean stress (σ_m) of zero. For a hill material of nearly uniform-sized spheres and no embedded grid, $n_l \cong 0.58$, and this value must be decreased to obtain a material with an embedded grid that has the same number of grains as the material with no embedded grid.

3. Set the friction coefficient to zero, and then allow the grains to rearrange until either the mean stress is near zero or static equilibrium is obtained. This step eliminates the large grain-grain overlaps by allowing the grains to move apart and flow uniformly into the grid apertures from above and below. The material is in an isotropic state at the end of this step.

4. Set the material friction coefficient to μ_{CA}, and then apply confinement by moving the vessel walls under control of a servomechanism until the wall pressures are within the specified tolerance of the material pressure and static equilibrium has been obtained. Setting

$\mu_{CA} = 0$ gives the densest packing, while progressively looser packings are obtained by increasing μ_{CA}. Typically, one sets $\mu_{CA} = 0$ to allow the grains to be compressed uniformly into the grid apertures, and thereby obtain a grid that is well-interlocked with the grain assembly.

5. Remove the grid constraint by freeing the grid balls so that they can translate and rotate. Repeat step 4 on the unconstrained grid to allow the grid to move and deform in response to the compressive forces imposed by the grains.
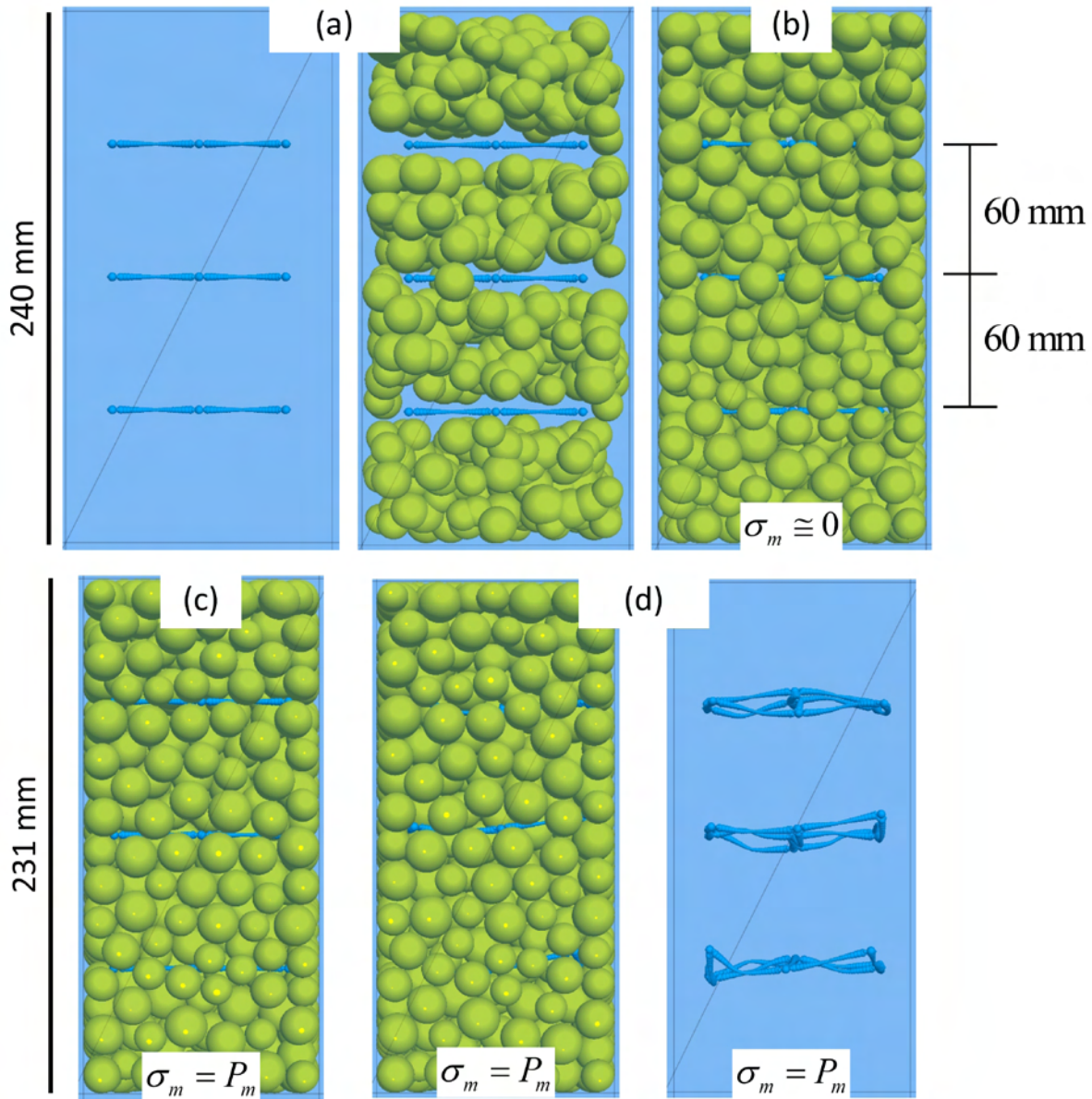
Figure 17   Grid-embedment procedure: (a) constrained grid and initial grain cloud at end of step 2, (b) constrained grid and relaxed grain cloud at end of step 3, (c) constrained grid and compacted granular assembly at end of step 4, and (d) unconstrained and deformed grid at end of step 5. The AG_SS20 model of the simple pavement-design example is shown in non-perspective view.

3.0   PAVEMENT-DESIGN EXAMPLES

There are two pavement-design examples in the **MatGen-HillGrid{-,_C5Q}** example-project directories. The AG example provides a base case at the lowest resolution sufficient to demonstrate system behavior, whereas the C5Q example provides a more realistic case. The AG example models a cuboid with three 2 by 2 grids containing material with a narrow grain-size distribution subjected to simple boundary conditions. The C5Q example models a cuboid with one 6 by 6 grid containing material with a broad grain-size distribution that matches the upper end of the MnDOT Class 5Q material designation subjected to boundary conditions typical of an aggregate base layer.

3.1   Simple Example

The simple pavement-design example is in the **MatGen-HillGrid** example-project directory. The example serves as a base case, and provides materials at the lowest resolution sufficient to demonstrate system behavior. Two instances of a hill material with a narrow grain-size distribution of grain diameters uniformly distributed from 14 to 20 mm are created.[8] The first instance is denoted as the AG material, and the second instance has three flat Tensar SS20 biaxial geogrids embedded within it (centered within the material vessel and oriented perpendicular to the specimen axis with a 60-mm spacing) and is denoted as the AG_SS20 material (see Figures 18 to 20). The material microproperties are listed in Table 2, and the grid-set properties are listed in Table 3. The materials are dry while being created in a polyaxial material vessel (of initial 240-mm height and 120-mm width and depth, with a 500 MPa effective modulus) and packed at a 1 MPa material pressure as shown in Figure 18.

Table 2   Microproperties of AG Materials*

Property	Value
Common group:	
N_m	$\{AG, AG\_SS20\}$
$\{T_m, N_{cm}\},\ \alpha,\ C_\rho,\ \rho_v\left[kg/m^3\right]$	$\{4, hill\},\ 0.7,\ 0,\ 2650$
$S_g,\ T_{SD},\ \{D_{\{l,u\}}[mm], \phi\},\ D_{mult}$	$0,\ 0,\ \{14, 20, 1.0\},\ 1.0$
Packing group:	
$S_{RN},\ P_m[kPa],\ \varepsilon_P,\ \varepsilon_{lim},\ n_{lim}$	$10001,\ 1000,\ 1\times10^{-2},\ 8\times10^{-3},\ 2\times10^6$
$C_p,\ n_c,\ \mu_{CA},\ v_{lim}[m/s]$	$0,\ \{0.58, 0.427\},^1\ 0,^2\ 1.0$
Hill material group:	

---

[8] A hill material is defined as a granular assembly in which the hill contact model exists at all grain-grain contacts. The hill material behaves like an unsaturated granular material, and the grain-grain system behaves like two elastic spheres that may have a liquid bridge — refer to Potyondy (2016b) for a comprehensive description of the model.

$E_g\,[\text{GPa}],\ \nu_g,\ \mu,\ \alpha_h,\ \psi\,[\text{kPa}]$	29, 0.15, 0.4, 0, 0

* Hill material parameters are defined in Table 2 of Potyondy (2016b).

[1] The cloud porosity for the AG_SS20 material is decreased so that this material has a similar number of grains as the AG material.

[2] The friction coefficient during confinement application is zero to obtain a dense packing.

Table 3 Grid Set Properties of SS20 Grids*

Property	Value
Grid set group:	
$n_g,\ s_z\,[\text{mm}],\ \{n_x, n_y\},\ \mathbf{c}\,[\text{mm}],\ C_t$	$\left\{\begin{array}{l} \left[3,\ 60.0,\ \{3,3\},\ (-39.0,-39.0,-60.0),\ 0\right],\ \text{AG} \\ \left[1,\ \text{NA},\ \{6,6\},\ (-97.5,-97.5,0),\ 0\right],\ \text{C5} \end{array}\right.$
$D_n\,[\text{mm}],\ \kappa_r,\ l_r\,[\text{mm}],\ n_c$	4.0, 0.9, 39.0, 7
$\bar{R}_n\,[\text{mm}],\ \bar{R}_m\,[\text{mm}],\ \bar{\lambda}_j,\ C_e$	$2.9,\ 1.0,\ 1.0,\ \left\{\begin{array}{l} 0,\ \text{AG} \\ 1,\ \text{C5} \end{array}\right.$
Material properties group:	
$\alpha_g,\ \rho_g\,\left[\text{kg/m}^3\right],\ E_g^*\,[\text{MPa}],\ \kappa_g^*$	0.7, 950, 700,[1] 2.0
$E_{gg}^*\,[\text{MPa}],\ \kappa_{gg}^*,\ \mu_{gg}$	500, 2.0, 0.5

* Grid-set parameters are defined in Table 1.

[1] SS20 properties in Stahl and te Kamp (2013) are 770 and 630 MPa in the TD and LD directions, respectively.

The aggregate properties are summarized as follows. There are approximately 550 granite grains modeled as spheres drawn from a narrow grain-size distribution, with grain diameters uniformly distributed from 14 to 20 mm. The grain density is $2650\ \text{kg/m}^3$. The Young's modulus and Poisson's ratio of the grains are 29 GPa and 0.15, respectively. The friction coefficient is 0.4. The suction is zero, because the material is dry. The damping constant is zero, because quasi-static conditions are enforced via local damping, with a local-damping factor of 0.7.

The grid material properties were taken from Stahl and te Kamp (2013). The grid density is $950\ \text{kg/m}^3$, which is similar to the $946\ \text{kg/m}^3$ for polypropylene (Wikipedia, 2015a). The grid effective modulus is $700\ \text{MPa}$, which is approximately one-half of the $1.5-2.0\ \text{GPa}$ for

polypropylene (Wikipedia, 2015b).[9] The grid stiffness ratio is two. The structural properties of the grid (quantified by the rib tensile stiffness and the junction torsional stiffness) match those of a Tensar SS20 biaxial geogrid. The material properties of the grid-grain interface were chosen as follows. The grid-grain effective modulus should be large enough to prevent excessive grid-grain overlap, and the value was set equal to that of the material vessel. The grid-grain stiffness ratio was set equal to the grid stiffness ratio. The grid-grain friction coefficient was set to 0.5.

The two materials at the end of material genesis are shown in Figures 18 and 19, and the configuration of a grid layer is shown in Figure 20. Both materials have approximately 550 spherical grains, with grain diameters uniformly distributed from 14 to 20 mm. The 17.0 mm average grain diameter gives a vessel resolution (number of grains across the smallest vessel dimension) of 7.1. The AG_SS20 material has a grid resolution (number of grains across a grid aperture) of 2.3. Both materials are dry, packed at a 1.0 MPa material pressure, and have a porosity of 0.379. Both materials have approximately the same number of dry hill contacts (1362 and 1328 for the AG and AG_SS20 materials, respectively), while the AG_SS20 material has an additional 2388 internal grid contacts and 421 grid-grain contacts. The internal grid contacts join the 1143 grid balls to one another via parallel bonds (denoted as grid bonds in Figure 20).

We confirm that the materials form well-connected grain assemblies at the 1 MPa material pressure by plotting the mean stress and noting that the measurement-based value has reached the wall-based value, which is equal to the 1 MPa material pressure (see Figure 21). The material with the embedded grid requires more cycles to achieve this state, and the measurement-based mean stress lags behind the wall-based value. The vessel walls move inwards relatively fast under the control of a servomechanism such that a portion of the wall-based load is an inertial load caused by accelerating the particles. Additional cycles must occur to allow the loading acting on the material boundary to propagate into the material and cause it to contract inwards. This inertial effect becomes more pronounced for models with more particles.[10]

---

[9] Our value is approximately one-half that of the physical material because of the extensive parallel-bond overlinking, whereby as one proceeds along a rib, each rib ball is joined to the next two rib balls. The overlinking is removed by removing the mid-rib and tip-rib balls, and the structural properties of such a grid match those of a Tensar SS20 biaxial geogrid by setting the grid effective modulus to 1.7 GPa.
[10] The computational time could be reduced by employing the stress-installation procedure of Potyondy (2016a).
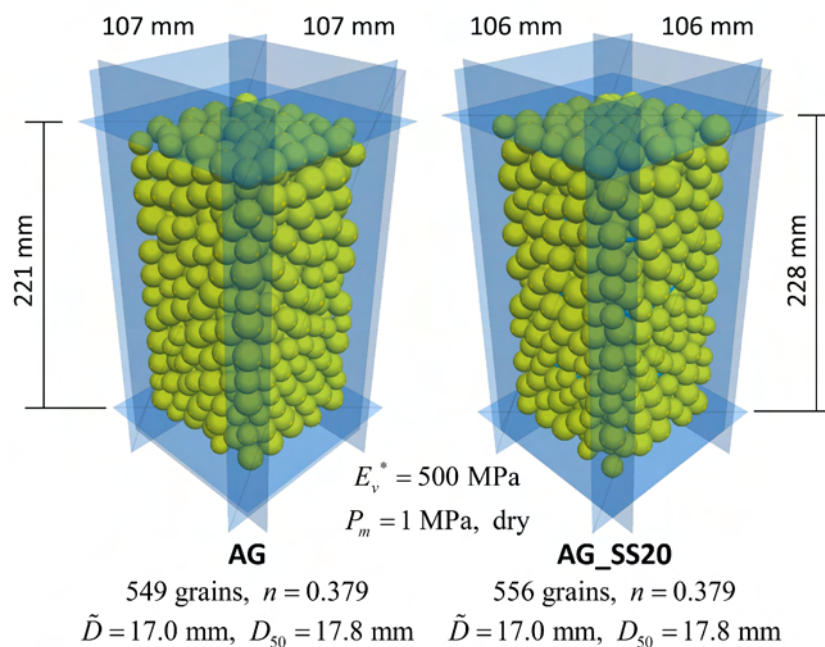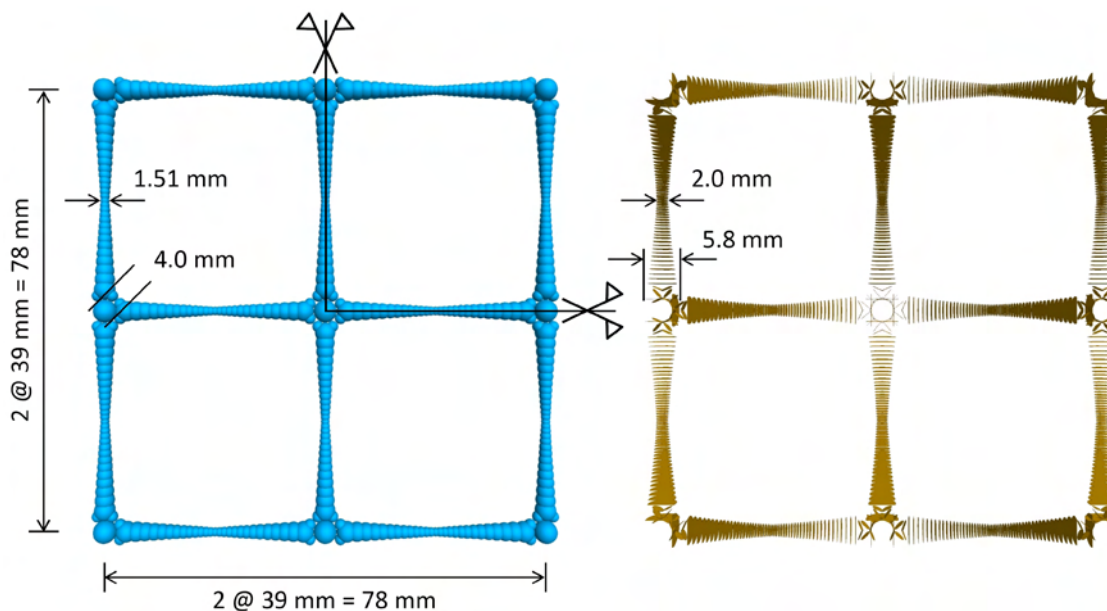
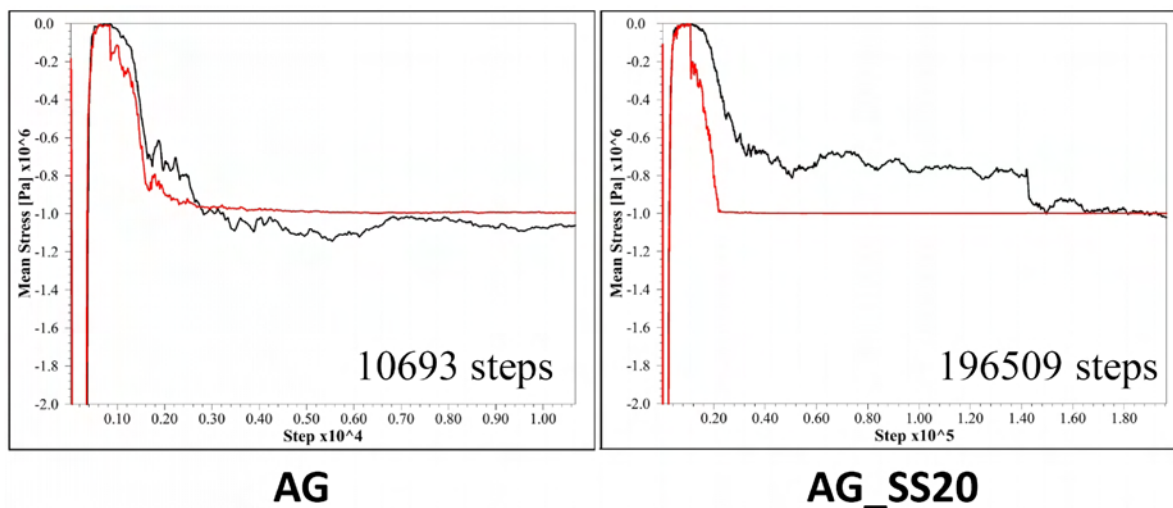*Figure 18   Dry AG and AG_SS20 materials at the end of material genesis.*
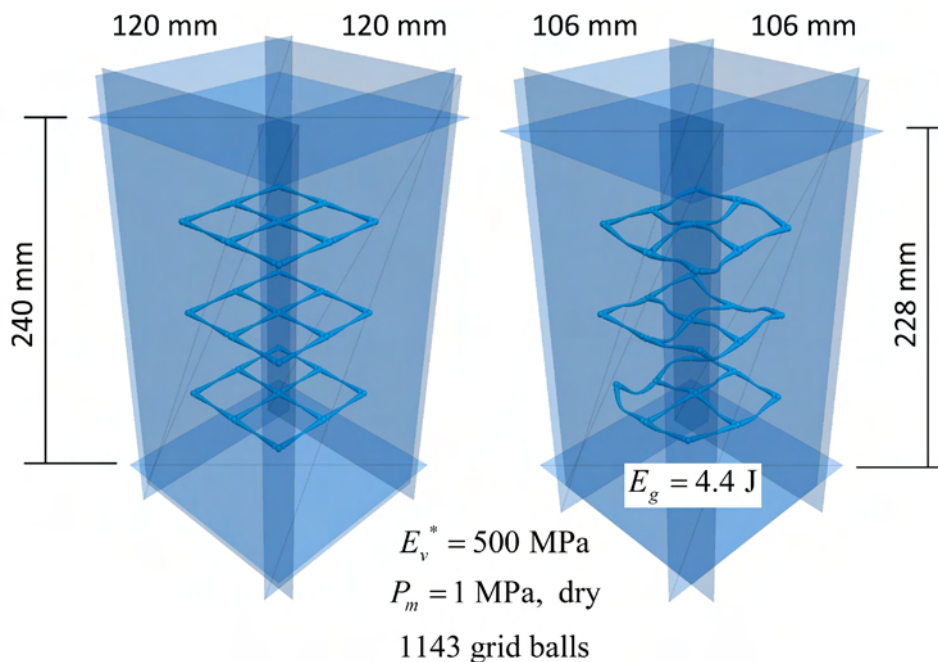
Figure 19   The embedded grid set in the AG_SS20 material in the polyaxial vessel at the start (left image) and end (right image) of material genesis.

Figure 20　　***The undeformed configuration of a grid layer in the AG_SS20 material showing grid balls (left image) and grid bonds (right image).***


Figure 21　　***Mean stress acting on the boundary (red) and within the material (black) versus step for the AG and AG_SS20 materials during material genesis.***

The macroscopically applied compressive load is carried by the granular material as force chains that propagate from one grain to the next across grain-grain contacts. The force-chain fabric is depicted as a network of cylinders, with a cylinder at each contact. Force magnitude corresponds with cylinder thickness and color, and force direction corresponds with cylinder orientation. An examination of the force-chain fabric at the end of material genesis reveals the following material characteristics. Both materials have a similar force-chain fabric, with maximum forces of approximately 2000 N (see Figure 22). The middle grid in the AG_SS20 material is being compressed by the grains with a maximum force of 250 N, and its front-most aperture is being loaded in tension (see Figure 23). The compressive forces acting on the grids cause them to deform, and the total strain energy stored in the three grids is 4.4 Joules (see Figure 19). If the grains were removed, and the model cycled to a new state of static equilibrium, the grids would return to their undeformed configurations.
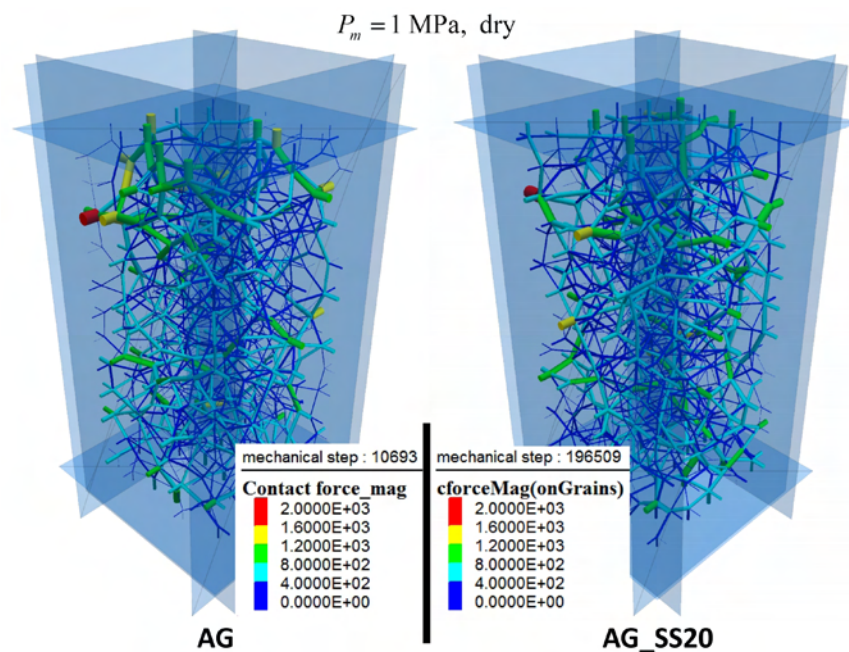
Figure 22 *Force-chain fabric in the AG and AG_SS20 materials in the polyaxial vessel at the end of material genesis.*
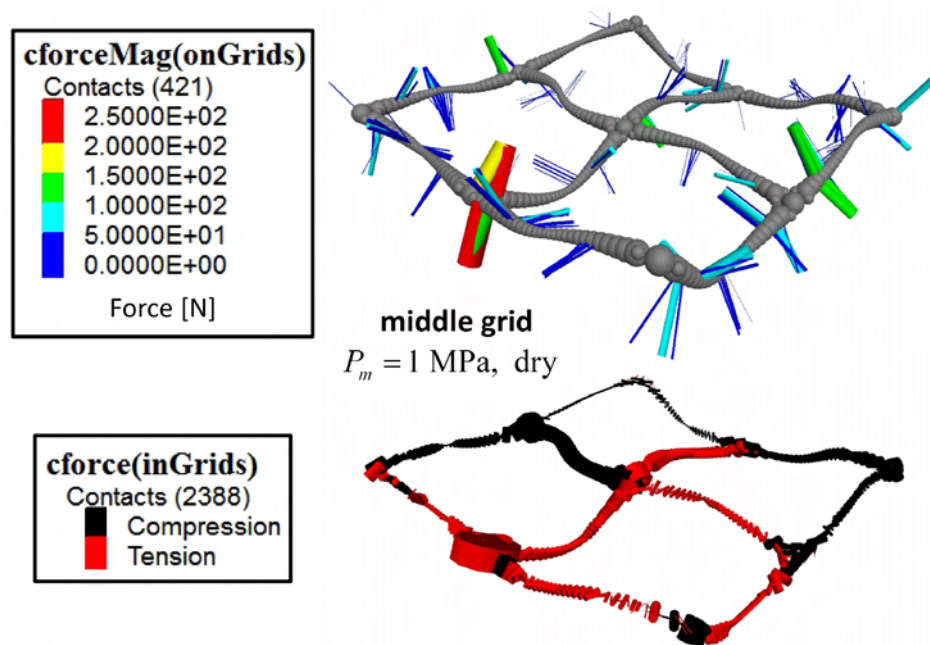
***Figure 23   Forces acting on and in the middle grid in the AG_SS20 material in
the polyaxial vessel at the end of material genesis.***

The AG materials are subjected to triaxial testing. The materials are tested dry and wet. The wet material has a 20 kPa suction added between all grains that are within 3 mm of one another at the end of material genesis. During each triaxial test, the confinement is 1 MPa, and a load-unload cycle is performed at an axial strain of one percent to produce the deformation fields shown in Figure 24, and the stress-strain curves in Figures 25 and 26. The response is hysteretic. The grid and moisture both increase the material strength (measured as the deviator stress at one percent axial strain). The grid delays the onset of material dilation. The resilient modulus of the dry AG material with no grid is measured as 239 MPa in Figure 27, and the resilient moduli for the other cases are similar. The grid has a negligible effect on the resilient modulus of this simple system, but the grid increases the resilient modulus of the more realistic system examined in the next section.[11]

---

[11] A demonstration of the confining effect of the grid could be obtained by performing a cyclic triaxial test similar to the one described in Section 3.2 of McDowell et al. (2006), and examining the force chains after partial unloading. The cyclic triaxial test has 10-kPa confinement. Deviator stress is cycled 10–20 kPa (3 times), 10–30 kPa (three times), and then 10–40 kPa (three times). The partial unloading consists of reducing the confinement to 5 kPa.
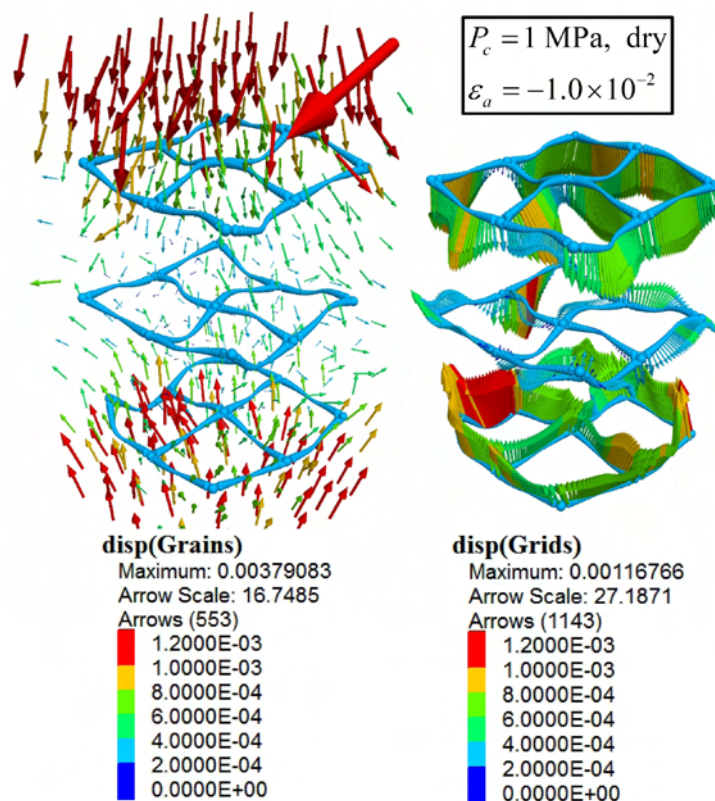
Figure 24 ***Displacement fields of the dry AG_SS20 material (left) and grid (right) after application of one percent axial strain. The top and bottom grids flow with the material and move toward one another. There is very little radial expansion to be resisted by the grids. The walls of the polyaxial vessel are not shown in these images.***
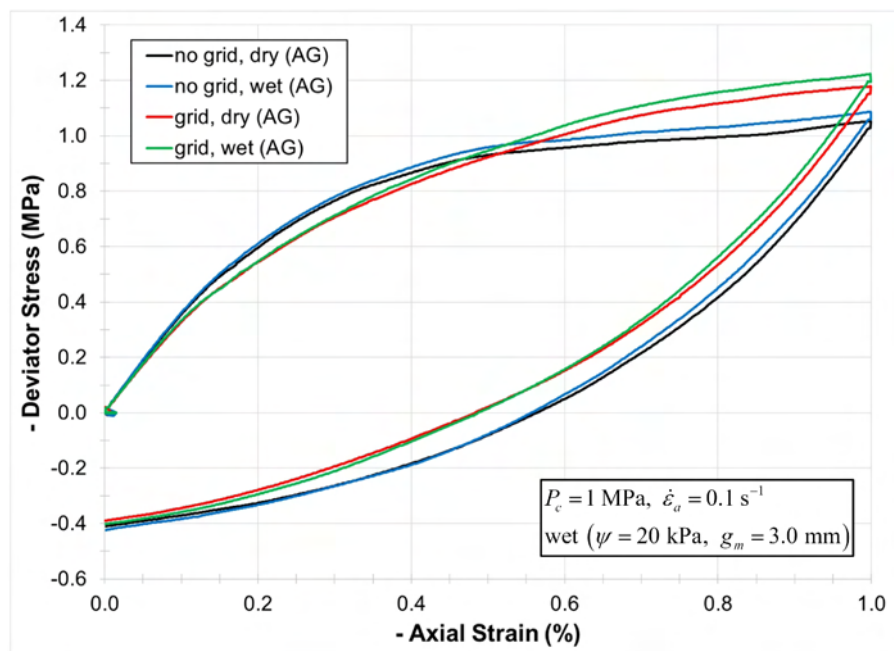
Figure 25   *Deviator stress versus axial strain for dry and wet AG and AG_SS20 materials tested at 1 MPa confinement.*
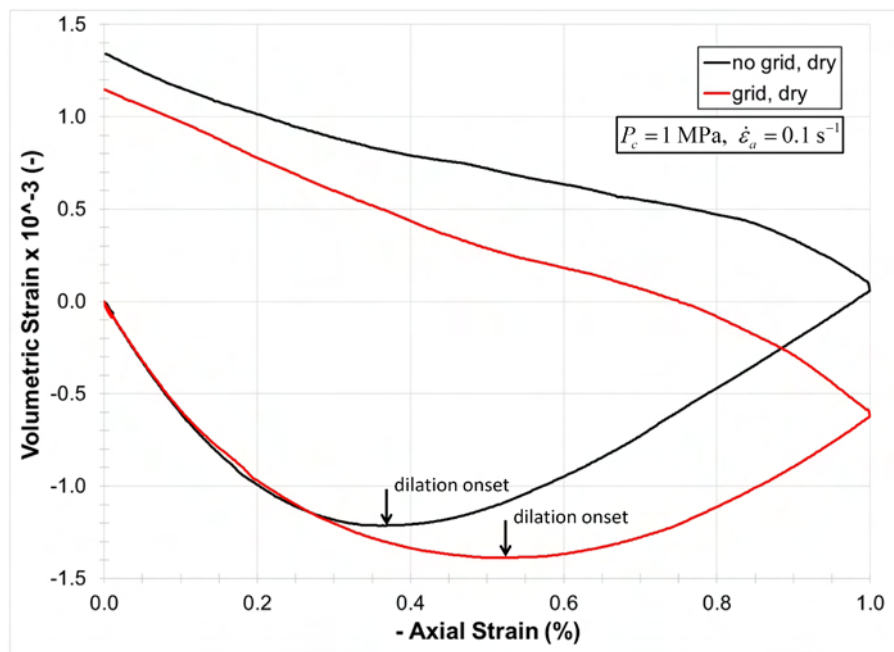
Figure 26   *Volumetric strain versus axial strain for dry AG and AG_SS20 materials tested at 1 MPa confinement, and dilation onset.*
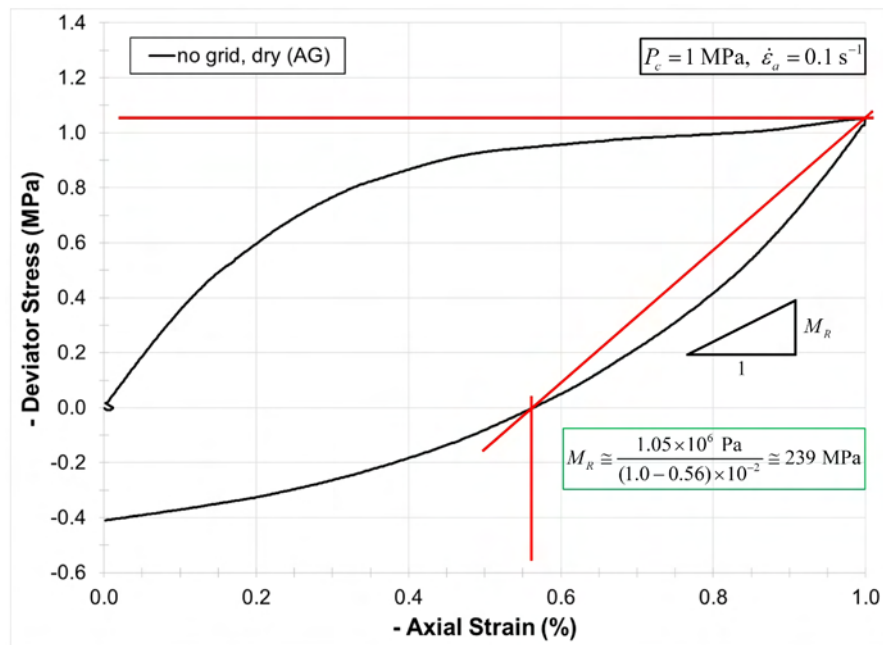
Figure 27   *Deviator stress versus axial strain for dry AG material tested at 1 MPa confinement, and resilient modulus.*

3.2   Realistic Example

The realistic pavement-design example is in the **MatGen-HillGrid_C5Q** example-project directory. Two instances of a hill material are created to represent the aggregate base layer of an asphalt-surface roadway (Potyondy et al., 2016; Siekmeier et al., 2016). The grain-size distribution lies within the upper end of the MnDOT Class 5Q aggregate base grading designation (see Figure 28). The first instance is denoted as the C5Q material, and the second instance has one flat Tensar SS20 biaxial geogrid embedded within it (centered within the material vessel and oriented perpendicular to the specimen axis) and is denoted as the C5Q_SS20 material (see Figure 29).
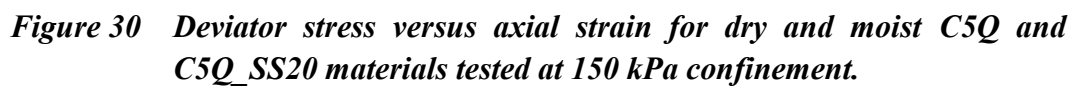
The C5Q materials are subjected to triaxial testing. The materials are tested dry and moist. The moist material has a 30 kPa suction added between all grains that are within 3 mm of one another at the end of material genesis.[12] During each triaxial test, the confinement is 150 kPa, and a load-unload cycle is performed at an axial strain of 0.02% to measure the resilient moduli of the dry and moist materials (see Figure 30).[13]

---

[12] The suction is typical for aggregates with gravimetric moisture content ranging from 5 to 10 percent.

[13] The confinement is similar to that defined in resilient modulus laboratory protocols, and axial strains correspond with vertical strains in the aggregate base layer for typical traffic loads.
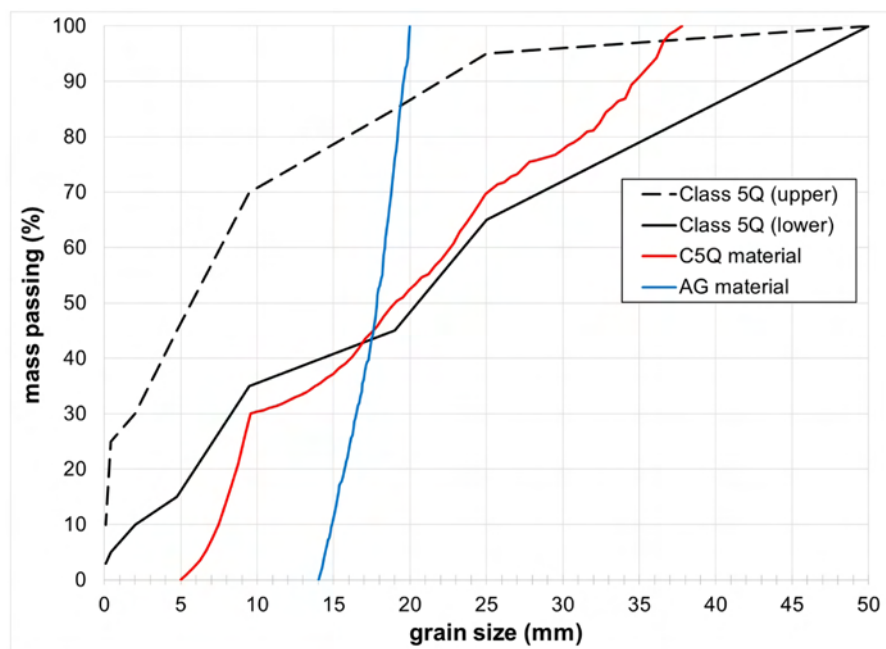
Figure 28 ***Grain size distribution curves for the C5Q and AG materials along with the limits of the MnDOT Class 5Q aggregate base grading designation.*** (Class 5Q limits from MnDOT (2016), Table 3138-3: Base and Surfacing Aggregate [containing less than 25 percent recycled aggregates].)

$n_c = 0.420, \ \mu_{CA} = 0$ $n_c = 0.376, \ \mu_{CA} = 0$

254 ➔ 241 mm   254 ➔ 241 mm   254 ➔ 238 mm   254 ➔ 238 mm

204 ➔ 190 mm $\mu = 0.4$ $E_g = 0.44$ J   204 ➔ 181 mm

$\varepsilon_{lim} = 8 \times 10^{-3}$

$P_m = 150$ kPa, dry $P_m = 150$ kPa, dry

C5Q   **C5Q_SS20**

11851 grains, $n = 0.284$ 11857 grains, $n = 0.290$

$\tilde{D} = 8.4$ mm, $D_{50} = 19.0$ mm $\tilde{D} = 8.3$ mm, $D_{50} = 18.0$ mm

Figure 29   *C5Q material and embedded grid set in the C5Q_SS20 material at the end of material genesis.*

$P_c = 150$ kPa, $\dot{\varepsilon}_a = 0.01$ s^{-1}

moist $\left(\psi = 30 \text{ kPa}, \ g_m = 3.0 \text{ mm} \right)$

C5Q : $\mu = 0.4, \ \mu_{CA} = 0$
C5Qf : $\mu = 0.4, \ \mu_{CA} = 0.4$

$M_R \cong 386$ MPa

$M_R \cong 332$ MPa $n = 0.284$, no grid

$M_R \cong 323$ MPa $n = 0.290$, grid

$M_R \cong 97$ MPa $n = 0.318$, no grid

$M_R \cong 92$ MPa $n = 0.341$, grid

Legend:
- C5Q, dry
- C5Q, moist
- C5Q_SS20, dry
- C5Q_SS20, moist
- C5Qf, dry
- C5Qf_SS20, dry

Figure 30   *Deviator stress versus axial strain for dry and moist C5Q and C5Q_SS20 materials tested at 150 kPa confinement.*

Adding moisture stiffens the material for both the no-grid and grid cases (increasing the resilient modulus from approximately 332 MPa to 386 MPa); however, the material stiffness is the same for the no-grid and grid cases. Why is this, and is this a general conclusion? Additional study has demonstrated that there is a general relationship between resilient modulus and material porosity, with resilient modulus decreasing as porosity increases from 0.28 to 0.35. By varying μ_{CA} from zero to the true material friction coefficient, two distinct curves are obtained, one for the no-grid model and the other for the grid model, with the no-grid curve lying beneath the grid curve. When μ_{CA} is non-zero, the material porosity of the no-grid specimen is less than that of the grid specimen. We speculate that the grid is inhibiting the packing process, forming a local region that is more porous than the surrounding region, and thereby increasing the overall material porosity.[14] The porosities of 0.284 and 0.290 for the present case are the lowest porosities that one can obtain for this material, because the friction coefficient has been set to zero $(\mu_{CA} = 0)$ during packing. For this case, the resilient moduli for the no-grid and grid models are approximately equal. The effect of the grid on material stiffness is found by comparing the resilient moduli for the no-grid and grid cases at the same material porosity. When this is done, we find that the presence of the grid increases the resilient modulus by factors ranging from 1.0 to approximately 2.5 depending on confinement and moisture conditions. The additional study will be presented in a subsequent version of this memo.

---

[14] The material porosity is obtained as the average value from three spherical measurement regions placed symmetrically along the axis of the largest vessel dimension (see section "Stress, Strain and Porosity in the Material" in Potyondy [2016a]).

4.0   REFERENCES

Bagshaw, S.A., P.R. Herrington, P. Kathirgamanathan and S.R. Cook. (2015) "Geosynthetics in Basecourse Reinforcement," Opus International Consultants Ltd., Report to NZ Transport Agency, Wellington, New Zealand, NZ Transport Agency Research Report 574, September 2015.

Buchanan, S. (2007) "Resilient Modulus: What, Why, and How?" Vulcan Materials Company, August 31, 2007. Document `2-Resilient-Modulus-Buchanan.pdf` accessed from www.vulcaninnovations.com/public/pdf on November 6, 2015

Chen, C., G.R. McDowell and N.H. Thom. (2013) "A Study of Geogrid-Reinforced Ballast using Laboratory Pull-Out Tests and Discrete Element Modelling," *Geomechanics and Geoengineering*, *8*(4), 244–253.

Clyne, T. (2001) "Monitoring Geosynthetics in Local Roadways 10-Year Performance Summary," Minnesota Department of Transportation, Saint Paul, MN, 2001.

Cook, R.D., D.S. Malkus and M.E. Plesha. (1989) *Concepts and Applications of Finite Element Analysis*, Third Edition, New York: John Wiley & Sons.

Crandall, S.H., N.C. Dahl and T.J. Lardner. (1978) *An Introduction to the Mechanics of Solids*, Second Edition, New York: McGraw-Hill Book Company.

Han, Z., and S.K. Vanapalli. (2016) "State-of-the-Art: Prediction of Resilient Modulus of Unsaturated Subgrade Soils," *Int. J. Geomechanics*, 10.1061/(ASCE)GM.1943-5622.0000631, 04015104.

Itasca Consulting Group, Inc. (2016) *PFC — Particle Flow Code in 2 and 3 Dimensions*, Version 5.0, Documentation Set of version 5.00.24 [May 8, 2016]. Minneapolis: Itasca.

Jas. H., M. Stahl, H. Konietzky, L. te Kamp and T. Oliver. (2015a) "Discrete Element Simulation of Geogrid Stabilized Sub-Base: Modelling and Calibration and Plate Load Simulation under Special Consideration of Important Boundary Conditions," to appear in *Sixth Symposium on Deformation Characteristics of Geomaterials* (Buenos Aires, Argentina, November 2015).

Jas. H., M. Stahl, H. Konietzky, L. te Kamp and T. Oliver. (2015b) "Discrete Element Modeling of a Trafficked Sub-Base Stabilized with Biaxial and Multi-Axial Geogrids to Compare Stabilization Mechanisms," *Proc. Geosynthetics 2015* (Portland, OR, February 15–18, 2015), pp. 245–254.

Konietzky, H., L. te Kamp, T. Groeger and C. Jenner. (2004) "Use of DEM to Model the Interlocking Effect of Geogrids under Static and Cyclic Loading," *Numerical Modeling in*

Micromechanics via Particle Methods, pp. 3–11, Y. Shimizu, R. Hart and P. Cundall, Eds., Taylor & Francis Group, London.

McDowell, G.R., O. Harireche, M. Konietzky, S.F. Brown and N.H. Thom. (2006) "Discrete Element Modelling of Geogrid-Reinforced Aggregates," *Proceeding of the Institution of Civil Engineers — Geotechnical Engineering*, **159**(1), 35–48.

Minnesota Department of Transportation, MnDOT. (2016) ***Standard Specifications for Construction***, 2016 Edition, Minnesota Dept. of Transportation, Saint Paul, MN.

Potyondy, D. (2016a) "Material-Modeling Support in PFC [fistPkg23]," Itasca Consulting Group, Inc., Technical Memorandum ICG7766-L (June 23, 2016), Minneapolis, Minnesota.

Potyondy, D. (2016b) "Hill Contact Model [version 4]," Itasca Consulting Group, Inc., Technical Memorandum ICG7795-L (June 23, 2016), Minneapolis, Minnesota.

Potyondy, D. O. (2015) "The Bonded-Particle Model as a Tool for Rock Mechanics Research and Application: Current Trends and Future Directions," *Geosystem Engineering, 18*(1), 1–28.

Potyondy, D., J. Siekmeier and L. Petersen. (2016) "Aggregate-Geogrid Interaction Model Incorporating Moisture Effects," in Transportation Research Board 2016 Annual Meeting Compendium of Papers.

Qian, Y., D. Mishra, E. Tutumluer and H.A. Kazmee. (2015) "Characterization of Geogrid Reinforced Ballast Behavior at Different Levels of Degradation through Triaxial Shear Strength Test and Discrete Element Modeling," *Geotextiles and Geomembranes*, **43**(5), 393–402.

Siekmeier, J., J. Bittmann, D. Potyondy and L. Petersen. (2016) "Introducing a Geogrid Gain Factor for Flexible Pavement Design," in *Proceedings University of Minnesota 64th Annual Geotechnical Engineering Conference* (Saint Paul, MN, March 4, 2016).

Skallman, J. (2010) "Geogrids (Multiaxial) on CSAH and MSAS Routes — General Specification, Granular Equivalent (G.E.) and Design Guidelines," Minnesota Dept. of Transportation, Saint Paul, MN, Tech. Memo. 10-SA-03, December 21, 2010.

Stahl, M. (2011) "Interaktion Geogitter-Boden: Numerische Simulation und Experimentelle Analyse," Ph.D. Thesis, Technische Universität Bergakademie Freiberg, Germany, Heft 2011-5 (in German).

Stahl, M., and H. Konietzky. (2011) "Discrete Element Simulation of Ballast and Gravel under Special Consideration of Grain-Shape, Grain-Size and Relative Density," *Granular Matter*, **13**, 417–428.

Stahl, M., H. Konietzkey, L. te Kamp and H. Jas. (2014) "Discrete Element Simulation of Geogrid-Stabilised Soil," *Acta Geotechnica*, **9**, 1073–1084.

Stahl, M., and L. te Kamp. (2013) "Project 13008: Geogrid Modelling with PFC3D — Generation and Calibration of Biaxial Geogrid SS20," Itasca Consultants GmbH, Gelsenkirchen, Germany, Report to Tensar International Ltd., United Kingdom, Report 01-2013, February 20, 2013.

Stahl, M., and L. te Kamp. (2012) "Project 12206: Geogrid Modelling with PFC3D — Generation and Calibration of TriAx-Geogrid TX160," Itasca Consultants GmbH, Gelsenkirchen, Germany, Report to Tensar International Ltd., United Kingdom, Report 01-2012, September 26, 2012.

Stille, B. (2015) "Geogrid Modeling Package," PowerPoint slide sets: **TensarSS20-Generate&Calibrate.ppt** and **GeogridPackage.pptx**.

Tanquist, B. (2012) *MnPAVE User's Guide*. Office of Materials, Minnesota Dept. of Transportation, Maplewood, MN, July 2012.

Wikipedia. (2015a) Entry for "density polypropylene" on June 4, 2015.

Wikipedia. (2015b) Entry for "young's modulus polypropylene" on June 4, 2015.

Technical Memorandum

Date: June 23, 2016

To: PFC 5 Documentation Set

From: David Potyondy

Re: Hill Contact Model [version 4]

Ref: ICG7795-L

This memo describes the hill contact model (version 4) as provided in the material-modeling support package for PFC 5.0.[1] A hill material is defined as a granular assembly in which the hill contact model exists at all grain-grain contacts, and this material behaves like an unsaturated granular material. The model formulation and test problems are provided in the first and second major sections, respectively. The test problems consist of a two-grain system, a grain assembly and a material-behavior study. The material-behavior study creates hill and linear materials to represent a typical aggregate base layer of an asphalt-surface roadway, and subjects them to triaxial testing to discern the effect of material type on material behavior. The creation and triaxial testing of a hill material is described in Potyondy (2016, User-Defined Material Example). A pavement-design package that supports creation and triaxial testing of the hill material containing geogrid is described in Potyondy et al. (2016).

---

[1] The material-modeling support package is described in Potyondy (2016). The hill contact model is referred to in commands and FISH by the name **hill**, and is provided as a dynamic link library (DLL) file that is loaded into *PFC3D* at runtime. The version number of the hill contact model is given by the command {**list contact modellist**} and listed in the "Minor" column.

TABLE OF CONTENTS

1.0   FORMULATION

The formulation of the hill contact model is provided in this section. The first three subsections summarize the notational conventions, the PFC model and the kinematic variables — refer to Itasca (2016, PFC Model Components) and Potyondy (2015) for a complete description of these concepts. The remaining subsections contain the formulation which begins with a definition of the hill material and is followed by the activity-deletion criteria, force-displacement law, properties, methods and time step estimation scheme of the hill contact model.

1.1   Notational Conventions

Vectors are denoted by boldface type, such as $\mathbf{v}$. The length or magnitude of $\mathbf{v}$ is denoted $\|\mathbf{v}\|$ or simply v. The addition of a hat denotes a unit vector, such that $\hat{\mathbf{v}} = \mathbf{v}/\|\mathbf{v}\|$. The addition of a dot denotes a time derivative, such as $\dot{\mathbf{v}} = \partial\mathbf{v}/\partial t$. There is a global coordinate system (xyz). The vector $\mathbf{v}$ can be expressed in the global coordinate system by the relations:

$$\mathbf{v} = \mathbf{v}(x, y, z) = v_x\hat{\mathbf{i}} + v_y\hat{\mathbf{j}} + v_z\hat{\mathbf{k}}$$
$$\text{with } v_x = \mathbf{v}\cdot\hat{\mathbf{i}}, \quad v_y = \mathbf{v}\cdot\hat{\mathbf{j}}, \quad v_z = \mathbf{v}\cdot\hat{\mathbf{k}} \tag{1}$$

where $\hat{\mathbf{i}}$, $\hat{\mathbf{j}}$ and $\hat{\mathbf{k}}$ are unit vectors directed along the positive x, y and z axes, respectively.

1.2   The PFC Model

The PFC programs (*PFC2D* and *PFC3D*) provide a general purpose, distinct-element modeling framework that includes a computational engine and a graphical user interface. A particular instance of the distinct-element model is referred to as a *PFC model*, which refers to both the 2D and 3D models. The PFC model simulates the movement and interaction of many finite-sized particles. The particles are rigid bodies with finite mass that move independently of one another and can both translate and rotate. Particles interact at pair-wise contacts by means of an internal force and moment. Contact mechanics is embodied in particle-interaction laws that update the internal forces and moments. The time evolution of this system is computed via the distinct-element method, which provides an explicit dynamic solution to Newton's laws of motion. The PFC model provides a synthetic material consisting of an assembly of rigid grains that interact at contacts and includes both granular and bonded materials.

We here generalize and expand upon the definition of the PFC model given above. The PFC model simulates the movement of particles and their mechanical interaction at pair-wise contacts. We denote each particle as a *body* to clarify that it is not a point mass, but instead, is a rigid body with finite mass and a well-defined surface. The PFC model consists of bodies and *contacts* (see Figure 1). There are three types of bodies: *balls*, *clumps* and *walls*. Bodies have surface properties that are

assigned to the *pieces* on the body surface. A ball consists of one piece, which is the ball itself, while the pieces of a clump and wall are called *pebbles* and *facets*, respectively. A ball is a rigid unit-thickness disk in 2D or sphere in 3D. A clump is a collection of pebbles that are rigid unit-thickness disks in 2D or spheres in 3D. Clumps model arbitrarily shaped rigid bodies. The pebbles comprising a clump can overlap but contacts do not exist between them; instead, contacts form between the pebbles on the boundary of a clump and other bodies. A wall is a collection of facets that are linear segments in 2D or triangles in 3D and that form a manifold and orientable surface.
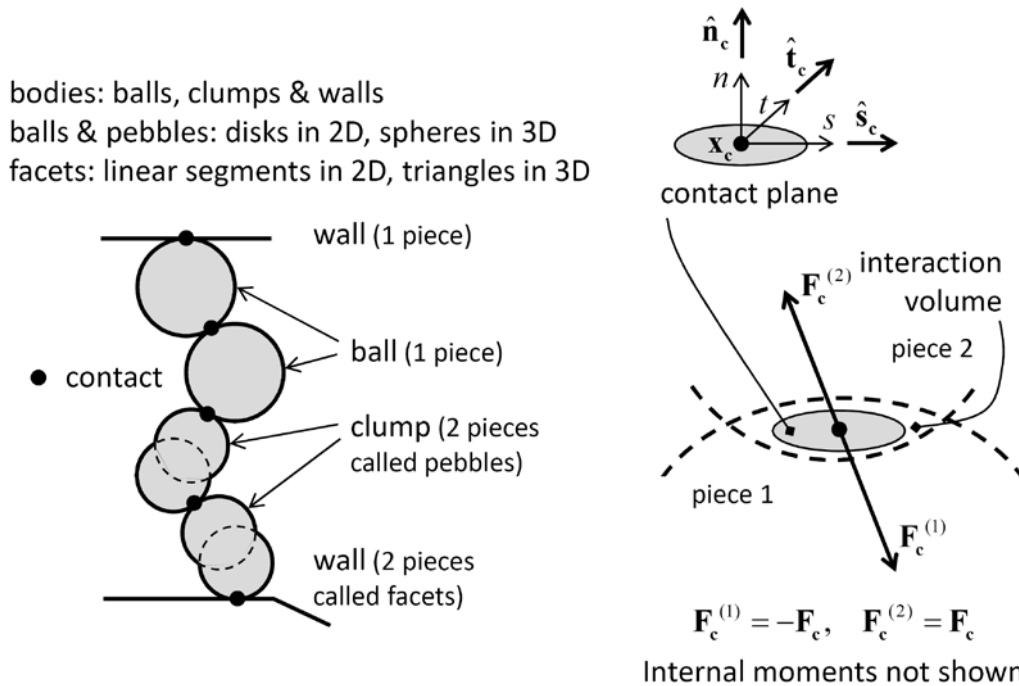
Figure 1　**PFC model showing bodies and contacts (left) and contact plane with internal force (right).** (From Fig. 1 of Itasca [2016][2].)

Contact mechanics is embodied in particle-interaction laws that employ a soft-contact approach for which all deformation occurs at the contacts between the rigid bodies. The mechanical interaction between the surfaces of two bodies occurs at one or more pair-wise mechanical contacts. Contacts are created and deleted based on body proximity by the contact-detection logic. A contact provides an interface between two pieces. The interface consists of a contact plane with location $(\mathbf{x}_c)$, normal direction $(\hat{\mathbf{n}}_c)$ and coordinate system (nst). The contact plane is centered within the interaction volume (either gap or overlap) of the two pieces, oriented tangential to the two pieces and rotated to ensure that relative motion of the piece surfaces remains symmetric w.r.t. the contact plane. Each contact stores a force $(\mathbf{F}_c)$ and moment $(\mathbf{M}_c)$ that act at the contact location in an equal

---

[2] In documentation set at PFC Model Components: PFC Model Formulation: Model Components.

and opposite sense on the two pieces. The internal force and moment are updated by the particle-interaction law, which takes the relative motion and surface properties of the two pieces as input. We refer to the particle-interaction law as a *contact model.*

1.3 Kinematic Variables

Kinematics considers the motion of systems of bodies without regard to the role of the forces causing the motion, while kinetics considers the relationship of the forces to the kinematic variables. The kinetics of the PFC model is embodied in the force-displacement law of each contact model. The kinematic variables that serve as the input to the force-displacement law are discussed here.

Contact resolution occurs when a new contact is detected during the cycle sequence, prior to the force-displacement calculations. During contact resolution, the contact state variables (see Table 1) are updated. Each contact model uses its properties along with the relative motion of the two contacting pieces to update the contact force and moment.

Table 1   Contact State Variables

Property	Description
m_c	effective inertial mass
Contact plane (see Figures 1 and 2)**:**	
$\mathbf{x_c}$	contact-plane location
$\hat{\mathbf{n}}_c$	contact-plane normal direction
$\hat{\mathbf{s}}_c$	contact-plane coord. system (s axis)
$\hat{\mathbf{t}}_c$	contact-plane coord. system (t axis)
g_c	contact gap ($g_c > 0$ is open)
Relative motion (see Figure 3)**:**	
$\dot{\boldsymbol{\delta}}$	relative translational velocity
$\dot{\boldsymbol{\theta}}$	relative rotational velocity
$\Delta\delta_n$	relative normal-displacement increment ($\Delta\delta_n > 0$ is opening)
$\Delta\boldsymbol{\delta}_s$	relative shear-displacement increment
$\Delta\theta_t$	relative twist-rotation increment

| $\Delta\boldsymbol{\theta_b}$ | relative bend-rotation increment $\left(\Delta\theta_{bs}, \Delta\theta_{bt}\right)$ |

The contact shown in Figure 2 has been created between the pieces of two bodies. Each contact has two ends, **end1** and **end2**, with the associated pieces and bodies labelled 1 and 2. The bodies are rigid; therefore, the motion of body (b) is described by its rotational velocity $\left(\boldsymbol{\omega}^{(b)}\right)$ and the translational velocity $\left(\dot{\mathbf{x}}^{(b)}\right)$ of its centroid $\left(\mathbf{x}^{(b)}\right)$. The contact state variables include the contact-plane information as well as the contact gap $\left(g_c\right)$, which is the minimal signed distance separating the piece surfaces. A vector quantity that lies on the contact plane ($\mathbf{S}$) can be expressed in the contact plane coordinate system by the relations:

$$\mathbf{S} = \mathbf{S}(s,t) = S_s \hat{\mathbf{s}}_c + S_t \hat{\mathbf{t}}_c$$
$$\text{with} \quad S_s = \mathbf{S} \cdot \hat{\mathbf{s}}_c, \quad S_t = \mathbf{S} \cdot \hat{\mathbf{t}}_c. \tag{2}$$
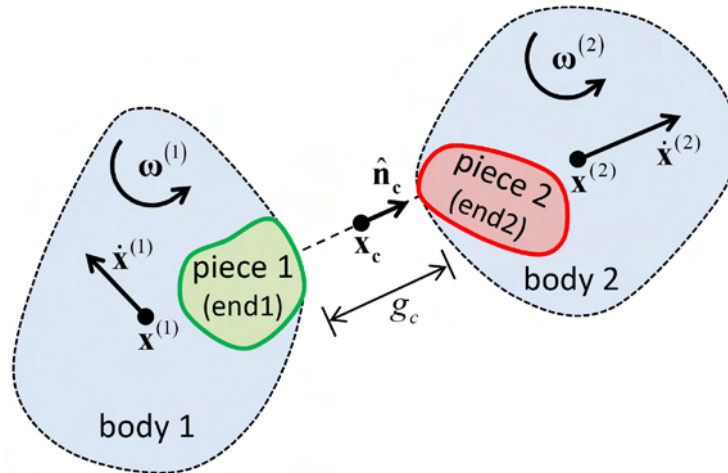
Figure 2   ***A contact between the pieces of two bodies.*** (From Fig. 1 of Itasca [2016][3].)

The relative motion of the piece surfaces at a contact is described by the relative translational $\left(\dot{\boldsymbol{\delta}}\right)$ and rotational $\left(\dot{\boldsymbol{\theta}}\right)$ velocities[4]:

$$\dot{\boldsymbol{\delta}} = \dot{\mathbf{x}}_c^{(2)} - \dot{\mathbf{x}}_c^{(1)}$$
$$\dot{\boldsymbol{\theta}} = \boldsymbol{\omega}^{(2)} - \boldsymbol{\omega}^{(1)}. \tag{3}$$

---

[3] In documentation set at PFC Model Components: Contacts and Contact Models: Contact Resolution.
[4] The relative rotational velocity is not employed by the hill contact model; thus, it is omitted from the following summary.

In this expression, $\dot{\mathbf{x}}_{\mathbf{c}}^{(b)}$ is the translational velocity of body (b) at the contact location:

$$\dot{\mathbf{x}}_{\mathbf{c}}^{(b)} = \dot{\mathbf{x}}^{(b)} + \boldsymbol{\omega}^{(b)} \times \left(\mathbf{x}_{\mathbf{c}} - \mathbf{x}^{(b)} \right) \tag{4}$$

where $\dot{\mathbf{x}}^{(b)}$ is the translational velocity of body (b); $\boldsymbol{\omega}^{(b)}$ is the rotational velocity of body (b); $\mathbf{x}_{\mathbf{c}}$ is the contact location and $\mathbf{x}^{(b)}$ is either the centroid (if the body is a ball or clump) or the center of rotation (if the body is a wall) of body (b). The contact location defines a point that is fixed w.r.t. each body, and thus, $\dot{\mathbf{x}}_{\mathbf{c}}^{(b)}$ is the translational velocity of that point in body (b).[5]

The relative translational velocity can be expressed as

$$\dot{\boldsymbol{\delta}} = \dot{\boldsymbol{\delta}}_{\mathbf{n}} + \dot{\boldsymbol{\delta}}_{\mathbf{s}}$$
$$\text{with} \quad \dot{\boldsymbol{\delta}}_{\mathbf{n}} = \left(\dot{\boldsymbol{\delta}} \cdot \hat{\mathbf{n}}_{\mathbf{c}} \right) \hat{\mathbf{n}}_{\mathbf{c}} = \dot{\delta}_n \hat{\mathbf{n}}_{\mathbf{c}}, \quad \dot{\boldsymbol{\delta}}_{\mathbf{s}} = \dot{\boldsymbol{\delta}} - \dot{\boldsymbol{\delta}}_{\mathbf{n}} \tag{5}$$

where $\dot{\boldsymbol{\delta}}_{\mathbf{n}}$ ($\dot{\delta}_n > 0$ is moving apart) and $\dot{\boldsymbol{\delta}}_{\mathbf{s}}$ are the relative translational velocities normal and tangential, respectively, to the contact plane, and the subscripts n and s correspond with normal and shear action, respectively (see Figure 3 — the centering of the contact within the interaction volume ensures that the relative displacement is symmetric w.r.t. the contact plane).

The relative displacement increment at the contact during a time step Δt is

$$\Delta\boldsymbol{\delta} = \Delta\delta_n \hat{\mathbf{n}}_{\mathbf{c}} + \Delta\boldsymbol{\delta}_{\mathbf{s}} \quad \left[\Delta\delta_{ss} = \Delta\boldsymbol{\delta}_{\mathbf{s}} \cdot \hat{\mathbf{s}}_{\mathbf{c}}, \ \Delta\delta_{st} = \Delta\boldsymbol{\delta}_{\mathbf{s}} \cdot \hat{\mathbf{t}}_{\mathbf{c}} \right]$$
$$\text{with} \quad \Delta\delta_n = \dot{\delta}_n \Delta t, \quad \Delta\boldsymbol{\delta}_{\mathbf{s}} = \dot{\boldsymbol{\delta}}_{\mathbf{s}} \Delta t \tag{6}$$

where $\Delta\delta_n$ is the relative normal-displacement increment and $\Delta\boldsymbol{\delta}_{\mathbf{s}}$ is the relative shear-displacement increment.

---

[5] The location of this point within each body may change — e.g., under increasing applied compression, the overlap increases and these points move deeper into each body.
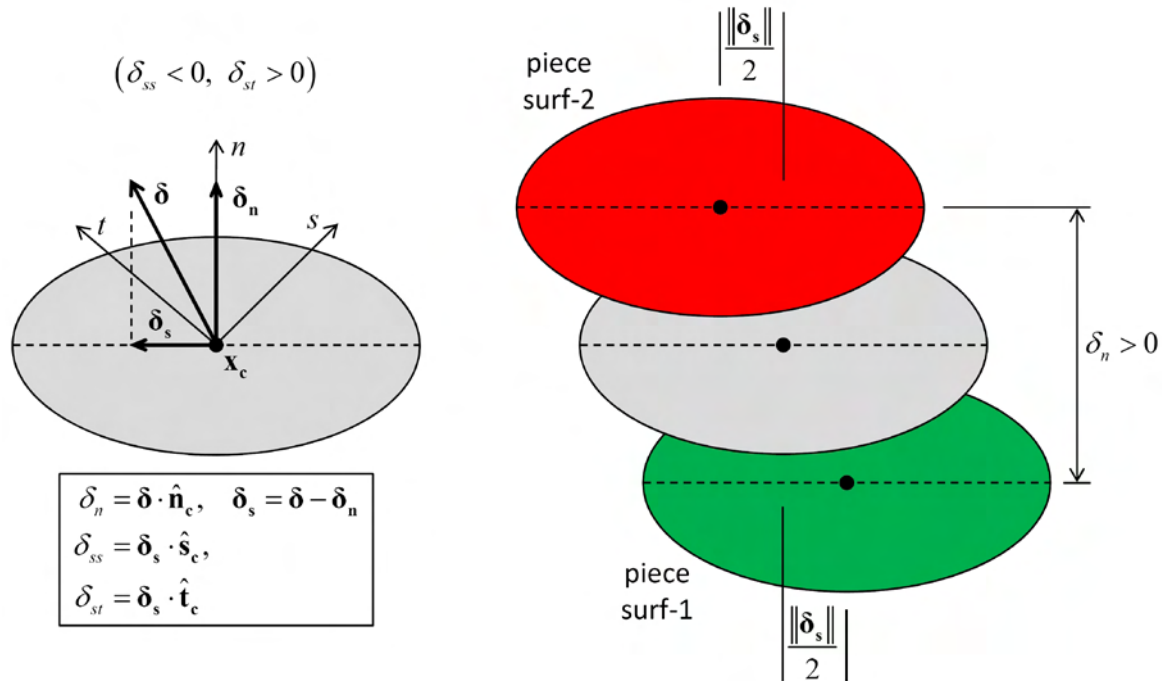
Figure 3 **Kinematics of a contact showing contact plane with relative displacement and motion of piece surfaces.** (From Fig. 7 of Itasca [2016][6].)

1.4   Hill Material

The present implementation of the hill contact model follows that of Tan and co-workers (Tan et al., 2014b), who refer to the synthetic material as a computational framework that "... has the potential to model a wide range of granular bases explicitly taking into account the coarse particle size distribution as well as the effects of moisture and fine particles.[7] The coarse particle size distribution is represented explicitly through the [discrete element] DEM particles. The fine particle size distribution and moisture are represented implicitly via the force model between the coarser DEM particles." Tan and co-workers suggest that this DEM approach "... offers a viable alternative to continuum models in which the form of the bulk moduli must be empirically determined. In contrast, the calibrated DEM model represents coarse particle movement distinctly and captures ... complex trends associated with particle size distribution and moisture content measured in experiments."

A hill material is defined as a granular assembly in which the hill contact model exists at all grain-grain contacts, and this material behaves like an unsaturated granular material. A hill material is

---

[6] In documentation set at PFC Model Components: Contacts and Contact Models: Contact Resolution.

[7] The hill contact model is described in Tan et al. (2014b), and is also described as Moisture Model III in Tan et al. (2014a). The present implementation follows Tan et al. (2014b), but differs by providing an incremental (as opposed to an absolute) update of the shear force that is more appropriate for static grain assemblies (see Appendix A).
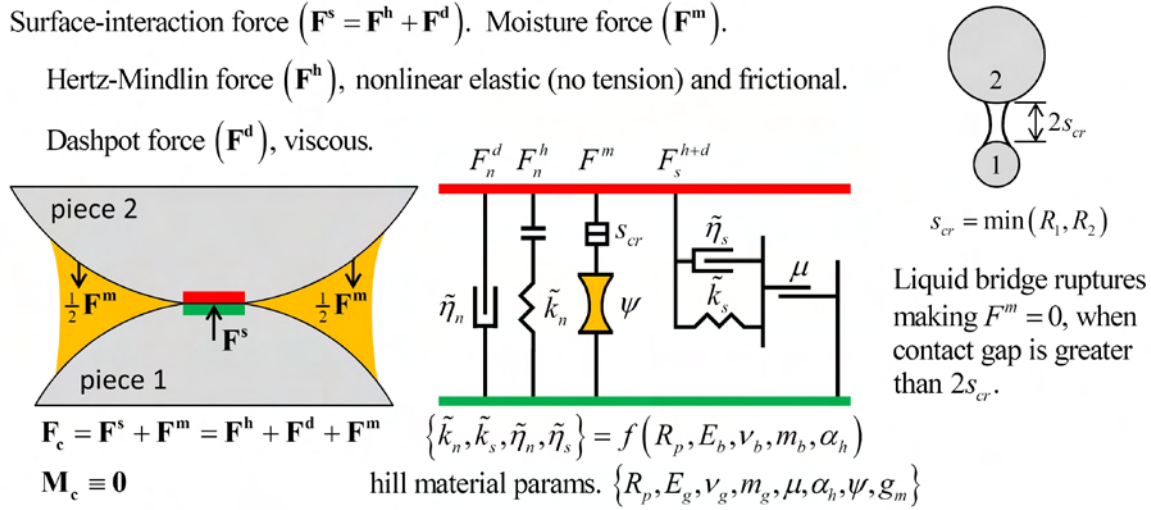
defined by the following parameters (see Table 2): local radii of grains $\left(R_p\right)$, Young's moduli, Poisson's ratios and densities of grains $\left(\{E_g, \nu_g, \rho_g\}\right)$, friction coefficient (μ), damping constant (α_h), suction (ψ) and moisture gap (g_m).[8] These parameters are used to set the grain mass and properties of the hill contact model (listed in Section 1.7).

Table 2 Hill Material Parameters

Parameter	Type	Range	Default	Description
Material microproperties are listed via `@mpListMicroProps`.				
Common material parameters are listed in Table 1 of Potyondy (2016).				
Packing parameters are listed in Table 7 of Potyondy (2016).				
Add moisture via `@hlm_makeWet(`ψ`,`g_m`)`, where ψ is suction and g_m is moisture gap. Remove moisture via `@hlm_makeDry`.				
Set and modify the following properties via `@hlm_setMatBehavior`.				
Hill material group:				
E_g, `hlm_youngMod`	FLT	$[0.0, \infty)$	0.0	Young's modulus of grains
ν_g, `hlm_poisRatio`	FLT	$(-1.0, 0.5]$	0.0	Poisson's ratio of grains
μ, `hlm_fricCoef`	FLT	$[0.0, \infty)$	0.0	friction coefficient
α_h, `hlm_dampCon`	FLT	$[0.0, 1.0]$	0.0	damping constant
ψ, `hlm_suction`	FLT	$[0.0, \infty)$	0.0	suction

The hill contact model may exist only at a grain-grain contact. The grain-grain system behaves like two locally elastic spheres that may have a liquid bridge (see Figure 4). The liquid bridge is present if the moisture state is wet, and absent if the moisture state is dry. The hill contact model provides the behavior of an infinitesimal, nonlinear elastic (no tension) and frictional interface that carries a compressive surface-interaction force and may carry a tensile moisture force. The contact force $(\mathbf{F_c})$ is the sum of the surface-interaction and moisture force, and the contact moment is zero.

---

[8] The grain shape, size distribution and density $\left(\rho_g\right)$ are listed in Table 1 of Potyondy (2016). If grains are clumps, then the local radii are the piece radii. Grain density is used to obtain grain mass $\left(m_g\right)$. If quasi-static conditions are enforced via local damping, then the damping constant is set to zero, and the local-damping factor (α) is set to 0.7.

Surface-interaction force $\left(\mathbf{F^s} = \mathbf{F^h} + \mathbf{F^d}\right)$. Moisture force $\left(\mathbf{F^m}\right)$.

Hertz-Mindlin force $\left(\mathbf{F^h}\right)$, nonlinear elastic (no tension) and frictional.

Dashpot force $\left(\mathbf{F^d}\right)$, viscous.

$s_{cr} = \min\left(R_1, R_2\right)$

Liquid bridge ruptures making $F^m = 0$, when contact gap is greater than $2s_{cr}$.

$\mathbf{F_c} = \mathbf{F^s} + \mathbf{F^m} = \mathbf{F^h} + \mathbf{F^d} + \mathbf{F^m}$

$\mathbf{M_c} \equiv \mathbf{0}$

$\left\{\tilde{k}_n, \tilde{k}_s, \tilde{\eta}_n, \tilde{\eta}_s\right\} = f\left(R_p, E_b, \nu_b, m_b, \alpha_h\right)$

hill material params. $\left\{R_p, E_g, \nu_g, m_g, \mu, \alpha_h, \psi, g_m\right\}$

Figure 4   ***Behavior and rheological components of the wet hill contact model. The forces acting on piece 2 are shown, equal and opposite forces act on piece 1.***

The surface-interaction force model is based on Hertz-Mindlin contact theory along with a damping mechanism and Coulomb sliding friction (Tsuji et al., 1992). The surface-interaction force consists of Hertzian and dashpot components $\left(\mathbf{F^s} = \mathbf{F^h} + \mathbf{F^d}\right)$ with the Hertz-Mindlin springs acting in parallel with the dashpots. The Hertz-Mindlin springs provide the nonlinear force-displacement response arising from the mutual compression of two elastic bodies, which induces a local deformation of the bodies in the vicinity of the contact surface.[9] The local deformation is determined by the shapes and elastic constants of the bodies in the vicinity of the contact surface.[10] Slip is accommodated by imposing a Coulomb limit on the total shear force $\left(F_s \leq \mu F_n\right)$ via the friction coefficient $\left(\mu\right)$. The stiffness and damping coefficients $\left(\left\{\tilde{k}_n, \tilde{k}_s, \tilde{\eta}_n, \tilde{\eta}_s\right\}\right)$ are internal model parameters that are obtained

---

[9] The nonlinear contact formulation of the Hertz-Mindlin springs is an approximation of the Hertz-Mindlin contact theory of Mindlin and Deresiewicz (1953), for which the normal force-displacement response is nonlinear elastic, and the tangential force-displacement response is nonlinear inelastic caused by the growth of a slip annulus emanating from the periphery of the contact surface. The inelastic behavior means that not only do the changes in stresses and displacement depend upon the initial state of loading, but also upon the entire past history of loading and instantaneous relative rates of change of the normal and tangential forces. The inelastic tangential behavior is removed in the formulation of the Hertz-Mindlin springs by using a tangential stiffness equal to the initial tangential stiffness before tangential motion occurs. The initial tangential stiffness depends on the normal force, and corresponds with the simplest case of varying oblique forces: application of normal force, followed by tangential force increasing monotonically from zero. The normal force-displacement response is obtained from Timoshenko and Goodier (1970, p. 409), and the tangential force-displacement response for the general case of different sphere radii and different elastic constants is obtained from the initial tangential compliance in Mindlin (1949, Eq. 78).

[10] The formulation of the Hertz-Mindlin springs is applicable to sphere-sphere and sphere-plane contacts between two linear elastic isotropic bodies. For the sphere-plane case, the radius of the body with the planar surface can be set to infinity. The present implementation of the hill contact model does not support sphere-plane contacts.

from the radii of the contacting pieces (R_p), the Young's moduli, Poisson's ratios and masses of the contacting bodies $(\{E_b, v_b, m_b\})$, and the damping constant (α_h).[11]

The moisture-force model is inspired by liquid-bridge models, which mechanistically capture the effect of liquid dispersed among particles on the macroscopic response of the granular system (Lian et al., 1993; Muguruma et al., 2000; Richefeu et al., 2008). The moisture force $(\mathbf{F^m})$ is present only if the moisture state is wet. It is an attractive force in the normal direction that is maximum when the pieces are in contact and decays exponentially until the contact gap reaches a critical value $(2s_{cr})$ at which the liquid bridge ruptures, making the moisture state dry and the force zero (see Figure 6). The moisture effect is accounted for in the hill material by considering the suction (negative pore pressure) associated with surface tension that holds pore water at the interparticle contacts in unsaturated granular material. The suction can be estimated from empirical relationships that relate suction of an unsaturated granular mixture to its volumetric moisture content, mixture composition, and bulk density (Gupta and Larson, 1979; Gupta et al., 2005&2007). These relationships are embodied in a suction parameter (ψ that is given as τ_{DEMeq} in Table 3 of Tan et al. (2014b)).[12]

Moisture is modeled in the hill material by adding suction between selected grains using the following procedure. Each hill contact has a moisture state that can be either wet or dry. When new grain-grain contacts form, they are assigned the dry hill contact model. Moisture can be added to the hill material at any time during a simulation via **@hlm_makeWet(ψ, g_m)**, where ψ is the suction

---

[11] The damping constant is related directly to the coefficient of restitution in Fig. 4 of Tsuji et al. (1992), and the coefficient of restitution is independent of the body properties.

[12] The suction parameter provides a simple means of adding soil suction to a representative volume of material at a grain-grain contact. A similar quantity, denoted as effective pressure, is defined in Potyondy and Emam (2008&2009), wherein suction behavior is modeled by adding capillary pressure-induced suction forces within a synthetic material consisting of circular particles bonded at their contact points. The representative volume in both the P&E and hill materials consists of two particles and their contact. In the P&E material, we define the capillary pressure as the average pressure in all voids in the representative volume, and note that capillary pressure varies with saturation. We then consider a surface that cuts through this volume, and note that the portion of the surface area that intersects the pore water in the voids is proportional to the saturation; thus, the effective pressure acting on the surface (P_e) is given by the product of the saturation and capillary pressure. As the saturation approaches zero, the capillary pressure approaches infinity, but the effective pressure is finite. The moisture force at a P&E contact is found by multiplying the effective pressure (P_e) by the cross section of the contact. The maximum moisture force at a hill contact is found by multiplying the suction (ψ) by the cross section of the contact shown in Figure 6. In the P&E model, the effective pressure is an internal variable equal to the product of saturation and capillary pressure, with the capillary pressure given by an empirical law of the van Genuchten form. In the hill model, the suction is a model parameter estimated from the empirical relationships of Gupta and co-workers (Gupta and Larson, 1979; Gupta et al., 2005&2007).

and g_m is the moisture gap. After this function has been invoked, the wet hill contact model with suction ψ will exist between all grains that are within the moisture-gap distance of one another.[13]

When using the hill material to represent a typical aggregate base of a pavement system, the sand- and finer-sized particles in the grain-size distribution of the physical material are often excluded from the model in order to reduce the number of particles and their associated computational expense. The absence of these fine particles is accounted for by use of a positive moisture gap, which extends the application of the suction to particles separated by this gap, and thereby accounts for the suction produced by the fine particles that partially fill the voids between the coarse particles in the modeled system. The friction coefficient may also be reduced to account for the stabilizing or lubricating effect of the fine particles between the coarse particles in the modeled system.

1.5   Activity-Deletion Criteria

A contact with the hill model is active if it is wet ($M = 2$) or if the contact gap is less than or equal to zero. The force-displacement law is skipped for inactive contacts.

1.6   Force-Displacement Law

The force-displacement law for the hill model updates the contact force and moment:

$$\mathbf{F_c} = \mathbf{F^s} + \mathbf{F^m}, \quad \mathbf{M_c} \equiv \mathbf{0} \tag{7}$$

where $\mathbf{F^s}$ is the surface-interaction force and $\mathbf{F^m}$ is the moisture force. The surface-interaction force consists of Hertzian and dashpot components with the Hertz-Mindlin springs acting in parallel with the dashpots:

$$\mathbf{F^s} = \mathbf{F^h} + \mathbf{F^d}. \tag{8}$$

The surface-interaction force is resolved into a normal and shear force:

$$\mathbf{F^s} = -F_n^{rs}\hat{\mathbf{n}}_c + \mathbf{F_s} \tag{9}$$

where $F_n^{rs} > 0$ is tension. The shear force lies on the contact plane and is expressed in the contact plane coordinate system:

---

[13] This operation may create new grain-grain contacts, and such contacts will be assigned the wet hill contact model with suction ψ. The new grain-grain contacts are created between grains that are within the moisture-gap distance of one another. Note that there are many grains in a typical granular assembly that are near to one another, but contacts may not exist between all of these near-neighbor pairs.

$$\mathbf{F_s} = F_{ss}\hat{\mathbf{s}}_{\mathbf{c}} + F_{st}\hat{\mathbf{t}}_{\mathbf{c}}. \tag{10}$$

The moisture force acts in the normal direction:

$$\mathbf{F^m} = -F^m\hat{\mathbf{n}}_{\mathbf{c}} \tag{11}$$

where $F^m > 0$ is tension (suction) and $F^m \geq 0$.

The force-displacement law for the hill model consists of the following steps (see Figure 5 and properties in Section 1.7).

1. Update F^m as follows (see Figure 6). If the contact is dry ($M \neq 2$), then $F^m = 0$; otherwise, set

$$F^m = \begin{cases} F^m_{\max}, & g_c < 0 \\ F^m_{\max}\exp\left(\dfrac{-g_c}{2s_{cr}}\right), & 0 \leq g_c \leq 2s_{cr} \\ 0, & g_c > 2s_{cr} \end{cases}$$

$$\text{with} \quad F^m_{\max} = \psi\left(\pi R_o^2\right) \tag{12}$$

$$s_{cr} = R_o = \min\left(R_1, R_2\right)$$

where R_p is the radius of piece (p). If the contact is wet and $g_c > 2s_{cr}$, then rupture the liquid bridge by setting $M = 1$.

2. Update the normal surface-interaction force:

$$F_n^s = F_n^h + F_n^d = \begin{cases} -\tilde{k}_n\delta_o^{\frac{3}{2}} - \tilde{\eta}_n\delta_o^{\frac{1}{4}}\dot{\delta}_o, & \delta_o > 0 \\ 0, & \delta_o \leq 0 \end{cases} \tag{13}$$

$$\text{with} \quad \delta_o = -g_c$$

where δ_o is the contact overlap ($\delta_o > 0$ is overlap) and $\dot{\delta}_o$ is the relative translational velocity normal to the contact plane defined such that $\dot{\delta}_o > 0$ is increasing overlap.

3. Update the shear force ($\mathbf{F_s}$) as follows (see Figure 7). Compute the shear strength:

$$F_s^\mu = -\mu F_n^s. \tag{14}$$

Compute a trial Hertz-Mindlin shear force:

$$\left(\mathbf{F_s^h}\right)^* = \left(\mathbf{F_s^h}\right)_o - \tilde{k}_s \delta_o^{\frac{1}{2}} \dot{\boldsymbol{\delta}}_s \Delta t \tag{15}$$

where $\left(\mathbf{F_s^h}\right)_o$ is the Hertz-Mindlin shear force at the beginning of the time step and $\dot{\boldsymbol{\delta}}_s$ is the relative translational velocity tangential to the contact plane. Update the Hertz-Mindlin shear force (insuring that it lies within the no-slip region):

$$\mathbf{F_s^h} = \begin{cases} \left(\mathbf{F_s^h}\right)^*, & \delta_o > 0 \text{ and } \left\|\left(\mathbf{F_s^h}\right)^*\right\| \leq F_s^{\mu} \\ F_s^{\mu} \hat{\mathbf{s}}^{\mathbf{h}}, & \delta_o > 0 \text{ and } \left\|\left(\mathbf{F_s^h}\right)^*\right\| > F_s^{\mu} \\ 0, & \delta_o \leq 0 \end{cases} \tag{16}$$

$$\text{with } \hat{\mathbf{s}}^{\mathbf{h}} = \left(\mathbf{F_s^h}\right)^* \Big/ \left\|\left(\mathbf{F_s^h}\right)^*\right\|.$$
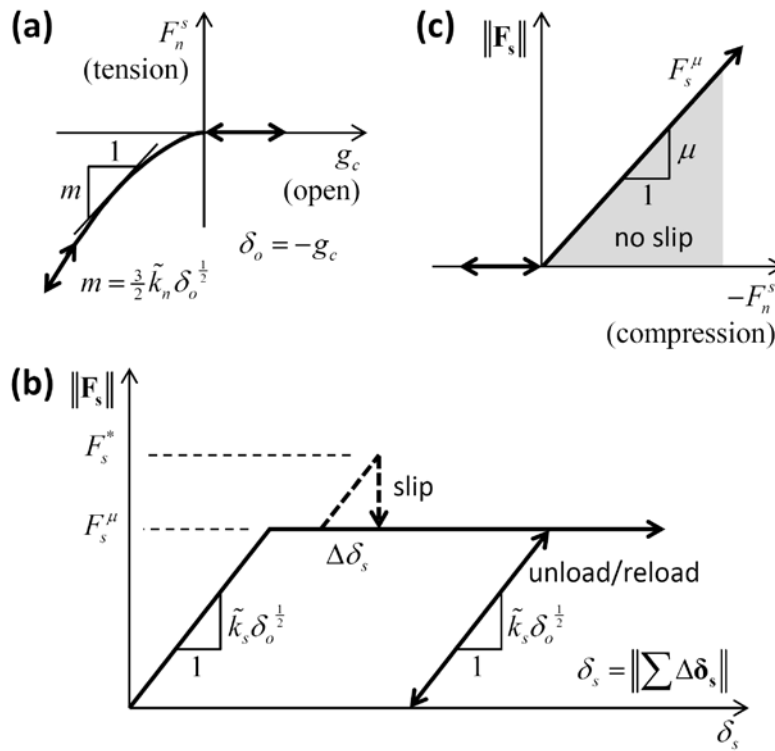
Compute a trial shear force:

$$\mathbf{F_s^*} = \mathbf{F_s^h} + \mathbf{F_s^d}$$
$$\text{with } \mathbf{F_s^d} = -\tilde{\eta}_s \delta_o^{\frac{1}{4}} \dot{\boldsymbol{\delta}}_s. \tag{17}$$
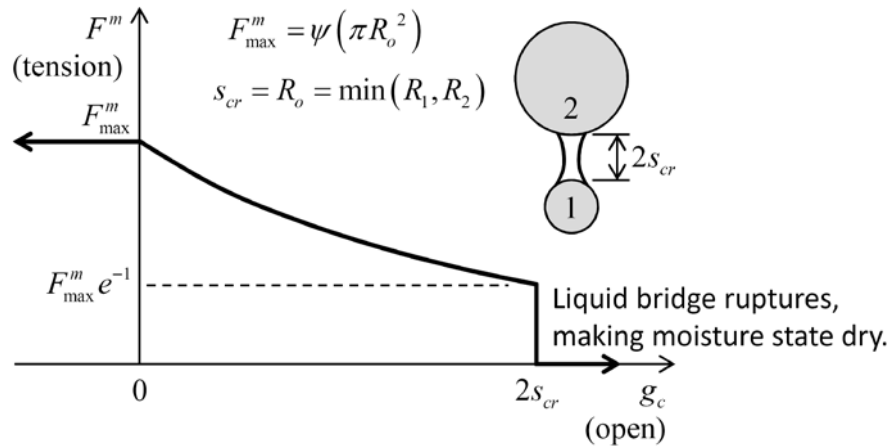
Update the shear force (insuring that it lies within the no-slip region):

$$\mathbf{F_s} = \begin{cases} \mathbf{F_s^*}, & \delta_o > 0 \text{ and } \left\|\mathbf{F_s^*}\right\| \leq F_s^{\mu} \\ F_s^{\mu} \hat{\mathbf{s}}, & \delta_o > 0 \text{ and } \left\|\mathbf{F_s^*}\right\| > F_s^{\mu} \\ 0, & \delta_o \leq 0 \end{cases} \tag{18}$$

$$\text{with } \hat{\mathbf{s}} = \mathbf{F_s^*} \Big/ \left\|\mathbf{F_s^*}\right\|.$$

Figure 5   *Force-displacement law for the dry hill model with inactive dashpots: (a) normal force versus contact gap, (b) shear force versus relative shear displacement and (c) slip envelope.*

Figure 6   *Moisture force versus contact gap for the wet hill model.*

$$\Delta \mathbf{F_s^h} = -\tilde{k}_s \delta_o^{\frac{1}{2}} \dot{\mathbf{\delta}}_s \Delta t = -\tilde{k}_s \delta_o^{\frac{1}{2}} \Delta \mathbf{\delta}_s \qquad\qquad \mathbf{F_s^d} = -\tilde{\eta}_s \delta_o^{\frac{1}{4}} \dot{\mathbf{\delta}}_s$$

$$F_s^\mu = -\mu F_n^s$$

Figure 7   *Update of the Hertz-Mindlin shear force and relative shear displacement (left) and shear force (right) of the hill model.*

1.7 Properties

The property information is separated into parameters and state variables such that the parameters define the model, while the state variables describe its current state. The properties table provides a concise property reference that combines the parameters and state variables. The property information for the hill model is given in Tables 3 to 5. For the first mapping in Table 4: R_e, E_e and G_e are the effective radius, Young's modulus and shear modulus, respectively, of the contact; R_p is the radius of piece (p); and E_b and v_b are the Young's modulus and Poisson's ratio, respectively, of body (b). For the second mapping in Table 4: m_e is the effective mass of the contact, and m_b is the mass of body (b).

Table 3   Hill Model Parameters

Parameter	Keyword	Description
	`hill`	model name
Associated with contacts:		
μ	`fric_coef`	friction coefficient
ψ	`suction`	suction
α_h	`damp_con`	damping constant
Associated with grains:		
E_b	`young_mod`	Young's modulus of body (b)

v_b	**pois_ratio**	Poisson's ratio of body (b)

Table 4 Hill Model State Variables

Variable	Keyword	Description
$\tilde{k}_n$	**nstiff_coef**	normal stiffness coeff. $\left[\mathrm{N\cdot m^{-\frac{3}{2}}}\right]$
$\tilde{k}_s$	**sstiff_coef**	shear stiffness coeff. $\left[\mathrm{N\cdot m^{-\frac{3}{2}}}\right]$

Mapping:

$$\tilde{k}_n = \tfrac{4}{3} E_e \sqrt{R_e}, \quad \tilde{k}_s = 8 G_e \sqrt{R_e}; \quad R_e = \left(\frac{1}{R_1} + \frac{1}{R_2}\right)^{-1}$$

$$E_e = \left(\frac{1-v_1^2}{E_1} + \frac{1-v_2^2}{E_2}\right)^{-1}, \quad G_e = \left(\frac{2(1+v_1)(2-v_1)}{E_1} + \frac{2(1+v_2)(2-v_2)}{E_2}\right)^{-1}$$

$\tilde{\eta}_n$	**ndamp_coef**	normal damping coeff. $\left[\mathrm{kg\cdot m^{-\frac{1}{4}}\cdot s^{-1}}\right]$
$\tilde{\eta}_s$	**sdamp_coef**	shear damping coeff. $\left[\mathrm{kg\cdot m^{-\frac{1}{4}}\cdot s^{-1}}\right]$

Mapping:

$$\tilde{\eta}_n = \alpha_h \sqrt{m_e \tilde{k}_n}, \quad \tilde{\eta}_s = \alpha_h \sqrt{m_e \tilde{k}_s}; \quad m_e = \left(\frac{1}{m_1} + \frac{1}{m_2}\right)^{-1}$$

δ_o	**overlap**	contact overlap ($\delta_o > 0$ is overlap)
M	**mois_state**	moisture state $\begin{cases} 0, & \text{dry} \\ 1, & \text{dry \& ruptured} \\ 2, & \text{wet} \end{cases}$
$\mathbf{F}^s$	**surf_force**	surface-interaction force $\left(-F_n^s, F_{ss}, F_{st}\right)$ where $F_n^s > 0$ is tension
F^m	**mois_force**	moisture force (F^m) where $F^m > 0$ is tension (suction)

Table 5 Hill Model Properties

Keyword	Symbol	Range	Default	Type	Modifiable
`fric_coef`	μ	$[0.0,\infty)$	0.0	FLT	yes
`suction`	ψ	$[0.0,\infty)$	0.0	FLT	yes
`damp_con`	α_h	$[0.0,1.0]$	0.0	FLT	yes
`young_mod`	E_b	$[0.0,\infty)$	0.0	FLT	no[+]
`pois_ratio`	ν_b	$(-1.0,0.5]$	0.0	FLT	no[+]
`nstiff_coef`	$\tilde{k}_n$	$[0.0,\infty)$	0.0	FLT	no
`sstiff_coef`	$\tilde{k}_s$	$[0.0,\infty)$	0.0	FLT	no
`ndamp_coef`	$\tilde{\eta}_n$	$[0.0,\infty)$	0.0	FLT	no
`sdamp_coef`	$\tilde{\eta}_s$	$[0.0,\infty)$	0.0	FLT	no
`overlap`	δ_o	$\mathbb{R}$	NA	FLT	no
`mois_state`	M	$\{0,1,2\}$	0	INT	no (set via methods)
`surf_force`	$\mathbf{F^s}$	$[\mathbb{R},\mathbb{R},\mathbb{R}]$	**0**	VEC3	no
`mois_force`	F^m	$[0.0,\infty)$	0.0	FLT	no

[+] Surface property of a body (ball or clump).

1.8   Methods

Table 6 Hill Model Methods

Method	Argument	Description
`make_wet`		Add moisture if $g_c \leq g_m$.
	`gap`	moisture gap (g_m)
`make_dry`		Remove moisture.

make_wet. Add moisture if the contact gap between the pieces is less than or equal to the moisture gap.[14] If moisture is added, then the moisture state becomes wet ($M = 2$) — the moisture force is unaffected and will be updated during the next cycle.

make_dry. Remove moisture. The moisture state becomes dry ($M = 0$) — the moisture force is unaffected and will be updated during the next cycle.

1.9   Time Step Estimation Scheme

The procedure to compute a stable time step in *PFC3D* 4.0 (see Section 1.6 in the Theory & Background volume of Itasca [2008]) requires that each contact model return the contact translational and rotational stiffnesses. For the hill model, the rotational stiffnesses are zero $\left(k_t = k_b \equiv 0 \right)$, and the translational stiffnesses are

$$k_n = \tfrac{3}{2} \tilde{k}_n \delta_o^{\frac{1}{2}}, \quad k_s = \tilde{k}_s \delta_o^{\frac{1}{2}} \tag{19}$$

where δ_o is the contact overlap. If $\delta_o \leq 0$ (which may occur when the contact is wet), then we return the stiffnesses that correspond with $\delta_o = \left(2.0 \times 10^{-4} \right) R_o$, with R_o given by Eq. (12). If the contact model includes dashpots, then the translational stiffnesses must be increased via

$$k_n := k_n / F(\beta_n)^2, \quad k_s := k_s / F(\beta_s)^2$$
$$F(\xi) = \sqrt{1 + \xi^2} - \xi, \quad 0 \leq \xi \leq 1 \tag{20}$$

where β_n and β_s are the critical damping ratios in the normal and shear directions, respectively. It may be possible to express the critical damping ratios in terms of the damping constant (α_h) and the contact overlap by analyzing the equation of motion for a fixed particle in contact with a free particle via the hill contact model.[15] Time limitations preclude the analysis from being done; therefore, we assume that the following relation holds:

$$\beta_n = \beta_s = \frac{\alpha_h}{2} \tag{21}$$

---

[14] One can ensure the existence of contacts between all pieces with a contact gap less than a specified moisture gap (g_m) by adding moisture to the material via the **hlm_makeWet** FISH function.

[15] The analysis will be similar to the analysis of Tsuji et al. (1992) in their derivation of the relationship between damping constant and coefficient of restitution.

and increase the translational stiffnesses via Eq. (20). It is expected that this will be sufficient for models that have small values of damping constant ($\alpha_h \leq 0.1$).[16]

2.0   TEST PROBLEMS

The pavement-design package provides the hill contact model, and supports creation of a hill material that can be subjected to triaxial testing. Test problems of two granite grains, and an assembly of granite grains are provided in the following subsections. An example of a hill material is provided in Potyondy (2016, User-Defined Material Example). There is a *PFC3D* project for each test problem, and these projects are in the **fistPkgN/ExampleProjects/.. HillContactModel** directory, where **N** is the version number of the material-modeling support package.

2.1   Two Granite Grains

The two-grain test problem is in the **Test-TwoGraniteGrains** example-project directory. The problem is shown in Figure 8 and described as follows. Two granite grains are stacked one atop the other. The bottom grain is fully fixed. The top grain is (A) moved down by 0.1 mm, and then (B) rotated by 0.02 radians. The granite grains are gravel-sized spheres with diameters ranging from 10–25 mm.

---

[16] The damping constant used in all of the simulations performed by Tan et al. (2014a) was 0.07 (as stated in their Appendix A), which corresponds with a restitution coefficient of 0.9. The damping constant is set to zero and local damping (with a local-damping factor of 0.7) is used when simulating quasi-static triaxial testing of the hill material.

$$A: \boldsymbol{\delta}^{(2)} = \{-0.1 \text{ mm}\} \, \hat{\mathbf{j}}, \quad B: \boldsymbol{\theta}^{(2)} = \{0.02 \text{ rad}\} \, \hat{\mathbf{k}}$$

$$\Delta\delta_n = -0.1 \text{ mm}, \quad \Delta\delta_{ss} = -99.0 \; \mu\text{m}, \quad \Delta\delta_{st} = 0$$
$$\Delta\theta_t = 0, \quad \Delta\theta_{bs} = 0, \quad \Delta\theta_{bt} = 0.02 \text{ rad}$$
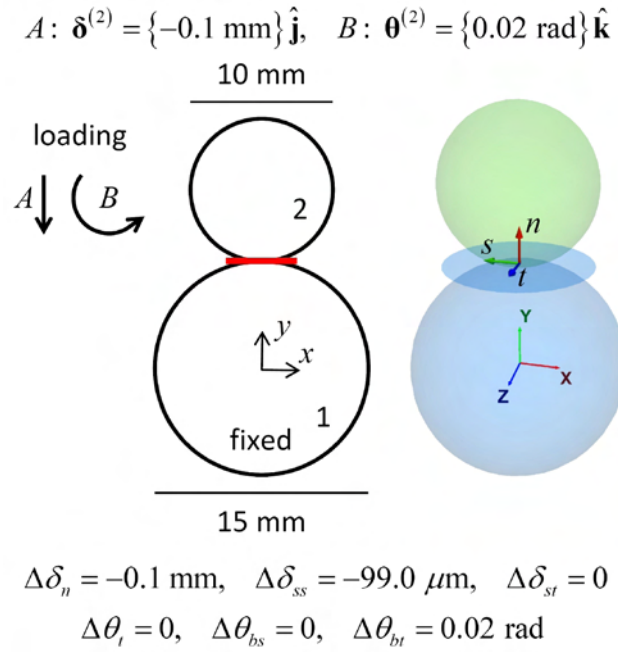
Figure 8   ***Two-grain test problem.***

The two-grain test problem is modeled with both the linear and hill contact models. The material properties are summarized in Figure 9 and described as follows. The density, Young's modulus and Poisson's ratio of granite are $2650 \; \text{kg/m}^3$, 29 GPa and 0.15, respectively. The friction coefficient is 0.4. The suction of the hill model is 200 kPa. We enforce quasi-static conditions via local-damping, with a local-damping factor of 0.7. Additional damping is applied to the hill model via a damping constant of 0.07, which corresponds with a 0.9 coefficient of restitution.

<div style="border: 1px solid black; border-radius: 15px; padding: 10px; text-align: center;">

granite

$\rho = 2650 \ \text{kg/m}^3, \ E = 29 \ \text{GPa}, \ \nu = 0.15$

$\mu = 0.4$

</div>

linear model:

grain density, effective modulus, stiffness ratio, friction coefficient
local-damping factor

$\rho_g = 2650 \ \text{kg/m}^3, \ \{E^* = 29 \ \text{GPa}, \ \kappa^* = 1.0\}$

$\mu = 0.4, \ \alpha = 0.7 \qquad \{k_n = k_s\} = 1.8221 \times 10^8 \ \text{N/m}$

hill model:

Young's modulus, Poisson's ratio and density of each grain
friction coefficient, suction, damping constant, local-damping factor

$E_g = 29 \ \text{GPa}, \ \nu_g = 0.15, \ \rho_g = 2650 \ \text{kg/m}^3, \ \mu = 0.4, \ \psi = 200 \ \text{kPa}$

$\alpha_h = 0.07, \ \alpha = 0.7$

Figure 9   Material properties of the two-grain test problem.

The force-displacement response of the linear model is shown in Figure 10. The normal force at the end of loading-stage B is given by

$$F_n = k_n g_c = \{1.8221 \times 10^8 \ \text{N/m}\}\{-0.1 \times 10^{-3} \ \text{m}\} = -1.8221 \times 10^4 \ \text{N}. \tag{22}$$

The shear force at the end of loading-stage B is given by

$$\begin{aligned}
F_{ss}^* &= -k_s \Delta \delta_{ss}, \quad F_{st}^* = -k_s \Delta \delta_{st} = 0 \\
&= -\{1.8221 \times 10^8 \ \text{N/m}\}\{-99.0 \ \mu\text{m}\} = 1.8039 \times 10^4 \ \text{N} \\
F_s^\mu &= -\mu F_n \\
&= -\{0.4\}\{-1.8221 \times 10^4 \ \text{N}\} = 7.2884 \times 10^3 \ \text{N}
\end{aligned} \tag{23}$$

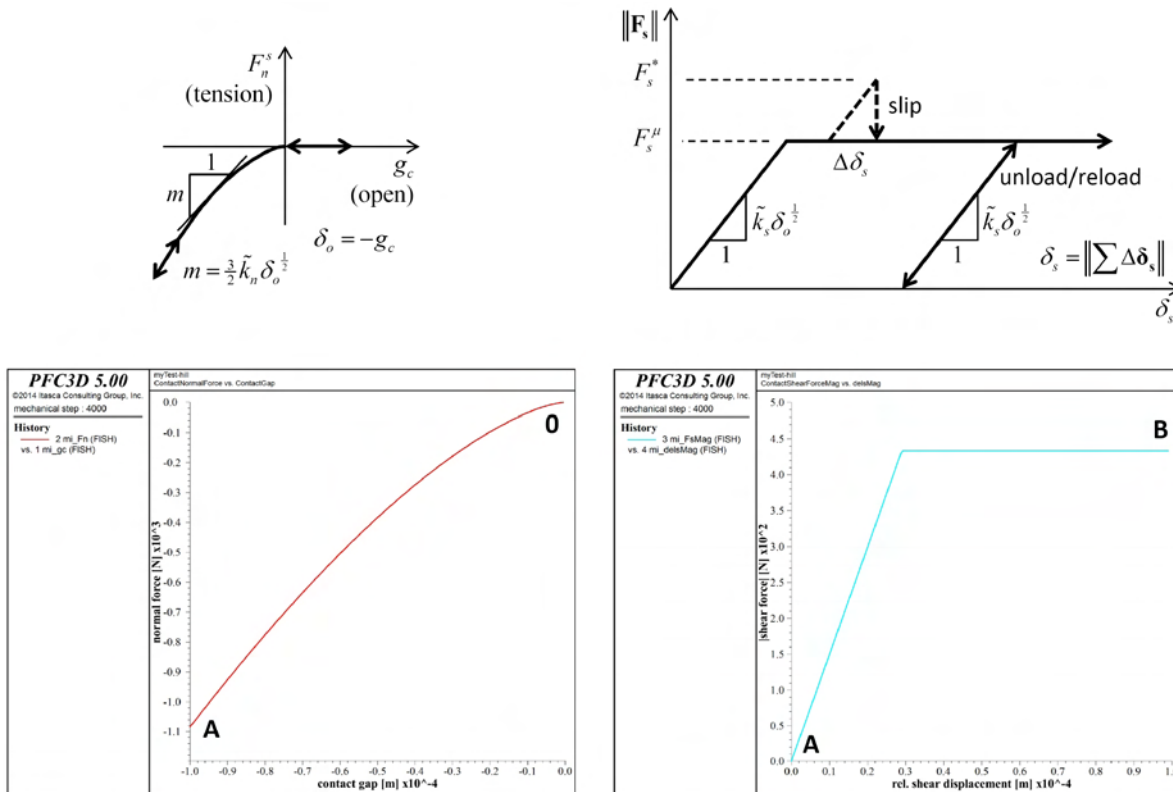$$F_{ss} = 7.2884 \times 10^3 \ \text{N}, \quad F_{st} = 0.$$
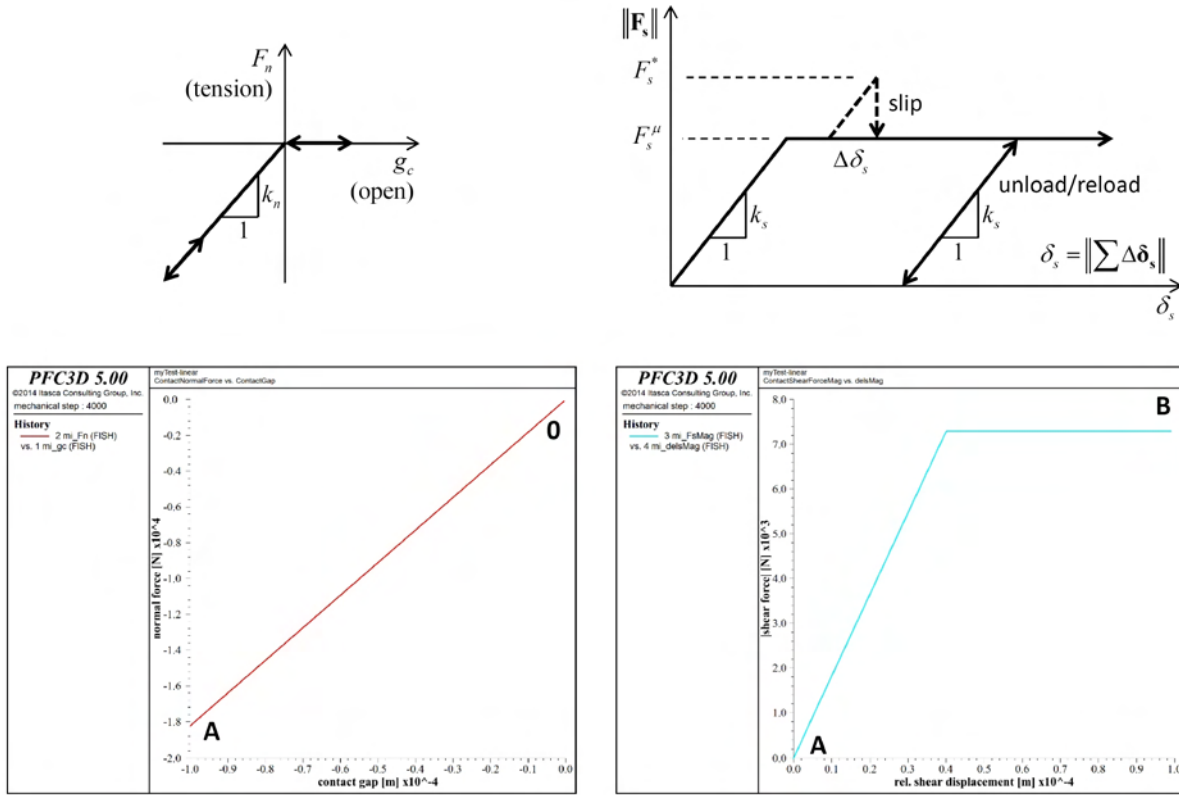
Figure 10   ***Force-displacement response of the linear model: normal force versus contact gap (left) and shear force versus relative shear displacement (right).***

The force-displacement response of the hill model is shown in Figure 11. The normal force at the end of loading-stage B is given by

$$E_e = \left(\frac{1-v_1^{\,2}}{E_1} + \frac{1-v_2^{\,2}}{E_2}\right)^{-1} = \left(\frac{2\left(1-\{0.15\}^2\right)}{29 \text{ GPa}}\right)^{-1} = 14.834 \text{ GPa}$$

$$R_e = \left(\frac{1}{R_1} + \frac{1}{R_2}\right)^{-1} = \left(\frac{1}{7.5 \text{ mm}} + \frac{1}{5.0 \text{ mm}}\right)^{-1} = 3.0 \text{ mm} \tag{24}$$

$$\tilde{k}_n = \tfrac{4}{3} E_e \sqrt{R_e} = \tfrac{4}{3}\left\{14.834\times10^9 \text{ N/m}^2\right\}\sqrt{3.0\times10^{-3} \text{ m}} = 1.0833\times10^9 \text{ N}\cdot\text{m}^{-\frac{3}{2}}$$

$$F_n^s = F_n^h + F_n^d = -\tilde{k}_n \delta_o^{\frac{3}{2}} + 0 = -\left\{1.0833\times10^9 \text{ N}\cdot\text{m}^{-\frac{3}{2}}\right\}\left\{0.1\times10^{-3} \text{ m}\right\}^{\frac{3}{2}} = -1.0833\times10^3 \text{ N}.$$

The shear force at the end of loading-stage B is given by

$$G_e = \left(\frac{2(1+v_1)(2-v_1)}{E_1} + \frac{2(1+v_2)(2-v_2)}{E_2} \right)^{-1}$$

$$= \left(\frac{4(1+0.15)(2-0.15)}{29 \text{ GPa}} \right)^{-1} = 3.4078 \text{ GPa}$$

$$R_e = \left(\frac{1}{R_1} + \frac{1}{R_2} \right)^{-1} = \left(\frac{1}{7.5 \text{ mm}} + \frac{1}{5.0 \text{ mm}} \right)^{-1} = 3.0 \text{ mm}$$

$$\tilde{k}_s = 8 G_e \sqrt{R_e} = 8 \left\{ 3.4078 \times 10^9 \text{ N/m}^2 \right\} \sqrt{3.0 \times 10^{-3} \text{ m}} = 1.4932 \times 10^9 \text{ N} \cdot \text{m}^{-\frac{3}{2}}$$

$$\left(F_{ss}^h \right)^* = -\tilde{k}_s \delta_o^{\frac{1}{2}} \Delta \delta_{ss}, \quad \left(F_{st}^h \right)^* = -\tilde{k}_s \delta_o^{\frac{1}{2}} \Delta \delta_{st} = 0 \tag{25}$$

$$= -\left\{ 1.4932 \times 10^9 \text{ N} \cdot \text{m}^{-\frac{3}{2}} \right\} \left\{ 0.1 \times 10^{-3} \text{ m} \right\}^{\frac{1}{2}} \left\{ -99.0 \ \mu\text{m} \right\} = 1.4783 \times 10^3 \text{ N}$$

$$F_s^\mu = -\mu F_n^s$$

$$= -\left\{ 0.4 \right\} \left\{ -1.0833 \times 10^3 \text{ N} \right\} = 4.3332 \times 10^2 \text{ N}$$

$$F_{ss} = 4.3332 \times 10^2 \text{ N}, \quad F_{st} = 0.$$

Figure 11 *Force-displacement response of the dry hill model with inactive dashpots: normal force versus contact gap (left) and shear force versus relative shear displacement (right).*

The linear model produces a much stiffer response than the hill model (see Figure 12). This is not surprising. The effective modulus of the linear model (and its corresponding normal stiffness) was set equal to that of granite, and this normal stiffness remains constant with increasing overlap, whereas the normal stiffness of the hill model increases with increasing overlap. The normal force of the hill model lags behind that of the linear model, and the stiffnesses (given by the slopes) become equal when the overlap reaches 12.5 mm. The normal force of the hill model finally exceeds that of the linear model when the overlap reaches 28.2 mm. The radius of the smaller grain is 5.0 mm, and thus, overlaps greater than 2.0 mm are unacceptable, because the overlap must remain small relative to the grain size for the soft-contact approach of the PFC model, in which all deformation occurs at the contacts between the rigid grains, to be valid. The behavior observed here will help guide the choice of properties for the linear and hill materials. There is a fundamental difference between the two models in that the linear model has a constant stiffness whereas the hill model has a stiffness that increases with increasing overlap. It is expected that the macroscopic modulus of a hill material will be more sensitive to confining pressure than that of a linear material.
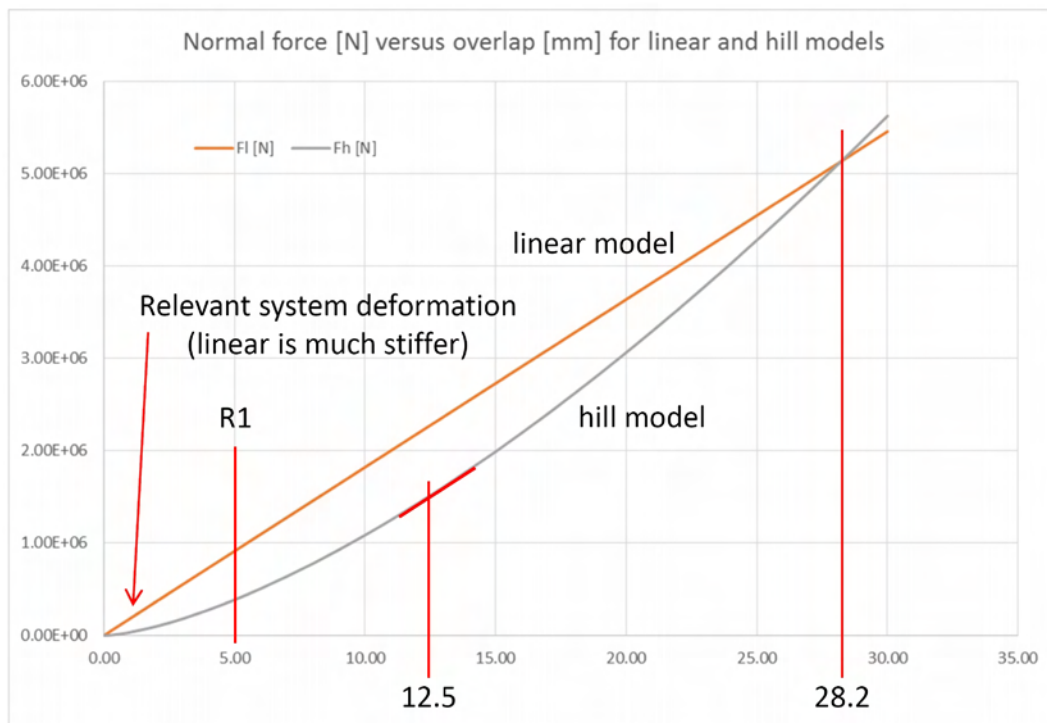
Figure 12   Normal force versus overlap for the linear and hill models.

We study the effect of the dashpots on the force-displacement response of the hill model as follows. We set the damping constant equal to zero (to insure that the normal and shear forces at the end of loading-stage B are not affected by the dashpots), and rerun the model to reach the end of loading-stage B. We then set the damping constant equal to 0.07, and move the top grain down at a velocity of 100 m/s for one time step (thereby increasing the overlap to 0.2 mm) and also increasing the normal force to 3.9604×10^3 N. Setting the velocity of the top grain to zero reduces the normal force to 3.0640×10^3 N. The computations that give these values are given by

$$m_1 = \rho\left(\frac{4}{3}\pi R_1^{\ 3}\right) = \left\{2650\ \text{kg}\middle/\text{m}^3\right\}\left(\frac{4}{3}\pi\left\{7.5\times10^{-3}\ \text{m}\right\}^3\right) = 4.6829\times10^{-3}\ \text{kg}$$

$$m_2 = \rho\left(\frac{4}{3}\pi R_2^{\ 3}\right) = \left\{2650\ \text{kg}\middle/\text{m}^3\right\}\left(\frac{4}{3}\pi\left\{5.0\times10^{-3}\ \text{m}\right\}^3\right) = 1.3875\times10^{-3}\ \text{kg}$$

$$m_e = \left(\frac{1}{m_1}+\frac{1}{m_2}\right)^{-1} = 1.0704\times10^{-3}\ \text{kg}$$

$$\tilde{\eta}_n = \alpha_h\sqrt{m_e\tilde{k}_n} = \{0.07\}\sqrt{\left\{1.0704\times10^{-3}\ \text{kg}\right\}\left\{1.0833\times10^{9}\ \text{N}\cdot\text{m}^{-\frac{3}{2}}\right\}} = 75.378\ \text{kg}\cdot\text{m}^{-\frac{1}{4}}\cdot\text{s}^{-1} \quad (26)$$

$$F_n^s = F_n^h + F_n^d = -\tilde{k}_n\delta_o^{\frac{3}{2}} - \tilde{\eta}_n\delta_o^{\frac{1}{4}}\dot{\delta}_o = -\left\{1.0833\times10^{9}\ \text{N}\cdot\text{m}^{-\frac{3}{2}}\right\}\left\{0.2\times10^{-3}\ \text{m}\right\}^{\frac{3}{2}} -$$

$$\left\{75.378\ \text{kg}\cdot\text{m}^{-\frac{1}{4}}\cdot\text{s}^{-1}\right\}\left\{0.2\times10^{-3}\ \text{m}\right\}^{\frac{1}{4}}\left\{100\ \text{m/s}\right\} = \left\{-3.0640\times10^{3}\ \text{N}\right\} - \left\{896.40\ \text{N}\right\}$$

$$= -3.9604\times10^{3}\ \text{N}.$$

We set the damping constant to zero (to insure that the normal and shear forces at the end of loading-stage B are not affected by the dashpots), the friction coefficient to 1000 (so that the shear force is not limited by the shear strength), and rerun the model to reach the end of loading-stage B, at which point the shear force is $1.4783\times10^{3}\ \text{N}$. We then set the damping constant equal to 0.07, and rotate the top grain at a rotational velocity of 1000 rad/s for one time step (thereby increasing the relative shear displacement to $103.95\ \mu m$) and also increasing the shear force to $1.5960\times10^{3}\ \text{N}$. Setting the rotational velocity of the top grain to zero reduces the shear force to $1.5522\times10^{3}\ \text{N}$. The computations that give these values are given by

$$\tilde{\eta}_s = \alpha_h\sqrt{m_e\tilde{k}_s} = \{0.07\}\sqrt{\left\{1.0704\times10^{-3}\ \text{kg}\right\}\left\{1.4932\times10^{9}\ \text{N}\cdot\text{m}^{-\frac{3}{2}}\right\}}$$

$$= 88.497\ \text{kg}\cdot\text{m}^{-\frac{1}{4}}\cdot\text{s}^{-1}$$

$$F_{ss} = F_s^h + F_s^d = -\tilde{k}_s\delta_o^{\frac{1}{2}}\Delta\delta_{ss} - \tilde{\eta}_s\delta_o^{\frac{1}{4}}\dot{\delta}_{ss} =$$

$$-\left\{1.4932\times10^{9}\ \text{N}\cdot\text{m}^{-\frac{3}{2}}\right\}\left\{0.1\times10^{-3}\ \text{m}\right\}^{\frac{1}{2}} \quad\quad\quad (27)$$

$$\left\{-99.0\ \mu m + \left(-1000.0\ \text{rad/s}\right)\left(4.95\times10^{-3}\ \text{m}\right)\left(1.0\times10^{-6}\ \text{s}\right)\right\} -$$

$$\left\{88.497\ \text{kg}\cdot\text{m}^{-\frac{1}{4}}\cdot\text{s}^{-1}\right\}\left\{0.1\times10^{-3}\ \text{m}\right\}^{\frac{1}{4}}\left\{\left(-1000.0\ \text{rad/s}\right)\left(4.95\times10^{-3}\ \text{m}\right)\right\} =$$

$$\left\{1.5522\times10^{3}\ \text{N}\right\} + \left\{43.806\ \text{N}\right\} = 1.5960\times10^{3}\ \text{N}, \quad F_{st} = 0.$$

We study the behavior of the moisture model by adding moisture to the two-grain test problem shown in Figure 8, and then allowing the system to reach static equilibrium. At this point, the moisture force is balanced by the surface force (see Figure 13).

moisture force is balanced by surface force

$$F_n^h = \tilde{k}_n \delta_o^{\frac{3}{2}} = F^m = F_{max}^m \quad \Rightarrow \quad \delta_o = 5.9463 \times 10^{-6} \text{ m}$$

$$\Delta = 5.9463 \times 10^{-6} \text{ m}$$
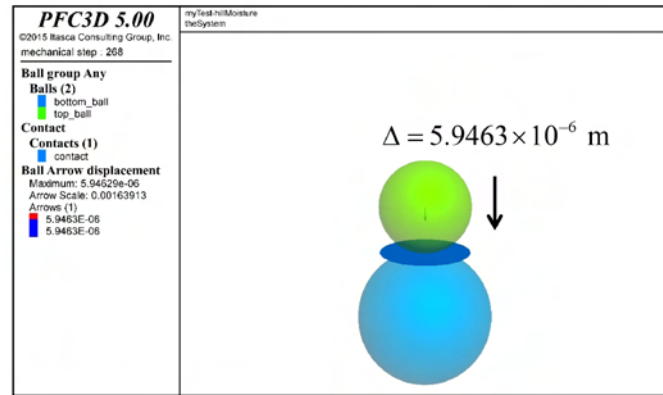
$F_n^s = -15.708$ N (compression)

$F^m = 15.708$ N (suction)

$F_c^n = -F_n^s - F^m = 0$

Figure 13   Initial state of the moisture-model test.

Next, the top ball is moved up to induce a tensile force in the contact, and when the top ball is released, the system returns to its initial state (see Figure 14). If the top ball is moved up a bit more, then the liquid bridge ruptures and the contact is deleted (see Figure 15). The top ball is then moved down until the gap is just less than 2.0 mm. At this point, moisture is added between all grains with a gap less than a moisture gap of 2.5 mm. This operation causes a new contact to be created and made moist so that when the top ball is released, the system returns to its initial state (see Figure 16).
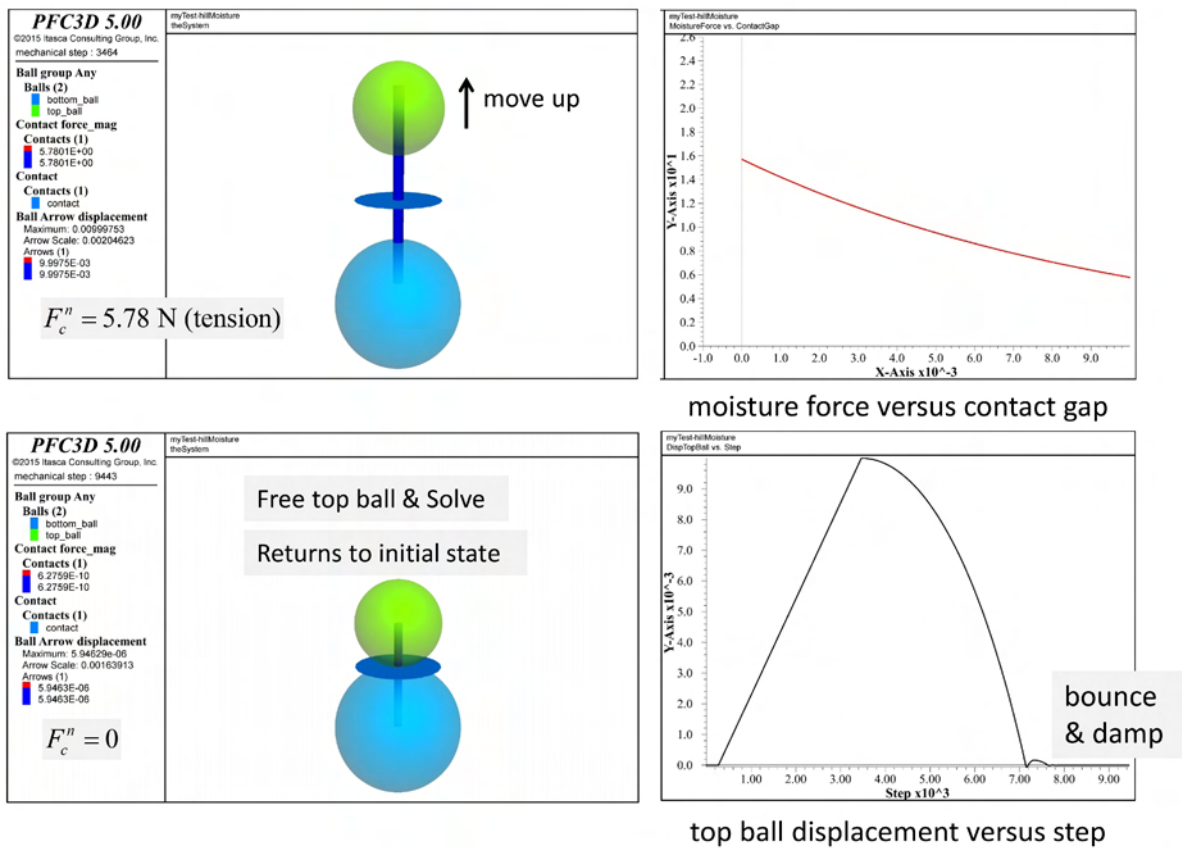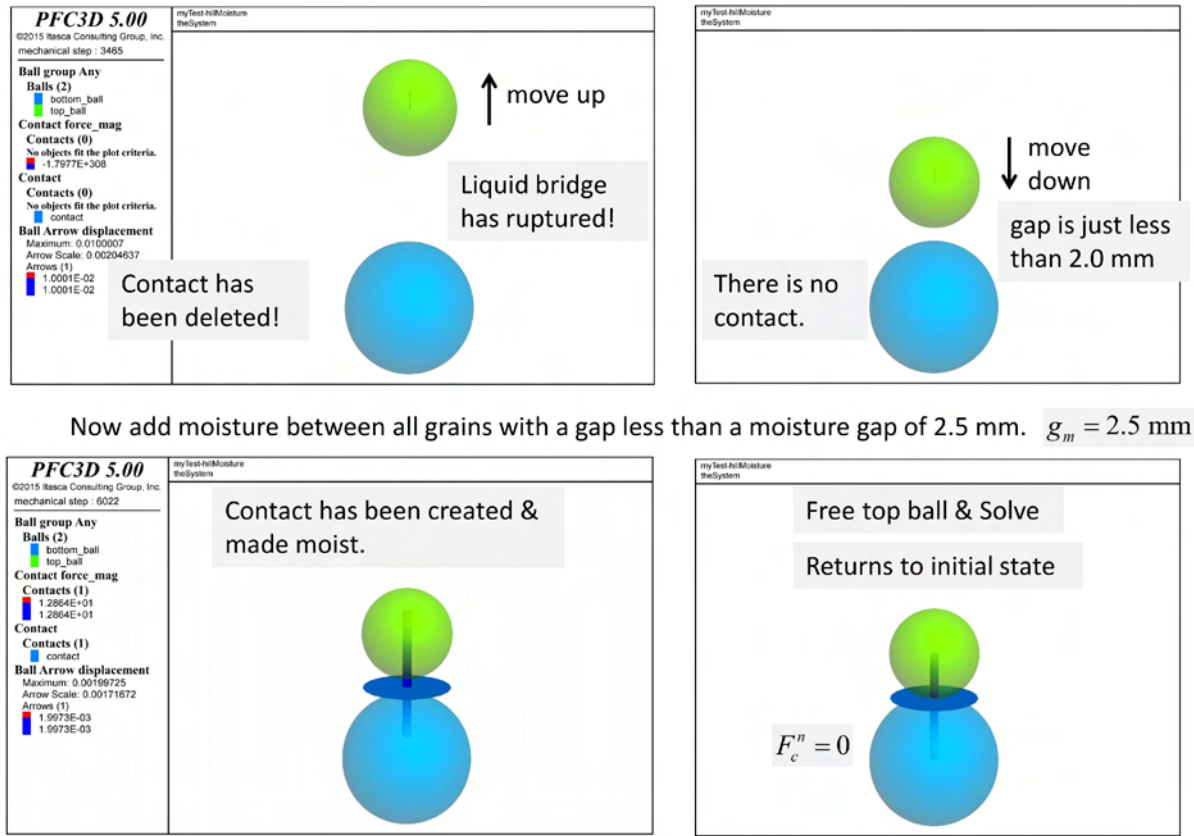
**Figure 14   Moisture-model test in which the top ball is moved up and then released.**
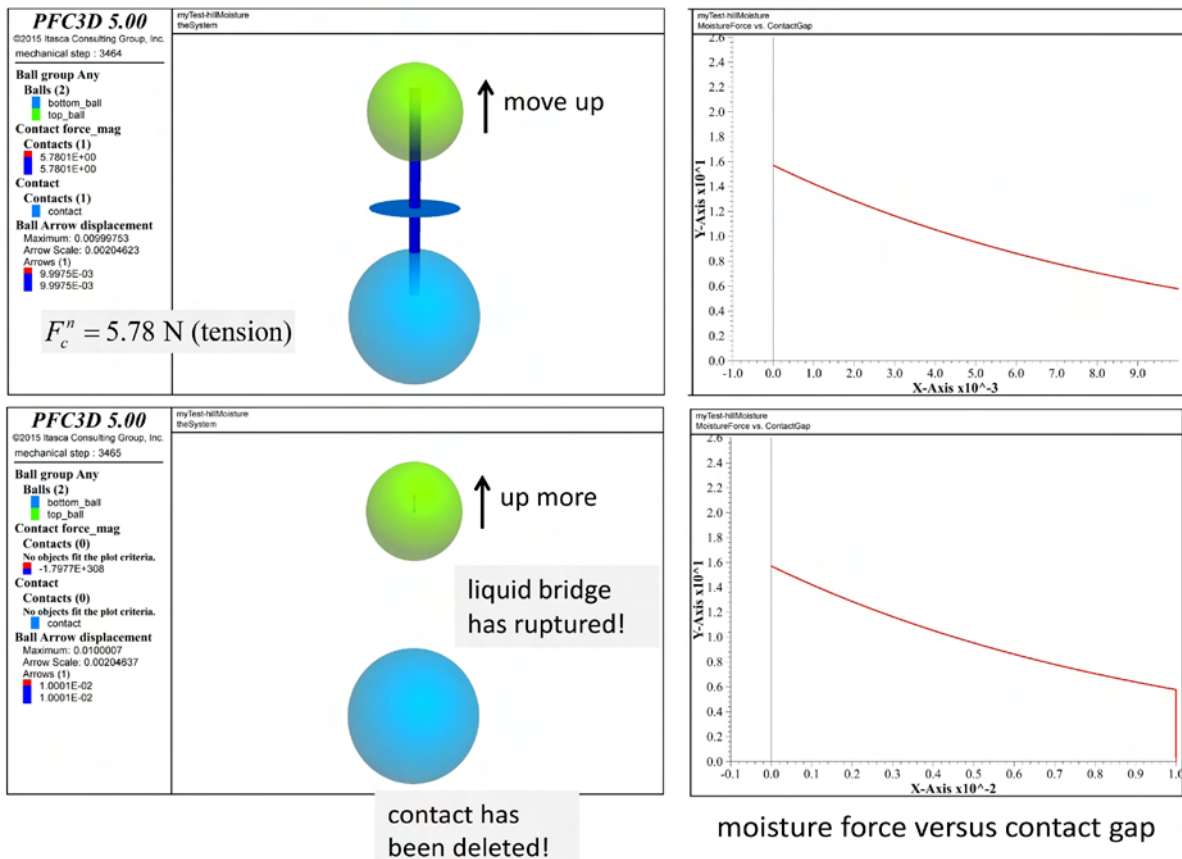
Figure 15   ***Moisture-model test in which the top ball is moved up until the liquid bridge ruptures.***

Now add moisture between all grains with a gap less than a moisture gap of 2.5 mm. $g_m = 2.5$ mm

Figure 16　**Moisture-model test in which the top ball is moved up until the liquid bridge ruptures, the top ball is moved down, moisture is added between all grains with a moisture gap less than 2.5 mm and the top ball is released.**

2.2　Assembly of Granite Grains

The grain-assembly test problem is in the **Test-AssemblyGraniteGrains** example-project directory. The problem is shown in Figure 17 and described as follows. The contact model assignment table (CMAT) is employed to ensure that all ball-ball contacts will be assigned the hill contact model and its associated properties, and all ball-facet contacts will be assigned the linear contact model and its associated properties. The model properties are given in Figure 9, but the effective modulus of the linear model is reduced to 29 MPa. A cubic packing of 27 10-mm diameter balls is generated within the center of a cubic box. Gravity is activated ($g = 9.81$ m·s^{-2}), and the model is allowed to reach static equilibrium. The total force on the bottom wall is found to equal the total weight of the balls ($W = 27\rho_g \left(\frac{4}{3} \pi R_g^{\,3} \right) g = 0.368$ N).
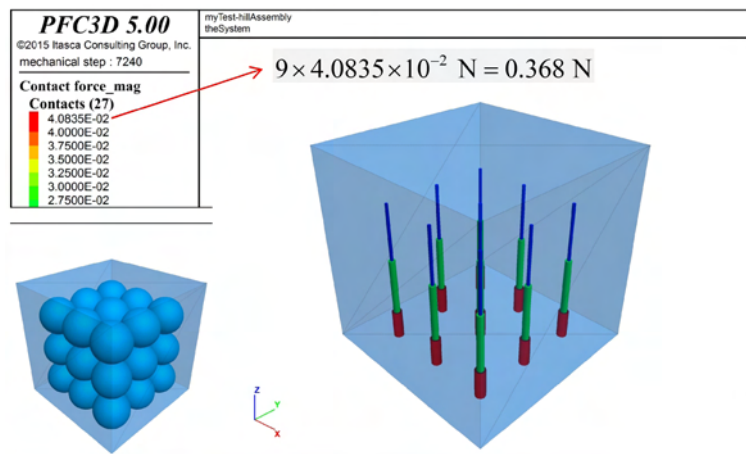
Figure 17　Grain-assembly test problem showing initial model, and model in static equilibrium after activating gravity.

2.3　Material-Behavior Study

The material-behavior study is in the **MatGen-Class5** example-project directory. Linear and hill materials are created to represent a typical aggregate base layer of an asphalt-surface roadway (Potyondy et al., 2016). The aggregate particles are modeled as granite spheres drawn from two grain-size distributions (see Figure 18). The first distribution (denoted as C5n) is narrow, with grain diameters that range from 14 to 20 mm. The second distribution (denoted as C5b) is broad to represent the upper end of the MnDOT Class 5 aggregate base grading designation. The materials are denoted as Class 5 materials with microproperties listed in Table 7. The materials are dry while being created in a cylindrical material vessel (of initial 240-mm height and 170-mm diameter, with a 500 MPa effective modulus) and packed via the boundary-contraction packing procedure at a 150 kPa material pressure as shown in Figure 19. The materials are then subjected to triaxial testing. During each triaxial test, the confinement is 150 kPa, and load-unload cycles are performed at axial strains of 0.02% and 0.05% to measure the resilient moduli (see Figures 20 and 21).[17]

---

[17] The confinement is similar to that defined in resilient modulus protocols, and axial strains correspond with vertical strains in the aggregate base layer for typical traffic loads.
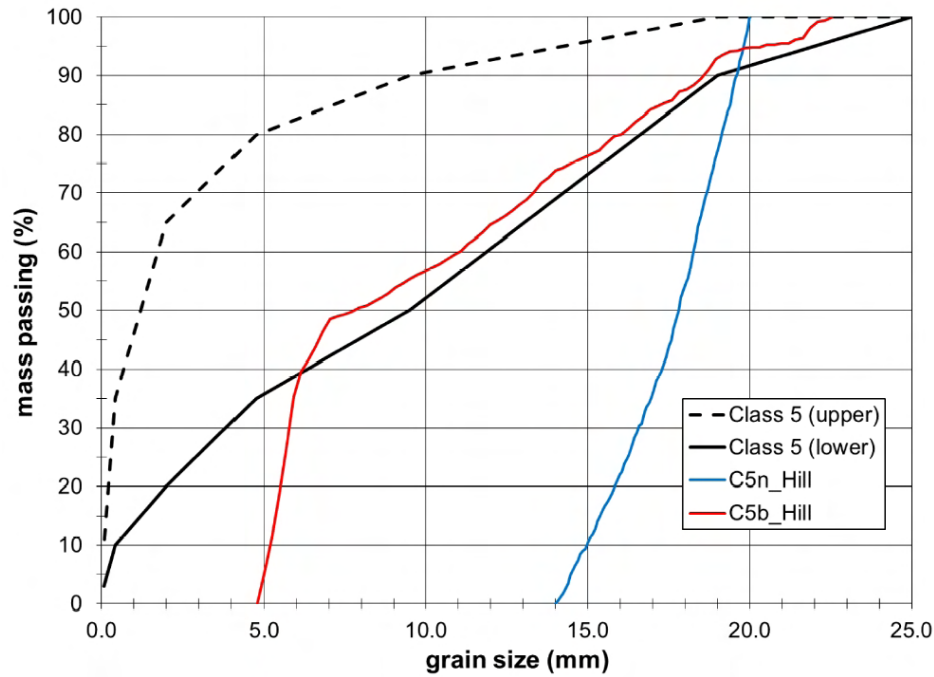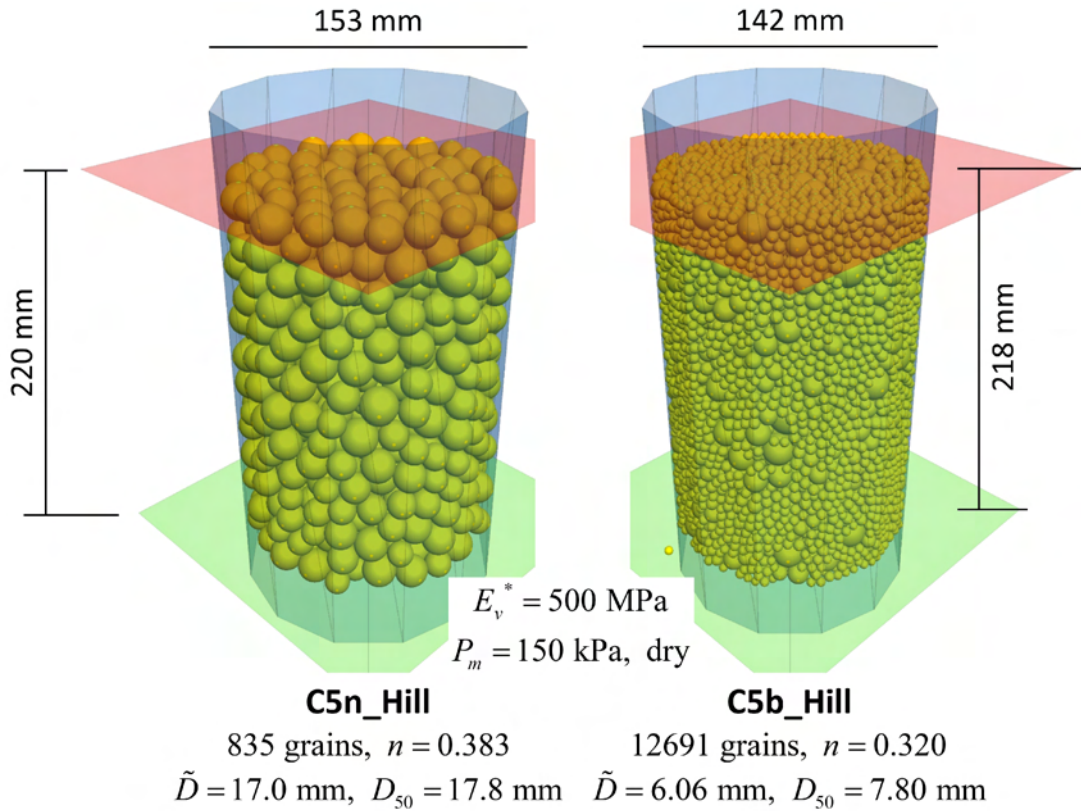
Figure 18 ***Grain size distribution curves for the Class 5 hill materials along with limits of the Class 5 grading designation. The linear materials have similar grain size distribution curves.***

Table 7 Microproperties of Class 5 Materials*

Property	Value
Common group:	
N_m	C5\{n,b\}_\{Linear,Hill\}
$T_m,\ \alpha,\ C_\rho,\ \rho_v\left[\text{kg}/\text{m}^3\right]$	\{0,4\}, 0.7, 0, 2650
$S_g,\ T_{SD},\ D_{mult}$	0, 0, 1.0
$\left\{D^{(j)}_{\{l,u\}}\ [\text{mm}],\ \phi^{(j)}\right\}$	$\{14,20,1.0\}$, C5n $\left[\begin{matrix}\{19.0,23.0,0.07\}^{(1)} & \{16.5,19.0,0.10\}^{(2)} \\ \{14.0,16.5,0.09\}^{(3)} & \{12.0,14.0,0.09\}^{(4)} \\ \{9.5,12.0,0.09\}^{(5)} & \{7.0,9.5,0.07\}^{(6)} \\ \{6.0,7.0,0.10\}^{(7)} & \{4.8,6.0,0.39\}^{(8)}\end{matrix}\right]$, C5b
Packing group:	
$S_{RN},\ P_m\,[\text{kPa}],\ \varepsilon_P,\ \varepsilon_{\lim},\ n_{\lim}$	10000, 150, 1×10^{-2}, 8×10^{-3}, 2×10^6
$C_p,\ n_c,\ \mu_{CA},\ v_{\lim}\,[\text{m/s}]$	0, 0.58, 0, 1.0
Linear material group (C5\{n,b\}_Linear)**:**	

| E^* [MPa], κ^*, μ	500, 1.5, 0.4
Hill material group (C5{n,b}_Hill)**:**	
E_g [GPa], v_g, μ, α_h, ψ [kPa]	29, 0.15, 0.4, 0, 20

* Linear material parameters are defined in Potyondy (2016), and Hill material parameters are defined in Table 2 of this memo.

153 mm

142 mm

220 mm

218 mm

$E_v^* = 500$ MPa
$P_m = 150$ kPa, dry

C5n_Hill
835 grains, $n = 0.383$
$\tilde{D} = 17.0$ mm, $D_{50} = 17.8$ mm

C5b_Hill
12691 grains, $n = 0.320$
$\tilde{D} = 6.06$ mm, $D_{50} = 7.80$ mm

Figure 19 *Class 5 hill materials packed at 150 kPa material pressure at the end of material genesis. The linear materials have similar packing and microstructural properties.*
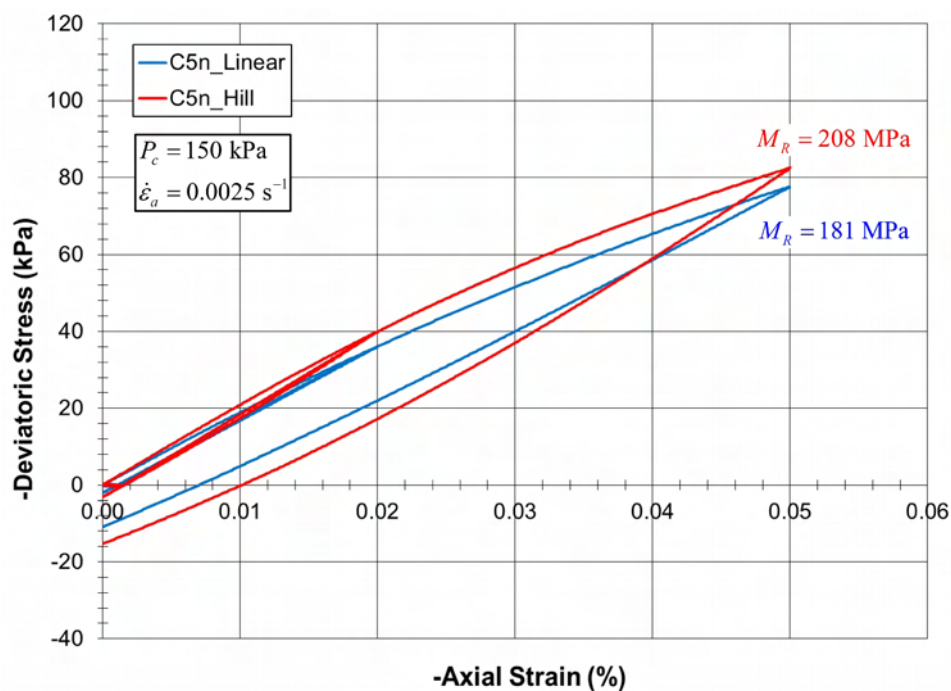
Figure 20 *Deviator stress versus axial strain for Class 5 materials with narrow grain-size distributions tested at 150 kPa confinement.*
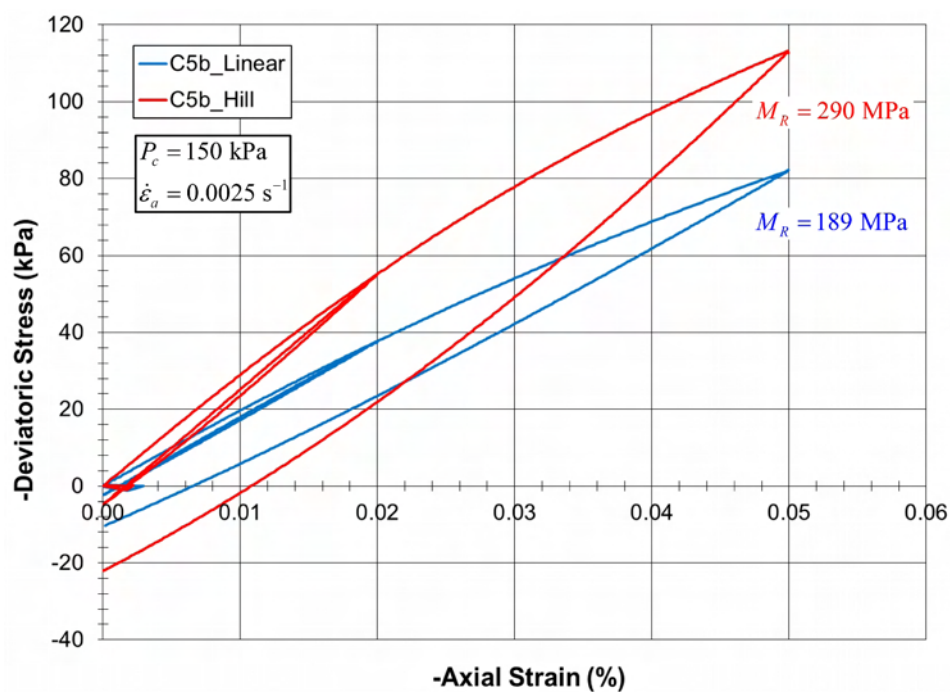
Figure 21 *Deviator stress versus axial strain for Class 5 materials with broad grain-size distributions tested at 150 kPa confinement.*

The linear and hill materials differ in the force-displacement response of their respective grain-grain systems. The linear material has linear springs that provide a linear force-displacement response, while the hill material has Hertz-Mindlin springs that provide a nonlinear force-displacement response. The stiffness of the linear springs remains constant, while the stiffness of the Hertz-Mindlin springs increases with increasing overlap. The following conclusions can be drawn from this study.

- The materials with the broad grain-size distribution pack to a lower porosity $(n = 0.320)$ than those with the narrow grain-size distribution $(n = 0.383)$.

- The stress-strain responses of both materials are similar. There is a hysteretic loop during each load-unload cycle. The size of the hysteretic loop is greater for the hill material.

- The materials with the broad grain-size distribution are stronger and stiffer than those with the narrow grain-size distribution. The increase of strength and stiffness is more pronounced for the hill material.

If moisture is added to the hill material, then it will behave like an unsaturated granular material. The hill material with the broad grain-size distribution is made wet before being subjected to the triaxial test described above. The wet material has a 20 kPa suction added between all grains that are within 3 mm of one another at the end of material genesis.[18] The stress-strain responses of the dry and wet hill materials are compared in Figure 22. The stress-strain responses are similar, and the resilient modulus is increased for the wet material.

{DP: Generate new plots for Figs. 20-22 with y-axes labelled "-Deviator Stress (kPa)".}

{DP: Perform a UCS test on the wet hill material described in the preceding paragraph. It may be necessary to reduce the material pressure during the dry packing process to 20 kPa. We expect the response to be similar to that of the wetted glass beads described in Richefeu et al. (2008): (a) the axial stress versus axial strain curve is steep, and then reaches a peak and remains plastic-like; and (b) a plot of peak axial stress (UCS) versus water content gives an increase of UCS (from 0 to 300 Pa) with increasing water content (from 0 to 12 percent).}

---

[18] The suction is typical for aggregates with gravimetric moisture content ranging from 5 to 10 percent.
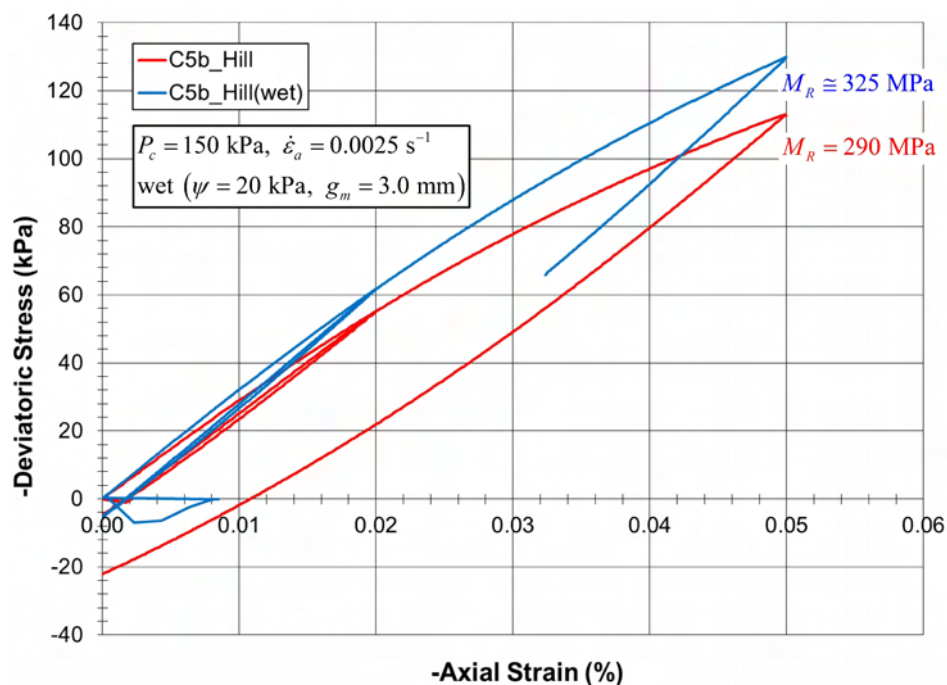
Figure 22   ***Deviator stress versus axial strain for dry and wet hill materials with broad grain-size distribution tested at 150 kPa confinement.***

3.0   REFERENCES

Gupta, S.C., and W.E. Larson. (1979) "Estimating Soil Water Retention Characteristics from Particle Size Distribution, Organic Matter Percent, and Bulk Density," *Water Resources Research*, *15*, 1633–1635.

Gupta, S., A. Ranaivoson, T. Edil, C. Benson, and A. Sawangsuriya. (2007) "Pavement Design Using Unsaturated Soil Technology," Minnesota Dept. of Transportation, Saint Paul, Minnesota, MnDOT 2007-11, 2007.

Gupta, S., A. Singh, and A. Ranaivoson. (2005) "Moisture Retention Characteristics of Base and Sub-base Materials," Minnesota Dept. of Transportation, Saint Paul, Minnesota, MnDOT 2005-06, 2005.

Itasca Consulting Group, Inc. (2016) *PFC — Particle Flow Code in 2 and 3 Dimensions*, Version 5.0, Documentation Set of version 5.00.24 [May 8, 2016]. Minneapolis: Itasca.

Itasca Consulting Group, Inc. (2008) *PFC3D — Particle Flow Code in 3 Dimensions*, Version 4.0, User's Manual. Minneapolis: Itasca.

Lian, G., C. Thornton and M.J. Adams. (1993) "A Theoretical Study of the Liquid Bridge Forces between Two Rigid Spherical Bodies," *J. Colloid and Interface Science*, *161*, 138–147.

Mindlin, R.D. (1949) "Compliance of Elastic Bodies in Contact," *Journal of Applied Mechanics, 16*(3), 259–268. Also cited as *Journal of Applied Mechanics, Transactions ASME*, **71**, A-259–268.

Mindlin, R.D., and H. Deresiewicz. (1953) "Elastic Spheres in Contact Under Varying Oblique Forces," *Journal of Applied Mechanics, 20*(3), 327–344.

Muguruma, Y., T. Tanaka and Y. Tsuji. (2000) "Numerical Simulation of Particulate Flow with Liquid Bridge between Particles (Simulation of Centrifugal Tumbling Granulator)," *Powder Tech.*, *109*, 49–57.

Potyondy, D. (2016) "Material-Modeling Support in PFC [fistPkg23]," Itasca Consulting Group, Inc., Technical Memorandum ICG7766-L (June 23, 2016), Minneapolis, Minnesota.

Potyondy, D. O. (2015) "The Bonded-Particle Model as a Tool for Rock Mechanics Research and Application: Current Trends and Future Directions," *Geosystem Engineering, 18(1)*, 1–28.

Potyondy, D., and S. Emam. (2009) "A Particle-Based Model for Studying Excavation Damage at Tournemire Underground Laboratory — Phase II: Hydric Damage and Tunnel Simulations," Itasca Consulting Group, Inc., Report to Institute of Radioprotection and Nuclear Safety (IRSN), Fontenay-Aux-Roses Cedex, France, ICG09-2454-13, May 2009.

Potyondy, D., and S. Emam. (2008) "A Particle-Based Model for Studying Excavation Damage at Tournemire Underground Laboratory — Phase I: Relevant Mechanisms," Itasca Consulting Group, Inc., Report to Institute of Radioprotection and Nuclear Safety (IRSN), Fontenay-Aux-Roses Cedex, France, ICG08-2454-31, October 21, 2008.

Potyondy, D., J. Siekmeier, and L. Petersen. (2016) "Aggregate-Geogrid Interaction Model Incorporating Moisture Effects," in Transportation Research Board 2016 Annual Meeting Compendium of Papers.

Richefeu, V., M.S. El Youssoufi, R. Peyroux and F. Radjai. (2008) "A Model of Capillary Cohesion for Numerical Simulations of 3D Polydisperse Granular Media," *International Journal for Numerical and Analytical Methods in Geomechanics*, *32(11)*, 1365–1383.

Tan, D., K. Hill and L. Khazanovich. (2014a) "Quantifying Moisture Effects in DCP and LWD Tests Using Unsaturated Mechanics," Dept. of Civil Engr., University of Minnesota, Final Report to Minnesota Dept. of Transportation, Saint Paul, Minnesota, MN/RC 2014-13, February 2014.

Tan, D.S., L. Khazanovich, J. Siekmeier and K.M. Hill. (2014b) "Discrete Element Modeling of Effect of Moisture and Fine Particles in Lightweight Deflectometer Test," *Transportation Research Record: Journal of the Transportation Research Board*, No. 2433, 58–67, 2014, DOI: 10.3141/2433-07. Washington, D.C.: Transportation Research Board of the National Academies.

Timoshenko, S.P., and J.N. Goodier. (1970) **Theory of Elasticity**, Third Edition, New York: McGraw-Hill Book Company, Inc.

Tsuji, Y., T. Tanaka and T. Ishida. (1992) "Lagrangian Numerical Simulation of Plug Flow of Cohesionless Particles in a Horizontal Pipe," *Powder Tech.*, *71*(3), 239–250.

APPENDIX A: INCREMENTAL UPDATE OF SHEAR FORCE

The present implementation of the Hill model differs from Tan et al. (2014b) by providing an incremental (as opposed to an absolute) update of the shear force, which is believed to be more appropriate for static grain assemblies. The justification for this modification is presented here.

The present implementation performs an incremental update of the shear force (of the form $\mathbf{F_s^*} = (\mathbf{F_s})_0 - \tilde{k}_s \delta_o^{\frac{1}{2}} \Delta \boldsymbol{\delta_s} + \mathbf{F_s^d}$ where $(\mathbf{F_s})_0$ is the shear force at the beginning of the time step) as opposed to an absolute update (of the form $\mathbf{F_s^*} = -\tilde{k}_s \delta_o^{\frac{1}{2}} \boldsymbol{\delta_s^e} + \mathbf{F_s^d}$ where $\boldsymbol{\delta_s^e}$ is the effective shear overlap). The absolute update does not pass the following physical thought experiment (see Figure 23). Constrain the motion of the two particles such that all motion is imposed. Apply a relative normal displacement $(\delta_o)_A$ and keep this value constant while applying a relative shear displacement of $(\delta_s)_A$ to obtain a shear force $(F_s)_A$. Double the relative normal displacement (such that $(\delta_o)_B = 2(\delta_o)_A$). What should happen to the shear force? The shear force should not change. Using an absolute update will increase the shear force, whereas using an incremental update will not change the shear force. As the shear force responds to relative shear motion, the current effective shear stiffness should be employed to obtain incremental updates to the shear force.
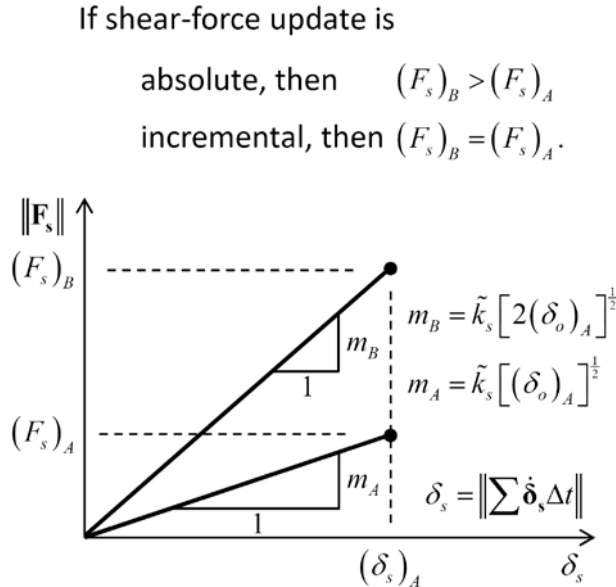
Figure 23 *Physical behavior during thought experiment in which the overlap is doubled. The shear force should not change. An absolute update of the shear force will increase the shear force, whereas an incremental update of the shear force will not change the shear force.*